Design, synthesis and characterization of a bioanode for microbial fuel cell

Jérémie-Luc Sanchez

▶ To cite this version:

Jérémie-Luc Sanchez. Design, synthesis and characterization of a bioanode for microbial fuel cell. Other. Université Paris Cité, 2019. English. NNT : 2019UNIP7195 . tel-03189382

HAL Id: tel-03189382
https://theses.hal.science/tel-03189382

Submitted on 3 Apr 2021

HAL is a multi-disciplinary open access archive for the deposit and dissemination of scientific research documents, whether they are published or not. The documents may come from teaching and research institutions in France or abroad, or from public or private research centers.

L'archive ouverte pluridisciplinaire **HAL**, est destinée au dépôt et à la diffusion de documents scientifiques de niveau recherche, publiés ou non, émanant des établissements d'enseignement et de recherche français ou étrangers, des laboratoires publics ou privés.

THÈSE DE DOCTORAT DE L'UNIVERSITÉ DE PARIS

préparée à Sorbonne Université

au Laboratoire de Chimie de la Matière Condensée de Paris

DESIGN, SYNTHESIS & CHARACTERIZATION OF A BIOANODE FOR MICROBIAL FUEL CELL

Conception, synthèse & caractérisation d'une bioanode pour pile à combustible microbienne

Soutenue par
Jérémie-Luc Sanchez
le 10 septembre 2019

École doctorale 474
FIRE – Frontières du Vivant

Spécialité
Science des matériaux & Biotechnologie

Composition du jury :

Benoît Piro *Professeur à l'Université de Paris*	Président du jury
François Guyot *Professeur au Muséum national d'Histoire naturelle*	Rapporteur
Dominique Larcher *Professeur à l'Université de Picardie-Jules-Verne*	Rapporteur
Hubert Perrot *Directeur de recherche CNRS à Sorbonne Université*	Examinateur
Christel Laberty-Robert *Professeur à Sorbonne Université*	Directrice de thèse

Except where otherwise noted, this work is licensed under
http://creativecommons.org/licenses/by-nc-nd/3.0/

Résumé de la thèse en français :

L’urgence climatique rend plus que jamais incontournable le développement de sources d’énergie propres. Fondés sur les travaux que M. C. Potter mena en 1911, un nombre croissant de chercheurs se sont intéressés à la possibilité d’utiliser des microorganismes pour produire de l’électricité, et ont démontré que ce projet est réalisable. De tels dispositifs, les piles à combustibles microbiennes (PCM), puisent dans l’activité métabolique de bactéries dégradant des molécules organiques, en récupérant les électrons issus de leur respiration. Ces biopiles sont ainsi une source d’énergie renouvelable. Cependant, les modèles existants aujourd’hui doivent être significativement améliorés avant de pouvoir représenter une technologie performante, stable, et rentable. Plusieurs approches existent pour atteindre cet objectif. Par exemple, le transfert électronique entre la bactérie et l’électrode peut être amélioré en travaillant sur la nature du microorganisme ou du consortium bactérien utilisé. Dans ce projet, nous cherchons plutôt à optimiser le matériau et l’architecture d’une anode colonisée par des bactéries au sein d’une PCM. La conception de ce nouveau système est fondée sur l’observation des limites des bioanodes actuellement utilisées.

Cette thèse s’intéresse ainsi à la conception d’une bioanode pour pile à combustible microbienne par électrofilage. Ce procédé permet la mise en forme de fibres de polymère nano à micrométriques par extrusion électro-assistée. Ainsi, nous obtenons une membrane de fibres entremêlées que l’on rend conductrice à l’aide de traitements thermiques ou de l’adjonction de particules carbonées. Les électrodes obtenues, adaptées à l’échelle bactérienne, sont ensuite colonisées par la bactérie électroactive *Shewanella oneidensis.* Cette étape est accomplie soit en laissant un biofilm se développer (*in situ* ou *ex situ*), soit en encapsulant les bactéries dans des fibres cœur-coquille. Par la suite, les bioanodes sont intégrées dans un montage de biopile pour évaluer leurs performances et caractéristiques électrochimiques. Les électrodes développées sont alors comparées aux performances mentionnées dans la littérature et montrent de remarquables densités volumiques de puissance et de courant (jusqu’à $3{,}26 \cdot 10^{3}\ \mathrm{A \cdot m^{-3}}$ et $296\ \mathrm{W \cdot m^{-3}}$ contre $2{,}08 \cdot 10^{3}\ \mathrm{A \cdot m^{-3}}$ et $500\ \mathrm{W \cdot m^{-3}}$ pour des réacteurs optimisés dans des conditions similaires (Ringeisen *et al.*, 2006)). Un procédé basé sur la cryodessiccation et visant la conservation à long terme des électrodes conçues est aussi présenté. Enfin, les bioanodes développées sont utilisées pour produire de l’électricité à partir de véritables eaux usées. De même, leurs performances sont évaluées et sont encourageantes ($4{,}4 \cdot 10^{3}\ \mathrm{A \cdot m^{-3}}$ et $438\ \mathrm{W \cdot m^{-3}}$).

Mots-clés en français : Électrochimie ; Matériaux ; Microbiologie ; Électrofilage ; Biopile ; Énergies propres.

« On ne découvre pas de terre nouvelle sans consentir à perdre de vue, d'abord et longtemps, tout rivage. »

– André Gide

Remerciements :

De nombreuses personnes m'ont conseillé, inspiré et appuyé dans la préparation de cette thèse ; il me sera difficile de toutes les citer ici.

Cependant, je souhaite remercier grandement ma directrice de thèse, Christel Laberty-Robert, pour son encadrement durant ces trois ans. Outre son aide scientifique inestimable et le recul qu'elle a apporté sur mon travail, elle a toujours été là pour me soutenir lors des passages difficiles.

Je tiens à remercier François Guyot et Dominique Larcher d'avoir accepté d'être les rapporteurs de ma thèse. Ils ont pris le temps de d'étudier avec attention mon travail et d'en discuter avec moi. J'ai pu profiter de leur excellence scientifique pour parfois aborder mes résultats sous un angle nouveau.

Dominique en particulier, avec Jennyfer Miot, ont régulièrement évalué l'avancement de mes travaux lors des comités de suivi de thèse et m'ont apporté de précieux conseils tout au long de ceux-ci.

Je souhaite également remercier Hubert Perrot et Benoît Piro d'avoir accepté de faire partie de mon jury de thèse. Le temps qu'il ont consacré à la lecture de mon manuscrit et la pertinence des questions qu'ils m'ont posé m'ont permis de prendre du recul sur certains aspects de mon travail.

Je tiens à remercier le Centre de Recherches Interdisciplinaire, la fondation Bettencourt Schueller et l'école doctorale FIRE – Frontières du Vivant. Son jury scientifique m'a accordé sa confiance et un financement sans lesquels je n'aurais pu mener à bien ces trois ans de travaux.

Je n'aurais pas non plus pu mener à terme cette thèse sans l'ambiance chaleureuse qui règne au sein du laboratoire, ni sans le soutien que l'on trouve au quotidien chez chacun de ses membres ; ses permanents, ses anciens, ses stagiaires et bien sûr, ses doctorants. Parmi ceux-ci, j'ai une pensée toute particulière pour Élise, Karol, Antoine, Théau et Florent, avec qui j'ai partagé mon bureau, pour le meilleur et pour le pire, pendant ces trois ans.

De même, ces remerciements ne seraient pas complets si je n'y mentionnais pas toutes celles et ceux que j'ai croisés pendant mes études. Depuis l'enfance, en classes préparatoires, à l'ESPCI, ou en thèse, je n'oublie pas les amis avec qui j'ai partagé un verre, une soirée ou un cours. J'en ai perdu de vue, j'en côtoie encore beaucoup.

Enfin, je souhaite sincèrement remercier ma famille pour leur aide et leur compréhension tout au long de mes études. Une page se tourne à présent, et je n'en serais pas là aujourd'hui sans le sens du travail que m'a confié ma mère, sans la curiosité scientifique qu'à fait grandir chez moi mon père. Papa, Maman, Anne-Carmen, et tous mes proches, merci.

TABLE OF CONTENTS

TABLE OF CONTENTS

General Introduction 23

References 26

Chapter 1. Literature review 31

- 1.1. Global energy context 31
- 1.2. From fuel cell to biofuel cell 32
  - 1.2.1. Overview of a fuel cell 32
  - 1.2.2. Biofuel cells 33
  - 1.2.3. Building a microbial fuel cell 36
  - 1.2.4. Microbial fuel cells & derived applications 37
- 1.3. Exoelectrogenic bacteria & microbial fuel cells 40
  - 1.3.1. Microbial respiration 40
  - 1.3.2. Exoelectrogenic bacteria & electron transfer 42
  - 1.3.3. Exoelectrogenic strains 47
  - 1.3.4. Biofilm & planktonic bacteria 50
- 1.4. Power generation in microbial fuel cells 52
  - 1.4.1. Thermodynamics & cell voltage 52
  - 1.4.2. Standard electrode potentials 52
  - 1.4.3. Open circuit voltage 53
- 1.5. Key factors of microbial fuel cell efficiency 54
  - 1.5.1. Bacterial metabolism 54
  - 1.5.2. Mass transport phenomena 55
  - 1.5.3. Architecture & electrodes 56
  - 1.5.4. Performances evaluations 56
- 1.6. Microbial fuel cells architectures & materials 60
  - 1.6.1. Cell architecture 60
  - 1.6.2. Cathode materials 61
  - 1.6.3. Separators 62
  - 1.6.4. Anode materials 63
- 1.7. Electrospinning & electrode materials 68
  - 1.7.1. Fundamentals 68

1.7.2. Electrospinning parameters 70
1.8. Conclusion & positioning of the study 79
1.8.1. Electrogenic microorganism 79
1.8.2. MFC reactor 80
1.8.3. Cathode & catholyte 80
1.8.4. Separator 80
1.8.5. Anode design 81
1.8.6. Layout of the study 81
References 83
Chapter 2. Carbon microfibers bioanode 99
2.1. Introduction & objectives 99
2.2. Lab-made electrospun carbon microfibers 100
2.2.1. Polyacrylonitrile & carbon fibers 100
2.2.2. Experimental procedure 103
2.3. Bioanode colonization process 119
2.3.1. Bacterial culture 120
2.3.2. Membrane precolonization & ready-to-use bioanodes 132
2.4. 3D ready-to-use carbon microfibers bioanode 139
2.4.1. Experimental procedure 139
2.4.2. Effect of bioanode stacking & thickness 139
2.4.3. Biofilm overgrowth 148
2.4.4. Microfibers architecture & diffusion limitations 149
2.5. Cryodesiccation & conservation 152
2.5.1. Experimental procedure 152
2.5.2. Bacteria viability & exoelectrogenic activity 154
2.6. Conclusion 160
References 161
Chapter 3. One-step electrospun conductive fibers 169
3.1. Introduction & objectives 169
3.2. Lab-made conductive membrane preparation 170
3.2.1. Electrospinning of a composite carbon–polymer fibers network 170

3.2.2. Lab-made carbon nanofibers load 170
3.2.3. Carbon black load 175
3.3. Dual electrospun network & composite carbon–polymer fibers 182
3.3.1. Experimental procedure 182
3.3.2. Dual electrospun mat characterization 184
3.4. Bacteria viability on composite carbon–polymer fibers 187
3.4.1. Live/dead assay 187
3.4.2. Electrochemical activity 188
3.5. Conclusion 194
References 195
Chapter 4. Core-shell architecture: Designing a one-step bacteria-encapsulating bioanode 201
4.1. Introduction & objectives 201
4.2. Lab-made core-shell coelectrospun fibers 202
4.2.1. Design of a coelectrospinning apparatus 202
4.2.2. Experimental procedure 203
4.2.3. Core-shell architecture characterization 206
4.3. Bacteria encapsulation 211
4.3.1. Bacterial culture 211
4.3.2. Core-shell coextrusion 211
4.3.3. Bacteria encapsulation characterization 212
4.4. Dual electrospun core-shell/conductive fibers scaffold network 216
4.4.1. Dual electrospinning setup 216
4.4.2. Network characterization 219
4.5. Integrated one-step conductive bioanode encapsulating electroactive bacteria 223
4.5.1. Electrospinning setup 223
4.5.2. Bioanode characterization 225
4.5.3. Integrated bioanode cryodesiccation 232
4.6. Conclusion 242
References 244
Chapter 5. Toward electricity generation from wastewaters 251
5.1. Introduction & objectives 251

5.2. Wastewaters characterization 253
5.2.1. Sample properties & organic matter content 253
5.2.2. Microbiome diversity analysis 254
5.3. Electrospun carbon electrode 257
5.3.1. MFC integration & electrochemical characterization 257
5.3.2. Post-mortem imaging 261
5.3.3. Effect on microbial diversity 262
5.4. Integrated bioanode 264
5.4.1. MFC integration & electrochemical characterization 264
5.4.2. Post-mortem imaging 266
5.5. Conclusion 269
References 270
General Conclusion 275
Prospects 277
References 279
Appendices 285
A.1. Abbreviations 285
A.2. Chemicals references 287
A.3. Experimental methods 288
A.3.1. Electrospinning 288
A.3.2. Coelectrospinning spinneret design 288
A.3.3. Heat treatments 290
A.3.4. Electrochemical measurements 290
A.3.5. Impedance spectroscopy 290
A.3.6. X-ray diffraction 290
A.3.7. X-ray photoelectron spectroscopy 291
A.3.8. Raman spectroscopy 291
A.3.9. Fourier transform infrared spectroscopy 291
A.3.10. N_2 physical adsorption 291
A.3.11. Mercury intrusion porosimetry 291
A.3.12. Scanning electron microscopy & energy-dispersive X-ray spectroscopy 292

A.3.13. Epifluorescence microscopy 292
A.3.14. Confocal microscopy 292
A.3.15. Cryodesiccation 292
A.3.16. Ball-milling 292
A.3.17. Thermogravimetric analysis & differential scanning calorimetry 292
A.3.18. Bacterial culture 293
A.3.19. 16S rRNA sequencing 294
A.3.20. Microbial fuel cell setup 294
A.3.21. Data treatment 296

GENERAL INTRODUCTION

GENERAL INTRODUCTION

Over the last few decades researchers have grown ever and ever more confident that the climate of our planet was changing and that most of this phenomenon was linked to human emissions of greenhouse gases[1]–[3]. At the same time fossil fuel sources appeared to be limited and light was shed on the dependence of the global economy on an ever-growing cheap flow of these resources to avoid stagnation or even crises[4],[5]. In the wake of these issues, both governments and the private sector have invested in developing alternative energy sources. Today, the best-known substitutes are nuclear power akin to renewable energy technologies such as hydro power, wind power or solar energy. The latter are already well developed, but their widespread adoption is still challenging without strong public incentives.

Among other energy systems that can rely on a sustainable process, fuel cells stand out. The most widespread and robust fuel cell system relies on the oxidation of dihydrogen at the anode, while dioxygen – usually from air – is reduced at the cathode[6],[7]. This process allows a steady electrical output yielding only water as a chemical byproduct. Nevertheless, both the oxidation and the reduction need expensive platinum catalysts to take place[8], and the worldwide production of hydrogen still heavily relies on steam reforming of natural gas, coal or oil[9] even if the water-splitting route is on the rise[10]. Furthermore, an efficient hydrogen logistic network has to be developed and the population educated on the matter[11] before hydrogen fuel cells can become widespread.

Besides, from the nineties and onward the scientific community have seen a steep increase in interest on an alternative to conventional electrochemical fuel cells with biofuel cells. In such bio-electrochemical systems the catalyst needed to promote the oxidation reaction is replaced by biological agents[12],[13] – microorganisms or purified enzymes – and the scope of potential fuels is greatly expanded to a broad range of organic molecules that are of little energy interest otherwise, and usually overlooked as worthless wastes. By specifically using electroactive bacteria, able to self-replicate and to thrive with a large autonomy, the so-called microbial fuel cells (MFC) may therefore be a competitive addition to the current energy mix. Accordingly, even if these systems invariably yield much smaller power outputs than their more classic counterparts, the 21st century has started to find commercially viable applications to this emerging technology[14]. Nowadays integration of MFCs is already actively investigated in wastewater treatment plants as a way to extract energy from organic wastes as well as partially depolluting water. Water extraction, treatment and distribution thus represent 4 % of the global electricity expenses[15] and as simple figure, wastewater may contain as much as 9.3-fold the energy needed to treat it[16]. Full-scale pilot MFCs integrated in a wastewater treatment plant have hence been recently tested[17]. Eventually, MFCs may be useful in niche applications that require low power output for prolonged timeframe in remote locations such as environmental probes.

Due to their heavily transdisciplinary nature, spanning from microbiology to electrochemistry, material science and engineering, MFCs need a thorough study to be optimized and set as a readily available energy source. Improvements can be made in understanding the biology of the electroactive bacteria[18] and the bacterial electron transfer at the electrode interface[19]. New materials may be developed to ensure optimal colonization and better electron transfer between the microorganisms and the electrode. Likewise, the architecture of the fuel cell must be enhanced to improved overall efficiency.

Better electrodes can therefore be designed by tailoring a bioanode architecture well-suited to the bacterial scale, such as conductive nano or microfibers[20]. In parallel, electrospinning[21] is a robust method that draws threads of polymer by electrostatically extruding a polymer solution that can then be exploited to produce the desired electrode architecture.

This thesis will accordingly focus on the design, the synthesis and the characterization of a new architecture for an MFC bioanode. Along this project a wild strain of *Shewanella oneidensis* will be used a model electroactive bacterium, as well as bacterial consortia from actual wastewaters. All electrospun membranes used as bioanode scaffolds will be made with a lab-scale electrospinning apparatus tweaked to address the conditions needed to produce the desired architectures. A particular attention will be paid to understanding the strengths and limits of electrospun fibers mats for an MFC application, and the main objective will be to eventually present a new bioanode design, embedding bacteria in a core-shell design and able to be stored for long term and ready to be used when needed. Both microbiological, electrochemical and chemical engineering techniques will be applied to meet this objective.

The first chapter introduces an overview of the current fuel cell technology and thoroughly presents the operation principle of an MFC. It then explores the biology foundations of bacterial electron transfers and exposes the various anodic materials which can be involved in such phenomena. It eventually focuses on the electrospinning process and how it can be applied to the generation of useful materials to be included in an MFC.

A second chapter presents the production of carbon microfibers bioanodes through a multi-step approach. From electrospinning of a polymer fibers mat and heat treatments to the bacterial colonization, ready-to-use conductive anodes are synthetized and their architecture, electrochemical behavior and stability are investigated. The influence of electrode thickness regarding nutrient diffusion and the degree of bacterial colonization are explored, before dealing with the bioanode conservation and viability through cryodesiccation.

A third chapter then exposes a route of one-step preparation of a conductive an electrospun fibers mat, removing the need for the impractical heat treatments. Different methods are compared and they are characterized by electronic microscopy, impedance spectroscopy and electrochemical assays. Finally, bacteria viability is evaluated on those electrospun networks.

Afterwards, a fourth chapter presents the integration of these results into a core-shell electrospun conductive network encapsulating the electroactive bacteria. This system is designed to allow a one-step preparation of a ready-to-use bioanode, easily storable and able to quickly recover an electrical output upon use. The encapsulation of bacteria is also shown to have an effect on their electron transfer, as well as improving the anodic stability of the MFC. Epifluorescence and confocal as well as electronic microscopies are used to investigate the architecture of the system. Electrochemical and impedance spectroscopy assays are also used to characterize the material. These results are evaluated and show that this method is a promising way to improve existing MFC bioanodes.

The electrodes presented in the first and fourth chapters are integrated into an MFC setup including real effluents from wastewaters. Their performances in current generation from an actual power source are investigated. The nature of the bacteria naturally occurring in wastewaters is also explored as well as their aptitude to exoelectrogenic activity. At last, the effect of the MFC power generation on the ecology of those wild bacteria is examined.

REFERENCES

[1] J. Zachos *et al.* Trends, Rhythms, and Aberrations in Global Climate 65 Ma to Present. *Science* **292,** 686–693 (2001).

[2] A. Grubler *et al.* A low energy demand scenario for meeting the 1.5 °C target and sustainable development goals without negative emission technologies. *Nat. Energy* **3,** 515–527 (2018).

[3] IPCC. *Climate Change 2013: The Physical Science Basis. Contribution of Working Group I to the Fifth Assessment Report of the Intergovernmental Panel on Climate Change*. (Cambridge University Press, 2013).

[4] International Energy Agency. *Key World Energy Statistics 2018*. (2018).

[5] J.-M. Jancovici & A. Grandjean. *Le plein s'il vous plaît! La solution au problème de l'énergie*. (Éditions du Seuil, 2006).

[6] S. Srinivasan. *Fuel cells: from fundamentals to applications*. (Springer Science & Business media, 2006).

[7] T. R. Ralph. "Principles of Fuel Cells". *Platin. Met. Rev.* **50,** 200–201 (2006).

[8] F. Barbir. PEM fuel cells. in *Fuel Cell Technology* 27–51 (Springer, 2006).

[9] K. S. V Santhanam, R. J. Press, M. J. Miri, A. V Bailey & G. A. Takacs. *Introduction to hydrogen technology*. (John Wiley & Sons, 2017).

[10] S. Park, Y. Shao, J. Liu & Y. Wang. Oxygen electrocatalysts for water electrolyzers and reversible fuel cells: status and perspective. *Energy Environ. Sci.* **5,** 9331 (2012).

[11] A. Bocarsly, D. M. P. Mingos & H. D. Abruña. *Fuel cells and hydrogen storage*. (Springer, 2011).

[12] K. Rabaey & W. Verstraete. Microbial fuel cells: Novel biotechnology for energy generation. *Trends Biotechnol.* **23,** 291–298 (2005).

[13] P. Atanassov *et al.* Enzymatic biofuel cells. *Interface-Electrochemical Soc.* **16,** 28–31 (2007).

[14] H. Wang & Z. J. Ren. A comprehensive review of microbial electrochemical systems as a platform technology. *Biotechnol. Adv.* **31,** 1796–1807 (2013).

[15] International Energy Agency. *World Energy Outlook 2016*. (OECD, 2016).

[16] B. E. Logan & J. M. Regan. Microbial fuel cells--challenges and applications. *Environ. Sci. Technol.* **40,** 5172–5180 (2006).

[17] H. Hiegemann *et al.* An integrated 45 L pilot microbial fuel cell system at a full-scale wastewater treatment plant. *Bioresour. Technol.* **218,** 115–122 (2016).

[18] B. E. Logan. Exoelectrogenic bacteria that power microbial fuel cells. *Nat. Rev. Microbiol.* **7,** 375–381 (2009).

[19] J. K. Fredrickson & J. M. Zachara. Electron transfer at the microbe-mineral interface: A grand challenge in biogeochemistry. *Geobiology* **6,** 245–253 (2008).

[20] D. Pinto. Electronic transfer within a microbial fuel cell. Better understanding of Experimental and Structural Parameters at the Interface between Electro-active Bacteria and Carbon-based Electrodes. *École doctorale Physique et chimie des matériaux (Paris)* (Sorbonne Université, 2016).

[21] J. F. Cooley. Apparatus for electrically dispersing fluids. (1899).

1

LITERATURE REVIEW

TABLE OF CONTENTS

Chapter 1. Literature review 31
- 1.1. Global energy context 31
- 1.2. From fuel cell to biofuel cell 32
  - 1.2.1. Overview of a fuel cell 32
  - 1.2.2. Biofuel cells 33
    - 1.2.2.1. Enzymatic fuel cells 34
    - 1.2.2.2. Microbial fuel cells 34
  - 1.2.3. Building a microbial fuel cell 36
  - 1.2.4. Microbial fuel cells & derived applications 37
- 1.3. Exoelectrogenic bacteria & microbial fuel cells 40
  - 1.3.1. Microbial respiration 40
  - 1.3.2. Exoelectrogenic bacteria & electron transfer 42
    - 1.3.2.1. Mediated & indirect transfer 43
    - 1.3.2.2. Direct transmembrane transfer 44
    - 1.3.2.3. Direct nanowires transfer 44
  - 1.3.3. Exoelectrogenic strains 47
    - 1.3.3.1. *Shewanella oneidensis* MR-1 49
    - 1.3.3.2. Pure strains & bacteria consortia 49
  - 1.3.4. Biofilm & planktonic bacteria 50
- 1.4. Power generation in microbial fuel cells 52
  - 1.4.1. Thermodynamics & cell voltage 52
  - 1.4.2. Standard electrode potentials 52
  - 1.4.3. Open circuit voltage 53
- 1.5. Key factors of microbial fuel cell efficiency 54
  - 1.5.1. Bacterial metabolism 54
  - 1.5.2. Mass transport phenomena 55
  - 1.5.3. Architecture & electrodes 56
  - 1.5.4. Performances evaluations 56
    - 1.5.4.1. Electrodes potential & current monitoring 56
    - 1.5.4.2. Power & power density 57

1.5.4.3. Polarization & power curves ... 57
1.5.4.4. Cyclic voltammetry ... 58
1.6. Microbial fuel cells architectures & materials ... 60
1.6.1. Cell architecture ... 60
1.6.2. Cathode materials ... 61
1.6.3. Separators ... 62
1.6.4. Anode materials ... 63
1.6.4.1. Metal electrodes ... 64
1.6.4.2. Carbon-based materials ... 64
1.7. Electrospinning & electrode materials ... 68
1.7.1. Fundamentals ... 68
1.7.2. Electrospinning parameters ... 70
1.7.2.1. Solution properties ... 70
1.7.2.2. Conductivity & solution charge density ... 72
1.7.2.3. Electric field & feed rate ... 72
1.7.2.4. Setup dimensions ... 73
1.7.2.5. Ambient conditions ... 74
1.7.2.6. Spinneret & collector ... 76
1.8. Conclusion & positioning of the study ... 79
1.8.1. Electrogenic microorganism ... 79
1.8.2. MFC reactor ... 80
1.8.3. Cathode & catholyte ... 80
1.8.4. Separator ... 80
1.8.5. Anode design ... 81
1.8.6. Layout of the study ... 81
References ... 83

CHAPTER 1. LITERATURE REVIEW

1.1. Global energy context

According to the *Key World Energy Statistics 2018* edited by the International Energy Agency[1] (IEA) the world energy demand in 2017 peaked at 13 972 Mtoe (million tons of oil equivalent, with 1 toe = 11 630 kWh), with nearly continuous increase over last decades. It has thus more than doubled since 1973 and the establishment of the IEA. According to the most likely scenario modelling the future of energy systems (New Policies Scenario), this trend is expected to go on and the world energy demand to rise as high as 17 715 Mtoe in 2040, unless drastic policies are implemented to meet the recent international agreement on climate change and energy transition. Indeed, the world energy supply as of 2017 is largely dominated – at almost 85 % – by fossil fuel consumption. In this context, both due to the urge of reducing greenhouse gases emission to tackle climate change and because of the finite amount of fossil resources on Earth, new energy sources must be developed and optimized.

Renewable energies such as wind power, hydro power or solar energy are of great interest to address this issue but they are intermittent sources of energy and their efficiencies greatly vary with the power plant location. Coupling with batteries may help to address this issues but raises questions about their detrimental effect on the environment linked to their production and to recycling difficulties. Nuclear power can also support this transition but suffers from both safety risks and nuclear fuel supply limits. In the meantime alternative continuous energy production devices such as fuel cells[2] can help to diversify the energy mix. They need an external supply of fuel but do not suffer from intermittent production and thus represent a good alternative to non-renewable energy sources.

1.2. From fuel cell to biofuel cell

1.2.1. Overview of a fuel cell

Fuel cells are electrochemical devices that can continuously produce an electric tension as long as they are supplied with fuel[3],[4]. They consist of two coupled electrodes, one – the anode – where takes place the oxidation of a fuel, a cathode where an oxidant – usually air oxygen – is reduced and an electrolyte allowing the diffusion of produced ions between the two electrodes. The electrons liberated by the oxidation can flow through the external circuit to the cathode side and power an electrical charge.

The invention of the fuel cell is generally attributed to Christian Friedrich Schönbein who discussed in 1838 the electric current generation of a crude device of his own consuming hydrogen and oxygen dissolved in water. The first design of a lab-scale fuel cell was published a year later by William Grove who used platinum electrodes to catalyze the process. This system was then extensively studied and refined by Francis T. Bacon[5]. Bacon then reached a fuel cell producing 1 kW in 1932, and up to 5 kW in 1959 in the wake of the space race and the Apollo program. The first commercial fuel cells were developed in 2007 and keep on being optimized up to this day[6],[7].

Diverse fuels and architectures have been investigated such as hydrogen alkaline fuel cells[8], direct methanol fuel cells[9] or high temperature solid oxide fuel cells[10]. Indeed just like Schönbein's first attempt, hydrogen-oxygen fuel cells remain the most studied and commercially available[2],[11].

One of the best understood architectures is the hydrogen-oxygen proton exchange membrane fuel cell, or PEMFC (**Figure 1.1**). This design has the advantage of producing only water as a chemical byproduct but needs expensive platinum or bimetallic compounds catalysts[12],[13] and specific conditions to speed up the oxidation and reduction rates. This architecture typically yields an electric power density of about 10^4 $W{\cdot}m^{-2}$ regarding the anode surface[14]. Moreover, we still lack a safe and extended hydrogen distribution network, and most of it is today produced through fossil fuels steam reforming[12] and therefore is not a truthful renewable energy. Nevertheless a lot of attention has been recently drawn to the water-splitting process to provide a clean source of hydrogen[15]. Fuel cells could then be coupled with intermittent renewable energy source such as wind or solar power. Accordingly, energy-production peaks could be used to electrolyze water and store the resultant hydrogen, then powering fuel cells to release current upon low productivity periods.

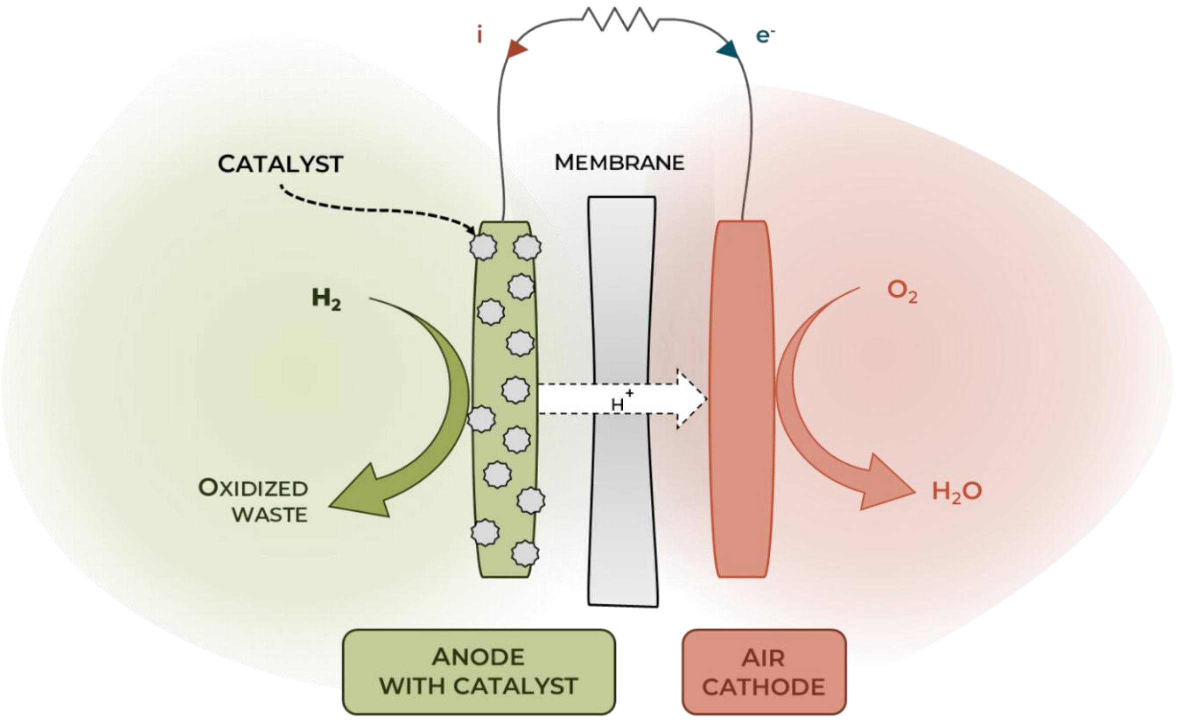

Figure 1.1 – General architecture of a proton exchange membrane fuel cell

In a common hydrogen-oxygen proton exchange membrane fuel cell the half-reactions at the electrodes are:

$$\begin{cases} H_2 = 2H^+ + 2e^- & \textbf{Anode} \\ O_2 + 4H^+ + 4e^- = 4H_2O & \textbf{Cathode} \end{cases} \quad \textbf{[1.1]}$$

1.2.2. Biofuel cells

Following the aforementioned challenges underlying conventional fuel cells, interest has sparked in exploring the electrochemical activity of biological components to replace the hydrogen fuel and expensive catalysts (as platinum). The idea behind this endeavor lies in the fact that both particular enzymes[16] and microorganisms[17] are able to perform redox reactions on a wide range of organic and inorganic substrates. If one could harvest the resulting electrons on electrodes it would be possible to design a fuel-cell like bioelectrochemical device generating an electric power. Such devices are therefore dubbed “biofuel cells”. They rely on enzymes – in enzymatic fuel cells (EFC) – or microorganisms such as bacteria, yeast or algae – in microbial fuel cells (MFC) – to act as biological catalysts[18]–[20]. These biofuel cells can theoretically use a broad range of fuels that can be sourced from biomass such as small organic molecules (e.g. sugars and carbohydrates).

1.2.2.1. Enzymatic fuel cells

Enzymes are proteins that have a catalytic activity. They are ubiquitous in the living world as they allow a broad range of normally kinetically-blocked reactions to take place, shaping the living cell as we know it. The first report of an extracted enzyme dates back to 1833 when Anselme Payen and Jean-François Persoz treated an aqueous malt solution with ethanol and dried out a substance able to hydrolyze starch. Through the decades, similar extracts were isolated until James B. Sumner showed in 1926 that the urease enzyme was fully protein-made and purified it, leading to a join Nobel Prize in Chemistry with John H. Northrop and Wendell M. Stanley in 1946. Eventually more and more enzymes were purified and studied until they were gradually adopted to catalyze many reactions in medicine, chemistry and industry.

Among the wide number of enzymes referenced today, those able to catalyze redox reactions are designated as oxidoreductases. An enzymatic fuel cell uses enzymes of this class attached to an anode to oxidize the proper fuel molecules and transfer the resulting electrons to the electrode. Three main ways of immobilization of the enzymes are reported: surface adsorption via Van der Waals interactions[21], covalent grafting through specific amino-acids[22] or encapsulation into a conductive matrix[23],[24]. Each enzyme is a specific catalyst of one or a few target molecules and thus less prone to poisoning or chemical deactivation. A compartment separator which is necessary in conventional fuel cells where the catalysts at the two electrodes are non-specific is here therefore optional[25]–[28]. However, EFC remain expensive due to the cost of purified enzymes and their relatively narrow stability window[29].

Nevertheless, the enzymes specificity, versatility and the miniaturization allowed by a membrane-less architecture can overcome their costs in some cases and a few EFC systems have been recently developed. One can cite biosensors[30],[31], wearable electronics[32], portable powering devices[33] or implantable EFC[34]–[36]. Power generated by enzymatic bioanode EFC ranges from 100-200 $\mu W \cdot cm^{-2}$ in implantable glucose-O_2 devices[37],[38] to 2.04 $mW \cdot cm^{-2}$ reported for an ethanol-O_2 system[22]. Furthermore, EFC integrating a conventional ethanol anode and an enzymatic cathode catalyzing O_2 reduction without the need for platinum catalysts have been reported with a power output up to 12 $mW \cdot cm^{-2}$ using a laccase enzyme[39].

1.2.2.2. Microbial fuel cells

The first report of electricity generation by microorganisms dates back to 1911 when Michael Cressé Potter grew *Saccharomyces cerevisiae* in nutrient medium and measured an electric potential of 0.32 V by immerging electrodes into it[40]. Branet Cohen later produced up to 0.9 V with *Proteus vulgaris* in 1931[41]. This subject remained however little studied until 1966 when a symposium by Kenneth Lewis rationalized the topic of biofuel cells and listed the important issues to be studied[42]. In the late 1980s, it was suggested to add redox mediators to the medium to improve the electron transfer[43],[44]. Studies on MFCs have then started to rise.

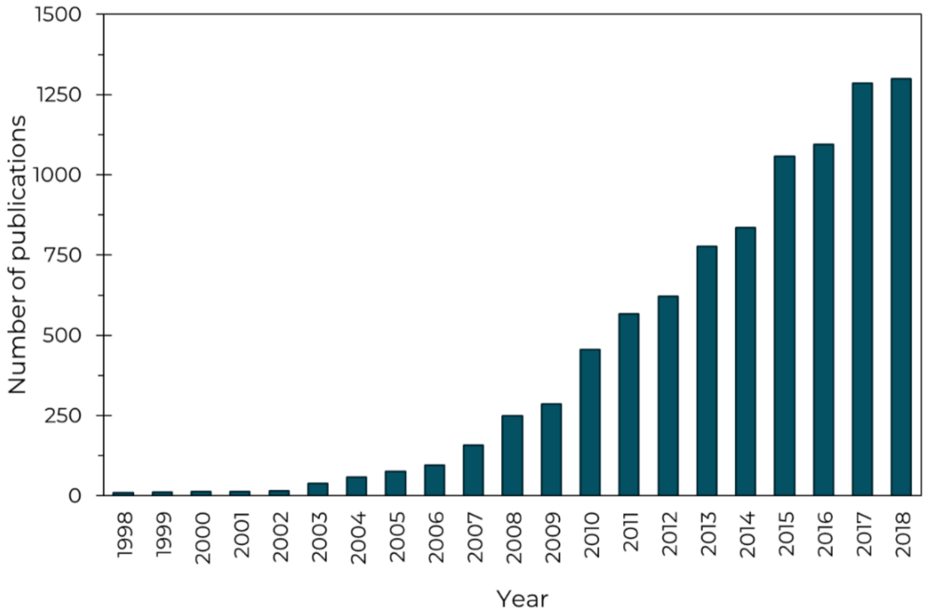

Figure 1.2 – Number of publications for articles on the keyword "Microbial Fuel Cell"
Source: Web of Science

A turning point was reached in 1997 when Kim *et al.*[45]–[47] and later Rabaey *et al.*[48],[49] demonstrated that some bacterial species could sustain electron transfer without the need for these added redox mediators – which are usually expensive and somewhat toxic to microorganisms. This finally marked a steep increase in interest on MFCs. The improvements made so far in anode materials, preferred strains & bacteria consortia and general architecture then led to ever better current output eventually ranging from 10 $mW \cdot m^{-2}$ to more than 10 $W \cdot m^{-2}$ and are still promised to further improvements[50].

More conventional proton exchange membrane fuel cells however yield power densities up to 10 $kW \cdot m^{-2}$ that are clearly out of grasp for MFCs[14]. It limits their usefulness for direct energy production from biomass, even if particular setups such as the use a neutral hydrolysate from corn has been shown to produce almost 1 $W \cdot m^{-2}$ in an MFC[51]. Nevertheless, as said before the true advantages of MFCs lie both in their lack of requirement of rare materials, and in their ability to harness energy from usually overlooked fuels. In particular, organic matter rich wastewaters are a source of usable molecules[52]. Logan and Rabaey estimated that wastewater actually contains as much as 9.3-fold the energy needed to treat it[53]–[55], which was applied in functional setups since the mid-2000s[56],[57]. Other applications include environmental sensors and the powering of devices located in places difficult to access, especially in rivers and deep-water environments. Low-power sensors such as the Benthic Unattended Generator are already sustained with sediment microbial fuel cells and need no maintenance for prolonged amount of time[58],[59]. Ultimately when access to electricity is scarce, MFCs can in last resort be used to power electronic devices[60] or even machines operating in remote environments such as the EcoBots[61],[62].

1.2.3. Building a microbial fuel cell

Microbial fuel cells therefore use microorganisms to extract the chemical energy from a fuel – or, from the microbe point of view, a nutrient – and gather the electrons produced by its oxidative metabolism via an electrode – the bioanode. The microorganisms usually performing this task are dubbed "exoelectrogenic" as they are able to transfer electrons outside their cells to a chemical receiver, or a solid substrate[63], and are generally bacteria. The main architectural specificity of an MFC over a conventional fuel cell lies in the nature of the anodic catalyst: it is the electroactive bacterium, planktonic or embedded in a biofilm (**Figure 1.3**).

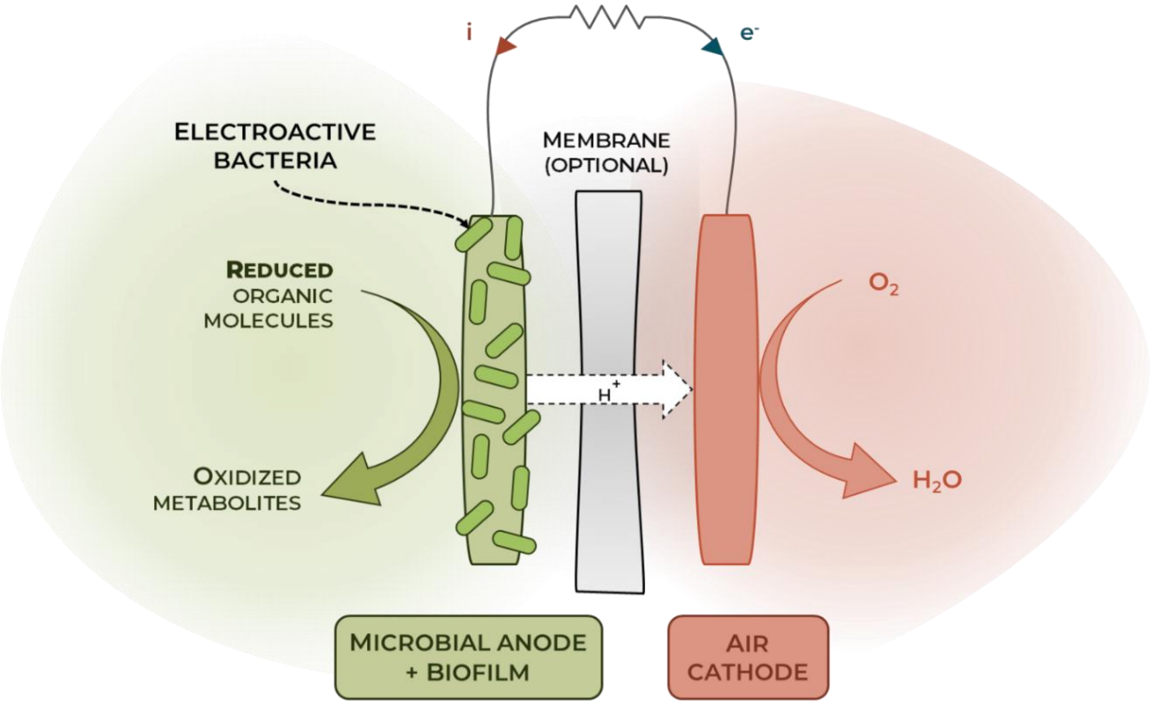

Figure 1.3 – General architecture of a microbial fuel cell with an air cathode

Therefore, an MFC is constituted by two electrodes compartments that might be separated by a cation-exchange membrane to prevent cathodic ions to pollute the anodic compartment while letting protons pass. Organic matter such as lactate and glucose is oxidized by bacteria at the anode releasing electrons, protons and CO_2. It is worth noting that the aforementioned released CO_2 is already part of the biogeochemical carbon cycle if the fuel is not synthetized from petrochemistry. Thus, oxidation of organic matter extracted from biomass will not contribute to climate change. Electrons flow from the anode to the cathode through the external circuit and may power a charge. Protons also diffuse to the cathodic compartment and in the case of an air cathode, recombine with electrons and oxygen to yield water. Bacteria can also be used at the cathode, resulting in a biocathode able to catalyze a wide range of cathodic reactions[50],[63]–[66].

Replacing usual catalysts or enzymes with bacteria has the beneficial effect of virtually suppressing their progressive deactivation thanks to their ability to self-replicate. In conditions avoiding biofilm overgrowth and progressive biofouling, a system can be stable over prolonged amounts of time. Biosensors have been reported to remain effective under cycling even after 5 years[67].

Additionally microorganisms showing far less substrate specificity than enzymes are able to oxidize a broader range of electron donors, optimizing they productivity in complex chemical environments such as wastewater or industry effluents[65].

1.2.4. Microbial fuel cells & derived applications

MFCs can also be tweaked in a variety of ways to do more than producing electricity. Modified microbial electrochemical systems have also been developed upon the base MFC architecture to widen its fields of application. By alternatively seeding bacteria on the cathode instead of the anode or poising an external potential on the electrodes rather than collecting the current produced by a conventional MFC, many more chemical reactions can be achieved through this system (**Figure 1.4**)[65]

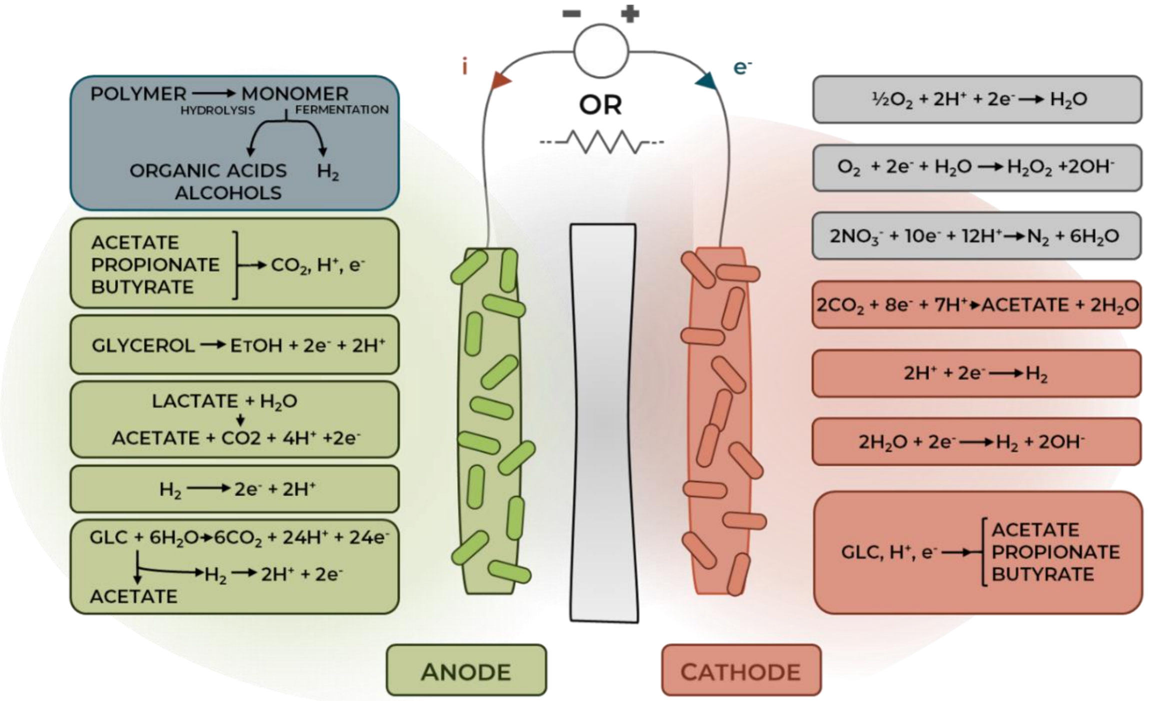
–
+
i
e^-
OR
POLYMER → MONOMER
HYDROLYSIS
FERMENTATION
ORGANIC ACIDS
ALCOHOLS
H_2
ACETATE
PROPIONATE
BUTYRATE
CO_2, H^+, e^-
$GLYCEROL \rightarrow ETOH + 2e^- + 2H^+$
$LACTATE + H_2O$
$ACETATE + CO2 + 4H^+ + 2e^-$
$H_2 \rightarrow 2e^- + 2H^+$
$GLC + 6H_2O \rightarrow 6CO_2 + 24H^+ + 24e^-$
$H_2 \rightarrow 2H^+ + 2e^-$
ACETATE
$½O_2 + 2H^+ + 2e^- \rightarrow H_2O$
$O_2 + 2e^- + H_2O \rightarrow H_2O_2 + 2OH^-$
$2NO_3^- + 10e^- + 12H^+ \rightarrow N_2 + 6H_2O$
$2CO_2 + 8e^- + 7H^+ \rightarrow ACETATE + 2H_2O$
$2H^+ + 2e^- \rightarrow H_2$
$2H_2O + 2e^- \rightarrow H_2 + 2OH^-$
GLC, H^+, e^-
ACETATE
PROPIONATE
BUTYRATE
ANODE
CATHODE

Figure 1.4 – Overview of anodic and cathodic reactions in a bioelectrochemical system. Blue indicates reactions that do not directly result in current generation but that produce potential molecules for current generation. Green indicates reactions that can produce current. Grey indicates reactions that can occur spontaneously or can be accelerated by adding additional power. Finally, orange depicts reactions where power addition is required. The stoichiometry of the reactions is principally theoretical because many conversions lead to side products as well as biomass formation.

Adapted from Logan & Rabaey, 2012

Among energy-producing systems and beyond conventional MFCs, one can cite microbial biosensors, remediation cells and desalination cells.

Biosensors are the simplest as they consist of an MFC monitored by a three-electrode potentiostatic configuration. The electroactive bacterial strain is here chosen not in order to yield the biggest current possible but accordingly to its selectivity toward a desired molecule to be dosed. The current produced is measured precisely by a potentiostat, and with appropriate calibration the concentration of the molecule can be deduced[67],[68].

A microbial bioremediation cell is used to remove or degrade chemical pollutants. By using specific strains able to use pollutants as electron donors or acceptors it has been shown that such devices can be used to reduce soluble UO_2^{2+} (U^{VI}) to insoluble U^{IV} in contaminated waters by poising the electrodes at - 500 mV[69], or to convert polluting nitrates to nitrites[70]. Bacteria able to couple the oxidation of organic matter with metal ions reductions are dubbed Dissimilatory Metal-Reducing Bacteria (DMRB) and are thus useful for these applications.

MFC systems can also be adapted to sea water desalination, e.g. by coupling an MFC with a standard desalination cell. Integrated MFC-desalination platforms have also been developed. By adding a third chamber between the anodic and cathodic compartments separated by anion-exchange and cation-exchange membranes, designs able to produce electricity while extracting ions from sea water flowing through the third compartment are reported (**Figure 1.5**)[71],[72].

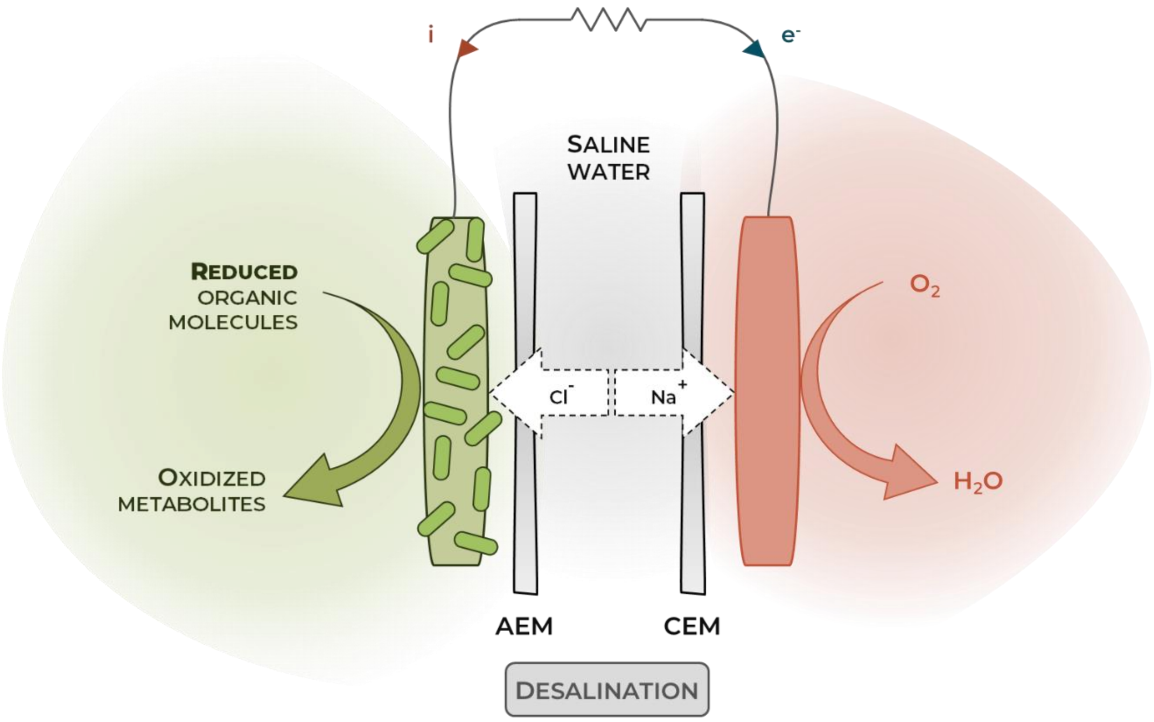

Figure 1.5 – General architecture of an integrated microbial desalination cell
Adapted from Jacobson *et al.*, 2011

All those systems fall within the range of energy productive microbial electrochemical systems. However, overall many other chemical reactions can be catalyzed if an external power source is added to the system.

For instance, the cathodic biocatalyzed electrolysis process of water and hydrogen production can be carried out by applying an extra voltage within the 0.3-0.4 V range to an MFC setup[73]–[76] – compared with the usual voltage above 1.6 V needed for unbiocatalyzed electrolysis (**Figure 1.6**).

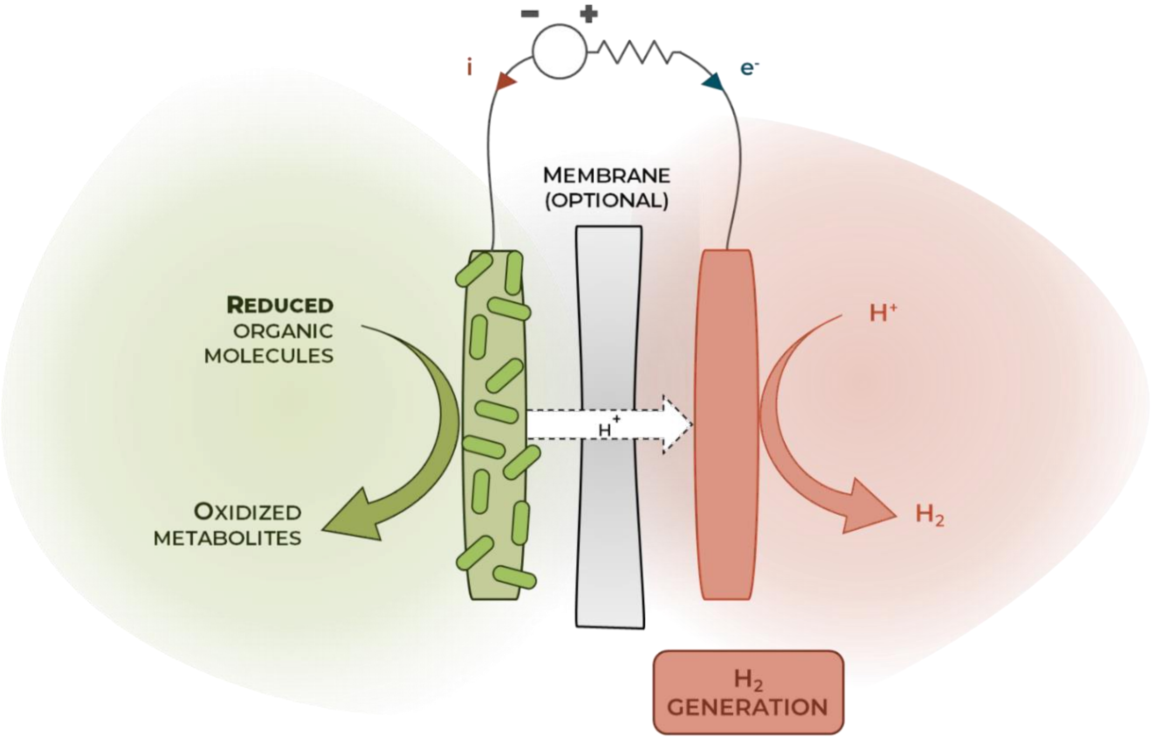
i
e-
Membrane (optional)
Reduced organic molecules
Oxidized metabolites
H+
H+
H2
H2 generation

Figure 1.6 – General architecture of a microbial electrolysis cell

Finally, by reversing the polarity of an MFC and poising a potential to a bacteria-colonized cathode, the design can convert CO_2 into small organic molecules. These molecules may be of chemical interest and be used elsewhere additionally to trap CO_2 (**Figure 1.7**)[70],[77],[78].

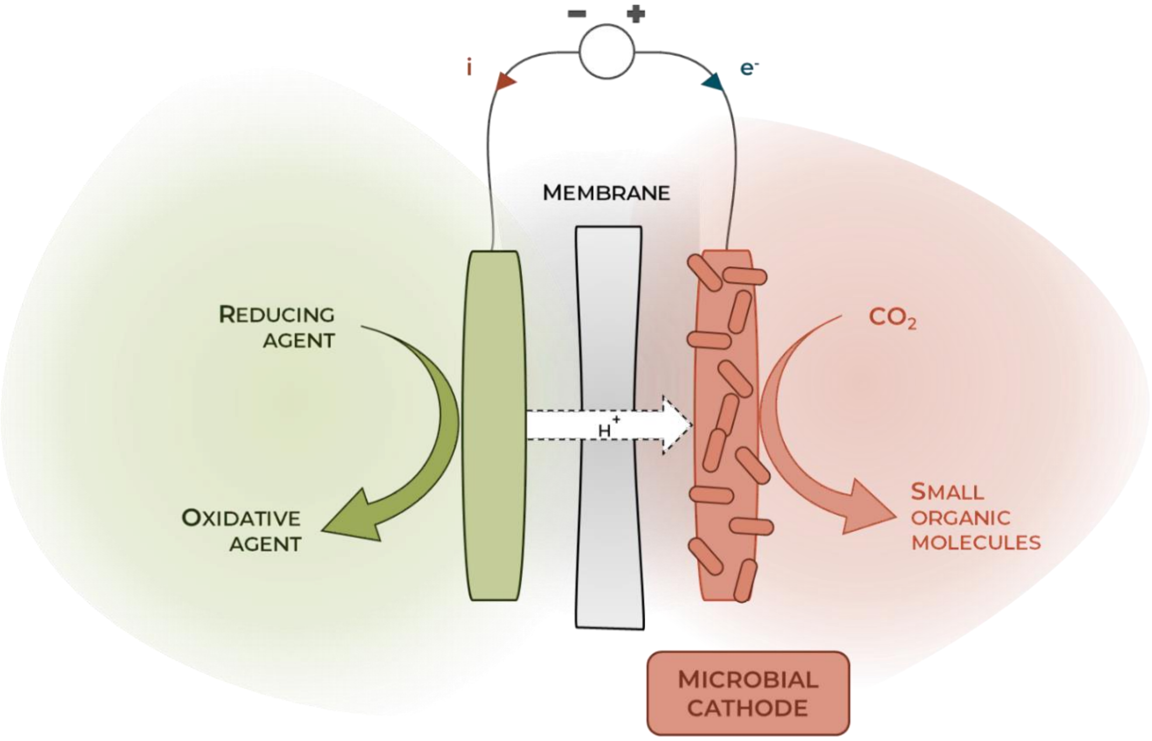
i
e-
Membrane
Reducing agent
Oxidative agent
H+
CO2
Small organic molecules
Microbial cathode

Figure 1.7 – General architecture of a microbial electrosynthesis cell

1.3. Exoelectrogenic bacteria & microbial fuel cells

1.3.1. Microbial respiration

The biochemistry of every organism known to this day requires adenosine triphosphate (ATP) to provide energy to many endothermic processes in living cells. The hydrolysis of ATP into adenosine diphosphate (ADP) and phosphate is characterized by a standard Gibbs free energy variation in biological conditions $\Delta G^{0'} = -30.5\ kJ{\cdot}mol^{-1}$ which is used to drive the aforementioned processes (**Figure 1.8**). Cells then regenerate ADP back into ATP either through photophosphorylation in plants, exothermic reactions such as glycolysis or TCA cycle, or thanks to the cellular respiration[79].

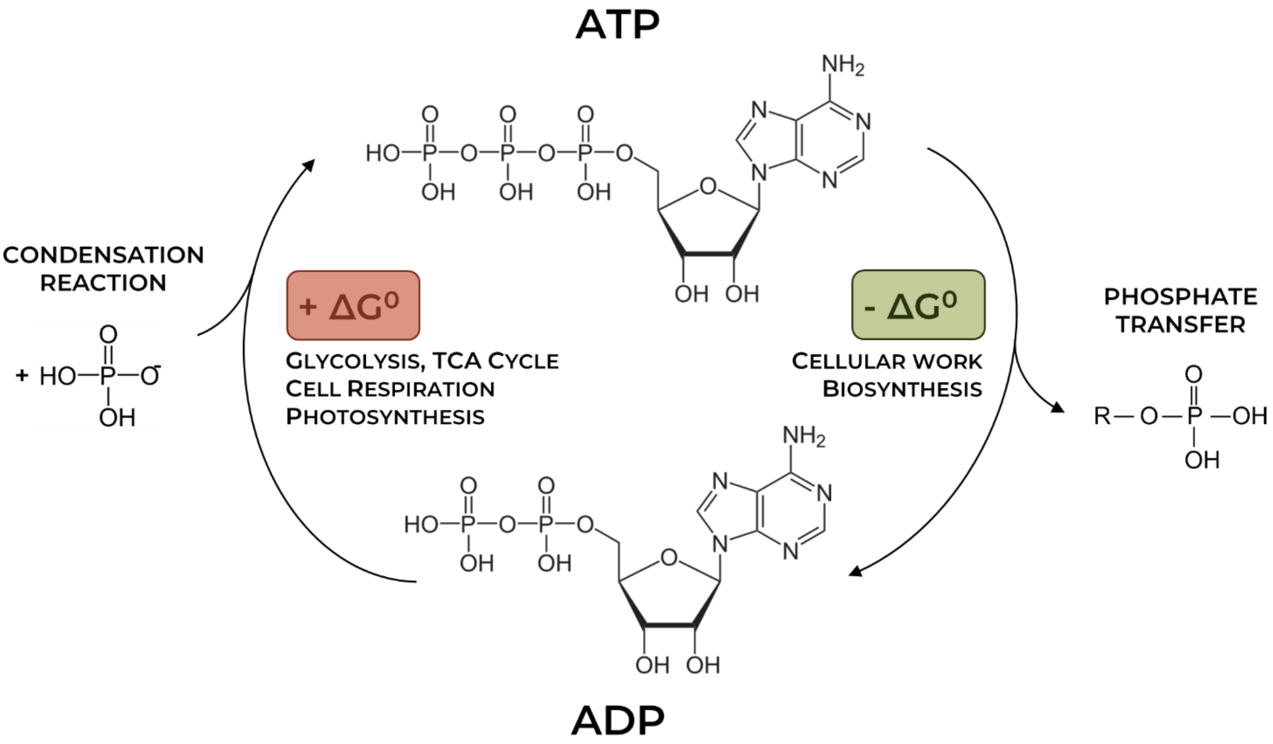

Figure 1.8 – Overview of the ATP & ADP phosphorylation cycle

The latter case, cellular respiration, represents the series of metabolic processes that converts the chemical energy of nutrients – usually low electrochemical potentials reduced organic molecules such as glucose or lactate – to eventually phosphorylate back ADP into ATP (**Figure 1.9**)[80], and to liberate some waste products. These chemical reactions are on the whole exothermic and most of them are oxidations. Therefore, a higher electrochemical potential final acceptor is needed to capture the electrons generated by these reactions. Depending on the final acceptor the respiration chain is either aerobic or anaerobic.

In aerobic organisms, the final acceptor is dioxygen. Molecular oxygen is a highly oxidizing agent and therefore a good final electron acceptor. When oxygen is not available the cell can either use a fermentation process which does not involve the respiratory chain to regenerate ATP, or in some organisms – and many bacteria – use an electron acceptor different from O_2.

Anaerobic respiration depicts this second case. Final electron acceptors range from oxidized organics like fumarate or nitrate in *E. coli*, sulfate in many deltaproteobacteria to metal ions such as Fe^{III} in dissimilatory metal-reducing bacteria such as *Geobacter* or *Shewanella* species. Additionally, many different species are also able to transfer their electrons to a conductive anode such as in MFCs[81].

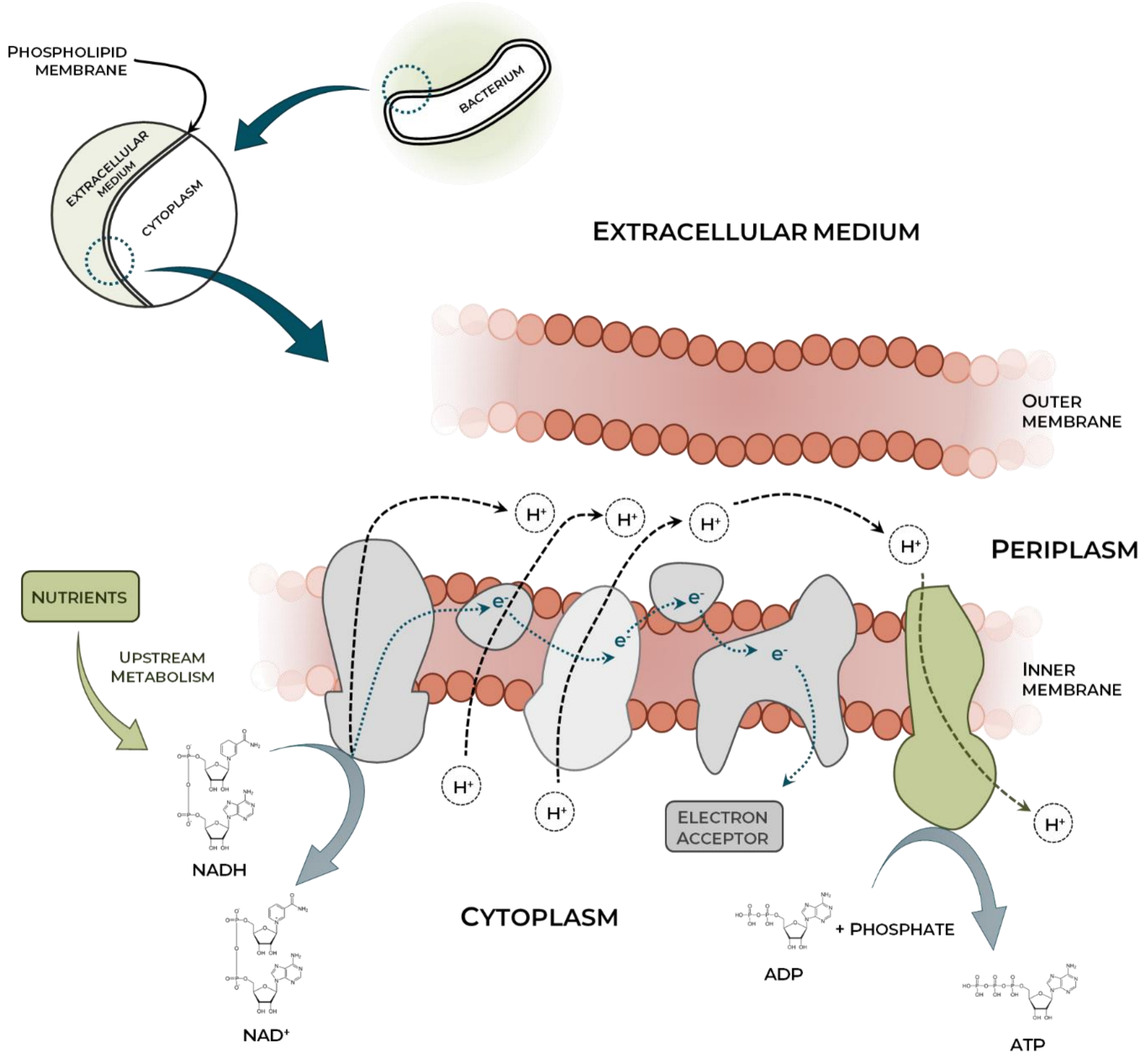
PHOSPHOLIPID MEMBRANE
BACTERIUM
EXTRACELLULAR MEDIUM
CYTOPLASM
EXTRACELLULAR MEDIUM
OUTER MEMBRANE
PERIPLASM
H^+
e^-
NUTRIENTS
UPSTREAM METABOLISM
INNER MEMBRANE
NADH
ELECTRON ACCEPTOR
CYTOPLASM
NAD⁺
ADP
+ PHOSPHATE
ATP

Figure 1.9 – Simplified overview of the cellular respiration process
Adapted from Mitchell *et al.*, 1961

Generally, three types of anaerobes are distinguished:

- **Facultative** anaerobes that can use O_2 when present or either ferment or use anaerobic respiration in its absence;
- **Aerotolerant** organisms that cannot use O_2 but are not harmed by its presence;
- **Obligate** anaerobes that cannot grow in presence of O_2.

1.3.2. Exoelectrogenic bacteria & electron transfer

Anaerobes able to transfer their final respiratory chain electrons outside the cell are indeed of particular interest for MFCs application. These microorganisms capable of exocellular electron transfer are dubbed “exoelectrogens”[50] but have also been described as “electrochemically active” bacteria[82], “anode respiring” bacteria[83] or “electricigens”[84].

Among exoelectrogens, bacteria capable of metal oxides reduction – dissimilatory metal-reducing bacteria – have been extensively studied. So far, three mechanisms of electron transfer have been identified.

Electrochemical redox mediators, or electron shuttles, can be excreted by the bacteria – like flavins – and indirectly transfer electrons between them and the final acceptor, being regenerated in the process (**Figure 1.10**). Fermentative metabolites unable to be reduced again by the bacterium can also serve as shuttles[48].

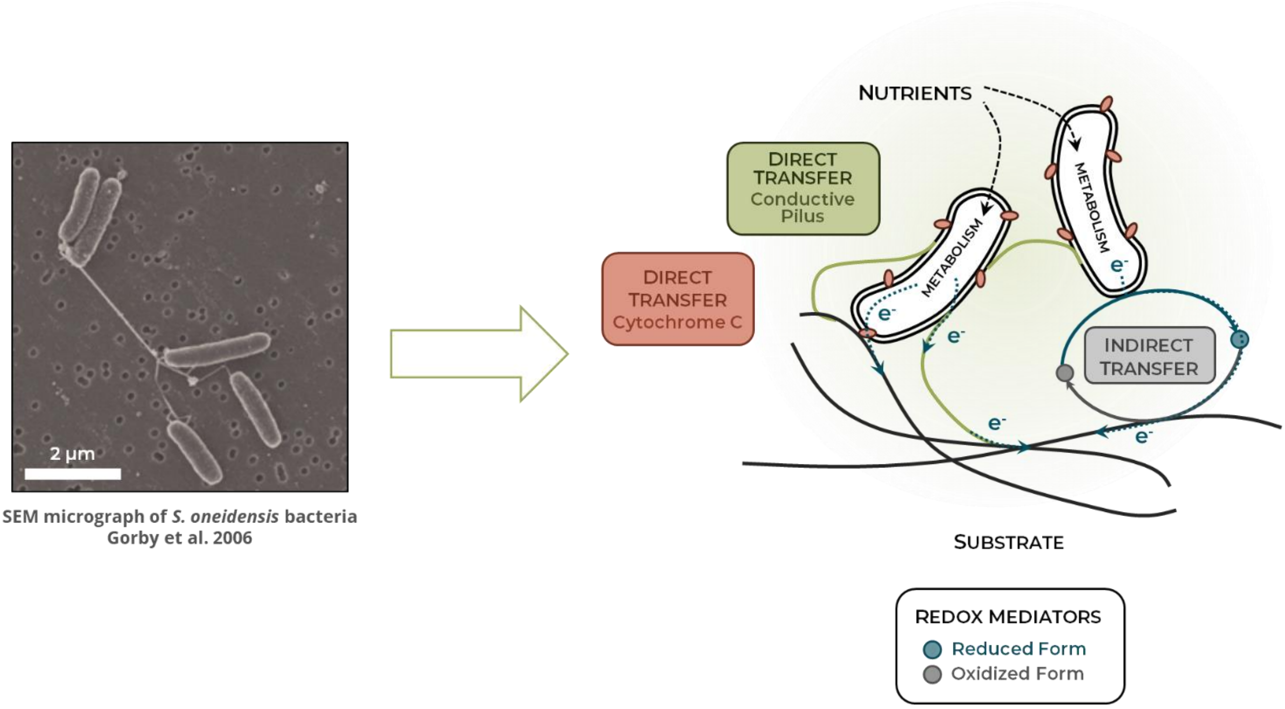

SEM micrograph of *S. oneidensis* bacteria
Gorby et al. 2006

Figure 1.10 – Overview of the exocellular electron transfer routes
Adapted from Gorby *et al.*, 2006 & Reguera *et al.*, 2005

Direct electron transfer (DET) can occur at the surface of bacteria growing on a bulk electron acceptor such as insoluble oxides or indeed an electrode[85]. In this case the transfer is ensured by redox outer membrane proteins classified as cytochromes. Cytochromes are coenzymes involved in the respiratory chain, made up of one or several haems – a complex consisting of an iron ion coordinated to a porphyrin as a tetradentate ligand, and to one or two axial ligands[86] (**Figure 1.11**). The reversible change from the Fe^{II} to the Fe^{III} oxidation state of the iron is responsible for the redox properties of the haem and cytochromes and allows electron transfer. Furthermore, two groups have highlighted a third transfer mechanism by showing that some bacteria are able to grow conductive appendages – so-called “nanowires” – capable of transferring electrical currents away[87],[88].

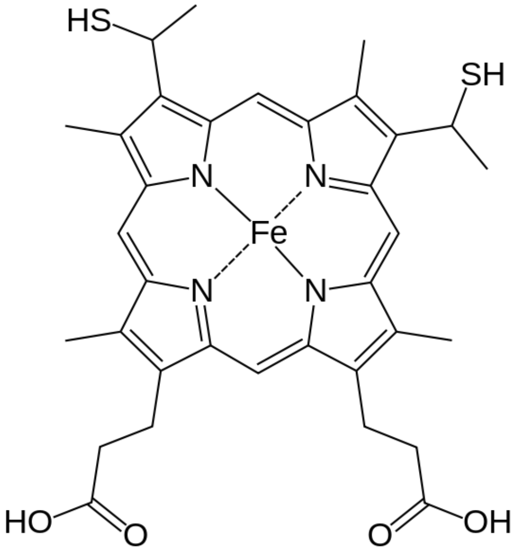

Figure 1.11 – Example of haem, the haem c, found in the cytochrome c.

However, many different types of bacteria seem able to produce currents in MFCs setups, a lot of them exhibit only small power densities when used as pure cultures[49],[89]. Bacteria consortia can exhibit synergies between strains in electron transfer. It has for instance been shown that *Brevibacillus* sp. PTH1 present in some mixed cultures MFCs produces little power as a pure culture unless *Pseudomonas* sp. is added to the medium[90].

It is worth noting that the aforementioned mechanisms are not mutually exclusive and can coexist in many bacteria. For instance, the pure culture exoelectrogenic bacteria *Shewanella oneidensis* can carry out both mediated and direct electron transfers, while *Geobacter sulfurreducens* only perform direct electron transfer.

1.3.2.1. Mediated & indirect transfer

Most cells are able to undergo fermentation and to produce reduced fermentative metabolites that can be secreted. Under certain circumstances those products can consequently react with an electron acceptor such an MFC anode to give up their electrons.

Mediated electron transfer (MET) on the other hand relies on the secretion of soluble intermediate molecules able to undergo reversible redox reactions between the bacterium and a final electron acceptor and is not as widespread as fermentation in the bacteria domain.

Redox mediators have been widely studied since the inception of bioelectricity generation. In the first decades of MFC research, little was known about exoelectrogenic bacteria and synthetic mediators were extensively used to overcome the incapacity of bacteria such as *Escherichia coli* to transfer electrons[91]. Various artificial redox mediators have been shown to improve current density in MFCs such as soluble neutral red, methyl viologen, methylene blue, AQDS or thionin[64],[92]–[94] or grafted mediators on the electrode surface[95]. However due to their cost and cell toxicity, no widespread use of artificial mediator is reasonable[96].

Natural mediator secretion have been demonstrated in the early 2000s in *Pseudomonas aeruginosa*[48],[49],[94],[97]. Furthermore, mediator accumulation has been linked to an increase in power density[98] while its depletion led to a decrease.

Finally studies tend to show that some bacterial strains exhibit a solely mediator-driven electron transfer – such as *Escherichia coli* or *Pseudomonas aeruginosa* – while some seem to be only partially relying on indirect electron transfer (IET)[99]–[101] – like *Shewanella oneidensis* – or even not at all[64] – as *Geobacter sulfurreducens*.

1.3.2.2. Direct transmembrane transfer

Because cell membranes are mainly made of non-conductive materials such as phospholipids, polysaccharides and proteins direct transmembrane electron transfer was long believed impossible without the help of redox mediators. However, the observation of dissimilatory metal-reducing bacteria has shown that some bacterial strains were able to grow at the surface of metallic oxides while reducing it. Thorough study hinted that membrane proteins could be responsible for this behavior and mutagenesis experiments targeting multi-hemes c-type cytochromes demonstrated that they were indeed engaged in this direct transmembrane transfer in some bacterial strains[102]–[104].

1.3.2.3. Direct nanowires transfer

In 2002 Lovley *et al.* observed for the first time that when grown on insoluble Fe^{III} electron acceptor *Geobacter metallireducens* bacteria grew pili appendages between them and the oxide (**Figure 1.12**) and hypothesized that they may help in establishing contact with the electron acceptor[105].

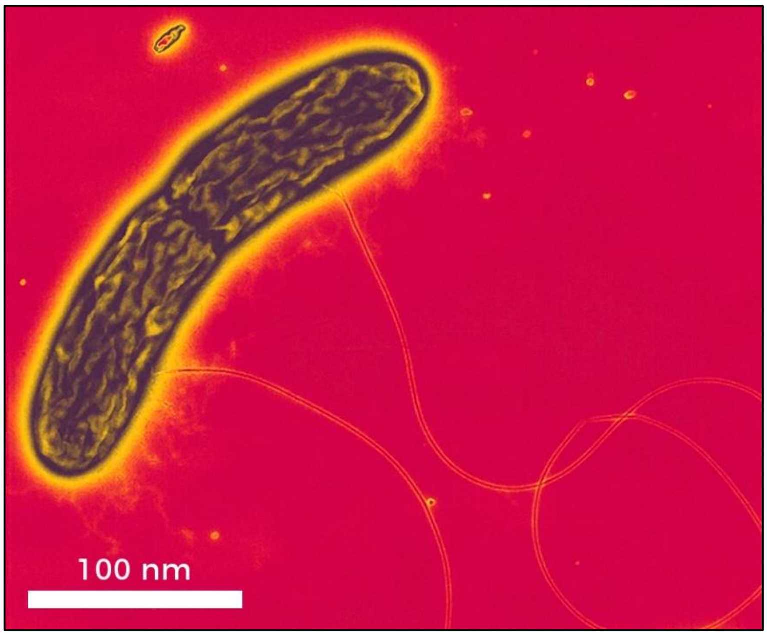

Figure 1.12 – False-color *Geobacter metallireducens* growing pili
From Lovley *et al.*, 2002

A few years later in 2005 both Lovley and Reguera *et al.* proposed that these appendages may be conductive and help directly the bacteria to transfer their electrons. Conducting-probe atomic force microscopy (AFM) on pili produced by *Geobacter sulfurreducens* and *Shewanella oneidensis* shown that they were indeed able to conduct electricity (**Figure 1.13**)[87],[88]. In *Shewanella oneidensis* connective pili have also been observed between bacteria and suggest that they may be involved in quorum sensing and electron exchange among cells[50] or even between different species[87].

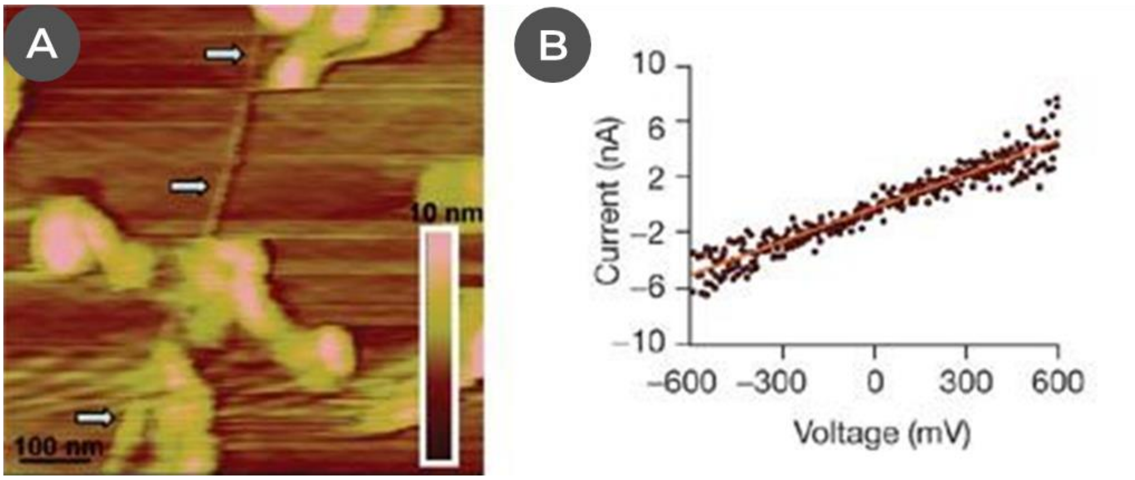

Figure 1.13 – Conducting-probe atomic force microscopy on *G. sulfurreducens* pili with (A) the topography of a pilus (indicated by arrows) and non-pilin globular proteins and (B) the correspondence between current and applied voltage on a section of the pilus.
From Lovley *et al.*, 2005

El-Naggar *et al.* further cemented these results by growing *Shewanella oneidensis* between gold electrodes on a SiO_2/Si plate[106]. Long-range electron transfer was observed at a rate of up to 10^9 electrons·s^{-1} at 100 mV with AFM (**Figure 1.14**).

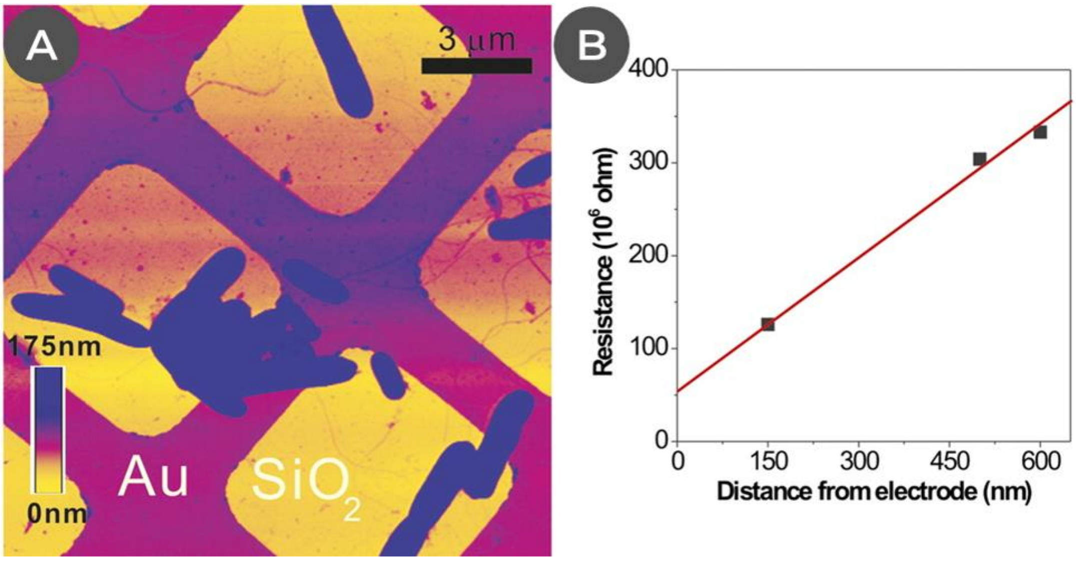

Figure 1.14 – CP-AFM of a bacterial nanowire with (A) the topographic AFM image showing air-dried *Shewanella oneidensis* MR-1 cells and extracellular appendages deposited randomly on a SiO_2/Si substrate patterned with Au microgrid and (B) a plot of total resistance as a function of distance between AFM tip and Au electrode.

From El-Naggar *et al.*, 2010

Two mechanisms are currently considered to account for pili electrical conductivity. On the one hand electrons could hop from one cytochrome c (*c*-Cyt) to another through the nanowire guaranteeing its conductivity (**Figure 1.15.A**)[87],[107]. Mutations knocking out genes encoding for MtrC and OmcA cytochromes c in *S. oneidensis* led to non-conductive structures. Alternatively a metal like conductivity may be triggered by the delocalization of p-orbitals electrons through the amino acids π-bonds conjugation along the pilus (**Figure 1.15.B**)[108],[109]. Finally, some authors state that a mix of both mechanisms could also be responsible for the conductivity (**Figure 1.15.C**)[110]. Furthermore, the electron transport mechanisms seem to be different throughout the genera considered. Even if no definitive consensus has been reached so far, pili made of periplasmic extension functionalized with *c*-Cyt related proteins seems for instance more plausible for *S. oneidensis*[111] while pilin-based structures exhibiting p-orbital delocalization are preferred in the case of *G. sulfurreducens*[108].

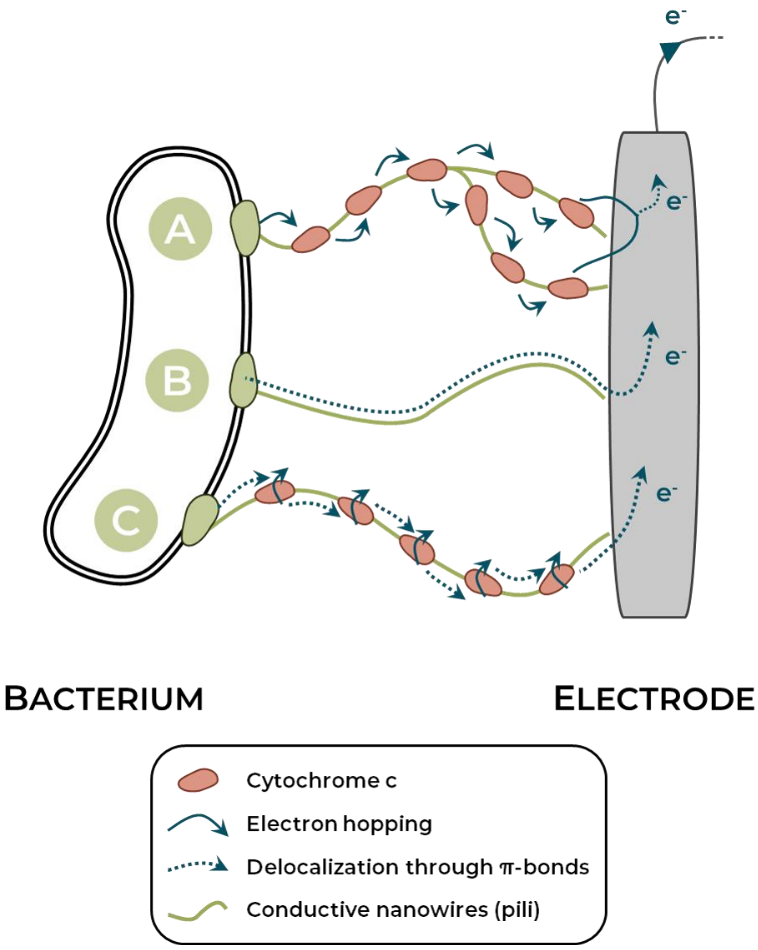
e-
A
B
C
e-
e-
e-
BACTERIUM
ELECTRODE
Cytochrome c
Electron hopping
Delocalization through π-bonds
Conductive nanowires (pili)

Figure 1.15 – Overview of proposed mechanisms accounting for bacterial nanowires electrical conductivity

Adapted from Bonanni *et al.*, 2013 & Malvankar *et al.*, 2015

1.3.3. Exoelectrogenic strains

A wide range of exoelectrogenic microorganisms have been discovered so far and applied to MFC power generation. The first to be identified and used in power production was *Shewanella putrefaciens* IR-1, a dissimilatory metal reducing bacterium, in 1999[112] rapidly followed by other species (**Table 1.1**)[50]. They belong to a broad range of phyla from the DMRBs to the fungi kingdom and the full understanding of their exoelectrogenic capabilities is still under investigation.

Table 1.1 – Overview of exoelectrogenic bacteria without exogenous mediators need
Adapted from Logan, 2009

Year	Microorganism	Comment
1999	*Shewanella putrefaciens* IR-1	Direct proof of electrical current generation in an (MFC by a dissimilatory metal-reducing bacterium)
2001	*Clostridium butyricum* EG3	First gram-positive bacterium shown to produce electrical current in an MFC
2002	*Desulfuromonas acetoxidans*	Identified in a sediment MFC community and shown to produce power (Deltaproteobacteria)
	Geobacter metallireducens	Shown to generate electricity in a poised potential system (Deltaproteobacteria)
2003	*Geobacter sulfurreducens*	Generated current without poised electrode (Deltaproteobacteria)
	Rhodoferax ferrireducens	Used glucose (Betaproteobacteria)
	A3 (*Aeromonas hydrophila*)	Deltaproteobacteria
2004	*Pseudomonas aeruginosa*	Produced low amounts of power through mediators such as pyocyanin (Gammaproteobacteria)
	Desulfobulbus propionicus	Deltaproteobacteria
2005	*Geopsychrobacter electrodiphilus*	Psychrotolerant (Deltaproteobacteria)
	Geothrix fermentans	Produced an unidentified mediator (phylum Acidobacteria)
2006	*Shewanella oneidensis* DSP10	Achieved a high power density (2 $W \cdot m^{-2}$ or 500 $W \cdot m^{-3}$) by pumping cells grown in a flask into a small (1.2 mL) MFC (Gammaproteobacteria)
	S. oneidensis MR-1	Various mutants identified that increase current or lose the ability for current generation (Gammaproteobacteria)
	Escherichia coli	Found to produce current after long acclimation times (Gammaproteobacteria)
2008	*Rhodopseudomonas palustris* DX-1	Produced high power densities of 2.72 $W \cdot m^{-2}$ compared with an acclimated waste-water inoculum (1.74$W \cdot m^{-2}$) (Alphaproteobacteria)
	Ochrobactrum anthropi YZ-1	An opportunistic pathogen, such as *P. aeruginosa* (Alphaproteobacteria)
	Desulfovibrio desulfuricans	Reduced sulfate when growing on lactate; resazurin in the medium was not thought to be a factor in power production (Deltaproteobacteria)
	Acidiphilium sp. 3.2Sup5	Current at low pH and in the presence of oxygen in a poised potential system (Alphaproteobacteria)
	Klebsiella pneumoniae L17	The first time this species produced current without a mediator (Gammaproteobacteria)
	Thermincola sp. strain JR	Phylum Firmicutes
	Pichia anomala	Current generation by a yeast (kingdom Fungi)

1.3.3.1. *Shewanella oneidensis* MR-1

Within this wide scope of MFC-usable microorganisms *Shewanella oneidensis* MR-1 stands among the most studied. This strain was firstly isolated by Myers & Nealson in 1988 in sediments from Lake Oneida, NY, USA, where abnormally high levels of reduced manganese Mn^{2+} were attributed to its activity[113]. *Shewanella oneidensis* MR-1 – where MR stands for manganese reducing – is a facultative anaerobe gammaproteobacterium bacillus (**Figure 1.16**). It is classified among DMRBs and is able to reduce manganese oxide as well as other oxidized metals such as iron, uranium or lead as well as sulfate, nitrate or chromates when grown anaerobically[114].

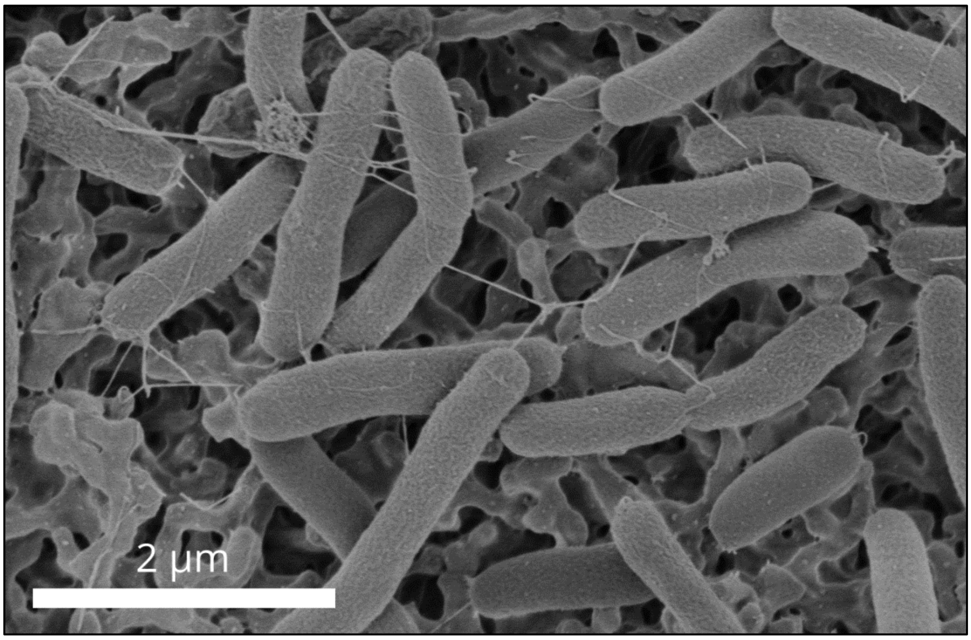

Figure 1.16 – SEM-FEG micrograph of *S. oneidensis* MR-1 on cellulose fibers
Adapted from Hogan, 2018

Shewanella oneidensis MR-1 is able to perform both direct and indirect electron transfer. Direct transmembrane electron transfer is linked to cytochromes c based multi-hemes proteins among which CymA in the inner membrane, MtrA in the periplasm and MtrC & OmcA in the outer membrane[115]. Nanowires likewise need cytochromes c for proper conductivity and deletions of related genes impair pili electron transfer[106] as well as direct transmembrane transfer[102]. Finally, direct transfer in *Shewanella oneidensis* MR-1 is mediated by riboflavins and supernatant replacement in MFCs is related to a transient sharp drop in power output[99].

1.3.3.2. Pure strains & bacteria consortia

If a broad range of pure microbial strains are prone to exoelectrogenesis on their own, the best power outputs have been so far obtained with mixed culture – or consortia. In 2004 Rabaey *et al.* reported that repeated transfer of a bacterial consortium from wastewater in new MFCs increased the initial power output from $0.6\ W \cdot m^{-2}$ up to $4.31\ W \cdot m^{-2}$ and changed the dominant bacterial species[49].

It can be hinted that pure cultures are often badly adapted to real wastewater media and consortia are able to degrade a much wider range of organics than pure strains. Additionally in enriched cultured some strains cannot grow on their own but rather develop a synergetic interaction with other species to degrade and consume nutrients[47],[116].

However, for bacteria-electrode interactions studies and optimization of the electrodes and the architecture of an MFC, pure culture remains useful as they are simpler to understand.

1.3.4. Biofilm & planktonic bacteria

According to the IUPAC[86] a biofilm is an aggregate of microorganisms – pure strains or consortia – in which cells that are frequently embedded within a self-produced matrix of extracellular polymeric substances (EPSs) adhere to each other and usually to a surface. EPSs are mainly made up of polysaccharides, proteins, lipids, DNA and various secreted organics and the resulting matrix can be adapted to the environment by the embedded cells[117]–[120]. Planktonic cells on the other hand are free to float in the medium.

Exoelectrogenic bacteria embedded in a biofilm may transfer electrons both through direct and indirect pathways enhancing electron transfer while planktonic cells are limited to indirect transfer[121]. However within a biofilm, all bacteria are not electroactive as local architecture and conditions can limit their access to the electrode (**Figure 1.17**). Nevertheless, inactive bacteria can still be of exoelectrogenesis importance as they may secrete mediators or break down some organic matter into better electron sources for other cells[50].

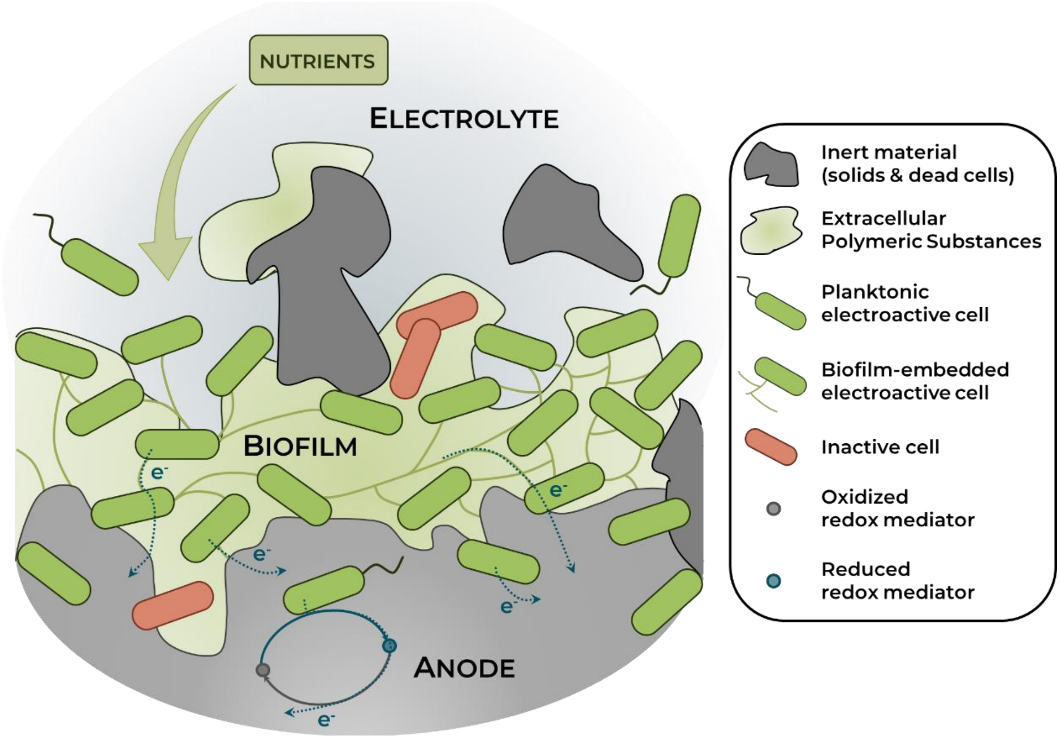
NUTRIENTS
ELECTROLYTE
BIOFILM
ANODE
e-
e-
e-
e-
e-
Inert material (solids & dead cells)
Extracellular Polymeric Substances
Planktonic electroactive cell
Biofilm-embedded electroactive cell
Inactive cell
Oxidized redox mediator
Reduced redox mediator

Figure 1.17 – Biofilm architecture of exoelectrogenic bacteria in an MFC
Adapted from Logan *et al.*, 2009

On a bioanode, the biofilm can exceed 80 µm in thickness[122] and may in some case limit the overall efficiency of the system[65]. Inert material can limit access to the electrode for the cells and hinder ions diffusion leading to nutrient depletion and to a pH gradient build-up inside the biofilm that can affect electrochemical behaviors.

1.4. Power generation in microbial fuel cells

The theoretical electromotive force generated by an MFC can be evaluated using thermodynamic calculations and compared to experimental results to evaluate the causes of losses.

1.4.1. Thermodynamics & cell voltage

Electricity may be generated in an MFC only if the overall reaction is thermodynamically favorable. This can be assessed by calculating the Gibbs free energy of the reaction which can be considered as the maximum work that can be derived from it[123],[124]:

$$\Delta G_r = \Delta G_r^0 + RT \cdot \ln(\Pi) \qquad \textbf{[1.2]}$$

Here ΔG_r (J) is the Gibbs free energy in the given conditions, ΔG_r^0 (J) is the Gibbs free energy under standard conditions and Π is the reaction quotient defined as the activities of the products divided by those of the reactants. If the Gibbs free energy is negative then the reaction is favorable.

The cell electromotive force E_{emf} (V) is then defined as the potential difference between the two electrodes and related to the work produced W (J) and the Gibbs free energy as:

$$W = E_{emf}Q = -\Delta G_r \qquad \textbf{[1.3]}$$

The charge transferred in the reaction Q (C) is related to the number of electrons exchanged by reaction n (mol) such as Q = nF hence:

$$E_{emf} = -\frac{\Delta G_r}{nF} \qquad \textbf{[1.4]}$$

Which can under standard conditions be written with E_{emf}^0 (V) being the standard cell electromotive force:

$$E_{emf}^0 = -\frac{\Delta G_r^0}{nF} \qquad \textbf{[1.5]}$$

Therefore, the reaction can be linked to the potential of the cell as:

$$E_{emf} = E_{emf}^0 - \frac{RT}{nF}\ln(\Pi) \qquad \textbf{[1.6]}$$

For a favorable reaction the energy is positive and the corresponding electromotive force is the thermodynamic upper limit for the cell voltage[66].

1.4.2. Standard electrode potentials

The reaction occurring in an MFC can be analyzed in term of half-reactions with oxidation occurring at the anode and reduction occurring at the cathode. The respective potentials can be calculated as:

$$E_{anode} = E_{anode}^0 - \frac{RT}{nF}\ln(\Pi_{anode}) \qquad \textbf{[1.7]}$$

$$E_{cathode} = E^{0}_{cathode} - \frac{RT}{nF}\ln(\Pi_{cathode}) \qquad \textbf{[1.8]}$$

The standard potentials E^0 (V) are tabulated and reported relative to the standard hydrogen electrode (SHE) under standard conditions.

The cell electromotive force is then calculated as:

$$E_{emf} = E_{cathode} - E_{anode} \qquad \textbf{[1.9]}$$

1.4.3. Open circuit voltage

This calculated electromotive force is a thermodynamic value that does not take into account various losses and cell limitations inherent to a real system. The Open Circuit Voltage (OCV) is the voltage value that can be measured in absence of current between the two MFC electrodes. In an ideal system, it should approach the electromotive force theoretical value but in practice it is almost always much lower.

The potential difference is referred to as an “overpotential” and can be attributed to various origins either biological, diffusive or related to ohmic losses.

1.5. Key factors of microbial fuel cell efficiency

The maximum theoretical electromotive force for an MFC is on the order of 1.1 V[66] and the highest MFC OCV achieved so far approaches 1.04 V[125]. However, such artificial potentials are attained with heavy anodic alkalization and cathodic acidification and this is achieved at the cost of a dramatic fall in power output and long-term stability.

Maximum functional MFCs OCV usually revolve around 0.80 V[126] and remain even below over current generation. The difference between the cell measured voltage and the theoretical electromotive force is the sum of the overpotentials of the two electrodes and the ohmic loss of the system. It is referred to as the "overvoltage" of the cell:

$$E_{cell} = E_{emf} - (\Sigma\eta_a + |\Sigma\eta_c| + IR_\Omega) \qquad \textbf{[1.10]}$$

The respective overpotentials of the anode and the cathode are $\Sigma\eta_a$ (V) and $|\Sigma\eta_c|$ (V) and IR_Ω is the overall ohmic losses at a current I (A) with a total resistance of the system R_Ω (Ω). Overpotentials are usually current dependent.

The MFC cell voltage can also be described as a linear function of the current:

$$E_{cell} = OCV - IR_{int} \qquad \textbf{[1.11]}$$

Here IR_{int} is the total internal loss of the system at a current I and an internal resistance R_{int} (Ω). By comparing equations **[1.10]** and **[1.11]**, we can note that overpotentials in open circuit conditions are included in OCV. Current-dependent overpotentials are henceforth included in IR_{int}. A maximum power output will then be reached when the external resistance is equal to R_{int}.

Improvements of the MFC performances can then be seek by reducing the ohmic resistance of the system or by mitigating overpotentials.

Those overpotentials can generally be attributed to either[66]:

- **Bacterial metabolic** losses;
- **Mass transport** & **concentration** losses;
- **Activation** losses;
- **Ohmic** losses**.**

1.5.1. Bacterial metabolism

The bacteria use reduced organic molecules at low electrochemical potentials as nutrients to transport electrons in the respiratory chain to a final higher potential acceptor to extract energy (**Figure 1.9**). The lower the potential of the electron donor and the higher the potential of the electron acceptor the more energy the bacteria will be able to extract. Electrochemical potentials in usual MFCs conditions can be calculated from **[1.7]** & **[1.8]** using tabulated standard potentials and Gibbs free energies (**Table 1.2**).

Table 1.2 – Standard potentials E_0 & theoretical potentials for typical conditions in MFCs E_{MFC}
All the potentials are shown against SHE
Adapted from Logan *et al.*, 2006

Electrode	Reaction	E_0 (V)	Conditions	E_{MFC} (V)
Anode	$CH_3COO^- + 4H_2O \rightarrow 2HCO_3^- + 9H^+ + 8e^-$	0.187[a]	$[HCO_3^-] = [CH_3COO^-] = 5\,mM, pH = 7$	- 0.296[b]
	$CH_3CHOHCOO^- + 6H_2O \rightarrow 3HCO_3^- + 14H^+ + 12e^-$[c]	0.155[a]	$[HCO_3^-]$ = [lactate] = 5 mM, pH = 7	- 0.349
Cathode	$O_2 + 4H^+ + 4e^- \rightarrow 2H_2O$	1.229	pO_2 = 0.2 atm, pH = 7	0.805[b]
	$O_2 + 4H^+ + 4e^- \rightarrow 2H_2O$	1.229	pO_2 = 0.2 atm, pH = 10	0.627
	$MnO_{2\,(s)} + 4H^+ + 2e^- \rightarrow Mn^{2+} + 2H_2O$	1.230	$[Mn^{2+}]$ = 5mM, pH = 7	0.470
	$O_2 + 2H^+ + 2e^- \rightarrow H_2O_2$	0.695	$pO_2 = 0.2\,atm, [H_2O_2] = 5\,mM, pH = 7$	0.328
	$Fe(CN)_6^{3-} + e^- \rightarrow Fe(CN)_6^{4-}$	0.361	$[Fe(CN)_6^{3-}] = [Fe(CN)_6^{4-}]$	0.361

[a] Calculated from tabulated Gibbs free energy data[127]. [b] Note that an MFC with an acetate oxidizing anode ($[HCO_3^-] = [CH_3COO^-]$ = 5 mM, pH = 7) and an oxygen reducing cathode **(**pO_2 = 0.2 atm, pH = 7) has a cell emf of 0.805 + 0.296 = 1.101 V. [c] Electrochemical redox couple HCO_3^-/lactate.

In an MFC, a important anode potential is therefore highly favorable for the bacteria as it enhances its total metabolic energy gain. However, a high electrode potential reduces to overall voltage of the MFC and should be kept as low as possible, but indeed not too low in order to avoid inhibiting electron transfer from the bacteria to the anode. If it is too low, the bacteria may switch to other electron acceptor or fermentation to optimize their metabolic gains. A compromise must be found between an acceptable MFC voltage and a good overall stability.

1.5.2. Mass transport phenomena

Electrochemical reactions can be limited by poor diffusion of chemical species which can lead to depletion of reactants and buildup of products concentrations at the medium/electrode interface[3].

At the anode an increase in oxidized species concentration or a limited supply of reduced ones toward the electrode can lead to an augmentation of the oxidized/reduced ratio at the anode surface and rise its potential. Similarly, the reverse phenomenon can occur at the cathode and cause a drop in cathodic potential.

Limitation of species influx to the biofilm can also occur and limit the bacterial intake of nutrients and subsequent catalysis of the oxidation reaction.

These concentration losses occur mainly at high current densities when diffusion cannot keep up with the reaction rate or in poorly mixed systems where diffusional gradients tend to establish.

1.5.3. Architecture & electrodes

Redox reactions often show activation losses due to the activation energy needed to transfer electrons from or to a chemical species. These species can either be present as a mediator in solution, at the bacterial or pilus surface or at the electrode surface in the case of cathodic reactions.

These activations losses often show a steep increase at low currents followed by a steady growth as the current density increase[66].

Activation losses can be tackled with by either increasing the electrode surface area, improving the electrode catalysis, establishing an enriched biofilm at the electrode surface or by increasing the operating temperature[66].

Losses always occur due to electrical resistance in the electrodes, electrical contacts or in the external circuit. Ionic resistance in the electrolytes or cation exchange membrane contributes largely to these ohmic losses.

These points can be tuned by improving the electrode architecture – for instance by reducing electrodes spacing – using high conductivity membranes and increasing the electrolytes concentrations, keeping in mind tolerance to bacteria.

1.5.4. Performances evaluations

Most MFC performances can be evaluated and compared using a potentiostat in either three – using a reference electrode in one the compartments – or two electrodes configurations.

Various physical magnitudes may then be recorded and be compared between two experiments.

1.5.4.1. Electrodes potential & current monitoring

Electrodes potentials can be determined by measuring their voltages against a reference electrode. Tabulated potentials are usually reported against the standard hydrogen electrode (SHE) which consists of a platinum wire in an ideal solution of unity-activity hydrogen ion solution with 1 bar bubbling hydrogen gas. However, such an electrode is not very practical to use and therefore other references electrodes with known potential against the SHE are usually used in lab setups. One widespread example is the silver/silver chloride (Ag/AgCl) reference electrode in a saturated KCl solution which exhibits at 25°C a potential of + 0.197 V against the SHE.

The electrodes potential depends on the solution pH and it must therefore be reported during an experiment.

At pH = 7 a usual range of electrode potential is - 0.20 to - 0.28 V vs. SHE (- 0.40 to - 0.48 V vs. Ag/AgCl) for the anode and 0.30 to 0.10 V vs. SHE (0.10 to - 0.10 V vs. Ag/AgCl)[66].

Additionally, when a potential is imposed by the potentiostat to an electrode a resulting current can be measured trough chronoamperometry.

1.5.4.2. Power & power density

The power output of an MFC is calculated as:

$$P = IE_{cell} \qquad \textbf{[1.12]}$$

Or when the voltage is measured through a fixed external resistance R_{ext}:

$$P = \frac{E_{cell}^2}{R_{ext}} \qquad \textbf{[1.13]}$$

In order to compare different systems, the power output is usually normalized by a characteristic of the reactor which depends on the application of the reactor[66]. Most of the time the normalization is done relatively to the projected anode surface area A_{anode}, which is where the biological reaction occurs. The power density relative to this surface is P_{anode} ($W \cdot m^{-2}$):

$$P_{anode} = \frac{E_{cell}^2}{A_{anode} R_{ext}} \qquad \textbf{[1.14]}$$

Sometimes when the cathode surface is clearly limiting or when the anode surface is difficult to estimate an alternative normalization by the cathode surface $P_{cathode}$ ($W \cdot m^{-2}$) may be used.

A normalization by the reactor or anodic compartment volume can be calculated for issuing engineering optimizations or comparisons with chemical fuel cells as the volumetric power P_v ($W \cdot m^{-3}$):

$$P_v = \frac{E_{cell}^2}{vR_{ext}} \qquad \textbf{[1.15]}$$

These values nevertheless refer to the directly measured power output. The maximum power can be calculated from a polarization curve.

1.5.4.3. Polarization & power curves

A polarization curve represents the evolution of the voltage as a function of the current or the current density. Polarization curve can be recorded with a potentiostat using a periodical increase of the load while the voltage is measured and the current calculated relatively to the load using Ohm's law. Polarization curves can be recorded for the whole MFC, the anode or the cathode using a reference electrode as the counter electrode in the two latter cases.

Polarization curves can generally be divided in three parts (**Figure 1.18.A**)[66],[128]:

a. From the OCV, a steep decrease in voltage is usually observed corresponding to the **activation losses**;
b. The voltage then decrease linearly and more slowly as the **ohmic losses** are dominant;

c. There is a rapid fall in voltage at higher current where the **concentration losses** are finally dominant.

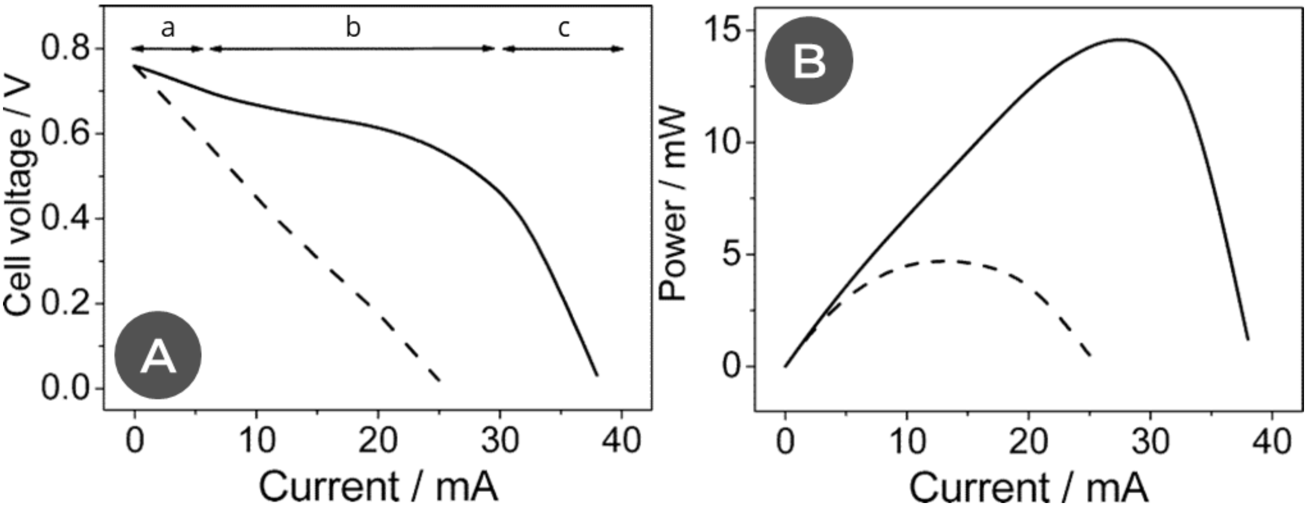

Figure 1.18 – Polarization (A) and power (B) curves of an MFC operating on starch. The solid curves are the original data; the dashed curves represent a mathematically manipulated dataset in which the effect of an increase of the ohmic resistance with 20 Ω is illustrated. The increase of the ohmic resistance resulted in a linear polarization curve (dashed line). From the slope of this curve and Ohm's law an internal resistance of 30 Ω can be determined.

Adapted from Logan *et al.*, 2006 & Niessen *et al.*, 2004

In most MFCs more linear polarization curves are found (dashed line). For such polarization curves the value of the internal resistance R_{int} of the MFC can be calculated as the slope of the line.

Moreover, a power curve shows the evolution of the power or the power density as a function of the current or the current density. It is calculated from the polarization curve (**Figure 1.18.B**)

1.5.4.4. Cyclic voltammetry

Using a potentiostat, it is easy to linearly scan the potential of the electrode through the time and record the corresponding current. The resulting current vs. potential plot is known as a voltammogram. If the scan only goes in one direction the technique is called linear sweep voltammetry and cyclic voltammetry when it goes back to the starting potential afterwards (**Figure 1.19**). The potential scan speed is known as the scan rate and is usually reported in $V \cdot s^{-1}$.

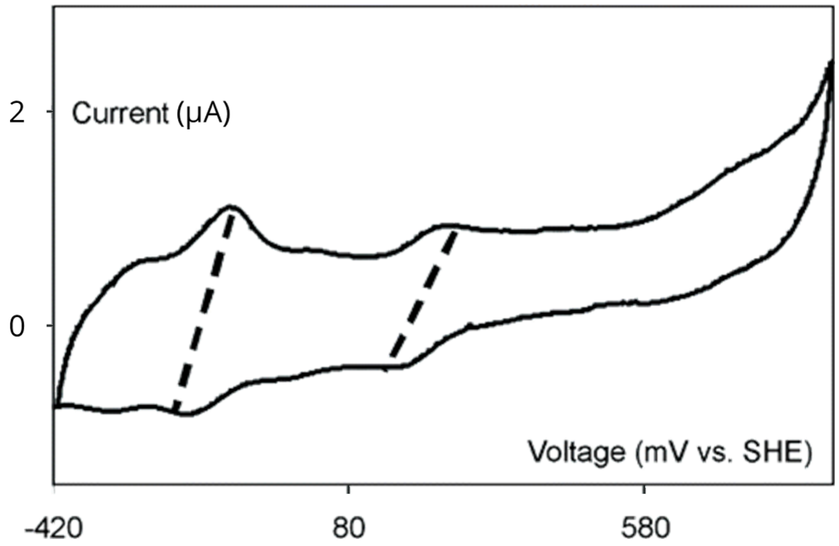

Figure 1.19 – Cyclic voltammogram (solid line) of an electrochemically active mixed microbial community. The dashed lines connect the oxidation and reduction peaks of redox active compounds.

Adapted from Rabaey *et al.*, 2004 & Logan *et al.*, 2006

The resulting cyclic voltammogram (CV) usually shows peaks that can be attributed to oxidation (when decreasing potential) and reduction (when increasing potential) of redox active materials and the corresponding currents may give insights in the efficiency of the electron transfers.

Cyclic voltammetry is useful to study the electrochemical properties of a redox species and in MFCs may be used to determine the nature and extent or exoelectronic transfers. From a cyclic voltammogram of an MFC the standard redox potentials of the redox active components[49],[87], the electrochemical activity of the exoelectrogenic microorganisms[48] and the performance of novel electrode materials[129] can be estimated.

1.6. Microbial fuel cells architectures & materials

A broad array of cell architectures and electrodes materials as well as separator membranes have been used in lab-scale and commercial MFCs.

1.6.1. Cell architecture

General cell architecture is a key leverage in improving the performances of MFCs as most internal and ohmic losses can be mitigated by tweaking its geometry and dimensions.

A lot of different configurations have been explored in both lab-scale[48],[130]–[134] and continuous flow[56],[135]–[138] MFCs (**Figure 1.20**).

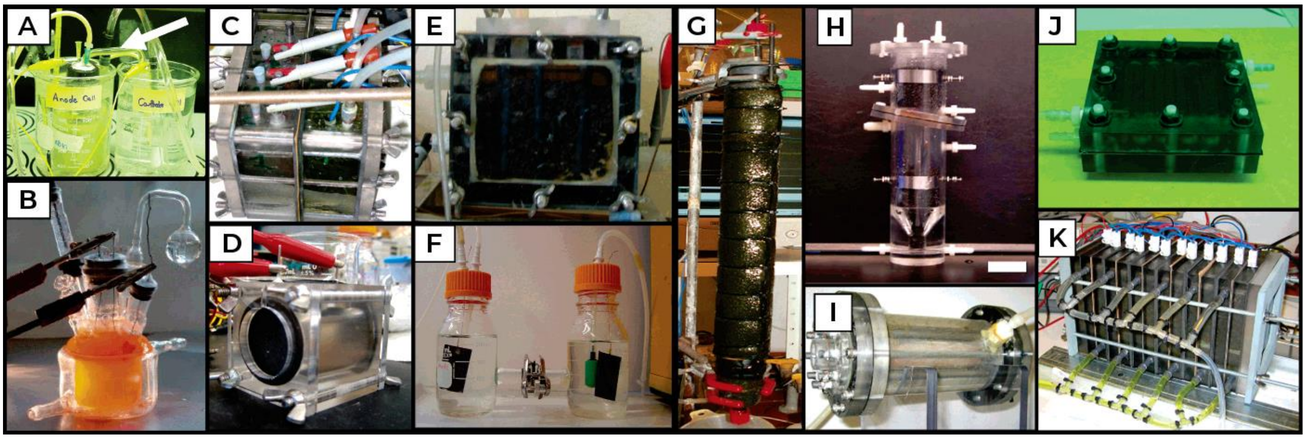

Figure 1.20 – Types of (A)–(F) lab-scale & (G)–(K) continuous operation MFCs. (A) Salt-bridge type; (B) Photoheterotrophic type; (C) Four batch-types separated by a membrane; (D) Single-chamber with air cathode; (E) Batch-type; (F) Two-chamber H-type with gas sparging; (G), (H) Upflow tubular type; (I) Single-chamber with inner concentric air cathode; (J) Flat-plate design with serpentine pattern design inside; (K) Stacked MFCs with 6 MFCs joined in a block.

Adapted from Logan *et al.*, 2006

The simplest design is the traditional batch-mode “H” shape MFC where two chambers containing the electrolytes are connected by either a salt bridge or an ion exchange membrane[130]. Because of the high internal resistance of a salt bridge, a two-chambered MFC rather separated by an ion exchange membrane is a robust way to quickly assess the efficiency of a new electrode material or microorganism. However, these systems exhibit most of the time a low power density due to the ratio of cathode to anode surfaces[139], the membrane surface area[140] and above all high internal resistance and electrode-based losses.

When aiming for better power densities an obvious strategy is therefore to decrease the internal resistance of the system which can be done by decreasing the distance between the electrodes or the electrolytic volume. Liu *et al.*, for instance report an increase in power density from 720 $mW{\cdot}cm^{-2}$ to 1210 $mW{\cdot}cm^{-2}$ by reducing the distance between the electrodes from 4 to 3 cm, however noting that by decreasing it up to 1 cm the power density also decreased as a result of hindered oxygen diffusion[141]. When using air as a cathodic reactant it is also possible to work in a single-chamber reactor which also reduces internal resistance by limiting the volume of electrolyte[133].

Various variations of the basic shape design have also been developed to provide commercially efficient continuous flow MFCs. Among other, architectures exhibiting a cylindrical MFC with a tubular concentric inner air cathode have been proposed[142] along upflow MFCs where the anolyte circulates through a porous anode[136] or with hydrogen fuel cell resembling devices where a PEM is sandwiched between the two electrodes[49].

Eventually voltage and performances can be improved by linking many MFCs together in series[138].

1.6.2. Cathode materials

Cathodic reactions efficiency are critical for a proper MFC performance[143] and various catholytes have been reported in the literature.

For lab-scale applications, potassium ferricyanide[49],[144],[145], iron permanganate[146], or copper are used thanks to their high redox potential and well-understood behavior. Nevertheless, their cost and toxicity limit their applications for scale-up and industrial use.

The most widely used system however is the air cathode, as air oxygen is free and readily available, and presents a high redox potential $E_0(O_2/H_2O) = 1.23$ V vs. SHE even if its reaction rate is lower than for potassium ferricyanide or iron permanganate. The electrode may be directly in contact with the air without the need for a catholyte but the main drawback of air electrodes nonetheless remains the high costs of its platinum catalyst and various approaches have been proposed to reduce Pt loading[139],[147],[148]. Non-precious metal catalyst such as iron phthalocyanine or cobalt tetramethoxyphenylporphyrin are also considered as platinum alternative for MFC cathodes[129].

Beyond chemical catalysts, the use of microorganisms to catalyze a cathodic reaction may also be developed[149]. The feasibility of this approach was demonstrated in 2005 by Bergel *et al.* who designed a MFC using a platinum anode for hydrogen oxidation, a Nafion® PEM and a stainless steel cathode either raw or covered in seawater biofilm[150]. While the biofilm-powered cathode was immersed in a seawater circulating medium a maximum power density of 0.3 $W{\cdot}m^{-2}$ was observed which fell at only 0.015 $W{\cdot}m^{-2}$ when the biofilm was removed. The difference was attributed to a catalytic effect of the biofilm for oxygen reduction and opened the path to the replacement of expensive chemical catalysts. This result was confirmed in a membrane-less wastewater MFC by Aldrovandi *et al.*, stating that diffusion rather than catalytic activity was limiting the power production[151]. Apart from biocatalyzed oxygen reduction, denitrification has been proposed as a valuable depolluting cathodic reaction[152]. The denitrification process consists in the bioreduction of nitrate ions NO_3^- into nitrite NO_2^- then into NO, N_2O and eventually N_2 and has been shown to be an efficient MFC cathodic reaction. Another approach to biocatalyzed cathodic reactions lies in bacterially mediated biocathodes. In 2005 a group used *Leptothrix discophora* to biomineralize manganese ions into manganese oxide which was in turn reduced at the surface of the cathode, coupling it with the anodic glucose oxidation by *Klebsiella pneumoniae*[153].

Eventually it has been suggested to replace cathodic catalysts by other microorganisms like algae[143], yeasts, or even enzymes to develop hybrid biofuel cells[154].

1.6.3. Separators

The separator is a key component of the hydrogen fuel cell. It is usually a proton exchange membrane and avoids the diffusion of anodic hydrogen and cathodic oxygen gases to diffuse to the other electrode, while allowing the protons produced by hydrogen oxidation to diffuse to the cathodic compartment to recombine with oxygen.

In most MFCs as no conflicting gases are used a separator membranes is not strictly required and numerous membraneless MFCs are reported in the literature[151].

However, many MFCs designs use such separators as having two separate compartments prevents unwanted substrate, bacterial or chemical diffusion from one electrolyte to the other. This can be useful when the catholyte is toxic for the bacteria or to avoid electrode poisoning by either bacteria or substrate at the cost of increasing the internal resistance of the MFC due to proton diffusion loss and increased solution volume.

In a fuel cell setup when the electrodes are polarized an electric field is established between them which induces the migration of ions toward the oppositely-charged electrodes. The nature of the ion-exchange membrane is determined by the ions produced. Such separators are usually polymer membranes grafted with charged groups (**Figure 1.21**)[155].

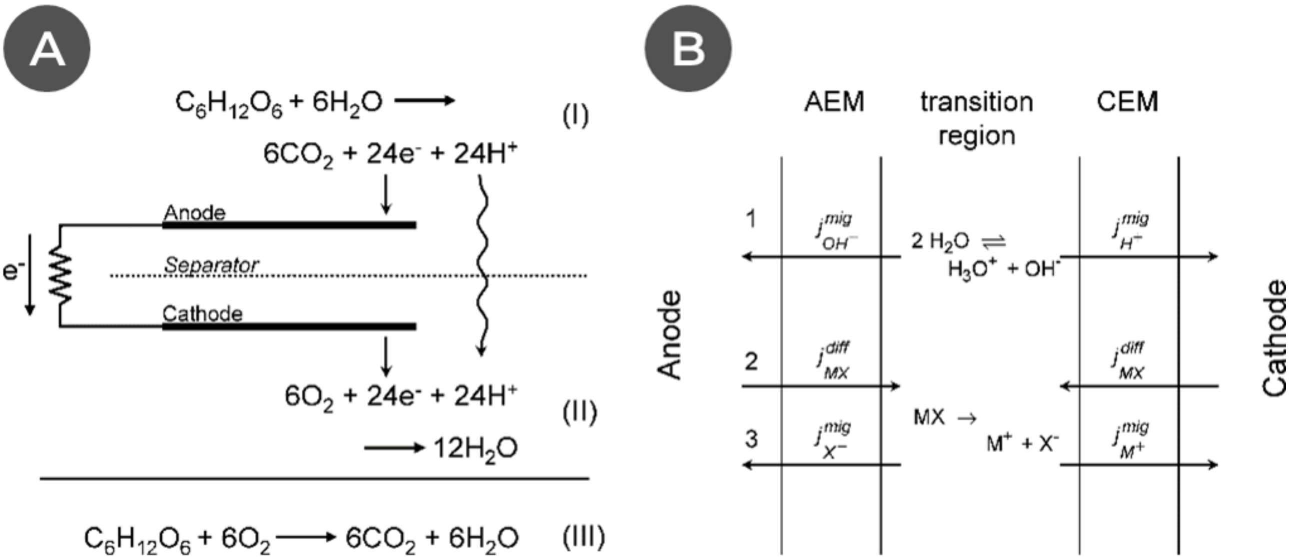
A
$C_6H_{12}O_6 + 6H_2O \longrightarrow$ (I)
$6CO_2 + 24e^- + 24H^+$
Anode
Separator
Cathode
e^-
$6O_2 + 24e^- + 24H^+$ (II)
$\longrightarrow 12H_2O$
$C_6H_{12}O_6 + 6O_2 \longrightarrow 6CO_2 + 6H_2O$ (III)
B
AEM
transition region
CEM
Anode
Cathode
1
$j^{mig}_{OH^-}$
$2\,H_2O \rightleftharpoons H_3O^+ + OH^-$
$j^{mig}_{H^-}$
2
j^{diff}_{MX}
j^{diff}_{MX}
3
$j^{mig}_{X^-}$
$MX \rightarrow M^+ + X^-$
$j^{mig}_{M^+}$

Figure 1.21 – Effect of ion exchange membranes in MFCs with (A) a simplified model of the redox reactions and charge-balancing ion transfer in an MFC and (B) a schematic illustration of the structure of and the ion fluxes across a bipolar membrane.

From Harnisch *et al.*, 2008

They are divided in two categories depending on the nature of the charges:

- Cation exchange membranes (CEM) are grafted with negative groups such as $–SO_3^-$ and allows only positively charged ions to diffuse. This category includes for instance the widely used Nafion® proton exchange membrane;
- Anion exchange membranes (AEM) are grafted with positive groups such as $–NR^{4+}$ and let only diffuse negatively charges ions.

It is worth noting that in both case small parasite migrations are nevertheless observed, and that both types of membranes are eventually prone to biofouling by bacteria biofilms which can decrease MFC performances over time[50].

Most dual-chambered MFCs use proton exchange membranes to separate its two compartments, but non-ionic alternatives have also been considered and studied including ultrafiltration membranes[156], cellulose nitrate, polycarbonate, cellulose, nylon membranes[157], wool, glass fiber[158] and salt bridges[159].

1.6.4. Anode materials

Because the biocatalyzed reaction in an MFC usually takes place at the anode, its material must be thoroughly optimized. The main parameters that must be considered for a suitable bioanode are:

- Electrical conductivity;
- Specific surface area and/or porosity;
- Cytocompatibility and toxicity;
- Sensibility to corrosion and bio-corrosion;
- Stability against biofouling;
- Cost and availability.

In order to find a balance between them, most MFCs anodes are either metal-based or carbon-based, and various architectures have been developed to optimize their behavior (**Figure 1.22**)[160].

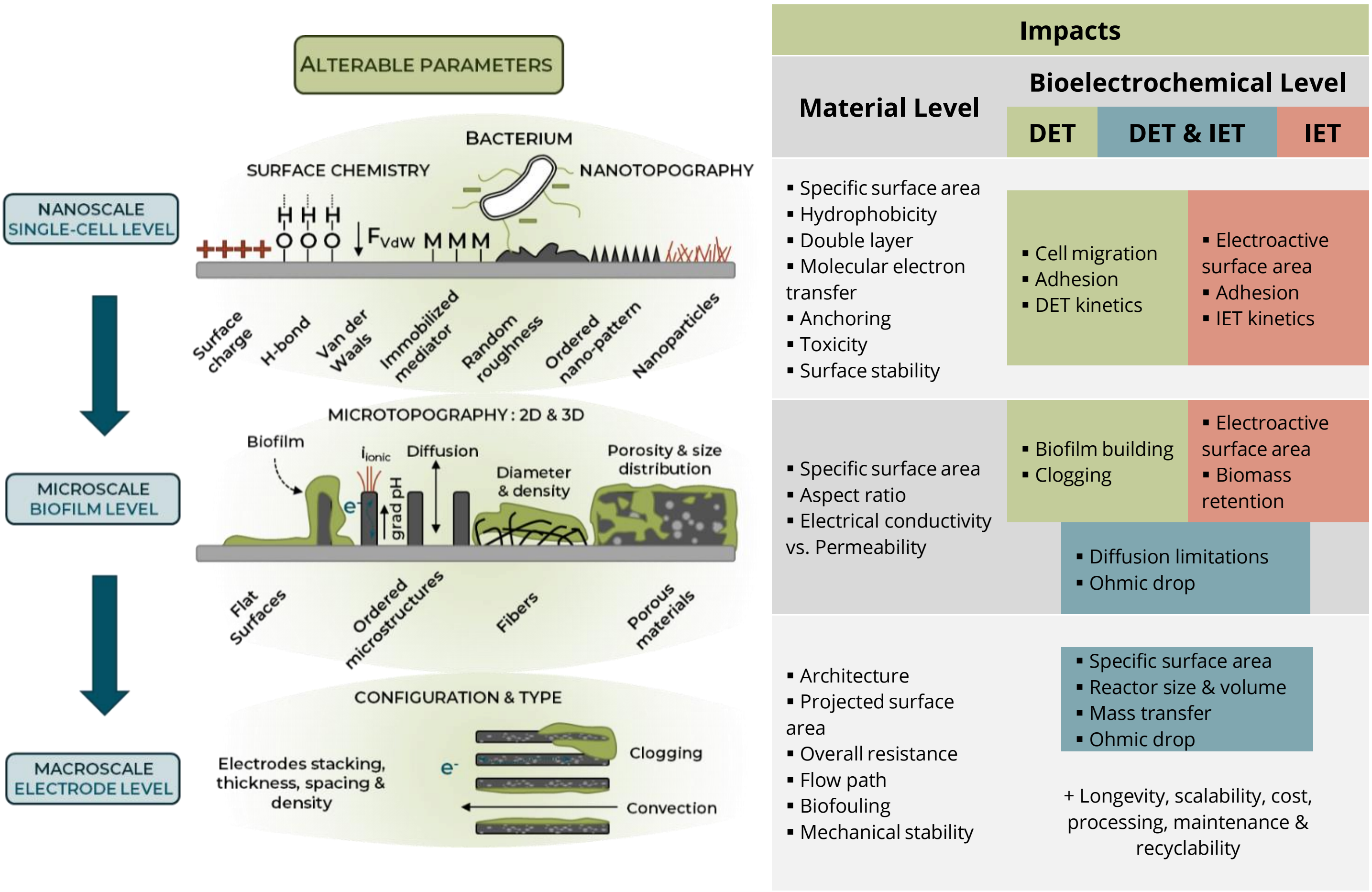
ALTERABLE PARAMETERS
NANOSCALE SINGLE-CELL LEVEL
MICROSCALE BIOFILM LEVEL
MACROSCALE ELECTRODE LEVEL
BACTERIUM
SURFACE CHEMISTRY
NANOTOPOGRAPHY
++++
H H H
O O O
Fvdw
M M M
Surface charge
H-bond
Van der Waals
Immobilized mediator
Random roughness
Ordered nano-pattern
Nanoparticles
MICROTOPOGRAPHY : 2D & 3D
Biofilm
iionic
Diffusion
e-
grad pH
Diameter & density
Porosity & size distribution
Flat surfaces
Ordered microstructures
Fibers
Porous materials
CONFIGURATION & TYPE
Electrodes stacking, thickness, spacing & density
e-
Clogging
Convection
Impacts
Material Level
Bioelectrochemical Level

Material Level	DET	DET & IET	IET
▪ Specific surface area ▪ Hydrophobicity ▪ Double layer ▪ Molecular electron transfer ▪ Anchoring ▪ Toxicity ▪ Surface stability	▪ Cell migration ▪ Adhesion ▪ DET kinetics		▪ Electroactive surface area ▪ Adhesion ▪ IET kinetics
▪ Specific surface area ▪ Aspect ratio ▪ Electrical conductivity vs. Permeability	▪ Biofilm building ▪ Clogging	▪ Diffusion limitations ▪ Ohmic drop	▪ Electroactive surface area ▪ Biomass retention
▪ Architecture ▪ Projected surface area ▪ Overall resistance ▪ Flow path ▪ Biofouling ▪ Mechanical stability		▪ Specific surface area ▪ Reactor size & volume ▪ Mass transfer ▪ Ohmic drop + Longevity, scalability, cost, processing, maintenance & recyclability	

Figure 1.22 – Impacts of anode properties on microbial electrocatalysis

Adapted from Guo *et al.*, 2015

1.6.4.1. Metal electrodes

Metal anodes are a simple and robust choice as long as they are noncorrosive and nontoxic to bacteria. This usually excludes common metals as iron which is easily corroded and copper whose ions are toxic even a low concentration. On the other hand noble metals such as platinum and gold[161],[162] and other metals stable in MFC conditions like stainless steel[163] and titanium[164] have been widely reported as MFC anodes.

Various architectures are described in the literature such as mesh, scrubber, foam, plates and sheets[165] and satisfactory performances are usually achieved[166].

1.6.4.2. Carbon-based materials

Nonetheless, the most versatile choice and the most widely used material for a bioanode is carbon. Carbon anodes are commercially available under a broad list of architectures, from compact graphite plates, rods and granules to fibrous felt, cloth, paper, fibers or foam and glassy carbon. Carbon stands out due to its good electrical conductivity, high biocompatibility & chemical stability, to its wide availability and cheap cost[164],[167],[168].

Technical commercial materials include[165],[169] (**Figure 1.23**):

- **Carbon rods**, simple and inexpensive but suffer from a low specific surface area and porosity[168];
- **Graphite plate**, 2D graphitic material with the same qualities and drawbacks as carbon rods[167];
- **Carbon paper** (e.g. Toray paper), made out of carbon powder or fibers bound with or without binder on a PTFE substrate, porous and easy to handle but fragile and expensive (1000 USD·m^{-2})[170];
- **Carbon cloth, tissue or mesh**, 2D woven micrometric carbon fibers, high porosity and surface area, flexible but expensive[171];
- **Carbon fibers veil**, 2D nonwoven carbon fibers similar with carbon cloth[172];
- **Graphite or activated carbon granules**, micrometric carbon particles, usually compacted to ensure electrical conductivity[173];
- **Graphite fibers brush**, carbon fibers radially arranged around a titanium collector, with high specific surface area but easily clogged[174];
- **Carbon and graphite felt**, 3D nonwoven network of carbon fibers (around 12 µm in diameter) with high porosity and high specific surface area (around 0.2 m^2.g^{-1})[167];
- **Carbon foams** (e.g. Reticulated vitreous carbon), made out of a sponge-like carbon matrix, with similar characteristics as carbon felt but more expensive[169];
- **Low-tech carbon materials** such as carbonized cardboard, cheap and easy to produce but with poorer performances compared with commercial alternatives[175].

The choice among these materials is determined by the application sought. Carbon rods and plates are the simplest materials and are well adapted to studies requiring a plain anodic material for basics theoretical investigations, and deliver the lowest power density. Carbon paper is expensive but has been widely used in the literature, producing power density ranging from 20 to 250 mW·m^{-2}. Other 2D carbon materials produce even higher power densities thanks to their high specific surfaces and are also extensively reported as bioanodes. The good performances of these materials have led to the investigation of 3D carbon materials with power densities ranging from 50 to 1000 mW·m^{-2}. Furthermore, compaction of carbon granules is extensively used in commercial continuous-flow MFCs as it allows the easy circulation of the anolyte for power output reaching more than 50 W·m^{-3}. Eventually preliminary studies on low-tech material such as carbonized cardboard show promising results, with stable and functional establishment of biofilm and current generation.

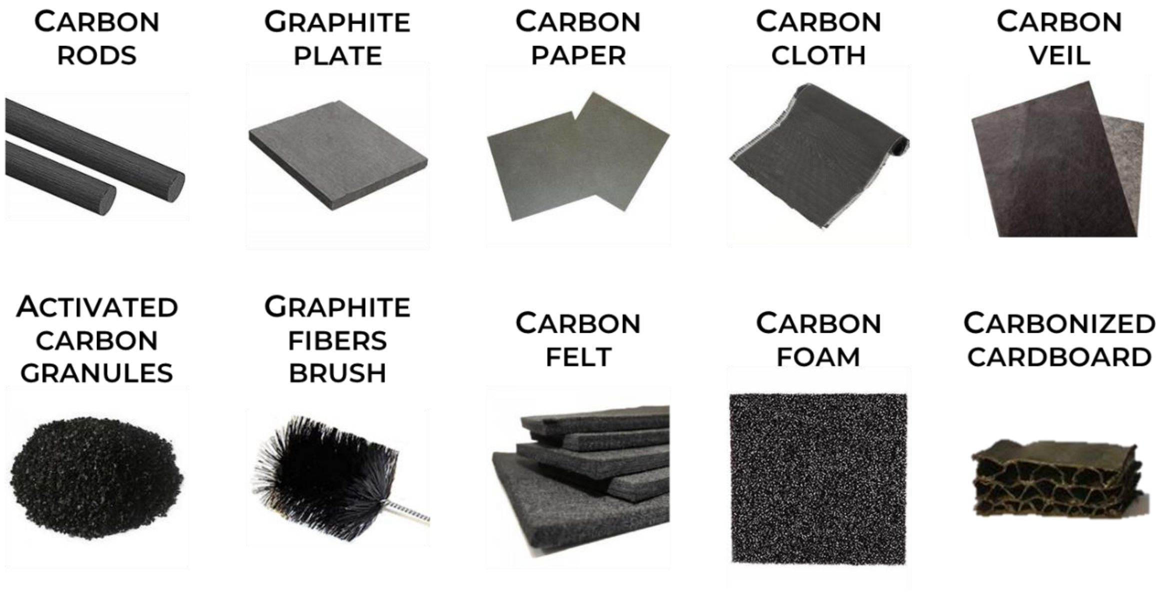
CARBON RODS
GRAPHITE PLATE
CARBON PAPER
CARBON CLOTH
CARBON VEIL
ACTIVATED CARBON GRANULES
GRAPHITE FIBERS BRUSH
CARBON FELT
CARBON FOAM
CARBONIZED CARDBOARD

Figure 1.23 – Photographs of majors anodic carbon materials used in MFCs
Adapted from Santoro *et al.*, 2017

The surface treatment of carbon materials has also been shown to improve its performances in an MFC. Chemical surface modification by acidic or ammonia treatment has been consistently shown to improve acclimation time, power output and coulombic efficiency by adding charged groups on the anode surface[176]–[178].

Alternatively, the immobilization of various particles on the carbon surface has been thoroughly investigated. Increase in power output is reported for absorption of carbon nanotubes[179], reduced graphene oxide[180] or neutral red[93] among others. Despite the performances gains, the cost of these additives remains nonetheless high.

Research has been furthermore conducted on the influence of the surface area, roughness and scale on MFCs performances. Inoue *et al.* investigated in particular the effect of bacteria-scaled surface geometry on current output and concluded that the current production is linearly linked to the surface area (**Figure 1.24**)[181].

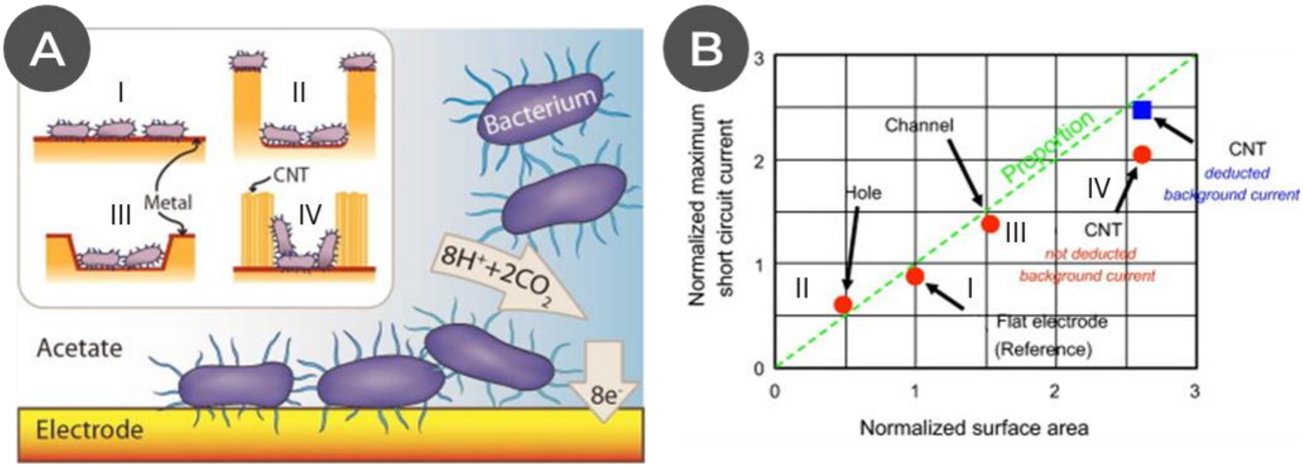
A
I
II
III
IV
CNT
Metal
Bacterium
$8H^+ + 2CO_2$
$8e^-$
Acetate
Electrode
B
Normalized maximum short circuit current
Normalized surface area
0
1
2
3
Proportion
Channel
Hole
CNT
deducted background current
CNT
not deducted background current
Flat electrode (Reference)
I
II
III
IV

Figure 1.24 – Overview of the effect of the anode surface structure on an MFC current output. (A) Representation of the bacteria on (I) a flat anode, (II) with a hole, (III) with a channel and (IV) with vertically aligned CNTs. (B) Linear relationship between the current output & the surface area.

From Inoue *et al.*, 2012

Henceforth, developing better scaled materials seems to be a good strategy for improving bacterial electron transfer and the power output of an MFC. Eventually a micron-sized anodic material can take advantage of the superiority of ultramicroelectrodes regarding the diffusion of a redox substrate[182] toward the bacterium[183],[184].

1.7. Electrospinning & electrode materials

In 1899, John F. Cooley patented a method to extrude fibers from a polymer solution exposed to an electrostatic field, nowadays know as electrospinning[185]. Largely ignored until the mid-1990s and a sparkling interest in the field of nanoscience, this technique is able to produce continuous fibers ranging from a few micrometers to the nanometer scale. Since then the electrospinning process has seen a surge in popularity researchers started to realize its huge potential (**Figure 1.25**).

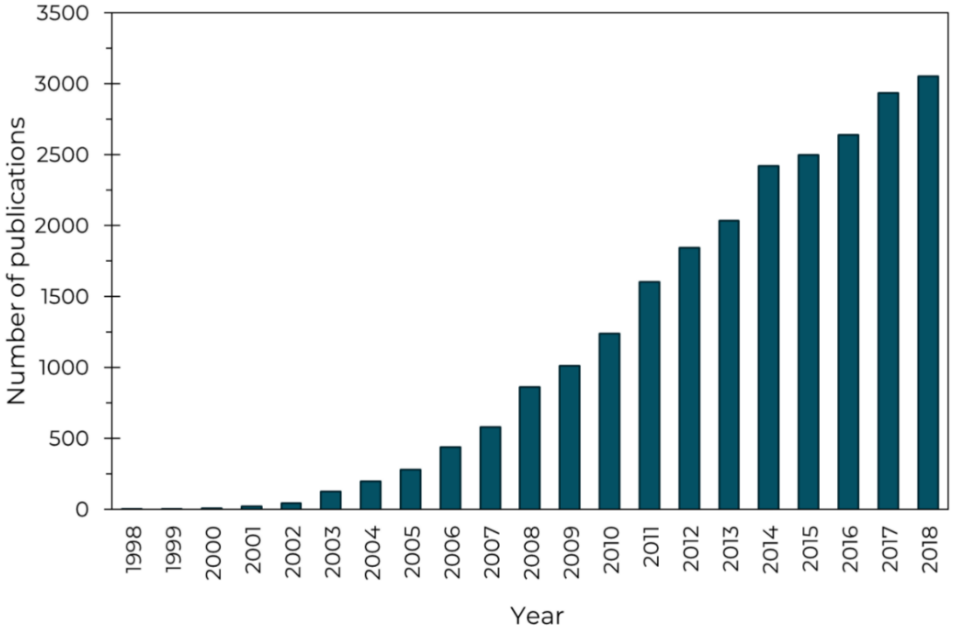

Figure 1.25 – Number of publications for articles on the keyword "Electrospinning"
Source: Web of Science

1.7.1. Fundamentals

By applying a high voltage – from 1 to more than 30 kV – between a metal spinneret – typically a hypodermic syringe needle – supplied with a polymer solution and a grounded conductive collector the liquid tends to be electrically charged and the electrostatic repulsion between the dissolved polymer chains opposes to the surface tension (**Figure 1.26**). The resulting competition forces the droplet to stretch and by applying a high enough electrostatic field it is possible to overcome the surface tension. The resulting breaking point forms a so-called "Taylor cone" where a polymer solution jet is extruded between the spinneret and the substrate. Once drawn the fibers start to dry out as the solvent evaporate and when dried enough stop to be accelerated by the electric field. The solidified jet undergoes an instability process and deposes as a random nonwoven mat on the collector.

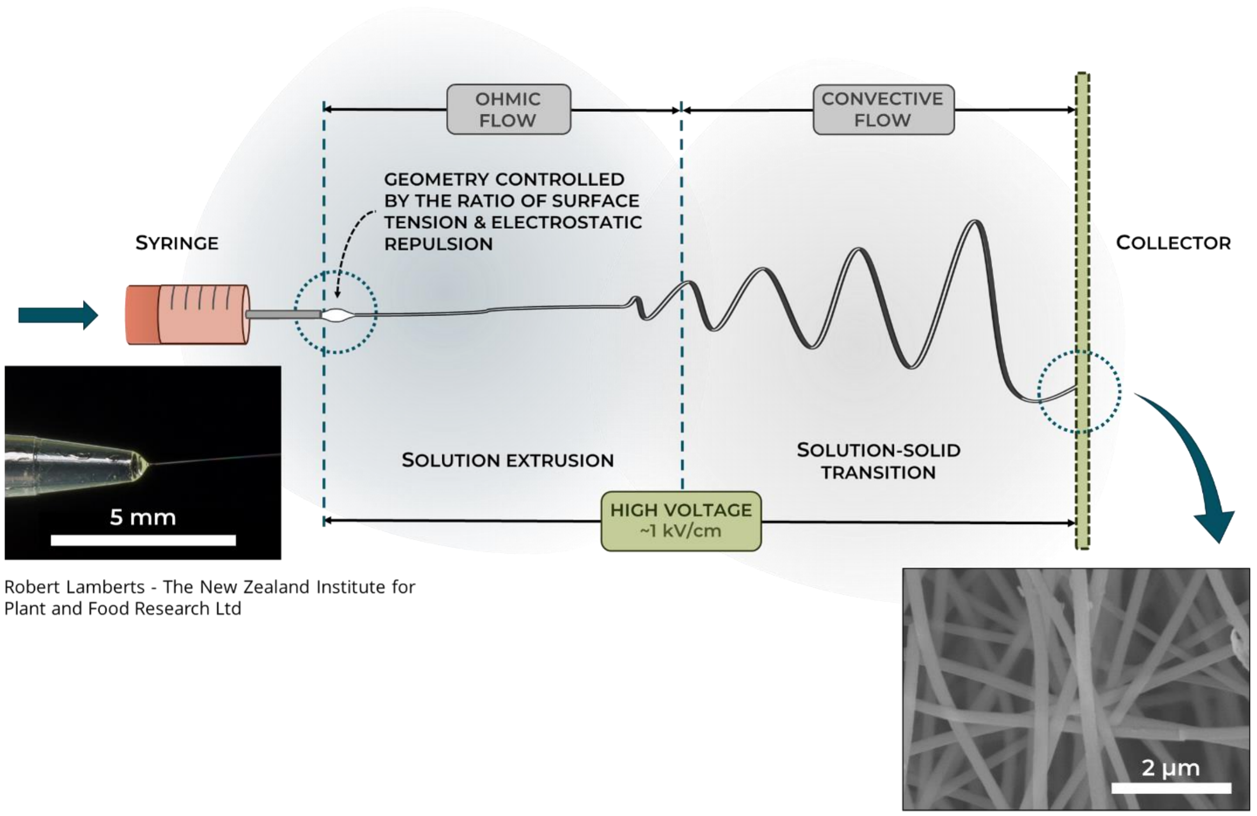
OHMIC FLOW
CONVECTIVE FLOW
GEOMETRY CONTROLLED BY THE RATIO OF SURFACE TENSION & ELECTROSTATIC REPULSION
SYRINGE
COLLECTOR
5 mm
SOLUTION EXTRUSION
SOLUTION-SOLID TRANSITION
HIGH VOLTAGE ~1 kV/cm
2 µm

Robert Lamberts - The New Zealand Institute for Plant and Food Research Ltd

SEM-FEG micrograph of electrospun fibers

Figure 1.26 – Overview of an electrospinning setup

A lot of solvent/polymer mixtures have been successfully electrospun to this day for a broad range of applications (**Table 1.3**).

Table 1.3 – Examples of polymer/solvent electrospinning mixes and their applications

Polymer	Solvent	Application
Polycarbonate (PC)	Dichloromethane	Sensors[186]
	DMF/THF	Textiles[187]
Poly(acrylonitrile) (PAN)	DMF	Carbon fibers[188]
Poly(vinyl alcohol) (PVA)	H_2O	Filtration[189]
Poly(ethylene oxide) (PEO)	H_2O; Ethanol	Photonics[190]
	Chloroform; Acetone	Microelectronics[191]
Polystyrene (PS)	THF; DMF; Chloroform	Catalysis[192]
Polyaniline/PEO	Chloroform	Conductive fibers[193]
Poly(3,4-ethylenedioxythiophene):poly(styrenesulfonate)/PVA	H_2O/DMSO	Strain sensors[194]

1.7.2. Electrospinning parameters

A lot of experimental parameters are to be taken in account to optimize the electrospinning process and yield fibers with the desired size and morphology.

1.7.2.1. Solution properties

The polymer concentration and molecular weight are of critical importance for a proper electrospinning process.

In a polymer solution, it exists a critical concentration c^* which depends on the considered polymer, molecular weight and solvent, over which polymer chains overlap (**Figure 1.27**)[195].

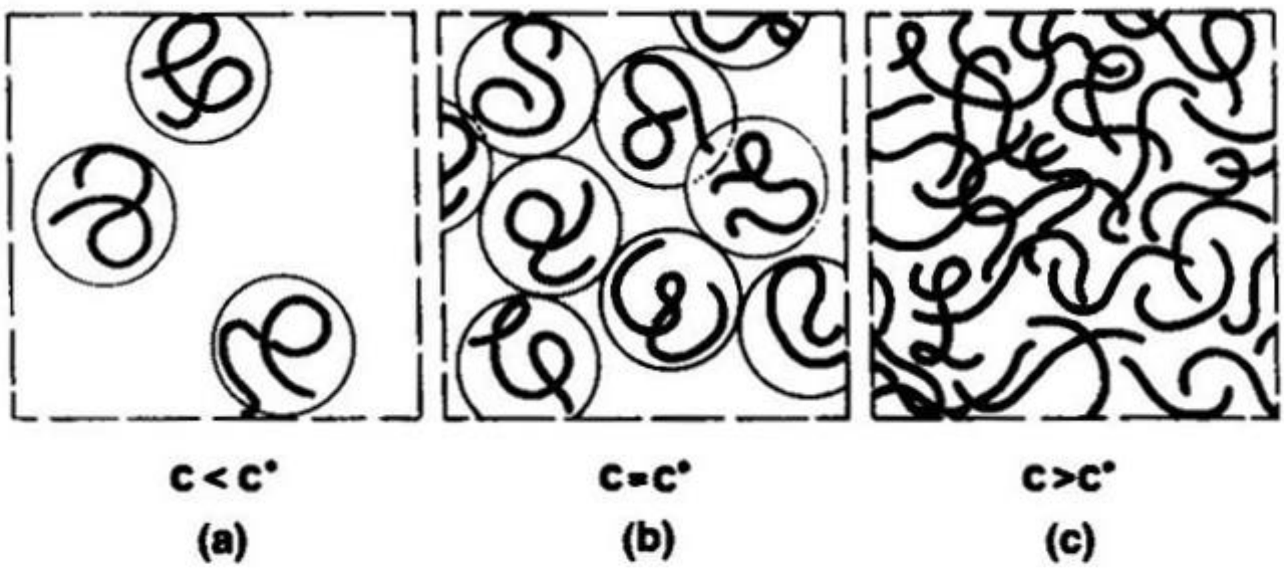

Figure 1.27 – Definition of a diluted polymer solution $c < c^*$, of the overlap concentration c^*, and of a semi-diluted polymer solution $c > c^*$.

From de Gennes, 1979

Under this critical concentration no extrusion is possible as the solution viscosity is too low to sustain a fiber morphology. By increasing the concentration, it is possible to produce polymer droplets (electrospraying), then beaded fibers, and eventually proper fibers increasing in diameter as the concentration keeps increasing[196] until the solution viscosity is too high to properly flow and to be electrospun (**Figure 1.28**)[197].

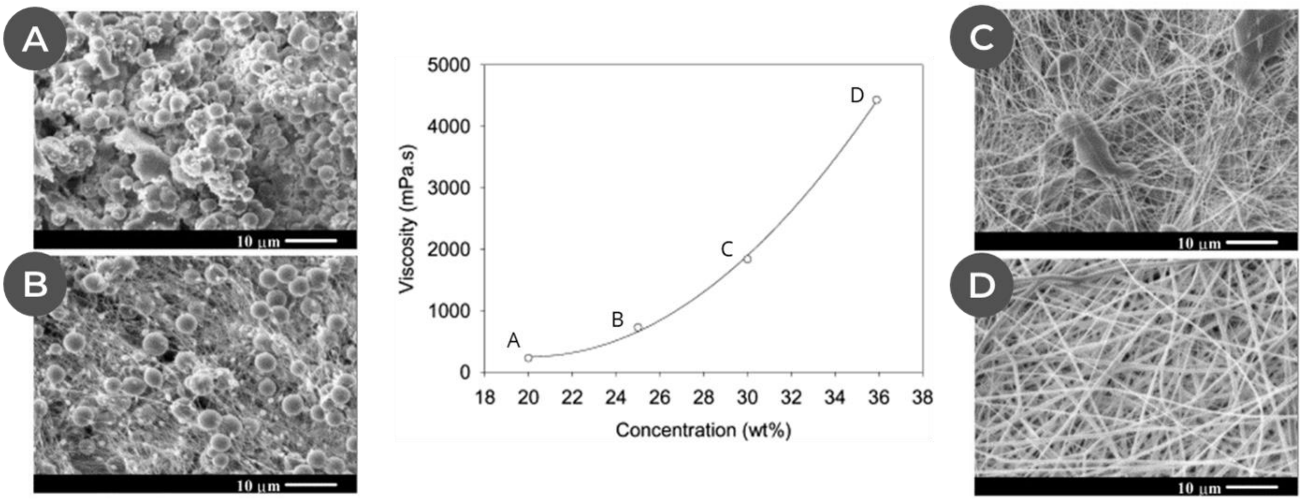

Figure 1.28 – Evolution of poly(lactic acid) in DMF morphology relatively to the solution concentration.

From Zong *et al.*, 2002

By increasing the mass average molar mass M_w the viscosity also rise. It leads to a higher solution viscosity and a similar evolution in architecture (**Figure 1.29**)[196].

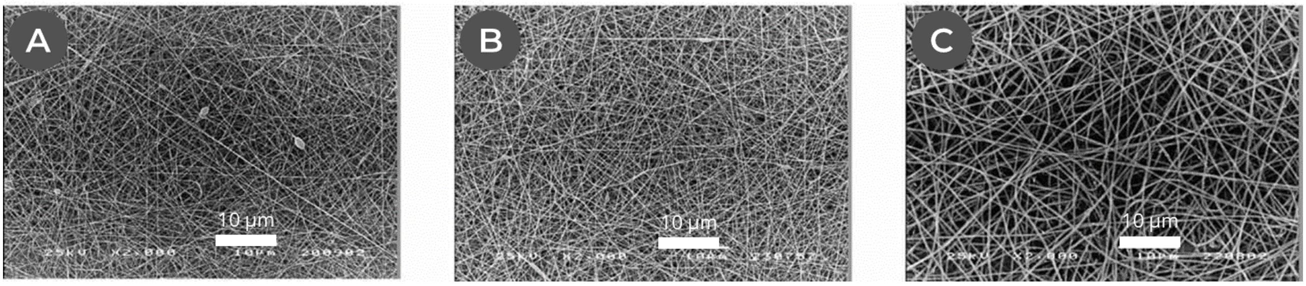

Figure 1.29 – SEM micrographs of electrospun materials obtained from solutions of 34 wt wt/vol% polyamide in 85 vol% formic acid at M_w of (A) 17 kDa, (B) 20 kDa and (C) 32 kDa.

Adapted from Mit-uppatham *et al.*, 2004

Finally the nature of the solvent also plays a critical role, as solvents with high surface tensions tend to produce more instable Taylor cones and yield beaded fibers (**Figure 1.30**)[198]. Furthermore the dielectric constant of the solvent need to be high enough to allow its charge under the applied electric field[199].

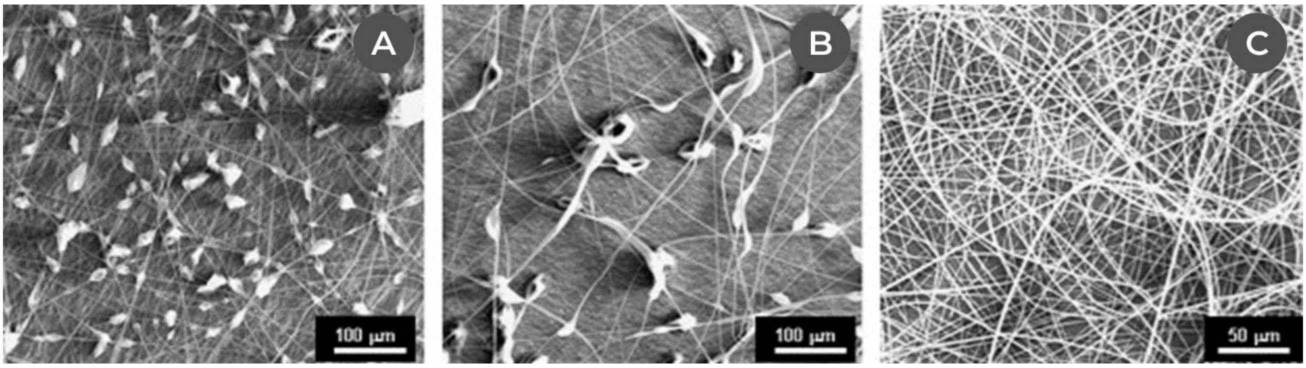

Figure 1.30 – SEM micrographs of electrospun polystyrene fibers obtained from 20 wt/vol% PS solution in (A) THF, (B) $CHCl_3$ & (C) DMF.

Adapted from Uyar & Besenbacher, 2008

1.7.2.2. Conductivity & solution charge density

The solution conductivity and charge density can be tuned by the addition of salts, charged surfactants or a blend of solvents[200].

A higher conductivity helps in forming more uniform fibers (**Figure 1.31**)[201], and usually thinner fibers[200],[202].

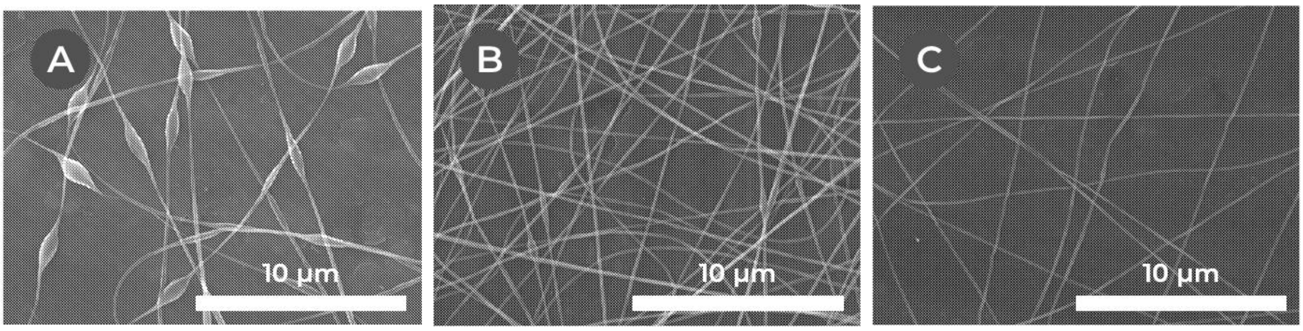

Figure 1.31 – Influence of the net charge density changes due to the addition of NaCl on the architecture of PEO in water electrospun fibers. The electric field is 0.7 kV/cm. The weight fraction of PEO is 3 %. (A) 1.23 C·L^{-1}; (B) 6.57 C·L^{-1}; (C) 28.8 C·L^{-1}.

Adapted from Fong *et al.*, 1999

1.7.2.3. Electric field & feed rate

Once the minimal tension between the spinneret and the collector is applied to overcome the surface tension and start the electrospinning process, most studies point toward a decreasing fiber diameter with an increased voltage (**Figure 1.32**)[203]. An electric field too high however can lead to electrospraying instead of electrospinning.

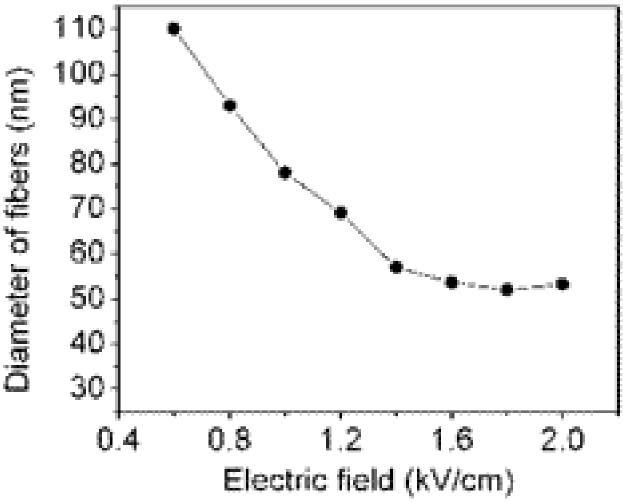

Figure 1.32 – Dependence of nanofibers diameter on electric field for a PVP/EtOH solution
Adapted from Li & Xia, 2003

The feeding rate of the spinneret must be balanced with the electric field to ensure a steady provisioning and stability of the Taylor cone as it is depleted by the extrusion. Additionally a greater injection rate is linked to bigger fibers (**Figure 1.33**)[203].

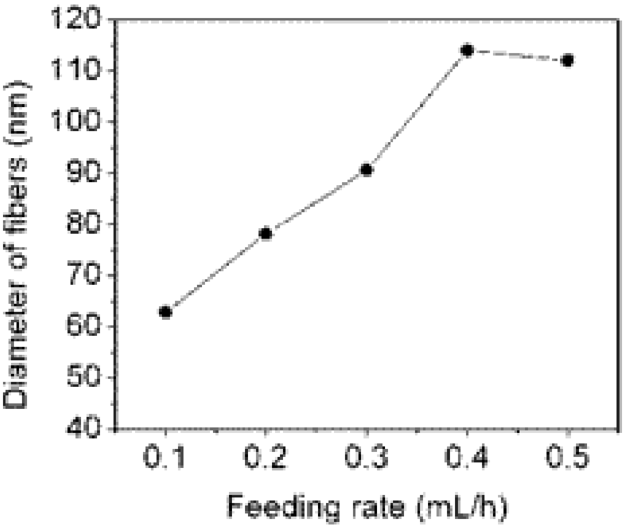

Figure 1.33 – Dependence of nanofibers diameter on feeding rate for a PVP/EtOH solution
Adapted from Li & Xia, 2003

1.7.2.4. Setup dimensions

The distance between the spinneret and the collector is linked to the diameter of the electrospun fibers. A greater distance is correlated to smaller fibers, and a smaller one to bigger fibers sometimes fused together as the solvent does not have the time to evaporate properly (**Figure 1.34**)[204].

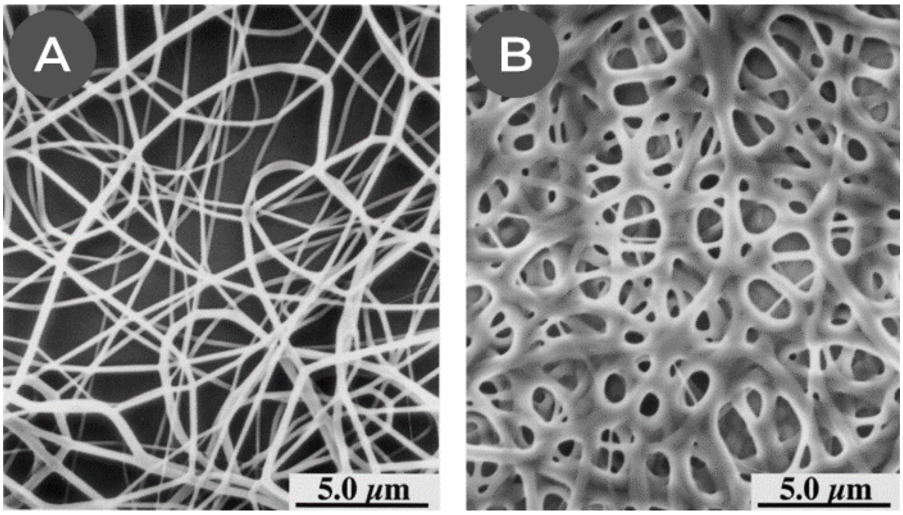

Figure 1.34 – SEM micrographs of electrospun nylon 6-6 in formic acid at (A) 2.0 cm & (B) 0.5 cm.
Adapted from Uyar & Besenbacher, 2008

1.7.2.5. Ambient conditions

Temperature and relative humidity are critical parameters for the stability and reproducibility of the electrospinning process.

Higher temperature implies both quicker evaporation of the solvent as derived from the Clausius–Clapeyron relation and a decrease in solution viscosity due to higher molecular agitation. Because of these two competing factors, the effect on the diameter and architecture of the fibers varies with the solution composition[205],[206]. A tight control of the setup temperature is required for an efficient electrospinning procedure.

The second important ambient parameter is relative humidity (RH). An increased relative humidity can lead to the formation of pores on the surface of electrospun nanofibers consecutively to the condensation of water droplets on the surface of the fibers during the drying step (**Figure 1.35**)[207].

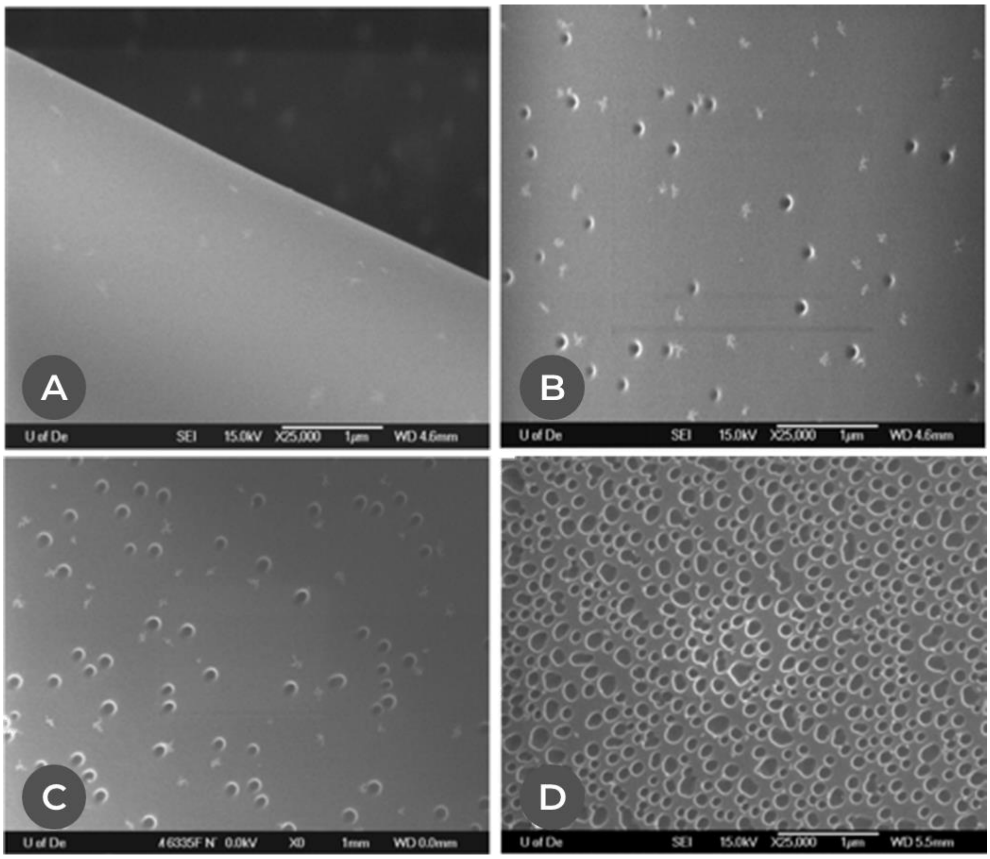

Figure 1.35 – SEM-FEG micrographs of electrospun polystyrene in THF when varying the relative humidity of (A) < 25 %, (B) 31-38 %, (C) 40-45 % and (D) 50-59 %.

Adapted from Casper *et al.*, 2004

Additionally a high relative humidity can hinder the evaporation of the solvent and disrupt the extrusion of fibers – especially when the said solvent is water (**Figure 1.36**)[208].

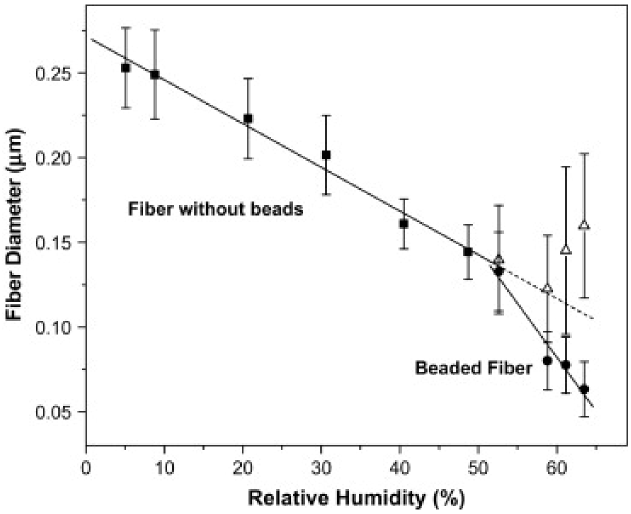

Figure 1.36 – Average fiber diameters of poly(ethylene oxide) in water nanofibers electrospun at different relative humidity.

From Tripatanasuwan *et al.*, 2007

1.7.2.6. Spinneret & collector

The collector substrate must be electrically conductive and set to a smaller potential than the spinneret to generate an electrostatic field between them – it is therefore usually grounded. The collector is either planar or rotating, the latter helping with extrusion. By rotating a drum collector quick enough, it is possible to align the electrospun fibers (**Figure 1.37**)[209].

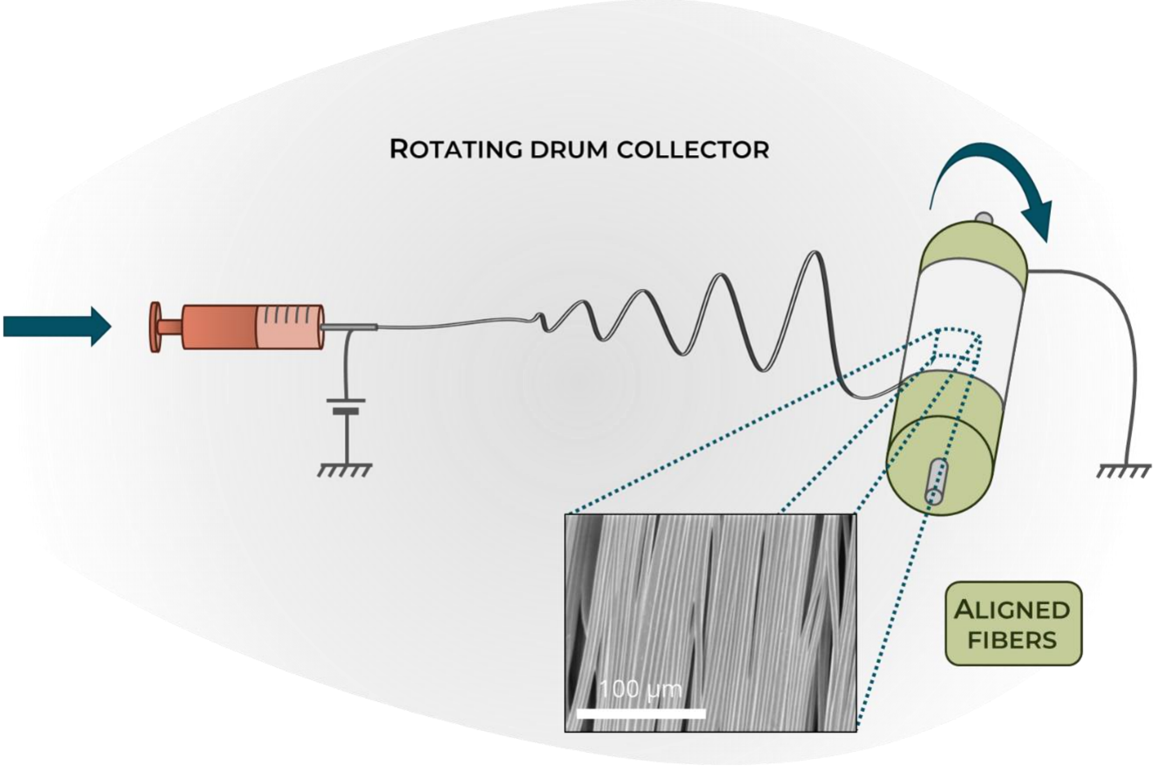

Figure 1.37 – Effect of a rotating drum collector on the alignment of electrospun fibers
Adapted from Pham *et al.*, 2006 & Chew *et al.*

The spinneret width influences the diameter of the fibers and the stability of the Taylor cone. Multiple spinnerets may be used to increase the fiber production throughput or to coelectrospin different solutions together[200]. Furthermore, coaxial multiple-capillary spinnerets can be designed to produce core-shell nanofibers (**Figure 1.38**)[210],[211], filled, hollow or encapsulating particles or bacteria[212]–[215].

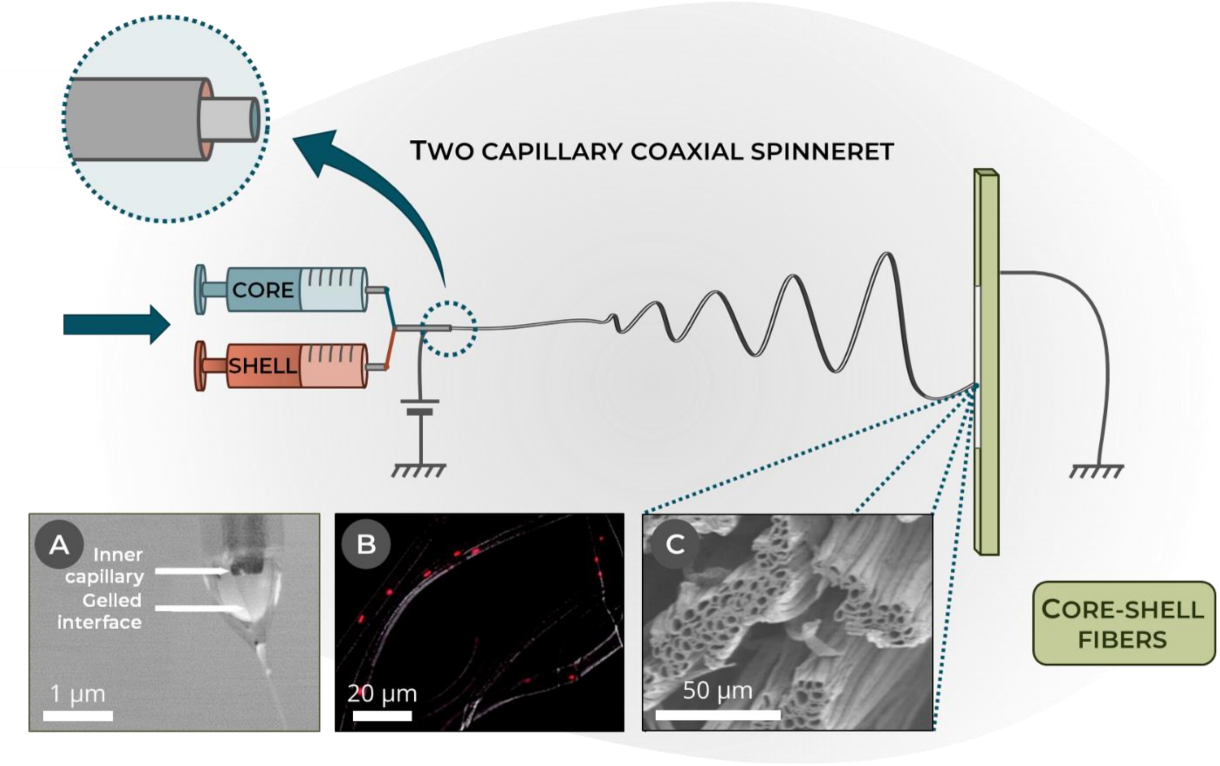
TWO CAPILLARY COAXIAL SPINNERET
CORE
SHELL
CORE-SHELL FIBERS
A
Inner capillary
Gelled interface
1 µm
B
20 µm
C
50 µm

Figure 1.38 – Production of core-shell nanofibers by a coaxial two-capillary spinneret. (A) Compound pendant drop containing a PCL shell and PEO core solution. The protrusion of the inner capillary outside the shell capillary and the gelled interface between the solutions are seen. (B) Fluorescent microscopy of DsRed-expressing *Pseudomonas putida* S12 encapsulated in PCL-shell–PEO-core fibers & (C) High Resolution SEM micrographs of hollow PCL-shell–PEO-core fibers.

Adapted from Klein *et al.*, 2009 & Dror *et al.*, 2007

Eventually the effect of the various electrospinning parameters must be carefully taken into account when designing an experiment and usually their fine tuning is required to obtain the desired morphology (**Table 1.4**)[200].

Table 1.4 – Overview of the effect of electrospinning parameters
Adapted from Pham *et al.*, 2006

Parameter	Effect on electrospun fibers
Polymer concentration & mass	Required to be high enough to avoid beaded fibers; rising it increases the diameter.
Solvent nature	Surface tension cannot be too high; dielectric constant must be high enough.
Conductivity & charge density	Higher conductivity usually yields smaller & more uniform fibers.
Electric field	Minimal electric field required to trigger electrospinning; increasing it reduces diameter.
Feed rate	Must be balanced with electric field for stable process; rising it increases diameter.
Setup dimensions	Minimal distance between spinneret & collector required to let the fibers dry out; increasing it reduces diameter up to a point.
Temperature	Increasing it usually decreases diameter.
Relative humidity	High RH leads to pores on the fibers & sometimes hinders solvent evaporation.
Collector	Must be conductive and set to a smaller potential than the spinneret; rotating collectors can help extrusion and align fibers.
Spinneret	Width influences the diameter; coaxial spinnerets can yield core-shell fibers.

1.8. Conclusion & positioning of the study

A lot of progress in all aspects of microbial fuel cells has been achieved since the initial discovery of bacterial electroactivity by Potter in 1911. Following a steep rise in interest in the 80s and 90s and thanks to many crucial advancements, microbial electrochemical systems have since then started to appear as a realistic actor of the energy mix. Even if current practical commercial implementations of MFCs, such as wastewater treatment and energy generation or sensor powering might still seem niche applications, a few decisive improvements in MFCs performances may trigger a wider adoption of this power source relying on so far neglected sustainable resources.

MFCs performances are influenced by various levels of its architecture, and thus may be improved by targeting the:

- Microorganism;
- Cell architecture;
- Cathode;
- Separator;
- Anode.

Optimizing electron transfer show significant potential for performances improvement, and controlling the interfaces between the electrode and the bacteria at various length scales is therefore critical. Henceforth, this work focuses on the development of a new bioanode design by electrospinning, and requires simple and robust choices concerning the other parts of the cell to ensure minimal limitations and the best reproducibility while undertaking anode refinements.

1.8.1. Electrogenic microorganism

The MFC power generation relies on electron transfer from the end respiratory chain of a microorganism to a higher potential outside electron acceptor, in this case the anode. Electron transfer may be either indirect through redox mediators or direct through transmembrane proteins or conductive pili.

The literature reports both the use of pure exoelectrogenic strains or wastewater-borne bacteria consortia, each with pros and cons. Pure strains have the advantage of being simpler to control with usually better understood exoelectrogenic pathways, while consortia-based MFCs exhibit higher power densities thanks to synergy between the strains and are obviously closer to a commercial application by using wastewater-occurring microorganisms.

In this study both strategies will be considered. Most of the new materials developments will be carried out using the *Shewanella oneidensis* CRBIP17.141 strain – closely related to *Shewanella oneidensis* MR-1 – provided by the *Centre de Ressources Biologiques de l'Institut Pasteur* (CRBIP). *Shewanella oneidensis* is a facultative aerobe easy to grow in both

aerobic and anaerobic conditions and exhibiting both indirect and direct electron transfers. Opening work on materials validated by *Shewanella oneidensis* will also be conducted using consortia from wastewater provided by the *Syndicat Interdépartemental pour l'Assainissement de l'Agglomération parisienne* (SIAAP).

1.8.2. MFC reactor

The architecture of the MFC reactor is crucial for the power output of the cell as it influences its ohmic losses. Apart from its dimensions, cells architectures are roughly divided between batch-mode and continuous operation MFCs. The former must be periodically reloaded with nutrients but are well adapted to lab-scale studies thanks to their simplicity and reproducibility, while the latter are closer to commercial applications.

Consequently, this work will focus on the batch-mode architecture, with a tight control on the distance between electrodes and on electrolytes volumes.

1.8.3. Cathode & catholyte

A few cathodic reactants are reported in the literature, chiefly with dioxygen as it is readily available and heavily used in other fields of fuel cell research, and with more laboratory convenient alternatives with high redox potential and well-understood behaviors. Among these, potassium ferricyanide is widely used with a standard potential $E_0([Fe(CN)_6]^{3-}/[Fe(CN)_6]^{4-}) = 0.361$ V vs. SHE. A last option relies on the use of microorganisms at the cathode to catalyze various reduction reactions.

The chosen cathode depends on aforementioned cathodic redox couple. Air cathodes performing oxygen reduction are mainly platinum or carbon/platinum electrodes, efficient and usually open-to-air, but expensive. On the other hand, lab-scale cathodic reactants such as potassium ferricyanide can be reduced on a broad range of electrodes, including cheap carbon felt. Finally, biocathodes are still subject to research and are most of the time carbon-based.

Because of the focus of this work on anode improvements, potassium ferricyanide will be used as the cathodic reactant and carbon felt as the cathode.

1.8.4. Separator

In MFCs, the separator between anodic and cathodic compartments is optional but has nonetheless several advantages. It prevents diffusion of cathodic reactants into the anolyte, which can be toxic to the anodic microorganisms. In particular, in the case of strictly anaerobic bacteria, it prevents oxygen diffusion from the cathodic compartment. Similarly, it avoids the colonization and possible fouling of the cathode by anodic bacteria. The separator must also be chosen according to its ability to let protons migrate between the two compartments to allow their recombination at the cathode and avoid anolyte acidification.

This work therefore uses dual-compartments reactors to assess the MFC performances, with Nafion® cation-exchange membrane as the separator.

1.8.5. Anode design

Most bioanodes are either metal or carbon-based. Carbon anodes are widely reported in the literature as the cheapest and most versatile choice for MFCs. Surface area and roughness of the material have been linked to better performances and most MFC setups are based on 3D carbon anodes such as carbon felt or carbon paper. Nevertheless, further improvements could be made by developing a micron-sized anodic material that can take advantage of both a bacteria-scaled surface and the superiority of ultramicroelectrodes regarding the diffusion of a redox substrate toward the aforesaid bacterium.

In this study, we will focus on developing a new bioanode design through electrospinning and on exploring the influence of various architecture improvements, such as pre-colonization and electrode stacking and core-shell microfibers electrodes. The performances of the novel material will be compared with carbon felt as a widely used commercial alternative.

1.8.6. Layout of the study

From the electroactive microorganism to the MFC broad structure, various aspects of the fuel cell can be enhanced to improve its overall performances. In this work we choose to design a new bioanode architecture better suited to the bacterium scale in order to optimize its electron transfer.

A first part of the study presents the synthesis of a carbon microfibers bioanode through a multi-step approach. An electrospun fiber mat of polyacrylonitrile is subjected to heat treatments to produce a carbon paper subsequently colonized by electroactive bacteria – *Shewanella oneidensis* CRBIP17.141. The resulting membranes are integrated in a lab-scale two compartments MFC setup to investigate their electrochemical behavior and stability and are compared with commercial carbon felt anodes. Post-mortem analyses are conducted on the bioanodes to evaluate bacterial colonization. The influence of the electrode thickness is also evaluated regarding nutrients diffusion and the depth of bacterial colonization. Long-term bioanode conservation is explored through cryodesiccation.

A second part of the study focuses on the development of a one-step preparation pathway of conductive electrospun electrodes. By removing the need for impractical heat treatments, a quicker way to produce anode is proposed, and a subsequent integration of the bacteria into the electrode is proposed. Various fabrication methods are compared and characterized by electronic microscopy, impedance spectroscopy and electrochemical assays. The bacterial viability is then evaluated on those electrospun networks.

A third part proposes an integration of these results to develop a novel bioanode design. A core-shell electrospun conductive network encapsulating the electroactive bacteria is presented allowing a one-step preparation of a ready-to-use bioanode, easily storable and able to quickly recover its power output upon use. The effect of the encapsulation on the bacteria and on electron transfer is addressed as well as the stability of the MFC output. The architecture of the bioanode is investigated by epifluorescence and confocal as well as electronic microscopies. The new material electrochemical characteristics are also assessed through redox as well as impedance spectroscopy experiments. At last, the performances of the new design are evaluated and are shown to be an encouraging way of improving current MFC bioanodes.

Eventually a fourth chapter explores the integration of the electrodes presented in the previous chapters into an MFC setup including real effluents from wastewaters. Their performances in current generation from the organic wastes sourced in the wastewater are investigated and are shown to be encouraging. The nature of the bacteria naturally occurring in wastewaters is also explored as well as their aptitude to exoelectrogenic activity. At last, the effect of the integration of our bioanodes and of power generation on the ecology of those strains is examined.

REFERENCES

[1] International Energy Agency. *Key World Energy Statistics 2018*. (2018).

[2] S. Srinivasan. *Fuel cells: from fundamentals to applications*. (Springer Science & Business media, 2006).

[3] J. Larminie & A. Dicks. *Fuel cell systems explained*. *Fuel* (2003).

[4] X. Li, L. Fields & G. Way. Principles of fuel cells. *Platin. Met. Rev* **50,** 200–201 (2006).

[5] M. L. Perry & T. F. Fuller. A Historical Perspective of Fuel Cell Technology in the 20th Century. *J. Electrochem. Soc.* **149,** S59 (2002).

[6] A. D. S. Tantram. Fuel cells: past, present and future. *Energy Policy* **2,** 55–66 (1974).

[7] A. J. Appleby. From Sir William Grove to today: fuel cells and the future. *J. Power Sources* **29,** 3–280 (1990).

[8] G. F. Mclean, T. Niet & N. Djilali. An assessment of AFC technology. *Int. J. Hydrogen Energy* **27,** 507–526 (2002).

[9] S. Wasmus & A. Küver. Methanol oxidation and direct methanol fuel cells: a selective review. *J. Electroanal. Chem.* **461,** 14–31 (1999).

[10] E. Ivers-Tiffée, A. Weber & D. Herbstritt. Materials and technologies for SOFC-components. *J. Eur. Ceram. Soc.* **21,** 1805–1811 (2001).

[11] T. R. Ralph. "Principles of Fuel Cells". *Platin. Met. Rev.* **50,** 200–201 (2006).

[12] F. Barbir. PEM fuel cells. in *Fuel Cell Technology* 27–51 (Springer, 2006).

[13] K. S. V Santhanam, R. J. Press, M. J. Miri, A. V Bailey & G. A. Takacs. *Introduction to hydrogen technology*. (John Wiley & Sons, 2017).

[14] D. P. Wilkinson & B. Columbia. *Proton Exchange Membrane Fuel Cells: Materials Properties and Performance*. (CRC Press, 2009).

[15] A. Fujishima & K. Honda. Electrochemical Photolysis of Water at a Semiconductor Electrode. *Nature* **238,** 37–38 (1972).

[16] E. J. Toone. *Advances in Enzymology and Related Areas of Molecular Biology*. (Wiley, 2011).

[17] E. Schoffeniels & D. Margineanu. Cell Membranes and Bioelectrogenesis. in 30–53 (Springer, Dordrecht, 1990).

[18] R. A. Bullen, T. C. Arnot, J. B. Lakeman & F. C. Walsh. Biofuel cells and their development. *Biosens. Bioelectron.* **21,** 2015–2045 (2006).

[19] L. B. Wingard, C. H. Shaw & J. F. Castner. Bioelectrochemical fuel cells. *Enzyme Microb. Technol.* **4,** 137–142 (1982).

[20] A. Shukla, P. Suresh, S. Berchmans & A. Rajendran. Biological Fuel Cells and Their Applications. *Curr. Sci.* **87,** (2004).

[21] C. F. Blanford, R. S. Heath & F. A. Armstrong. A stable electrode for high-potential, electrocatalytic O2 reduction based on rational attachment of a blue copper oxidase to a graphite surface. *Chem. Commun.* **0,** 1710 (2007).

[22] M. A. Alonso-Lomillo *et al.* Hydrogenase-coated carbon nanotubes for efficient H2 oxidation. *Nano Lett.* **7,** 1603–8 (2007).

[23] Y. Degani & A. Heller. Direct electrical communication between chemically modified enzymes and metal electrodes. 2. Methods for bonding electron-transfer relays to glucose oxidase and D-amino-acid oxidase. *J. Am. Chem. Soc.* **110,** 2615–2620 (1988).

[24] S. Cosnier. Biomolecule immobilization on electrode surfaces by entrapment or attachment to electrochemically polymerized films. A review. *Biosens. Bioelectron.* **14,** 443–56 (1999).

[25] A. Heller. Miniature biofuel cells. *Phys. Chem. Chem. Phys.* **6,** 209 (2004).

[26] K. E. Geckeler. *Advanced Macromolecular and Supramolecular Materials and Processes*. (Springer US, 2003).

[27] N. Mano, F. Mao & A. Heller. A Miniature Biofuel Cell Operating in A Physiological Buffer. *J. Am. Chem. Soc.* **2,** 12962–12963 (2002).

[28] N. Mano, F. Mao & A. Heller. Characteristics of a Miniature Compartment-less Glucose−O2 Biofuel Cell and Its Operation in a Living Plant. *J. Am. Chem. Soc.* **125,** 6588–6594 (2003).

[29] I. Ivanov *et al.* Recent Advances in Enzymatic Fuel Cells: Experiments and Modeling. *Energies* **3,** 803–846 (2010).

[30] L. Murphy. Biosensors and bioelectrochemistry. *Curr. Opin. Chem. Biol.* **10,** 177–184 (2006).

[31] D. Grieshaber *et al.* Electrochemical Biosensors - Sensor Principles and Architectures. *Sensors* **8,** 1400–1458 (2008).

[32] J. Kim *et al.* Wearable Bioelectronics: Enzyme-Based Body-Worn Electronic Devices. *Acc. Chem. Res.* **51,** 2820–2828 (2018).

[33] A. Ruff *et al.* A fully protected hydrogenase/polymer-based bioanode for high-performance hydrogen/glucose biofuel cells. *Nat. Commun.* **9,** 3675 (2018).

[34] P. Cinquin *et al.* A Glucose BioFuel Cell Implanted in Rats. *PLoS One* **5,** e10476 (2010).

[35] S. Cosnier, A. Le Goff & M. Holzinger. Towards glucose biofuel cells implanted in human body for powering artificial organs: Review. *Electrochem. commun.* **38,** 19–23 (2014).

[36] A. Heller. Potentially implantable miniature batteries. *Anal. Bioanal. Chem.* **385,** 469–473 (2006).

[37] M. Cadet *et al.* An enzymatic glucose/O2 biofuel cell operating in human blood. *Biosens. Bioelectron.* **83,** 60–67 (2016).

[38] P. Ó Conghaile *et al.* Fully Enzymatic Membraneless Glucose/Oxygen Fuel Cell That Provides 0.275 mA cm –2 in 5 mM Glucose, Operates in Human Physiological Solutions, and Powers Transmission of Sensing Data. *Anal. Chem.* **88,** 2156–2163 (2016).

[39] W. Gellett, M. Kesmez, J. Schumacher, N. Akers & S. D. Minteer. Biofuel cells for portable power. *Electroanalysis* **22,** 727–731 (2010).

[40] M. C. Potter. Electrical Effects Accompanying the Decomposition of Organic Compounds. *Proc. R. Soc. B Biol. Sci.* **84,** 260–276 (1911).

[41] B. Cohen. The Bacteria Culture as an Electrical Half-Cell. *J. Bacteriol.* **21,** 18–19 (1931).

[42] K. Lewis. Symposium on bioelectrochemistry of microorganisms. IV. Biochemical fuel cells. *Bacteriol. Rev.* **30,** 101–13 (1966).

[43] A. M. Lithgow, L. Romero, I. C. Sanchez, F. A. Souto & C. A. Vega. Interception of the electron-transport chain in bacteria with hydrophilic redox mediators. I: Selective improvement of the performance of biofuel cells with 2, 6-disulphonated thionine as mediator. *J. Chem. Res. Synopses* 178–179 (1986).

[44] G. M. Delaney *et al.* Electron-transfer coupling in microbial fuel cells. 2. performance of fuel cells containing selected microorganism-mediator-substrate combinations. *J. Chem. Technol. Biotechnol. Biotechnol.* **34,** 13–27 (1984).

[45] B. H. Kim, D. H. Park, P. K. Shin, I. S. Chang & H. J. Kim. Mediator-less biofuel cell. (1999).

[46] H. Joo *et al.* A mediator-less microbial fuel cell using a metal reducing bacterium , Shewanella putrefaciens. *Enzyme Microb. Technol.* **30,** 145–152 (2002).

[47] B. H. Kim *et al.* Enrichment of microbial community generating electricity using a fuel-cell-type electrochemical cell. *Appl. Microbiol. Biotechnol.* **63,** 672–681 (2004).

[48] K. Rabaey, N. Boon, M. Höfte & W. Verstraete. Microbial phenazine production enhances electron transfer in biofuel cells. *Environ. Sci. Technol.* **39,** 3401–3408 (2005).

[49] K. Rabaey, N. Boon, S. D. Siciliano, M. Verhaege & W. Verstraete. Biofuel cells select for microbial consortia that self-mediate electron transfer. *Appl. Environ. Microbiol.* **70,** 5373–82 (2004).

[50] B. E. Logan. Exoelectrogenic bacteria that power microbial fuel cells. *Nat. Rev. Microbiol.* **7,** 375–381 (2009).

[51] Y. Zuo, P. C. Maness & B. E. Logan. Electricity production from steam-exploded corn stover biomass. *Energy and Fuels* **20,** 1716–1721 (2006).

[52] I. Shizas & D. M. Bagley. Experimental Determination of Energy Content of Unknown Organics in Municipal Wastewater Streams. *J. Energy Eng.* **130,** 45–53 (2004).

[53] Y. Ahn & B. E. Logan. Altering anode thickness to improve power production in microbial fuel cells with different electrode distances. *Energy and Fuels* **27,** 271–276 (2013).

[54] L. Huang, S. Cheng & G. Chen. Bioelectrochemical systems for efficient recalcitrant wastes treatment. *J. Chem. Technol. Biotechnol.* **86,** 481–491 (2011).

[55] R. A. Rozendal, H. V. M. Hamelers, K. Rabaey, J. Keller & C. J. N. Buisman. Towards practical implementation of bioelectrochemical wastewater treatment. *Trends Biotechnol.* **26,** 450–459 (2008).

[56] L. B. Liu H, Ramnarayanan R. Production of Electricity during Wastewater Treatment Using a Single Chamber Microbial Fuel Cell. *Environ. Sci. Technol.* **38,** 2281–2285 (2004).

[57] Z. He. Using Microbial Fuel Cells to Treat Raw Sludge and Primary Effluent for Bioelectricity Generation : Final Report. *Microb. Fuel Cell Technol.* 1–65 (2013).

[58] C. E. Reimers, L. M. Tender, S. Fertig & W. Wang. Harvesting energy from the marine sediment - Water interface. *Environ. Sci. Technol.* **35,** 192–195 (2001).

[59] L. M. Tender *et al.* Harnessing microbially generated power on the seafloor. *Nat. Biotechnol.* **20,** 821 (2002).

[60] I. A. Ieropoulos *et al.* Waste to real energy: The first MFC powered mobile phone. *Phys. Chem. Chem. Phys.* **15,** 15312–15316 (2013).

[61] I. Ieropoulos, J. Greenman, C. Melhuish & I. Horsfield. EcoBot-III: a robot with guts. *12th Int. Conf.*

Synth. Simul. Living Syst. 733–740 (2010).

[62] I. H. Ioannis Ieropoulos, Chris Melhuish, John Greenman. EcoBot-II: An artificial agent with a natural metabolism. *Int. J. Adv. Robot. Syst.* **1,** 295–300 (2005).

[63] B. E. Logan. *Microbial fuel cells*. (Wiley-Interscience, 2008).

[64] K. Rabaey & W. Verstraete. Microbial fuel cells: Novel biotechnology for energy generation. *Trends Biotechnol.* **23,** 291–298 (2005).

[65] B. E. Logan & K. Rabaey. Conversion of Wastes into Bioelectricity and Chemicals by Using Microbial Electrochemical Technologies. *Science* **337,** 686 LP – 690 (2012).

[66] B. E. Logan *et al.* Microbial fuel cells: Methodology and technology. *Environ. Sci. Technol.* **40,** 5181–5192 (2006).

[67] M. Kim *et al.* Practical field application of a novel BOD monitoring system. *J. Environ. Monit.* **5,** 640–643 (2003).

[68] Z. Xu *et al.* Flat microliter membrane-based microbial fuel cell as 'on-line sticker sensor' for self-supported in situ monitoring of wastewater shocks. *Bioresour. Technol.* **197,** 244–251 (2015).

[69] K. B. Gregory & D. R. Lovley. Remediation and recovery of uranium from contaminated subsurface environments with electrodes. *Environ. Sci. Technol.* **39,** 8943–8947 (2005).

[70] D. R. L. Kelvin B. Gregory, Daniel R. Bond. Graphite electrodes as electron donors for anaerobic respiration. *Environ. Microbiol.* **6,** 596 – 604 (2004).

[71] Z. Borjas, A. Esteve-Núñez & J. M. Ortiz. Strategies for merging microbial fuel cell technologies in water desalination processes: Start-up protocol and desalination efficiency assessment. *J. Power Sources* **356,** 519–528 (2017).

[72] K. S. Jacobson, D. M. Drew & Z. He. Use of a liter-scale microbial desalination cell as a platform to study bioelectrochemical desalination with salt solution or artificial seawater. *Environ. Sci. Technol.* **45,** 4652–4657 (2011).

[73] J. Ditzig, H. Liu & B. E. Logan. Production of hydrogen from domestic wastewater using a bioelectrochemically assisted microbial reactor (BEAMR). *Int. J. Hydrogen Energy* **32,** 2296–2304 (2007).

[74] H. Liu, S. Grot & B. E. Logan. Electrochemically assisted microbial production of hydrogen from acetate. *Environ. Sci. Technol.* **39,** 4317–4320 (2005).

[75] R. A. Rozendal, H. V. M. Hamelers, G. J. W. Euverink, S. J. Metz & C. J. N. Buisman. Principle and perspectives of hydrogen production through biocatalyzed electrolysis. *Int. J. Hydrogen Energy* **31,** 1632–1640 (2006).

[76] B. Logan, S. Grot, T. E. Mallouk & H. Liu. Bio-electrochemically assisted microbial reactor that generates hydrogen gas and methods of generating hydrogen gas. (2009).

[77] K. P. Nevin, T. L. Woodard, A. E. Franks, Z. M. Summers & D. R. Lovley. Microbial electrosynthesis: feeding microbes electricity to convert carbon dioxide and water to multicarbon extracellular organic compounds. *mBio* **1,** e00103-10 (2010).

[78] X. Cao *et al.* A completely anoxic microbial fuel cell using a photo-biocathode for cathodic carbon dioxide reduction. *Energy Environ. Sci.* **2,** 498–501 (2009).

[79] H. Lodish *et al. Molecular Cell Biology. 4th edition*. *Molecular Cell Biology. 4th edition* (2000).

[80] P. Mitchell. Coupling of Phosphorylation to Electron and Hydrogen Transfer by a Chemi-Osmotic type of Mechanism. *Nature* **191,** 144–148 (1961).

[81] B. E. Logan & J. M. Regan. Electricity-producing bacterial communities in microbial fuel cells. *Trends Microbiol.* **14,** 512–518 (2006).

[82] I. S. Chang *et al.* Electrochemically active bacteria (EAB) and mediator-less microbial fuel cells. *J. Microbiol. Biotechnol.* **16,** 163–177 (2006).

[83] B. E. Rittmann, R. Krajmalnik-Brown & R. U. Halden. Pre-genomic, genomic and post-genomic study of microbial communities involved in bioenergy. *Nat. Rev. Microbiol.* **6,** 604–612 (2008).

[84] D. R. Lovley. Bug juice: Harvesting electricity with microorganisms. *Nat. Rev. Microbiol.* **4,** 497–508 (2006).

[85] C. R. Myers & J. M. Myers. Localization of cytochromes to the outer membrane of anaerobically grown Shewanella putrefaciens MR-1. *J. Bacteriol.* **174,** 3429–3438 (1992).

[86] A. D. McNaught & A. Wilkinson. *Compendium of Chemical Terminology*. *The Gold Book* (Blackwell Science, 1997).

[87] Y. A. Gorby *et al.* Electrically conductive bacterial nanowires produced by Shewanella oneidensis strain MR-1 and other microorganisms. *PNAS* **103,** 11358–11363 (2006).

[88] G. Reguera *et al.* Extracellular electron transfer via microbial nanowires. *Nature* **435,** 1098–1101 (2005).

[89] Y. Zuo, D. Xing, J. M. Regan & B. E. Logan. Isolation of the Exoelectrogenic Bacterium Ochrobactrum anthropi YZ-1 by Using a U-Tube Microbial Fuel Cell. *Appl. Environ. Microbiol.* **74,** 3130–3137 (2008).

[90] T. H. Pham *et al.* Metabolites produced by Pseudomonas sp. enable a Gram-positive bacterium to achieve extracellular electron transfer. *Appl. Microbiol. Biotechnol.* **77,** 1119–1129 (2008).

[91] D. R. Bond & D. R. Lovley. Electricity Production by Geobacter sulfurreducens Attached to Electrodes. *Appl. Environ. Microbiol.* **69,** 1548–1555 (2003).

[92] D. H. Park, M. Laivenieks, M. V. Guettler, M. K. Jain & J. G. Zeikus. Microbial utilization of electrically reduced neutral red as the sole electron donor for growth and metabolite production. *Appl. Environ. Microbiol.* **65,** 2912–2917 (1999).

[93] J. B. McKinlay & J. G. Zeikus. Extracellular Iron Reduction Is Mediated in Part by Neutral Red and Hydrogenase in Escherichia coli. *Appl. Environ. Microbiol.* **70,** 3467–3474 (2004).

[94] U. Schröder. Anodic electron transfer mechanisms in microbial fuel cells and their energy efficiency. *Phys. Chem. Chem. Phys.* **9,** 2619–2629 (2007).

[95] M. Adachi, T. Shimomura, M. Komatsu, H. Yakuwa & A. Miya. A novel mediator-polymer-modified anode for microbial fuel cells. *Chem. Commun.* 2055–2057 (2008).

[96] J. C. Thrash & J. D. Coates. Review: Direct and Indirect Electrical Stimulation of Microbial Metabolism. *Environ. Sci. Technol.* **42,** 3921–3931 (2008).

[97] K. Rabaey *et al.* Microbial ecology meets electrochemistry: electricity-driven and driving communities. *ISME J.* **1,** 9–18 (2007).

[98] K. Rabaey, G. Lissens, S. D. Siciliano & W. Verstraete. A microbial fuel cell capable of converting glucose to electricity at high rate and efficiency. *Biotechnol. Lett.* **25,** 1531–1535 (2003).

[99] E. Marsili *et al.* Shewanella secretes flavins that mediate extracellular electron transfer. *PNAS* **105,**

3968–3973 (2008).

[100] H. von Canstein, J. Ogawa, S. Shimizu & J. R. Lloyd. Secretion of Flavins by Shewanella Species and Their Role in Extracellular Electron Transfer. *Appl. Environ. Microbiol.* **74,** 615 LP – 623 (2008).

[101] V. B. Wang *et al.* Comparison of flavins and a conjugated oligoelectrolyte in stimulating extracellular electron transport from Shewanella oneidensis MR-1. *Electrochem. commun.* **41,** 55–58 (2014).

[102] J. M. Myers & C. R. Myers. Role for outer membrane cytochromes OmcA and OmcB of Shewanella putrefaciens MR-1 in reduction of manganese dioxide. *Appl. Environ. Microbiol.* **67,** 260–269 (2001).

[103] J. M. Myers & C. R. Myers. Role of the tetraheme cytochrome CymA in anaerobic electron transport in cells of Shewanella putrefaciens MR-1 with normal levels of menaquinone. *J. Bacteriol.* **182,** 67–75 (2000).

[104] L. Shi, T. C. Squier, J. M. Zachara & J. K. Fredrickson. Respiration of metal (hydr)oxides by Shewanella and Geobacter: a key role for multihaem c-type cytochromes. *Mol. Microbiol.* **65,** 12–20 (2007).

[105] S. E. Childers, S. Ciufo & D. R. Lovley. Geobacter metallireducens accesses insoluble Fe(III) oxide by chemotaxis. *Nature* **416,** 767 (2002).

[106] M. Y. El-Naggar *et al.* Electrical transport along bacterial nanowires from Shewanella oneidensis MR-1. *PNAS* **107,** 18127–18131 (2010).

[107] R. M. Snider, S. M. Strycharz-Glaven, S. D. Tsoi, J. S. Erickson & L. M. Tender. Long-range electron transport in Geobacter sulfurreducens biofilms is redox gradient-driven. *PNAS* **109,** 15467–15472 (2012).

[108] N. S. Malvankar *et al.* Structural Basis for Metallic-Like Conductivity in Microbial Nanowires. *mBio* **6,** (2015).

[109] N. S. Malvankar *et al.* Tunable metallic-like conductivity in microbial nanowire networks. *Nat. Nanotechnol.* **6,** 573 (2011).

[110] P. S. Bonanni, D. Massazza & J. P. Busalmen. Stepping stones in the electron transport from cells to electrodes in Geobacter sulfurreducens biofilms. *Phys. Chem. Chem. Phys.* **15,** 10300–10306 (2013).

[111] S. Pirbadian *et al.* Shewanella oneidensis MR-1 nanowires are outer membrane and periplasmic extensions of the extracellular electron transport components. *PNAS* **111,** 12883–8 (2014).

[112] B. H. Kim *et al.* Electrochemical activity of an Fe(III)-reducing bacterium, Shewanella putrefaciens IR-1, in the presence of alternative electron acceptors. *Biotechnol. Tech.* **13,** 475–478 (1999).

[113] C. R. Myers & K. H. Nealson. Bacterial Manganese Reduction and Growth with Manganese Oxide as the Sole Electron Acceptor. *Science* **240,** 1319–1321 (1988).

[114] O. Bretschger *et al.* Current production and metal oxide reduction by Shewanella oneidensis MR-1 wild type and mutants. *Appl. Environ. Microbiol.* **73,** 7003–7012 (2007).

[115] M. Breuer, K. M. Rosso, J. Blumberger & J. N. Butt. Multi-haem cytochromes in Shewanella oneidensis MR-1: Structures, functions and opportunities. *J. R. Soc. Interface* **12,** (2015).

[116] P. Parameswaran, C. I. Torres, H.-S. Lee, R. Krajmalnik-Brown & B. E. Rittmann. Syntrophic interactions among anode respiring bacteria (ARB) and Non-ARB in a biofilm anode: electron balances. *Biotechnol. Bioeng.* **103,** 513–523 (2009).

[117] Y. Xiao *et al.* Extracellular polymeric substances are transient media for microbial extracellular electron transfer. *Sci. Adv.* **3,** (2017).

[118] Y. Jiao *et al.* Characterization of Extracellular Polymeric Substances from Acidophilic Microbial Biofilms. *Appl. Environ. Microbiol.* **76,** 2916–2922 (2010).

[119] M. Allesen-Holm *et al.* A characterization of DNA release in Pseudomonas aeruginosa cultures and biofilms. *Mol. Microbiol.* **59,** 1114–1128 (2006).

[120] R. M. Donlan. Biofilms: microbial life on surfaces. *Emerg. Infect. Dis.* **8,** 881–890 (2002).

[121] A. P. Borole *et al.* Electroactive biofilms: Current status and future research needs. *Energy Environ. Sci.* **4,** 4813–4834 (2011).

[122] S. T. Read, P. Dutta, P. L. Bond, J. Keller & K. Rabaey. Initial development and structure of biofilms on microbial fuel cell anodes. *BMC Microbiol.* **10,** 98 (2010).

[123] A. P. Fickett. *Electrochemical systems*. (Prentice Hall, 1973).

[124] A. J. Bard, R. Parsons & J. Jordan. *Standard Electrode Potentials for Aqueous Solutions*. (Marcel Dekker, 1985).

[125] L. Zhuang, S. Zhou, Y. Li & Y. Yuan. Enhanced performance of air-cathode two-chamber microbial fuel cells with high-pH anode and low-pH cathode. *Bioresour. Technol.* **101,** 3514–3519 (2010).

[126] H. Liu, S. Cheng & B. E. Logan. Production of Electricity from Acetate or Butyrate Using a Single-Chamber Microbial Fuel Cell. *Environ. Sci. Technol.* **39,** 658–662 (2005).

[127] R. K. Thauer, K. Jungermann & K. Decker. Energy conservation in chemotrophic anaerobic bacteria. *Microbiol. Mol. Biol. Rev.* **41,** 100–180 (1977).

[128] J. Niessen, U. Schröder & F. Scholz. Exploiting complex carbohydrates for microbial electricity generation - A bacterial fuel cell operating on starch. *Electrochem. commun.* **6,** 955–958 (2004).

[129] F. Zhao *et al.* Application of pyrolysed iron(II) phthalocyanine and CoTMPP based oxygen reduction catalysts as cathode materials in microbial fuel cells. *Electrochem. commun.* **7,** 1405–1410 (2005).

[130] B. Min, S. Cheng & B. E. Logan. Electricity generation using membrane and salt bridge microbial fuel cells. *Water Res.* **39,** 1675–1686 (2005).

[131] I. Rabaey, W. Ossieur, M. Verhaege & W. Verstraete. Continuous microbial fuel cells convert carbohydrates to electricity. *Water Sci. Technol.* **52,** 515–523 (2005).

[132] M. Rosenbaum, U. Schröder & F. Scholz. In Situ Electrooxidation of Photobiological Hydrogen in a Photobioelectrochemical Fuel Cell Based on Rhodobacter sphaeroides. *Environ. Sci. Technol.* **39,** 6328–6333 (2005).

[133] H. Liu & B. E. Logan. Electricity Generation Using an Air-Cathode Single Chamber Microbial Fuel Cell in the Presence and Absence of a Proton Exchange Membrane. *Environ. Sci. Technol.* **38,** 4040–4046 (2004).

[134] B. E. Logan, C. Murano, K. Scott, N. D. Gray & I. M. Head. Electricity generation from cysteine in a microbial fuel cell. *Water Res.* **39,** 942–952 (2005).

[135] K. Rabaey Clauwaert, P., Aelterman, P. and Verstraete, W. Tubular microbial fuel cell for efficient electricity generation. *Environ. Sci. Technol.* **39,** 8077–8082 (2005).

[136] Z. He, S. D. Minteer & L. T. Angenent. Electricity Generation from Artificial Wastewater Using an Upflow Microbial Fuel Cell. *Environ. Sci. Technol.* **39,** 5262–5267 (2005).

[137] B. Min & B. E. Logan. Continuous Electricity Generation from Domestic Wastewater and Organic Substrates in a Flat Plate Microbial Fuel Cell. *Environ. Sci. Technol.* **38,** 5809–5814 (2004).

[138] P. Aelterman, K. Rabaey, H. T. Pham, N. Boon & W. Verstraete. Continuous electricity generation at high voltages and currents using stacked microbial fuel cells. *Environ. Sci. Technol.* **40,** 3388–3394 (2006).

[139] S. Oh, B. Min & B. E. Logan. Cathode performance as a factor in electricity generation in microbial fuel cells. *Environ. Sci. Technol.* **38,** 4900–4904 (2004).

[140] S.-E. Oh & B. E. Logan. Proton exchange membrane and electrode surface areas as factors that affect power generation in microbial fuel cells. *Appl. Microbiol. Biotechnol.* **70,** 162–169 (2006).

[141] S. Cheng, H. Liu & B. E. Logan. Increased Power Generation in a Continuous Flow MFC with Advective Flow through the Porous Anode and Reduced Electrode Spacing. *Environ. Sci. Technol.* **40,** 2426–2432 (2006).

[142] Y. Zuo, S. Cheng, D. Call & B. E. Logan. Tubular Membrane Cathodes for Scalable Power Generation in Microbial Fuel Cells. *Environ. Sci. Technol.* **41,** 3347–3353 (2007).

[143] I. Gajda, J. Greenman, C. Melhuish & I. Ieropoulos. Photosynthetic cathodes for Microbial Fuel Cells. *Int. J. Hydrogen Energy* **38,** 11559–11564 (2013).

[144] D. H. Park & J. G. Zeikus. Electricity Generation in Microbial Fuel Cells Using Neutral Red as an Electronophore. *Appl. Environ. Microbiol.* **66,** 1292–1297 (2000).

[145] J. C. Biffinger, J. Pietron, R. Ray, B. Little & B. R. Ringeisen. A biofilm enhanced miniature microbial fuel cell using Shewanella oneidensis DSP10 and oxygen reduction cathodes. *Biosens. Bioelectron.* **22,** 1672–1679 (2007).

[146] T. R. Eliato, G. Pazuki & N. Majidian. Potassium permanganate as an electron receiver in a microbial fuel cell. *Energy Sources, Part A Recover. Util. Environ. Eff.* **38,** 644–651 (2016).

[147] T. H. Pham, J. K. Jang, I. S. Chang & B. H. Kim. Improvement of cathode reaction of a mediatorless microbial fuel cell. *J. Microbiol. Biotechnol.* **14,** 324–329 (2004).

[148] S. Cheng, H. Liu & B. E. Logan. Power Densities Using Different Cathode Catalysts (Pt and CoTMPP) and Polymer Binders (Nafion and PTFE) in Single Chamber Microbial Fuel Cells. *Environ. Sci. Technol. Technol. Technol.* **40,** 364–369 (2006).

[149] Z. He & L. T. Angenent. Application of Bacterial Biocathodes in Microbial Fuel Cells. *Electroanalysis* **18,** 2009–2015 (2006).

[150] A. Bergel, D. Féron & A. Mollica. Catalysis of oxygen reduction in PEM fuel cell by seawater biofilm. *Electrochem. commun.* **7,** 900–904 (2005).

[151] A. Aldrovandi *et al.* Sustainable power production in a membrane-less and mediator-less synthetic wastewater microbial fuel cell. *Bioresour. Technol.* **100,** 3252–3260 (2009).

[152] P. Clauwaert *et al.* Biological denitrification in microbial fuel cells. *Environ. Sci. Technol.* **41,** 3354–3360 (2007).

[153] A. Rhoads, H. Beyenal & Z. Lewandowski. Microbial fuel cell using anaerobic respiration as an anodic reaction and biomineralized manganese as a cathodic reactant. *Environ. Sci. Technol.* **39,** 4666–4671 (2005).

[154] S. R. Higgins, C. Lau, P. Atanassov, S. D. Minteer & M. J. Cooney. Hybrid Biofuel Cell: Microbial Fuel Cell with an Enzymatic Air-Breathing Cathode. *ACS Catal.* **1,** 994–997 (2011).

[155] F. Harnisch, U. Schroder & F. Scholz. The suitability of monopolar and bipolar ion exchange membranes as separators for biological fuel cells. *Environ. Sci. Technol.* **42,** 1740–1746 (2008).

[156] J. Sun, Y. Hu, Z. Bi & Y. Cao. Improved performance of air-cathode single-chamber microbial fuel cell for wastewater treatment using microfiltration membranes and multiple sludge inoculation. *J. Power Sources* **187,** 471–479 (2009).

[157] J. C. Biffinger, R. Ray, B. Little & B. R. Ringeisen. Diversifying biological fuel cell designs by use of nanoporous filters. *Environ. Sci. Technol.* **41,** 1444–1449 (2007).

[158] X. Zhang, S. Cheng, X. Wang, X. Huang & B. E. Logan. Separator Characteristics for Increasing Performance of Microbial Fuel Cells. *Environ. Sci. Technol.* **43,** 8456–8461 (2009).

[159] W.-W. Li, G.-P. Sheng, X.-W. Liu & H.-Q. Yu. Recent advances in the separators for microbial fuel cells. *Bioresour. Technol.* **102,** 244–252 (2011).

[160] K. Guo, A. Prévoteau, S. A. Patil & K. Rabaey. Engineering electrodes for microbial electrocatalysis. *Curr. Opin. Biotechnol.* **33,** 149–156 (2015).

[161] H. Richter *et al.* Electricity Generation by Geobacter sulfurreducens Attached to Gold Electrodes. *Langmuir* **24,** 4376–4379 (2008).

[162] S. R. Crittenden, C. J. Sund & J. J. Sumner. Mediating Electron Transfer from Bacteria to a Gold Electrode via a Self-Assembled Monolayer. *Langmuir* **22,** 9473–9476 (2006).

[163] D. Pocaznoi, A. Calmet, L. Etcheverry, B. Erable & A. Bergel. Stainless steel is a promising electrode material for anodes of microbial fuel cells. *Energy Environ. Sci.* **5,** 9645–9652 (2012).

[164] A. ter Heijne, H. V. M. Hamelers, M. Saakes & C. J. N. Buisman. Performance of non-porous graphite and titanium-based anodes in microbial fuel cells. *Electrochim. Acta* **53,** 5697–5703 (2008).

[165] C. Santoro, C. Arbizzani, B. Erable & I. Ieropoulos. Microbial fuel cells: From fundamentals to applications. A review. *J. Power Sources* **356,** 225–244 (2017).

[166] A. Baudler, I. Schmidt, M. Langner, A. Greiner & U. Schröder. Does it have to be carbon? Metal anodes in microbial fuel cells and related bioelectrochemical systems. *Energy Environ. Sci.* **8,** 2048–2055 (2015).

[167] S. K. Chaudhuri & D. R. Lovley. Electricity generation by direct oxidation of glucose in mediatorless microbial fuel cells. *Nat. Biotechnol.* **21,** 1229 (2003).

[168] C. E. Reimers *et al.* Microbial fuel cell energy from an ocean cold seep. *Geobiology* **4,** 123–136 (2006).

[169] J. Wei, P. Liang & X. Huang. Recent progress in electrodes for microbial fuel cells. *Bioresour. Technol.* **102,** 9335–9344 (2011).

[170] C. Santoro *et al.* The effects of carbon electrode surface properties on bacteria attachment and start up time of microbial fuel cells. *Carbon* **67,** 128–139 (2014).

[171] F. Li, Y. Sharma, Y. Lei, B. Li & Q. Zhou. Microbial Fuel Cells: The Effects of Configurations, Electrolyte Solutions, and Electrode Materials on Power Generation. *Appl. Biochem. Biotechnol.* **160,** 168 (2009).

[172] I. Ieropoulos, J. Greenman & C. Melhuish. Improved energy output levels from small-scale Microbial Fuel Cells. *Bioelectrochemistry* **78,** 44–50 (2010).

[173] P. Aelterman, M. Versichele, M. Marzorati, N. Boon & W. Verstraete. Loading rate and external resistance control the electricity generation of microbial fuel cells with different three-dimensional anodes. *Bioresour. Technol.* **99,** 8895–8902 (2008).

[174] B. Logan, S. Cheng, V. Watson & G. Estadt. Graphite Fiber Brush Anodes for Increased Power Production in Air-Cathode Microbial Fuel Cells. *Environ. Sci. Technol.* **41,** 3341–3346 (2007).

[175] A. Baudler, S. Riedl & U. Schröder. Long-Term Performance of Primary and Secondary Electroactive Biofilms Using Layered Corrugated Carbon Electrodes. *Front. Energy Res.* **2,** 30 (2014).

[176] H. Wang, Côté R., G. Faubert, D. Guay & J. P. Dodelet. Effect of the Pre-Treatment of Carbon Black Supports on the Activity of Fe-Based Electrocatalysts for the Reduction of Oxygen. *J. Phys. Chem. B* **103,** 2042–2049 (1999).

[177] Y. Feng, Q. Yang, X. Wang & B. E. Logan. Treatment of carbon fiber brush anodes for improving power generation in air–cathode microbial fuel cells. *J. Power Sources* **195,** 1841–1844 (2010).

[178] S. Cheng & B. E. Logan. Ammonia treatment of carbon cloth anodes to enhance power generation of microbial fuel cells. *Electrochem. commun.* **9,** 492–496 (2007).

[179] L. Peng, S.-J. You & J.-Y. Wang. Carbon nanotubes as electrode modifier promoting direct electron transfer from Shewanella oneidensis. *Biosens. Bioelectron.* **25,** 1248–1251 (2010).

[180] Y. Zhang *et al.* A graphene modified anode to improve the performance of microbial fuel cells. *J. Power Sources* **196,** 5402–5407 (2011).

[181] S. Inoue *et al.* Structural optimization of contact electrodes in microbial fuel cells for current density enhancements. *Sensors Actuators A Phys.* **177,** 30–36 (2012).

[182] J. Heinze. Ultramicroelectrodes in Electrochemistry. *Angew. Chemie Int. Ed. English* **32,** 1268–1288 (1993).

[183] S. Chen *et al.* Electrospun and solution blown three-dimensional carbon fiber nonwovens for application as electrodes in microbial fuel cells. *Energy Environ. Sci.* **4,** 1417–1421 (2011).

[184] S. Chen *et al.* Electrospun carbon fiber mat with layered architecture for anode in microbial fuel cells. *Electrochem. commun.* **13,** 1026–1029 (2011).

[185] J. F. Cooley. Apparatus for electrically dispersing fluids. (1899).

[186] M. Bognitzki *et al.* Polymer, Metal, and Hybrid Nano- and Mesotubes by Coating Degradable Polymer Template Fibers (TUFT Process). *Adv. Mater.* **12,** 637–640 (2000).

[187] H. L. Schreuder-Gibson *et al. Protective Textile Materials Based on Electrospun Nanofibers*. *Journal of Advanced Materials* **34,** (2002).

[188] M.-A. Kim *et al.* Strengthened PAN-based carbon fibers obtained by slow heating rate carbonization. *Sci. Rep.* **6,** 22988 (2016).

[189] X.-H. Qin & S.-Y. Wang. Filtration properties of electrospinning nanofibers. *J. Appl. Polym. Sci.* **102,** 1285–1290 (2006).

[190] G.-M. Kim *et al.* One-Dimensional Arrangement of Gold Nanoparticles by Electrospinning. *Chem. Mater.* **17,** 4949–4957 (2005).

[191] A. Theron, E. Zussman & A. L. Yarin. Electrostatic field-assisted alignment of electrospun nanofibres. *Nanotechnology* **12,** 384–390 (2001).

[192] H. Jia *et al.* Enzyme-carrying polymeric nanofibers prepared via electrospinning for use as unique biocatalysts. *Biotechnol. Prog.* **18,** 1027–1032 (2002).

[193] I. D. Norris, M. M. Shaker, F. K. Ko & A. G. MacDiarmid. Electrostatic fabrication of ultrafine conducting fibers: polyaniline/polyethylene oxide blends. *Synth. Met.* **114,** 109–114 (2000).

[194] N. Liu *et al.* Electrospun PEDOT:PSS–PVA nanofiber based ultrahigh-strain sensors with controllable electrical conductivity. *J. Mater. Chem.* **21,** 18962–18966 (2011).

[195] P.-G. de Gennes. *Scaling Concepts in Polymer Physics*. (Cornell University Press, 1979).

[196] C. Mit-uppatham, M. Nithitanakul & P. Supaphol. Ultrafine Electrospun Polyamide-6 Fibers: Effect of Solution Conditions on Morphology and Average Fiber Diameter. *Macromol. Chem. Phys.* **205,** 2327–2338 (2004).

[197] X. Zong *et al.* Structure and process relationship of electrospun bioabsorbable nanofiber membranes. *Polymer (Guildf).* **43,** 4403–4412 (2002).

[198] T. Uyar & F. Besenbacher. Electrospinning of uniform polystyrene fibers: The effect of solvent conductivity. *Polymer (Guildf).* **49,** 5336–5343 (2008).

[199] C. J. Luo, E. Stride & M. Edirisinghe. Mapping the Influence of Solubility and Dielectric Constant on Electrospinning Polycaprolactone Solutions. *Macromolecules* **45,** 4669–4680 (2012).

[200] Q. P. Pham, U. Sharma & A. G. Mikos. Electrospinning of Polymeric Nanofibers for Tissue Engineering Applications: A Review. *Tissue Eng.* **12,** 1197–1211 (2006).

[201] H. Fong, I. Chun & D. H. Reneker. *Beaded Nanofibers Formed During Electrospinning*. *Polymer* **40,** (1999).

[202] C. Zhang, X. Yuan, L. Wu, Y. Han & J. Sheng. Study on morphology of electrospun poly(vinyl alcohol) mats. *Eur. Polym. J.* **41,** 423–432 (2005).

[203] D. Li & Y. Xia. Fabrication of Titania Nanofibers by Electrospinning. *Nano Lett.* **3,** 555–560 (2003).

[204] C. J. Buchko, L. C. Chen, Y. Shen & D. C. Martin. Processing and microstructural characterization of porous biocompatible protein polymer thin films. *Polymer (Guildf).* **40,** 7397–7407 (1999).

[205] S. De Vrieze *et al.* The effect of temperature and humidity on electrospinning. *J. Mater. Sci.* **44,** 1357–1362 (2009).

[206] C. Wang *et al.* Electrospinning of polyacrylonitrile solutions at elevated temperatures. *Macromolecules* **40,** 7973–7983 (2007).

[207] C. L. Casper, J. S. Stephens, N. G. Tassi, D. B. Chase & J. F. Rabolt. Controlling Surface Morphology of Electrospun Polystyrene Fibers: Effect of Humidity and Molecular Weight in the Electrospinning Process. *Macromolecules* **37,** 573–578 (2004).

[208] S. Tripatanasuwan, Z. Zhong & D. H. Reneker. Effect of evaporation and solidification of the charged jet in electrospinning of poly(ethylene oxide) aqueous solution. *Polymer (Guildf).* **48,** 5742–5746 (2007).

[209] L. R. Manea, L. Hristian, A. L. Leon & A. Popa. Recent progress concerning the production of controlled highly oriented electrospun nanofibrous arrays. *IOP Conf. Ser. Mater. Sci. Eng.* **145,** 032007 (2016).

[210] Y. Dror *et al.* One-Step Production of Polymeric Microtubes by Co-electrospinning. *Small* **3,** 1064–1073 (2007).

[211] S. N. Reznik, A. L. Yarin, E. Zussman & L. Bercovici. Evolution of a compound droplet attached to a core-shell nozzle under the action of a strong electric field. *Phys. Fluids* **18,** (2006).

[212] S. Klein *et al.* Encapsulation of pseudomonas sp. ADP cells in electrospun microtubes for atrazine bioremediation. *J. Ind. Microbiol. Biotechnol.* **39,** 1605–1613 (2012).

[213] M. Gensheimer, A. Brandis-Heep, S. Agarwal, R. K. Thauer & A. Greiner. Polymer/Bacteria Composite Nanofiber Nonwovens by Electrospinning of Living Bacteria Protected by Hydrogel Microparticles.

Macromol. Biosci. **11,** 333–337 (2011).

[214] E. Zussman. Encapsulation of cells within electrospun fibers. *Polym. Adv. Technol.* **22,** 366–371 (2011).

[215] S. Klein *et al.* Encapsulation of bacterial cells in electrospun microtubes. *Biomacromolecules* **10,** 1751–1756 (2009).

2

CARBON MICROFIBERS BIOANODE

TABLE OF CONTENTS

Chapter 2. Carbon microfibers bioanode 99
- 2.1. Introduction & objectives 99
- 2.2. Lab-made electrospun carbon microfibers 100
  - 2.2.1. Polyacrylonitrile & carbon fibers 100
  - 2.2.2. Experimental procedure 103
    - 2.2.2.1. Polyacrylonitrile electrospinning 103
    - 2.2.2.2. Heat treatment 106
    - 2.2.2.3. Carbon membranes characterization 108
- 2.3. Bioanode colonization process 119
  - 2.3.1. Bacterial culture 120
    - 2.3.1.1. Growth media 120
    - 2.3.1.2. Culture protocol 121
    - 2.3.1.3. MFC integration & electrochemical characterization 122
    - 2.3.1.4. Post-mortem imaging 129
  - 2.3.2. Membrane precolonization & ready-to-use bioanodes 132
    - 2.3.2.1. Bacterial growth investigation 133
    - 2.3.2.2. Microscopy & biofilm formation evaluation 134
    - 2.3.2.3. MFC integration & electrochemical characterization 135
    - 2.3.2.4. Post-mortem imaging 137
- 2.4. 3D ready-to-use carbon microfibers bioanode 139
  - 2.4.1. Experimental procedure 139
  - 2.4.2. Effect of bioanode stacking & thickness 139
    - 2.4.2.1. MFC integration & electrochemical characterization 139
    - 2.4.2.2. Post-mortem imaging 146
  - 2.4.3. Biofilm overgrowth 148
  - 2.4.4. Microfibers architecture & diffusion limitations 149
- 2.5. Cryodesiccation & conservation 152
  - 2.5.1. Experimental procedure 152
  - 2.5.2. Bacteria viability & exoelectrogenic activity 154
    - 2.5.2.1. Live/dead test 154

2.5.2.2. Plate count ... 155
2.5.2.3. MFC integration & electrochemical characterization ... 156
2.5.2.4. Post-mortem imaging ... 158
2.6. Conclusion ... 160
References ... 161

CHAPTER 2. CARBON MICROFIBERS BIOANODE

2.1. Introduction & objectives

As research on microbial fuel cells progresses, crucial advancements are made and ever better power outputs and stability are reached, but a lot of room for refinement still exists.

Optimizing electron transfer at the interface between the anode and the bacteria offers a significant potential for performances improvements. In this chapter, we choose to focus on the synthesis of an electrospun mat of carbon micron scaled fibers and its colonization by electroactive bacteria. The resulting bioanode is integrated in a lab-scaled microbial fuel cell (MFC) and the effects of its architecture on electron transfer and power output are investigated.

The carbon microfibers mat is synthetized through a multi-step approach where a solution of polyacrylonitrile is electrospun and subsequently subjected to various heat treatments in controlled atmospheres (air and argon) in order to convert the precursor polymer to graphitic carbon.

The electrospun carbon electrodes are then either colonized in situ in a lab-scaled MFC reactor by an exoelectrogenic strain, *Shewanella oneidensis*, or precolonized and integrated into the reactor. Their electrochemical behavior and stability are therefore investigated and compared between them and with commercial carbon felt.

The effect of the electrode thickness on the bacterial colonization depth, nutrients diffusion and the MFC efficiency is evaluated. A way of optimizing its performances by stacking precolonized electrodes is also explored. Furthermore, the long-term storage of the bioanode through cryodesiccation is carried out and the MFC performances are evaluated and compared to the ones achieved for a bioanode freshly prepared.

2.2. Lab-made electrospun carbon microfibers

2.2.1. Polyacrylonitrile & carbon fibers

Carbon fibers – fibers composed mostly of carbon atoms – are widely used in a broad range of applications as they exhibit excellent electric conductivity, chemical and thermal stability, tensile properties and stiffness and a low density[1]. Most of the fibers manufactured today are produced from polyacrylonitrile (PAN) precursor (**Figure 2.1**) after extrusion of the polymer and a subsequent controlled pyrolysis of the precursor.

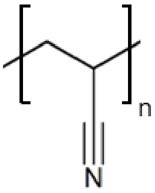

Figure 2.1 – Polyacrylonitrile (PAN) structure

The main steps of PAN conversion to carbon fibers usually involve the stabilization of precursor polymer to infusible fibers in air between 200 and 400°C followed by a high temperature treatment under argon inert atmosphere at around 1000°C to remove non-carbon elements such as hydrogen and nitrogen. A further optional step of graphitization up to 3000°C under inert atmosphere may be undertaken to reach an even higher carbon content (**Figure 2.2**). The resulting properties of the fibers is influenced mainly by its crystallinity, the crystalline distribution, molecular orientation, the carbon content and the amount of defects[1].

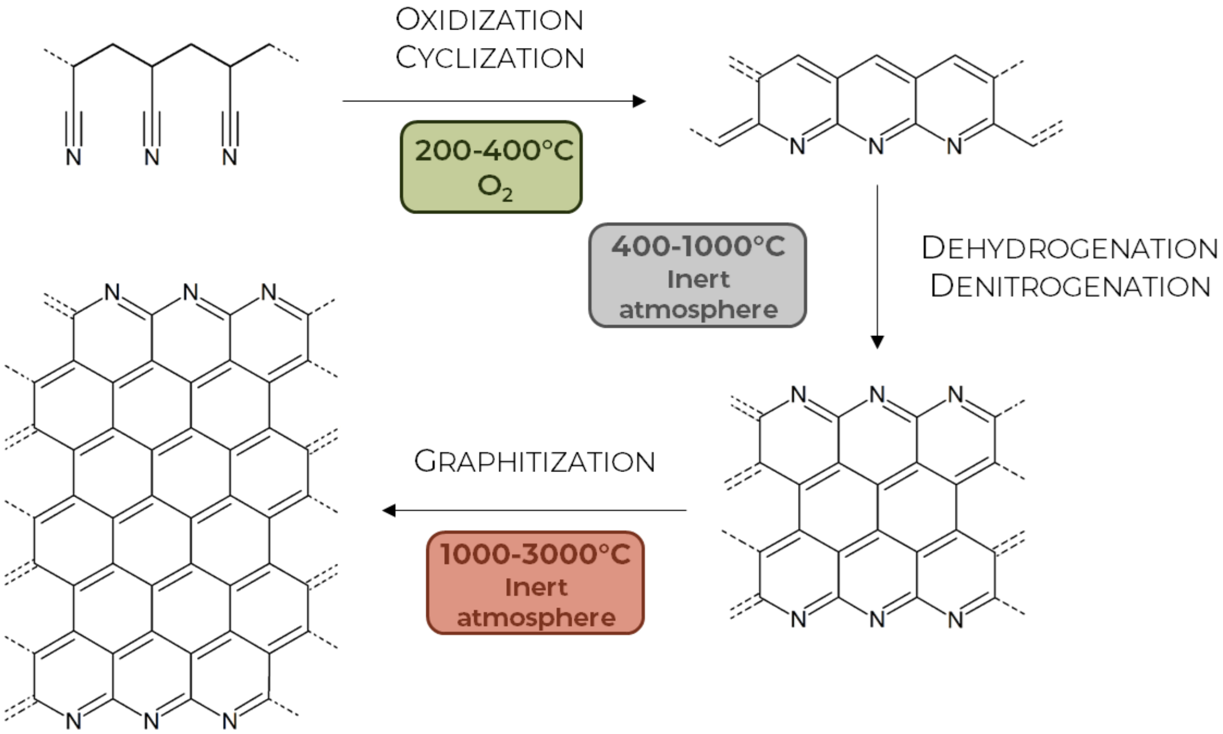
OXIDIZATION
CYCLIZATION
200-400°C
O_2
400-1000°C
Inert
atmosphere
DEHYDROGENATION
DENITROGENATION
GRAPHITIZATION
1000-3000°C
Inert
atmosphere
N

Figure 2.2 – Simplified process of PAN conversion to graphite-like layers
Adapted from Huang, 2009

The stabilization step is required to convert linear PAN molecules to a cyclic structure avoiding degradation and chain breakage during the next heating steps[2]. The cyclization/oxidation step is however a fairly complex process and is not fully understood especially at the molecular level. Various intermediate states have been proposed to describe the stabilization of PAN molecules under heating in air (**Figure 2.3**)[1]:

a. A cyclized and dehydrated structure usually considered to account for low temperature stabilizations[3];
b. Azomethine crosslinks between polymer chains[4];
c. Ether cyclic bridges[5];
d. Ketonic oxidized cyclic products[6];
e. Cyclic nitrone products[7];
f. g. h. Various structures in the oxidized molecule, where unreacted nitrile groups may be present[8]–[10].

The stabilization process has been investigated through scanning electron microscopy (SEM), X-ray diffraction (XRD)[11]–[13], Fourier transform infrared spectroscopy (FTIR)[11],[13], differential scanning calorimetry (DSC) and thermogravimetric analysis (TGA)[13]. All these studies emphasize the complex nature of the stabilization process. Furthermore, the stabilization step also leads to a partial dehydrogenation and denitrogenation of the products and the formation of a “ladder-like” compound (**Figure 2.3**).

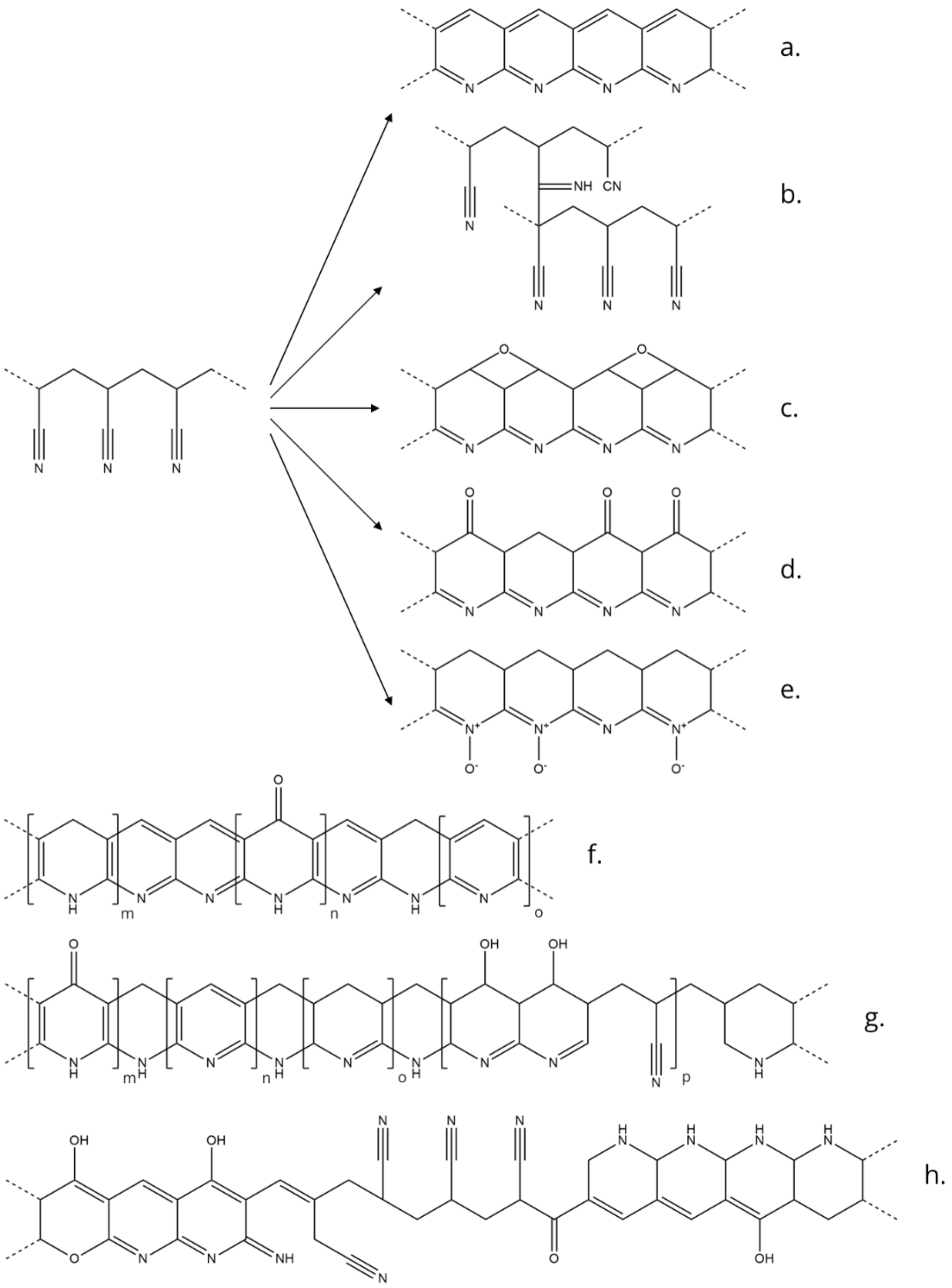

Figure 2.3 – Proposed products of the oxidation/cyclization of PAN
Adapted from Huang, 2009

The carbonization step involves a heat treatment of the infusible stabilized fibers under inert atmosphere (N_2 or Ar). A temperature of around 1000°C is sufficient to remove hydrogen, nitrogen, oxygen and other non-carbon elements to yield conductive conjugated layers of graphite-like ribbons[1].

Eventually, a last heating step under inert atmosphere up to 3000°C may be undertaken to reach even higher carbon content, conductivity and a higher Young's modulus in the fiber direction.

Carbon fibers synthetized from PAN precursor generally exhibit a turbostratic structure (**Figure 2.4**) where carbon crystallites are grown through a coalescence process between crystallites and by absorbing disorganized carbon clusters. The degree of organization is therefore relatively small but high enough to show good electrical conductivity and tensile strength[1].

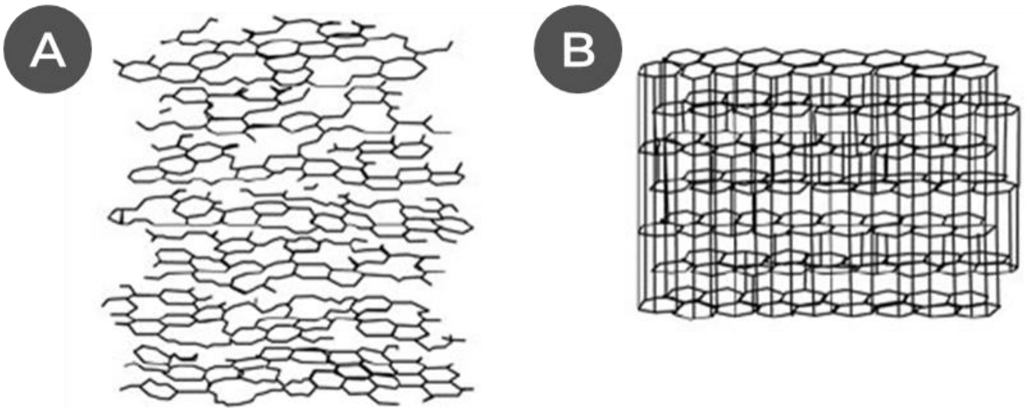

Figure 2.4 – Schematic representation of (A) a turbostratic and (B) a graphitic carbon structure
Adapted from Dasgupta & Sathiyamoorthy, 2003

2.2.2. Experimental procedure

The polyacrylonitrile (PAN, M_w ~ 150 000) was purchased from Sigma-Aldrich (USA). A 10 wt% PAN solution in N,N-Dimethylformamide (DMF, ≥99.8 %, AnalaR NORMAPUR® ACS, Reag. Ph. Eur. analytical reagent, used as received) purchased from VWR is prepared and stirred for 2 hours in a 80°C water bath to ensure complete dissolution of the PAN powder.

2.2.2.1. Polyacrylonitrile electrospinning

The aforementioned precursor solution is electrospun on a grounded aluminum foil on a roller using the Electrospinz (Blenheim, New Zealand) ES1™ lab-scale generator and apparatus (**Figure 2.5**). The roller is used to help fibers deposition by dragging them around it, but the speed is not sufficient to align them. The electrospinning parameters are set as follow and have been shown to yield a self-standing membrane made out of intermingled nonwoven fibers[14]:

- **Electric field**: around 1 kV·cm^{-1} set by tuning the voltage and distance between the needle and the collector respectively at 13 kV and 13 cm. The current never exceeded 9 µA;
- **Injection speed**: 30 µL·min^{-1} using a Fisherbrand™ syringe pump and a Terumo® 10cc Eccentric Luer Tip syringe equipped with a blunt-end needle ($Ø_{\text{internal}}$ = 0.75 mm);
- **Volume**: 2.25 mL is injected to ensure the deposition of a proper self-standing membrane;
- **Temperature**: 21°C thermostatted by the lab air-conditioner;
- **Relative humidity**: kept between 30 and 35 % by running the setup in a closed poly(methyl methacrylate) box connected to the lab dry compressed air outlet. Relative humidity higher than 70 % tend to form a gel due to the low water solubility of the PAN;

- **Substrate**: aluminum foil fixed on a roller with a speed set at around 400 rpm.

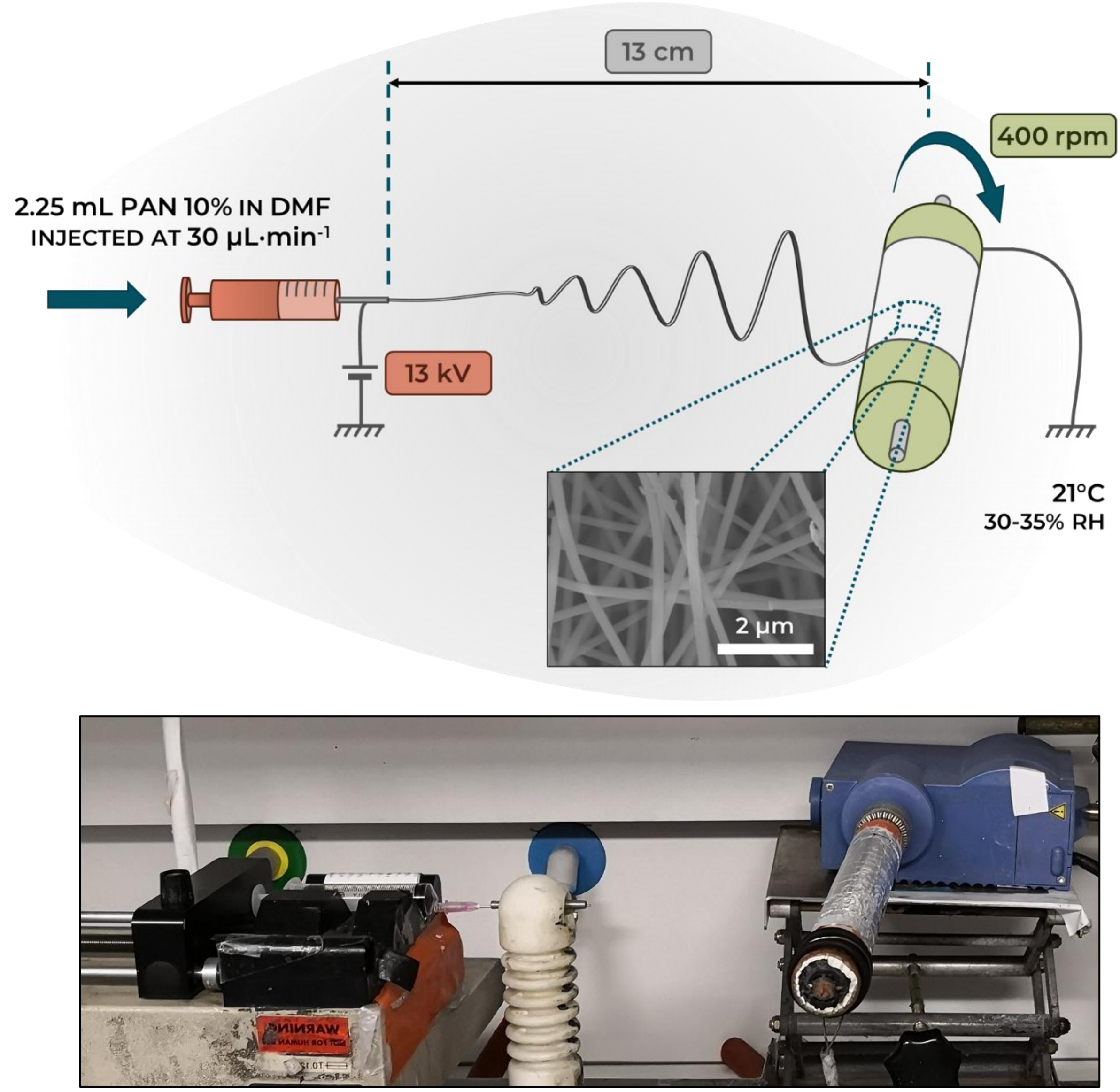
13 cm
400 rpm
2.25 mL PAN 10% IN DMF
INJECTED AT 30 µL·min-1
13 kV
21°C
30-35% RH
2 µm

Figure 2.5 – Overview of a PAN electrospinning setup

The resulting deposited electrospun fibers are dried overnight at 70°C under air to evaporate the residual DMF and form a self-standing membrane with a thickness of a few hundred micrometers ($h_{membrane}$ = 298 ± 78 µm) depending on the stability and homogeneity of the process (**Figure 2.6**).

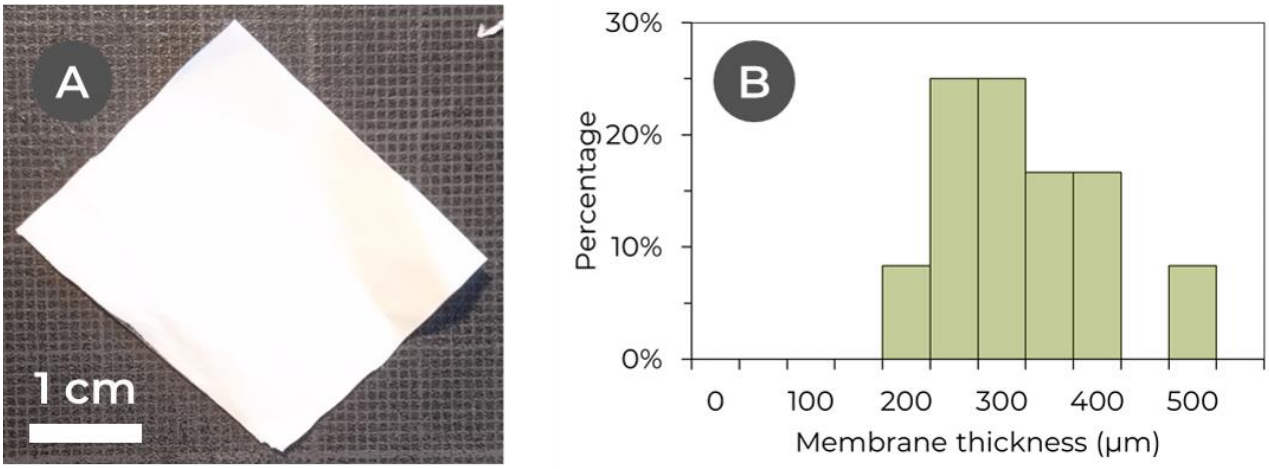

Figure 2.6 – (A) Self-standing PAN membrane after electrospinning (from a 10 wt% PAN in DMF solution) & (B) membrane thickness distribution; N = 12.

A scanning electron microscope (SEM) analysis of the fibers show at this stage a relatively low polydispersity ($Ø_{fibers}$ = 449 ± 98 nm) of the fibers. Their diameter and the interfiber distance (~ 1 µm, confirmed by mercury porosimetry) are comparable with the dimensions of a bacterium (typically of few micrometers in length) and should be well adapted to their colonization (**Figure 2.7**).

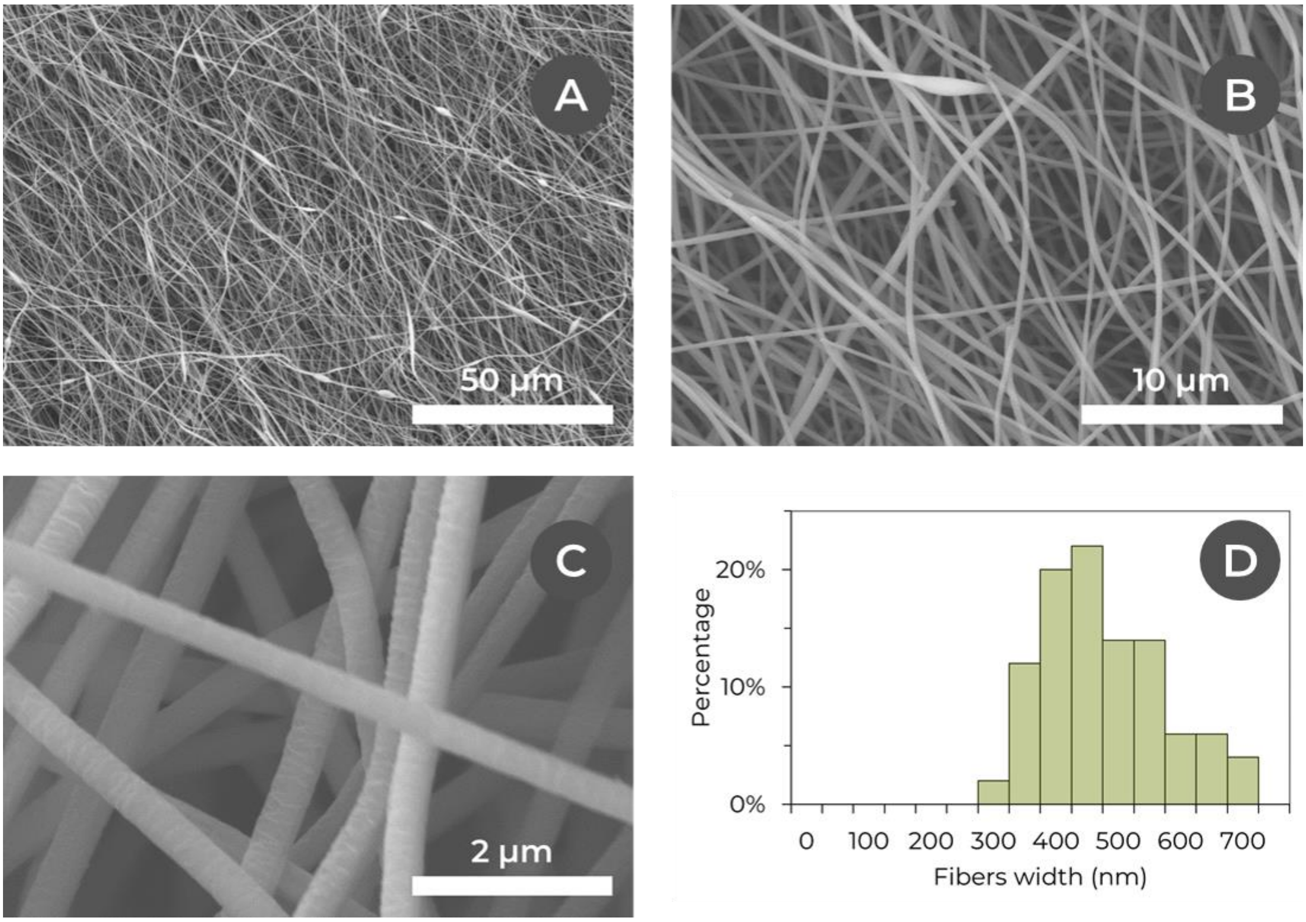

Figure 2.7 – (A), (B), (C) Scanning electron microscope–Field-emission gun (SEM-FEG) micrographs of a PAN electrospun membrane (from a 10 wt% PAN in DMF solution) & (D) fibers size distribution; N = 50.

2.2.2.2. Heat treatment

The membranes harvested after electrospinning are not conductive at this stage and required subsequent heat treatment – stabilization and carbonization/graphitization – in order to be converted to a carbon fiber mat[1]

The stabilization step is required to oxidize the PAN chains and avoid its thermal degradation during the next heating steps. It is conducted at 280°C under static air for 3 hours in a muffle oven.

The resulting membrane takes a brown or orange color and is still insulating.

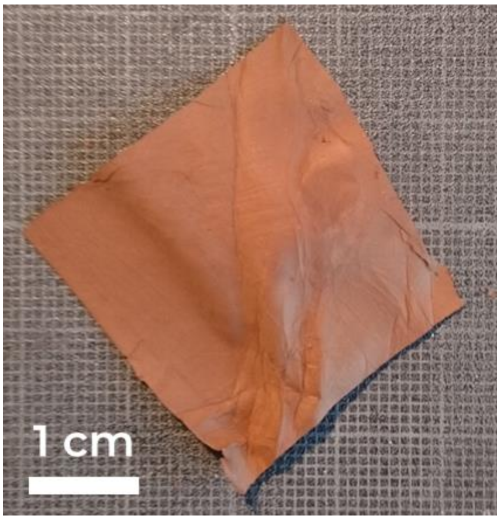

Figure 2.8 – Stabilized electrospun PAN membrane (from a 10 wt% PAN in DMF solution) after air oxidizing heat treatment at 280°C for 3 hours.

The structure of raw and stabilized electrospun PAN membranes has been studied by Fourier Transform Infrared (FTIR) spectroscopy. The FTIR spectra before and after stabilization show heavy changes (**Figure 2.9**). The stabilized membrane shows a decrease in C≡N stretching absorption band (around 2235 cm^{-1}) and in CH_2 absorption bands (around 2920 and 1450 cm^{-1}), and a heavy increase in conjugated absorption (between 1430 and 1830 cm^{-1}) and C-O-C bending and C-O stretching (between 1000 and 1400 cm^{-1}) which is consistent with the oxidized and cyclized products proposed in the literature. Note that due to the complex nature of the oxidative stabilization process, the identification of all the products issues from the stabilization process is difficult by solely using this approach.

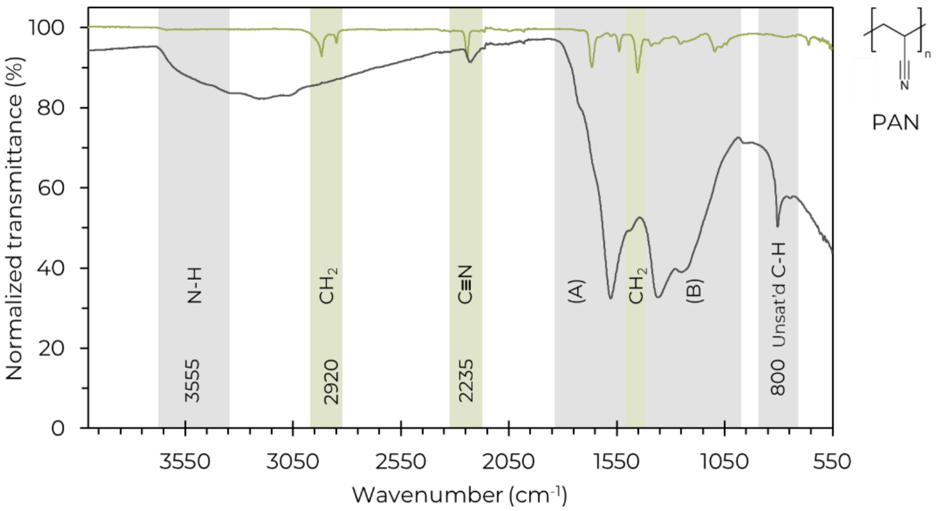

Figure 2.9 – FTIR spectra of raw electrospun PAN membrane (–, from a 10 wt% PAN in DMF solution) and a stabilized membrane (–, under air at 280°C for 3 hours). The two heavy bands in the stabilized membrane spectrum correspond to (A) conjugated double bonds, C-O, N-H & O-H & (B) C-O-C bending and C-O stretching, both characteristic of the oxidized and cyclized stabilization products. A blank was recorded and subtracted from the presented spectra.

The non-conductive stabilized product is then heated under Ar inert atmosphere (H_2O (5 bar) < 3 ppm, C_nH_m < 0.5 ppm, O_2 < 2 ppm; flow rate around 250 mL·min^{-1}) up to 940°C (10°C·min^{-1} for 50 minutes then 2.5°C·min^{-1} for 180 minutes) in a tubular quartz oven to yield a black carbonized membrane (**Figure 2.10**).

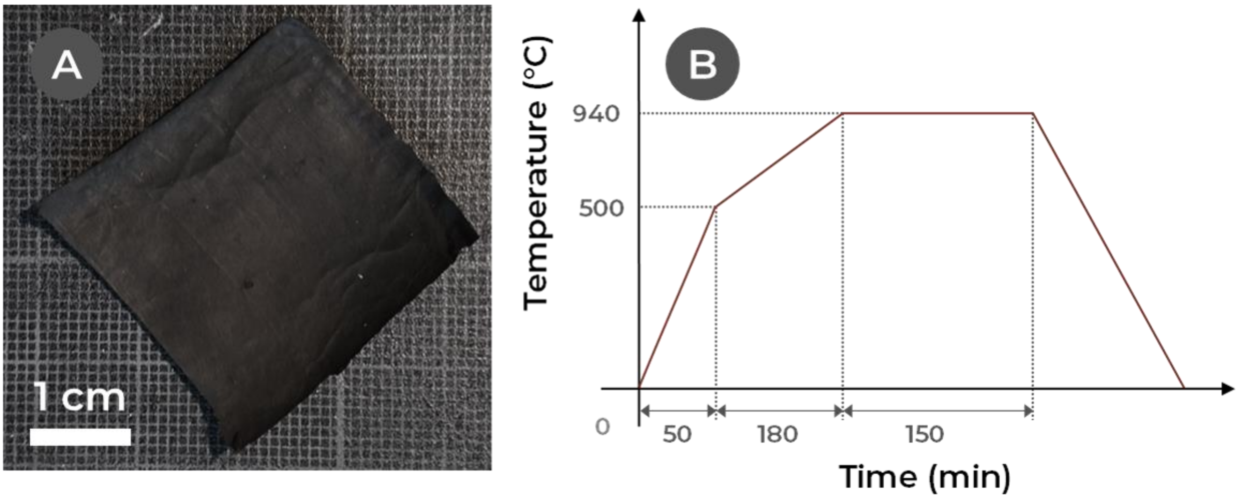

Figure 2.10 – (A) Self-standing electrospun carbon membrane after carbonization of a stabilized electrospun PAN membrane (from a 10 wt% PAN in DMF solution) & (B) carbonization treatment settings under argon flow.

An alternative heating procedure with CO_2 Laser heating under vacuum has also been explored at the *Conditions extrêmes et Matériaux: Haute Température et Irradiation* (CEMHTI) laboratory in Orléans in order to reach higher carbonization temperatures – up to 2000°C – and investigate the effect of a higher graphitization of the fibers.

The architecture of the resulting fibers mat is then investigated by scanning electron microscopy, its structural parameters by Raman spectroscopy, Fourier transform infrared spectroscopy and X-ray crystallography (XRD). Their surface elemental composition is measured by X-ray photoelectron microscopy (XPS). Eventually, their electrical and electrochemical properties have been estimated through respectively impedance spectroscopy and cyclic voltammetry.

2.2.2.3. Carbon membranes characterization

Architecture: Scanning electron microscopy shows that the carbon membranes are made of non-oriented fibers arranged into a 3D network, indicating that the polymer fibers are mostly transformed into carbon fibers. Additionally, a few of them appear broken (**Figure 2.11**). The average size of the fibers shrinks by around 40 % (**Figure 2.12**) ($Ø_{fibers}$ = 300 ± 98 nm in the electrospun carbon membrane). This can be explained by a loss of mass during the dehydrogenation/dehydration and denitrogenation of the stabilized fibers during the carbonization step. The breakage of some fibers might also be attributed to the mechanical stress and strain accumulated during this shrinkage at high temperature.

The volumetric mass density of the fibers is evaluated at $\rho_{electrospun\,membrane} = 0.09\ g{\cdot}cm^{-3}$ which is similar to the usual value of commercial carbon felt ($\rho_{carbon\,felt} = 0.12\ g{\cdot}cm^{-3}$ for Morgan Advanced Materials carbon felt).

The specific surface area of the electrospun carbon membrane is measured according to the Brunauer–Emmett–Teller N_2 physical adsorption method which estimates $SSA_{BET} \approx 470\ m^2{\cdot}g^{-1}$ (N = 3), exhibiting essentially mesoporosity. The macroporosity is checked by mercury porosimetry and SEM imaging. For comparison, activated carbon exhibits specific surface areas up to 3000 $m^2{\cdot}g^{-1}$, but show a lot of additional microporosity.

If we considered that the mat was made of cylindrical fibers of radius r (m) and volumetric mass density $\rho_{graphite} \approx 2.1\ g{\cdot}cm^{-3}$, the specific surface area of the sample would be $A_{specific} = \frac{2}{\rho \cdot r} \approx 7\ m^2{\cdot}g^{-1}$. However, N_2 adsorption experiments indicate a clearly higher specific surface area hinting that the mesoporosity of the fibers is indeed responsible for this high specific surface area. With m (g) the mass of the sample, d (m) the diameter of the sample and L (m) its thickness, the theoretical porosity of the material can be evaluated[15] as $\epsilon = 1 - \frac{4m}{\pi \cdot \rho \cdot d^2 \cdot L} \approx 96\ \%$. This is consistent with SEM observations (**Figure 2.11.A-C**).

Contact angle experiments have been carried out on the membrane and show a quick and full absorption of water droplets. The carbon fibers should be hydrophobic on their own, but the fibrous porous structure exhibited by SEM imaging turns the mat hydrophilic at a macroscopic level.

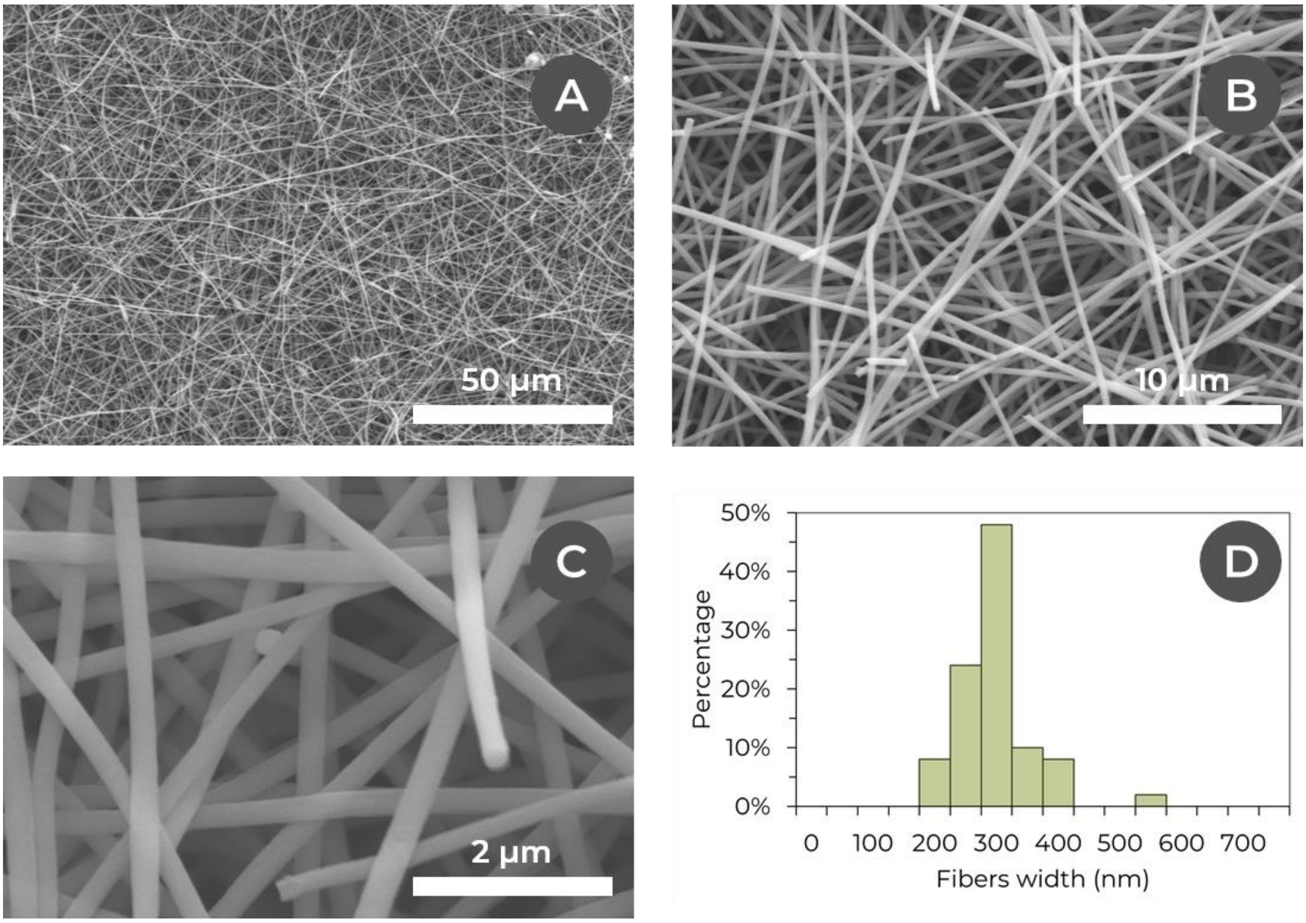
A
50 µm
B
10 µm
C
2 µm
D
Percentage
50%
40%
30%
20%
10%
0%
0
100
200
300
400
500
600
700
Fibers width (nm)

Figure 2.11 – (A), (B), (C) Scanning electron microscope–Field-emission gun (SEM-FEG) micrographs of a PAN electrospun membrane (from a 10 wt% PAN in DMF solution) stabilized (under air at 280°C for 3 hours) & carbonized (at 940°C under argon atmosphere). (D) Fibers size distribution; N = 50.

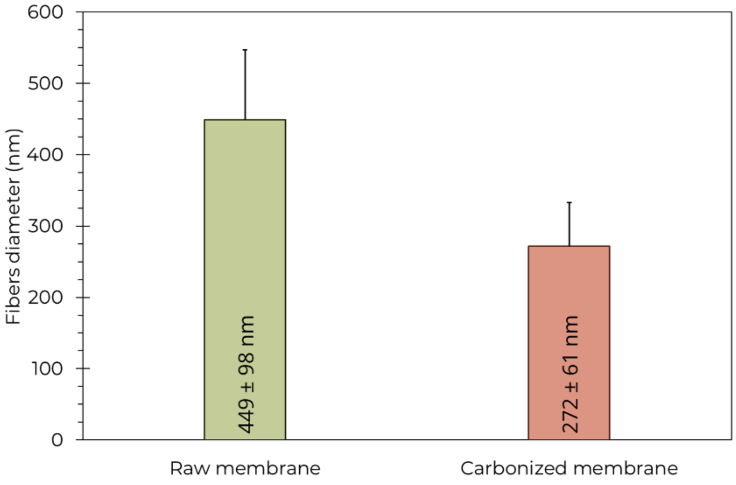

Figure 2.12 – Fibers diameter comparison between the raw electrospun mat (from a 10 wt% PAN in DMF solution) and the carbonized carbon membrane.

Structural parameters: FTIR, Raman spectroscopy and XRD are complementary to investigate the chemical changes undertaken by the electrospun PAN membranes through the heat treatment.

Raman spectroscopy (**Figure 2.13**) shows no band for the raw membrane – showing obviously no carbonization – and two bands at respectively around 1350 cm^{-1} and 1580 cm^{-1}, as well as a broad band between 2300 and 3600 cm^{-1} for the heat-treated electrospun membranes. Tabulated values[16] attribute these bands to the disorder of the carbon material structure (D-band, 1350 cm^{-1}), and the sp^2 hybridization of carbon in a graphite-like lattice (G-band, 1580 cm^{-1}). The broad band between 2300 and 3600 cm^{-1} is a composite of the second harmonic of these same bands (2D and D+G). With increasing temperature, we observe thinner and better D and G-resolved bands, accompanied by a decrease of the full width at half maximum (FWHM) of D and G bands. The same observations can be done for the second harmonics. A decrease in the width of the bands is linked to an increase in graphitization[16].

The ratio between the D and G bands, dubbed the R-value, decreases with the alignment of the graphitic plan and it is representative of the degree of graphitization. The R-value is then estimated from the Raman spectra of a PAN membrane stabilized under air at 280°C, pyrolyzed at 940°C, and for a PAN membrane carbonized by Laser under vacuum at 1500°C and 2000°C. The R-value (**Table 2.1**) decreases from the stabilized PAN ($\text{R-value}_{\text{stabilized}} = 1.29$) to the carbonized membranes ($\text{R-value}_{\text{carbonized, 940°C}} = 0.88$, $\text{R-value}_{\text{carbonized, 1500°C}} = 0.84$ & $\text{R-value}_{\text{carbonized, 2000°C}} = 1.03$). This observation is attributed to an augmentation of the fiber graphitization. However, an increase of R-value between 1500°C and 2000°C is observed and is unexplained as a higher graphitization of the fibers would be expected for higher temperature treatments.

Raman spectroscopy shows an expected increase in graphitization from the stabilized PAN membrane to the carbonized carbon membrane. We do observe a good conversion of the electrospun PAN fibers to graphite-like ones as early as 940°C.

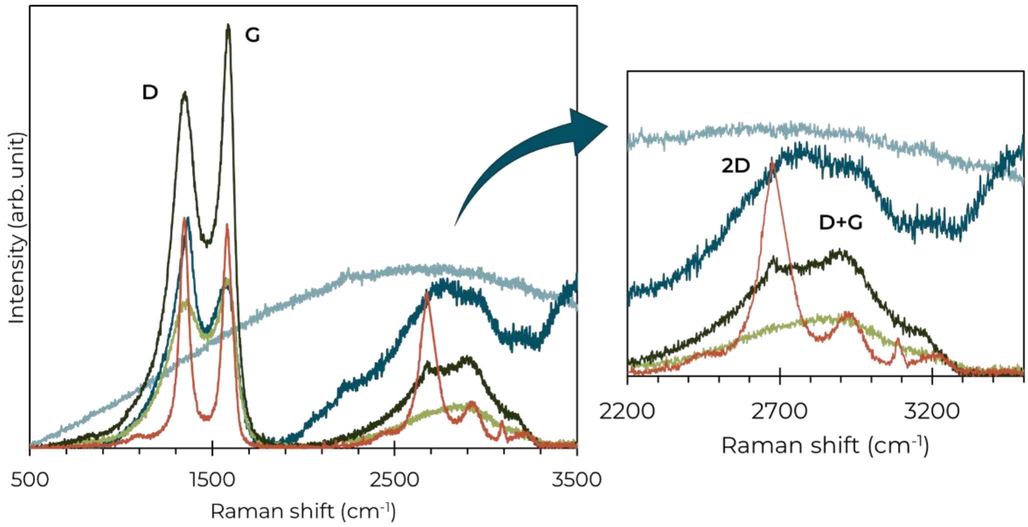

Figure 2.13 – Raman spectroscopy of an electrospun PAN membrane (from a 10 wt% PAN in DMF solution) at different stages of the heat treatment: – Raw membrane, – Stabilization at 280°C for 3 hours under air, – Carbonization at 940°C under argon, – Laser carbonization at 1500°C under vacuum, – Laser carbonization at 2000°C under vacuum. The baseline is corrected to remove the fluorescence background.

Collaboration with the CEMTHI laboratory, Orléans

Table 2.1 – Evolution of the D-band and G-band full width at half maximum (FWHM) as well as the R-values for stabilized and carbonized electrospun PAN membranes.

Sample	D-band FWHM (cm^{-1})	G-band FWHM (cm^{-1})	R-value
Stabilized 280°C (Air)	195	132	1.29
Carbonized 940°C (Ar)	104	170	0.88
Carbonized 1500°C (Laser/Vacuum)	215	134	0.84
Carbonized 2000°C (Laser/Vacuum)	66	74	1.03

X-ray diffraction pattern (**Figure 2.14**) shows for the raw membrane a wide peak at $2\theta \approx 17°$ which matches with amorphous PAN (010) plane (PDF 00-048-2119). This peak disappears in the stabilized and carbonized membrane. For these membranes, wide peaks at $2\theta \approx 26°$ and $2\theta \approx 42°$ appear, corresponding to the reflections of the (002) and (100) planes of carbon graphite (PDF 00-041-1487).

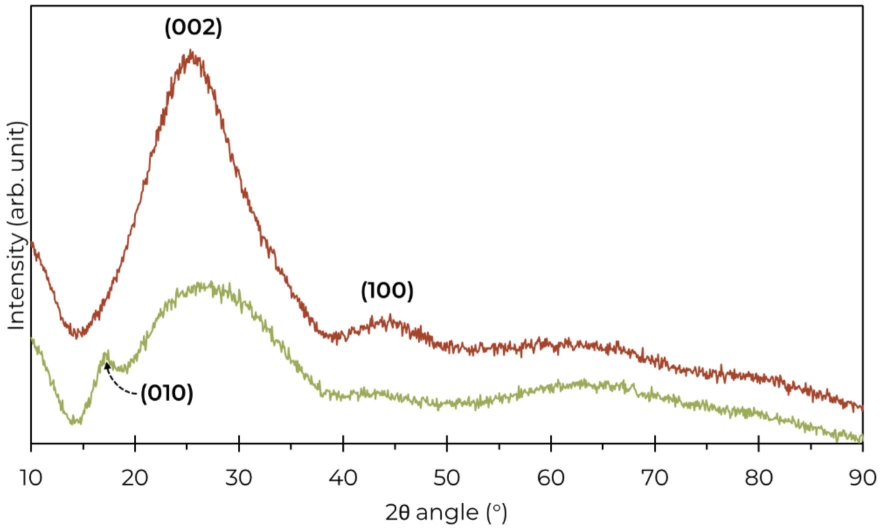

Figure 2.14 – X-ray diffraction pattern of a raw electrospun PAN membrane (–) (from a 10 wt% PAN in DMF solution) and an electrospun PAN membrane stabilized under air at 280°C for 3 hours and then carbonized at 940°C under argon atmosphere (–).

After carbonization, the FTIR spectrum (**Figure 2.15**) absorption strongly increases as expected for a graphitic material.

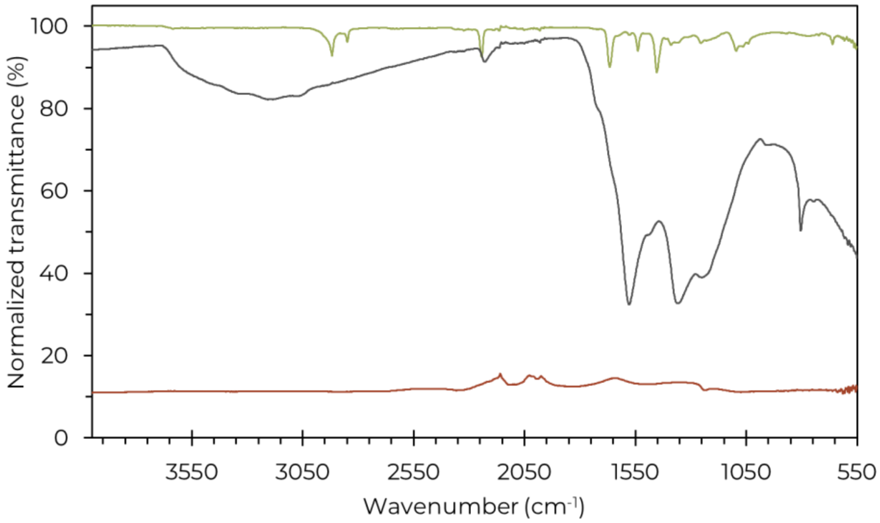

Figure 2.15 – FTIR spectra of raw electrospun PAN membrane (–, from a 10 wt% PAN in DMF solution), a stabilized membrane (–, under air at 280°C for 3 hours) & a carbonized membrane (–, at 940°C under argon atmosphere).

These characterizations experiments all point out a good conversion of the precursor PAN to graphite-like carbon. The level of graphitization is depending on the heat-treatment and decent value is achieved at 940°C. Accordingly, this temperature will be used for the rest of the experiments.

Surface elemental composition: The surface elemental composition of the carbonized fibers was measured by XPS with Antoine Miche (Laboratoire de Réactivité de Surface, Sorbonne Université).

The spectrum (**Figure 2.16**) reveals the majority presence of carbon in the sample surface (estimated at 87 %), as well as oxygen and nitrogen (respectively 7 % and 6 %).

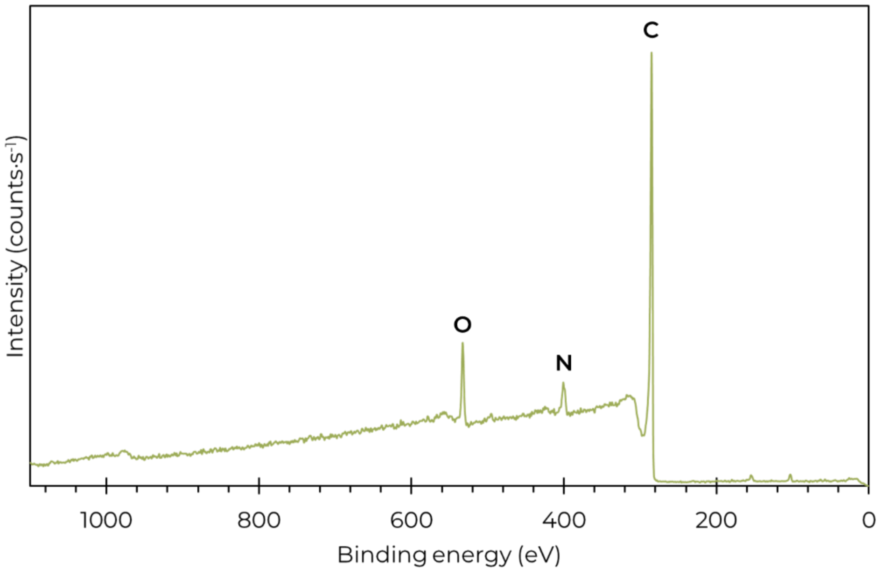

Figure 2.16 – XPS spectrum of a stabilized & carbonized electrospun PAN membrane (electrospun from a 10 wt% PAN in DMF solution, stabilized under air at 280°C for 3 hours and then carbonized at 940°C under argon atmosphere).

Electrical conductivity: The electrical conductivity of the electrospun carbon membrane is studied both by a two-electrode setup and impedance spectroscopy. The two-electrode setup investigates the surface conductivity (σ_S) while when coupled with impedance spectroscopy in PFTE/stainless steel Swagelok® cells (**Figure 2.17**) transverse conductivity (σ_T) is estimated. The two values are expected to be different in a planar fiber mat produced by electrospinning and will be compared to estimate the impact of the fibers organization.

As expected, the raw electrospun membrane as well as the stabilized membrane exhibit extremely low σ_T and σ_S, confirming that they are highly insulating. In contrast, σ_T and σ_S of 10^{-1} S·cm^{-1} to 10^{-2} S·cm^{-1} have been achieved for carbonized membranes – which is less than pure carbon materials (from 1.25·10 S·cm^{-1} for amorphous carbon to 3·10^{3} S·cm^{-1} for graphite in the basal plane)[17] but satisfactory enough for an electrode. For the carbonized sample, impedance spectroscopy reports a purely real value which is interpreted as its electrical resistance, without noticeable imaginary contribution. Note that the electrical conductivity of the membrane is usually higher when measured in the plane of the membrane. This can be explained by the fact that the electrospun membrane is made of fibers and the connectivity between the fibers is better ensured along their plane.

In order to estimate the bulk conductivity of the carbonized PAN reference, an electrospun carbon membrane was grinded by ball-milling (Ø = 2 cm, 80 rpm, 1 week) and pelletized under twice 8 tons. The pellet conductivity was then estimated by impedance spectroscopy at around 1 S·cm^{-1}.

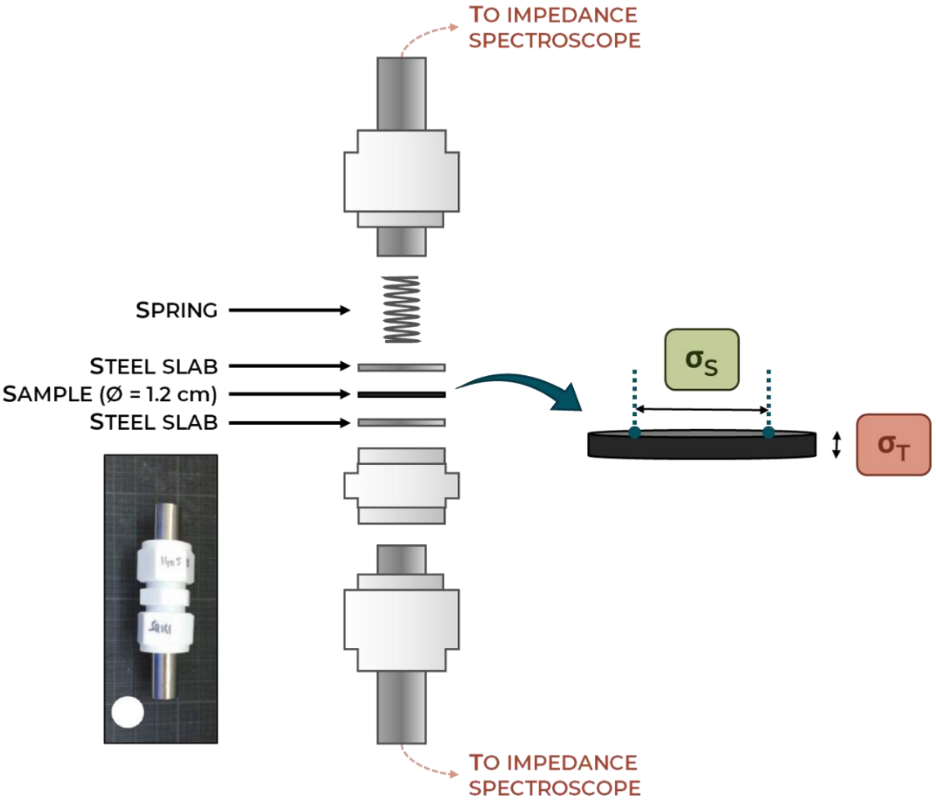

Heat treatment	**σ_S ($S \cdot cm^{-1}$)[a]**	**σ_T ($S \cdot cm^{-1}$)[b]**
Raw mat	$< 10^{-8}$	$< 10^{-12}$
Stabilized mat (280°C, Air)	$< 10^{-8}$	$< 10^{-12}$
Carbonized mat (940°C, Ar)	$\sim 10^{-1}$	$\sim 10^{-1}$ to 10^{-2}

Figure 2.17 – Swagelok cell setup & typical electrical conductivities σ_S & σ_T for the electrospun PAN membranes at different stages of the heat treatment (electrospun from a 10 wt% PAN in DMF solution, stabilized under air at 280°C, carbonized under argon at 940°C).

[a] Calculated from two-electrode setup measurements; maximum sensibility of 40 MΩ. [b] Calculated from impedance spectroscopy measurements; amplitude of 100 mV; maximum sensibility of ~ 10^8 Ω.

Electrochemical behavior: Capacitive and faradaic behaviors of the carbon membranes are evaluated by cyclic voltammetry (**Figure 2.19**) to check the efficiency of electrospun carbon membranes as an electrode. The measurements are conducted in a three electrodes configuration (Ag/AgCl, KCl saturated reference (Ref.), Pt wire counter electrode, and a carbon membrane working electrode), between -0.8 and +0.8 V vs. Ref. at various scan rates between 1 and 100 $mV \cdot s^{-1}$. The electrode dimensions are Ø = 1.4 cm, h = 157 µm and therefore S = 1.54 cm^2 and V = $2.42 \cdot 10^{-2}$ cm^3.

The capacitive response of the electrode is evaluated in a saline electrolyte (NaCl 150 mM in H_2O) and the faradaic response in the same electrolyte supplemented with 100 mM of $K_3[Fe(CN)_6]$.

In the saline electrolyte (**Figure 2.19.A**), a typical capacitive signal is indeed obtained. In these conditions, the polarized anode and cathode act as a condenser when positive and negative ions in the solution migrate respectively to the negatively and positively charges electrodes. This accumulation of charges Q (C) leads to the formation of a double layer of capacitance C (F) under the applied potential E (V), such as:

$$Q = C \cdot E \qquad \textbf{[2.1]}$$

When performing a cyclic voltammetry, E varies with time and the current i (A) is recorded. At the vertex potentials, the scan direction of E changes and the condenser discharge. Besides, the charge varies with the time t (s) such as:

$$Q = i \cdot t \qquad \textbf{[2.2]}$$

On the other hand, the capacitance C can be written as the product of the specific capacitance of the material κ ($F \cdot m^{-2}$) and the capacitive surface area A_c (m^2) such as:

$$C = \kappa \cdot A_c \qquad \textbf{[2.3]}$$

Using **[2.1]** and **[2.2]** we can then write with i_c (A) the capacitive current and v ($V \cdot s^{-1}$) the scan rate:

$$i_c = \frac{C \cdot E}{t} = C \cdot v \qquad \textbf{[2.4]}$$

And then by using **[2.3]**:

$$i_c = \kappa \cdot A_c \cdot v \qquad \textbf{[2.5]}$$

Tabulated values[18] give us a carbon specific capacitance $\kappa_{carbon} = 20\ \mu F \cdot cm^{-2}$ which let us calculate the high capacitive surface area of the system $A_c \approx 3.5\ m^2$, or $SSA_c \approx 1.6 \cdot 10^3\ m^2 \cdot g^{-1}$. This surface area correspond to the surface accessible for the small Na^+ and Cl^- ions. The specific surface area evaluated by the capacitance method is notably higher – albeit of the same order of magnitude – than the specific surface area measured by adsorption of N_2 ($SSA_{BET} \approx 470\ m^2 \cdot g^{-1}$). Nevertheless, the surface measured by capacitance represents the surface accessible to the electrolyte and is therefore more adapted to an aqueous electrode description[19]. It will hereafter be used to determine the specific surface areas of the electrospun carbon electrodes.

The addition of 100 mM of potassium ferricyanide (**Figure 2.19.B**) leads to a faradaic signal showing both oxidation and reduction peaks up to 20 $mV \cdot s^{-1}$, corresponding to the redox reaction $[Fe(CN)_6]^{3-} + e^- = [Fe(CN)_6]^{4-}$. These currents correspond to the flow of electrons triggered by the redox reaction occurring at the surface of the electrode – here the redox reaction of the couple $[Fe(CN)_6]^{3-}/[Fe(CN)_6]^{4-}$, and are expected to depend on the nature of the redox species, the CV scan rate, the nature of the electrode and its surface reactivity. These electrochemical phenomena are described by the Nernst equation – derived from the standard changes in the Gibbs free energy associated with a redox reaction.

For a redox half-reaction $x \cdot Ox + n \cdot e^- = y \cdot Red$, the Nernst equation can then be written, with R ($J \cdot K^{-1} \cdot mol^{-1}$) the ideal gas constant, T (K) the temperature and F ($C \cdot mol^{-1}$) the Faraday constant:

$$E = E^0 + \left(\frac{RT}{nF}\right) \cdot \ln\left(\frac{[Ox]^x}{[Red]^y}\right) \qquad \textbf{[2.6]}$$

The kinetics of the reaction are described by the Butler–Volmer equation:

$$j = j_0 \cdot \left\{ \exp\left[\frac{\alpha nF}{RT} \cdot (E - E_{eq})\right] - \exp\left[-\frac{(1-\alpha) \cdot nF}{RT} \cdot (E - E_{eq})\right] \right\} \qquad \textbf{[2.7]}$$

Here j (A·m^{-2}) is the current density, j_0 (A·m^{-2}) the exchange current density, E (V) the electrode potential, E_{eq} (V) its equilibrium potential and α the dimensionless charge transfer coefficient, describing the preferred evolution of the redox system – toward reduction or oxidation.

This equation can be written as a function of the activation overpotential $\eta = E - E_{eq}$:

$$j = j_0 \cdot \left\{ \exp\left[\frac{\alpha nF\eta}{RT}\right] - \exp\left[-\frac{(1-\alpha) \cdot nF\eta}{RT}\right] \right\} \qquad \textbf{[2.8]}$$

Three types of electrochemical behaviors and cyclic voltammograms shapes can be identified depending on the charge transfer rate at the surface of the electrode and the diffusion rate of the redox species from the electrolyte to the electrode (**Figure 2.18**)[20].

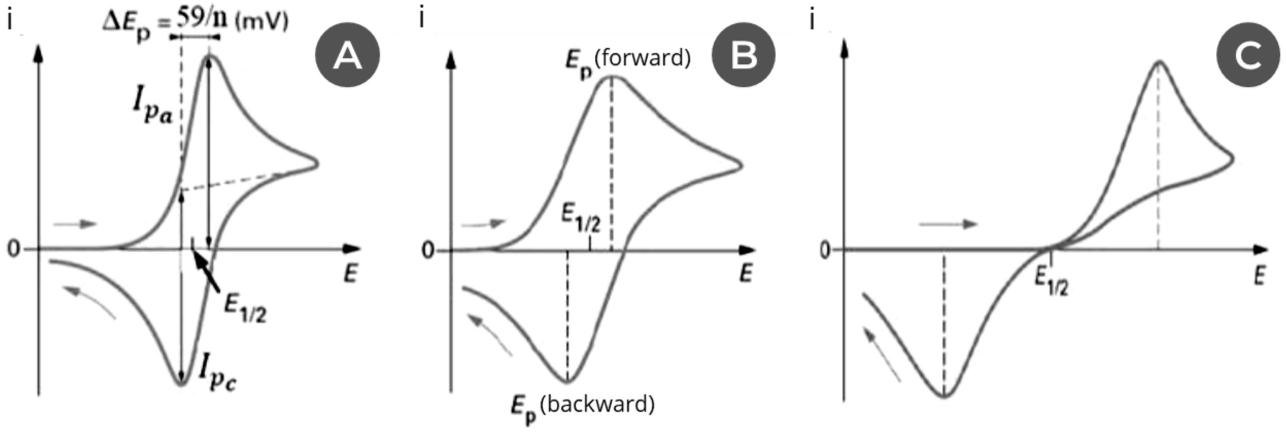

Figure 2.18 – Usual cyclic voltammogram shapes according to the charge transfer and diffusion rates. (A) Reversible; (B) Quasi-reversible; (C) Quasi-irreversible.

Adapted from Trémillon, 1993

- When the charge transfer is faster than the diffusion, the redox couple is fast and reversible (**Figure 2.18.A**). The peaks are ideally narrow and symmetrical, and their current intensity is linked to the scan rate and the faradaic surface as described by the Randles–Sevcik equation:

$$i_p = 0.4463 \cdot nFA_fC \cdot \left(\frac{nFvD}{RT}\right)^{\frac{1}{2}} \qquad \textbf{[2.9]}$$

Here A_f (m^2) is the faradaic surface area – which represents the surface accessible to the redox probes during the reaction –, C ($mol \cdot m^{-3}$) is the redox species concentration and D ($m^2 \cdot s^{-1}$) their diffusion coefficient.

The potential difference between the two peaks is independently of the scan rate $\Delta E_p = \frac{59}{n}$ mV at 25°C, where n is the number of electron exchanged during the reaction.

- When the charge transfer is slow but the reaction is reversible, the system is quasi-reversible (**Figure 2.18.B**). i_p increases with v but does not follow the Randles–Sevcik law, and is generally inferior to the value predicted by it. In this case, $\Delta E_p > \frac{59}{n}$ mV.
- Eventually when the charge transfer is slower than the mass transfer, the system is quasi-irreversible (**Figure 2.18.C**). The maximum peak intensity is proportional to the square root of the scan rate such as:

$$i_p = 0.4968 \cdot nFA_fC \cdot \left(\frac{\alpha nFvD}{RT}\right)^{\frac{1}{2}} \qquad \textbf{[2.10]}$$

Here, α is the charge transfer coefficient introduced in the Butler–Volmer equation.

For the electrospun carbon membrane, the shape of the cyclic voltammograms accounts for a quasi-irreversible reaction. This is confirmed by the increase of the potential difference between the oxidation and reduction peaks as function of the scan rate from around 0.25 V at 1 $mV \cdot s^{-1}$ up to 0.70 V at 10 $mV \cdot s^{-1}$ (**Figure 2.19.D**). The current densities of the oxidation and reduction peaks are estimated from the cyclic voltammograms (**Figure 2.19.B**) and their evolution as a function of the square root of the scan rate have been plotted (**Figure 2.19.C**). It evolves proportionally to the square root of the scan rate as expected for a quasi-irreversible probe. This quasi-irreversibility can be linked to the hydrophobicity and tortuosity of the architecture of the electrospun carbon membrane fibers, hindering the charge transfer of the redox probe.

With a diffusion coefficient[21] of $D_{ferrocyanide} = 0.667 \cdot 10^{-5}\ cm^2 \cdot s^{-1}$, and a charge transfer coefficient[22] of α = 0.23 the equation **[2.10]** let us estimate the faradaic surface of the electrospun carbon membrane. A_f is around 0.13 m^2, which represents only 3.7 % of the capacitive surface area. This results may be explained by the diffusion of the redox probe though the carbon electrospun membrane.

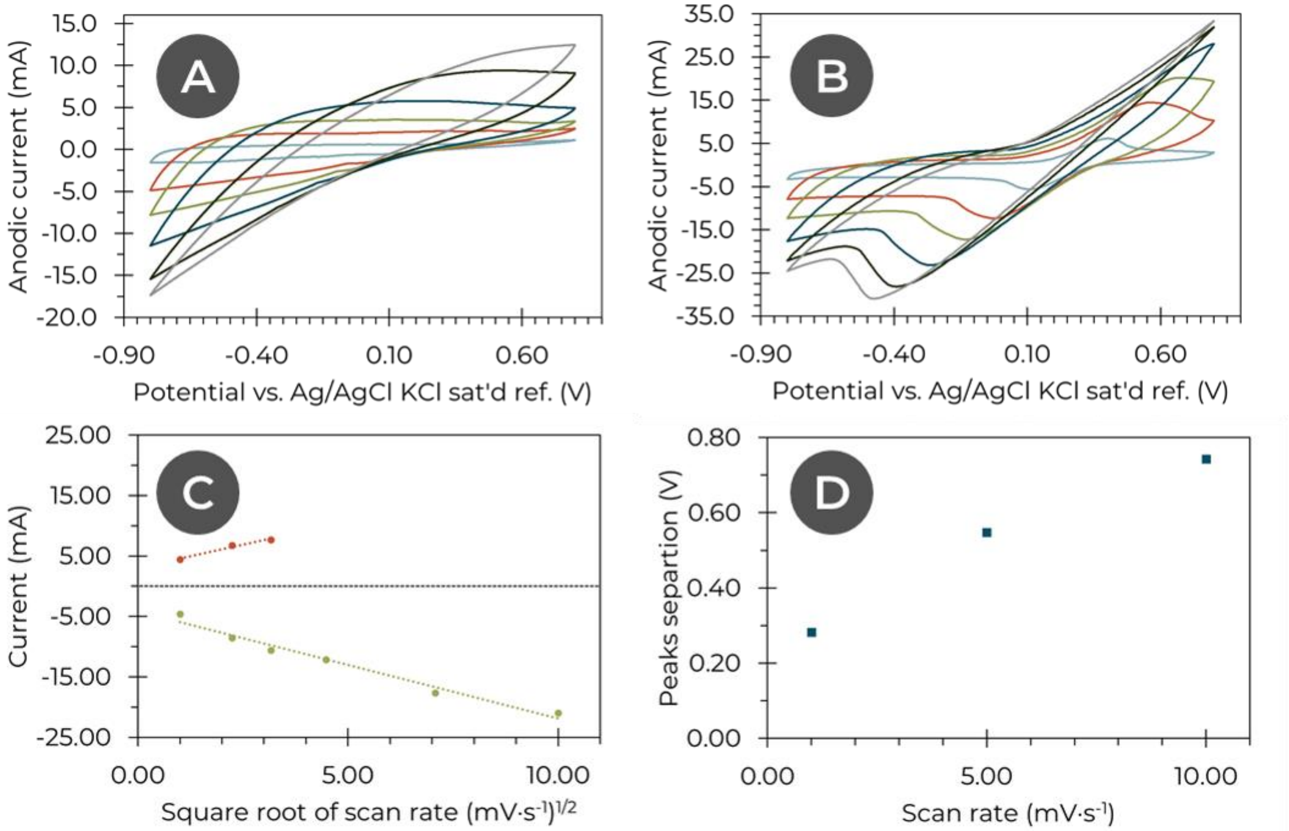

Figure 2.19 – Electrochemical characterization of an electrospun carbon membrane (electrospun from a 10 wt% PAN in DMF solution, stabilized under air at 280°C, carbonized under argon at 940°C, thickness of 157 µm). (A) Cyclic voltammetry of the capacitive response (NaCl 150 mM in H_2O); (B) Cyclic voltammetry of the faradaic response (NaCl 150 mM + $K_3[Fe(CN)_6]$ 100 mM in H_2O). Scan rate varying from 1 to 100 mV·s^{-1} (– 1 mV·s^{-1}, – 5 mV·s^{-1}, – 10 mV·s^{-1}, – 20 mV·s^{-1}, – 50 mV·s^{-1}, – 100 mV·s^{-1}). (C) Randles–Sevcik plot based on (B) for the $[Fe(CN)_6]^{4-}$ oxidation (•) & $[Fe(CN)_6]^{3-}$ reduction (•); (D) Evolution of the potential difference between oxidation and reduction peaks as a function of the scan rate.

Finally, the characterization of the electrospun carbon membrane confirms its suitability as an electrode even if the faradaic surface and reversibility of the system are limited by the tortuosity of the system at higher scan rates. Likewise, the current densities and electron transfer rates expected from the bacteria involved in an MFC should not be highly impeded by these limitations.

Mechanical properties: The electrospun carbon microfibers membranes are self-standing, but can be a bit brittle. Mechanical strength however improves with the thickness, and membranes thicker than 200-300 µm are easy to handle and to cut.

All these characterizations point out a good conversion of the PAN electrospun fibers to a self-standing, conducting mat of carbon microfibers. Thanks to its relatively simple synthesis process, the colonization process of these carbon electrospun membranes by electroactive bacteria will be conducted with the fibers first stabilized at 280°C under air then carbonized at 940°C under argon. In the next paragraphs, the carbon membrane will be called the “electrospun carbon electrode”.

2.3. Bioanode colonization process

Once synthesized and characterized, these electrospun carbon electrodes must be colonized by electroactive bacteria and be integrated into a microbial fuel cell reactor.

The model exoelectrogenic bacterial strain used in the subsequent colonization protocol is *Shewanella oneidensis* CRBIP17.141 and has been provided by the *Centre de Ressources Biologiques de l'Institut Pasteur* (CRBIP). Additional insights over more complex bacteria consortia will eventually be presented in Chapter 5 using wastewaters provided by the *Syndicat Interdépartemental pour l'Assainissement de l'Agglomération Parisienne* (SIAAP).

In order to determine the phylogenic vicinity of the provided strain among other *Shewanella* spp., a 16S rRNA (16S ribosomal RNA gene) sequence comparison between the *Shewanella oneidensis* CRBIP17.141 sequence provided by the *Institut Pasteur* and the National Center for Biotechnology Information (NCBI) 16S rRNA (Bacteria and Archaea) database through the BLASTN 2.9.0+ algorithm[23] was performed. The analysis shows a significant identity between the sample and references from the genus *Shewanella* (**Figure 2.20**). In particular, an identity of 99.03 % of bases was found between *Shewanella oneidensis* CRBIP17.141 and the *Shewanella oneidensis* MR-1 reference, and 99.45 % with the *Shewanella xiamenensis* strain.

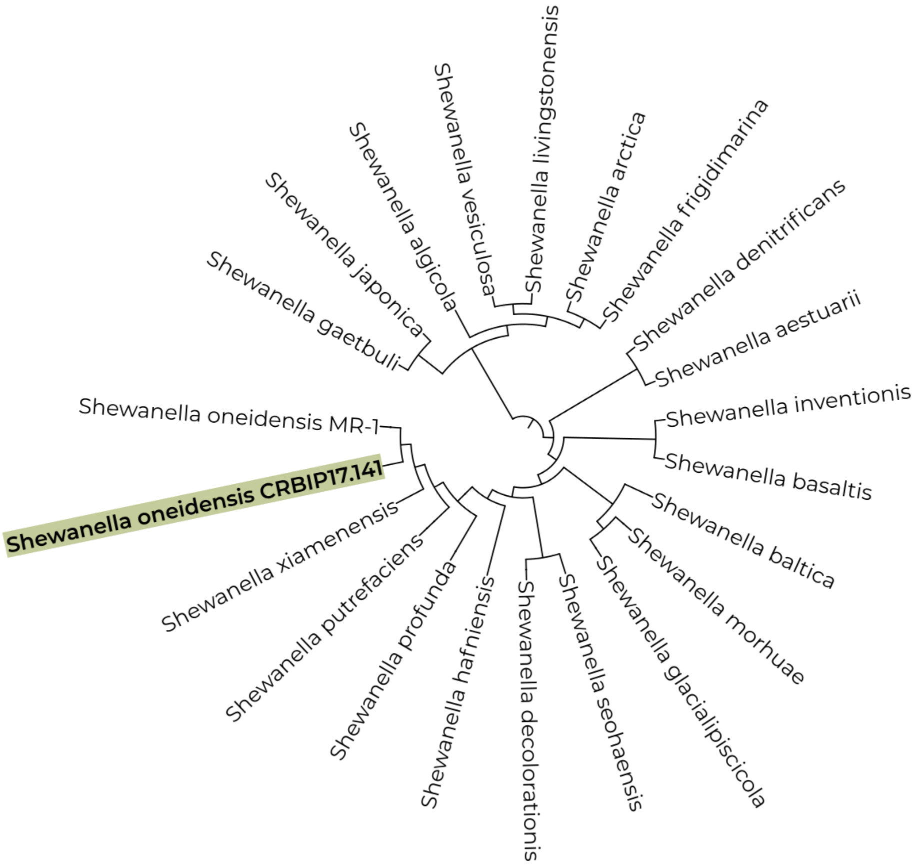
Shewanella gaetbuli
Shewanella japonica
Shewanella algicola
Shewanella vesiculosa
Shewanella livingstonensis
Shewanella arctica
Shewanella frigidimarina
Shewanella denitrificans
Shewanella aestuarii
Shewanella inventionis
Shewanella basaltis
Shewanella baltica
Shewanella morhuae
Shewanella glacialipiscicola
Shewanella seohaensis
Shewanella decolorationis
Shewanella hafniensis
Shewanella profunda
Shewanella putrefaciens
Shewanella xiamenensis
Shewanella oneidensis CRBIP17.141
Shewanella oneidensis MR-1

Kingdom	Bacteria
Phylum	Proteobacteria
Class	Gammaproteobacteria
Order	Alteromonadales
Family	Shewanellaceae[24]
Genus	*Shewanella*[25]

Figure 2.20 – Phylogenetic neighborhood of *Shewanella oneidensis* CRBIP17.141. Strains shown present at least 95 % nucleotide identity with the 16S rRNA CRBIP17.141 sequence according to the BLAST® algorithm.

Bacteria from the genus *Shewanella* have been extensively shown in the literature to exhibit an exoelectrogenic behavior[26], and *Shewanella oneidensis* MR-1 has in particular been widely studied as a model organism for microbial fuel cell setups[27],[28].

2.3.1. Bacterial culture

Shewanella oneidensis is a facultative anaerobe, able to degrade and thrive on a wide range of organic nutrients such as glucose and lactate. The following growth media and bacterial culture protocols are based on the work of Bretschger[27] and Baron[26],[29].

2.3.1.1. Growth media

Lysogeny broth (LB) Lennox medium (dry medium purchased from Sigma-Aldrich): 10 $g{\cdot}L^{-1}$ tryptone, 5 $g{\cdot}L^{-1}$ yeast extract, 5 $g{\cdot}L^{-1}$ NaCl are dissolved in Milli-Q water and adjusted at pH = 7. The medium is sterilized by autoclaving at 120°C for 20 minutes.

MR-1 minimal medium (chemicals purchased from Sigma-Aldrich): 0.46 $g{\cdot}L^{-1}$ NH_4Cl, 0.225 $g{\cdot}L^{-1}$ K_2HPO_4, 0.057 $g{\cdot}L^{-1}$ $MgSO_4{\cdot}7H_2O$, 0.225 $g{\cdot}L^{-1}$ KH_2PO_4, 0.225 $g{\cdot}L^{-1}$ $(NH_4)_2SO_4$ are dissolved in Milli-Q water. The solution is supplemented with solutions of trace elements (3.0 $g{\cdot}L^{-1}$ EDTA-$Na_2{\cdot}2H_2O$, 1.1 $g{\cdot}L^{-1}$ $FeSO_4{\cdot}7H_2O$, 0.19 $g{\cdot}L^{-1}$ $CoCl_2{\cdot}6H_2O$, 0.042 $g{\cdot}L^{-1}$ $ZnCl_2$, 0.024 $g{\cdot}L^{-1}$ $NiCl_2{\cdot}6H_2O$, 0.018 $g{\cdot}L^{-1}$ $Na_2MoO_4{\cdot}2H_2O$, 0.30 $g{\cdot}L^{-1}$ H_3BO_4, 0.002 $g{\cdot}L^{-1}$ $CuCl_2{\cdot}2H_2O$, 0.050 $g{\cdot}L^{-1}$ $MnCl_2{\cdot}4H_2O$ dissolved in Milli-Q water, adjusted to pH = 6.5, autoclaved at 120°C for 20 minutes) and selenite (0.50 $g{\cdot}L^{-1}$ NaOH, 0.003 $g{\cdot}L^{-1}$ $Na_2SeO_3{\cdot}5H_2O$, 0.004 $g{\cdot}L^{-1}$ $Na_2WO_4{\cdot}2H_2O$ in Milli-Q water, autoclaved at 120°C for 20 minutes), each at 0.1 % in volume. The resulting medium is then sterilized by autoclaving at 120°C for 20 minutes and supplemented with solutions of vitamins (4 $mg{\cdot}L^{-1}$ 4-aminobenzoic acid, 1 $mg{\cdot}L^{-1}$ D(+)-biotin, 10 $mg{\cdot}L^{-1}$ nicotinic acid, 5 $mg{\cdot}L^{-1}$ calcium D-pantothenate, 10 $mg{\cdot}L^{-1}$ pyridoxamine dihydrochloride, 10 $mg{\cdot}L^{-1}$ thiaminium dichloride, 50 $mg{\cdot}L^{-1}$ riboflavin dissolved in Milli-Q water, sterilized by ultrafiltration on a 0.22 µm membrane) and amino acids (2 $g{\cdot}L^{-1}$ L-glutamic acid, 2 $g{\cdot}L^{-1}$ L-arginine, 2 $g{\cdot}L^{-1}$ DL-serine, dissolved in Milli-Q water, sterilized by ultrafiltration on a 0.22 µm membrane), each at 0.1 % in volume. The pH is ultimately adjusted to 7 and the medium sterilized by ultrafiltration on a 0.22 µm membrane.

MR-1/Lactate (MR-1/L) medium: MR-1 minimal medium supplemented with 30 mM of sodium lactate (Sigma-Aldrich).

MR-1/Lactate-Fumarate (MR-1/LF) medium: MR-1 minimal medium supplemented with 30 mM of sodium lactate and 30 mM of sodium fumarate (Sigma-Aldrich).

The lactate ion is used by *S. oneidensis* as an electron donor, and the fumarate ion as a final electron acceptor in anaerobic conditions.

2.3.1.2. Culture protocol

Strain conservation: The *Shewanella oneidensis* CRBIP17.141 aliquot provided by the CRBIP is stored at -80°C in a glycerol stock (50 vol% overnight bacterial culture in LB medium, 50 vol% of 1:1 (w/w) glycerol in sterilized Milli-Q water).

Bacterial pre-culture: 15 mL of oxic sterile LB medium is inoculated with a fraction of the thawed aliquot and cultivated for 24 hours at 30°C and 150 rpm in an incubator.

Bacterial culture: 50 mL of oxic sterile MR-1/LF medium is inoculated with 1 mL of the pre-culture medium in sterile flasks for 8 hours at 30°C and then overnight at 21°C. The cell density is then determined by measuring the optical density of the cultured medium at 600 nm (OD_{600}) with a spectrophotometer. All subsequent changes in medium are done by centrifuging the cells at 5000 g for 20 minutes at 4°C before resuspending them in the desired conditions.

The optical density is proportional to the density of cells in the medium which evolves during the time upon colonization of a new medium without nutrients renewal through four phases (**Figure 2.21**)[30].

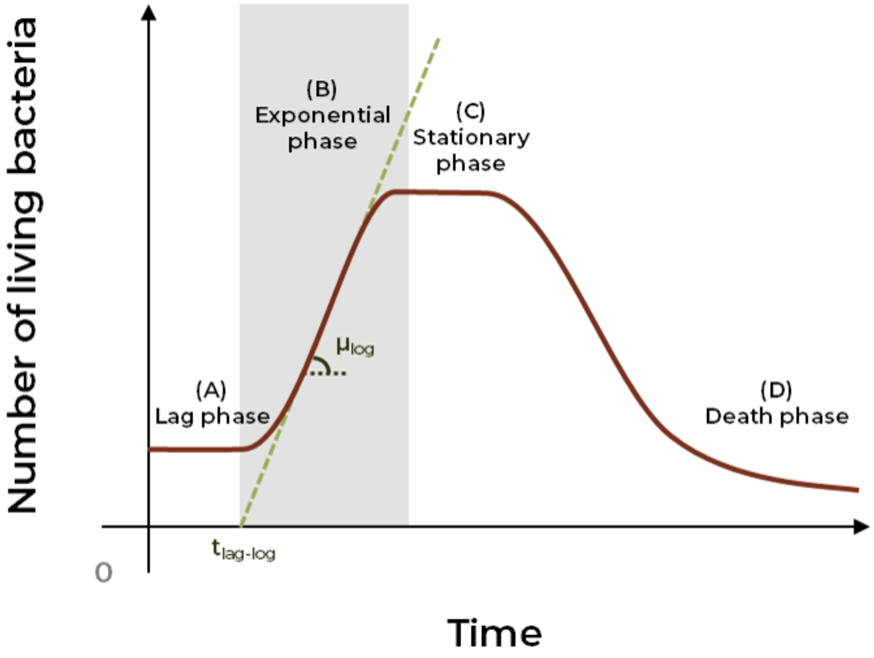

Figure 2.21 – Bacterial growth curve model

(A) The lag phase is characterized by a lack of cell division as the bacteria adapt to their new medium. During this phase the metabolism of the microorganisms is not dormant, but they are not able to divide yet;

(B) During the exponential phase (or logarithmic phase), the cell population is doubling at a constant rate μ_{log} depending on the bacterial strain and medium nature. The growth cannot continue indefinitely however as the medium eventually become depleted of nutrients and concentrated with cellular wastes;

(C) As the medium becomes depleted of nutrients and enriched with inhibiting wastes the death rate of the bacteria equals the growth rate and give rise to a stable stationary phase;

(D) The number of bacteria decreases as the lack of nutrients or other noxious conditions lead to their deaths.

Mutations often accumulate during the stationary phase, henceforth to ensure results reproducibility, bacteria from the culture must ideally be taken from the exponential phase.

The correlation between the optical density and the colony-forming unit (cfu) per volume can be evaluated by spreading a diluted bacterial culture sampled at a known optical density on LB-agar plates. After incubation at 37°C for 24 hours, the number of colonies can be directly linked to the number of viable bacteria in the sample. In the culture conditions, the number of bacteria as a function of time in the medium can therefore be evaluated (**Figure 2.22**)[14].

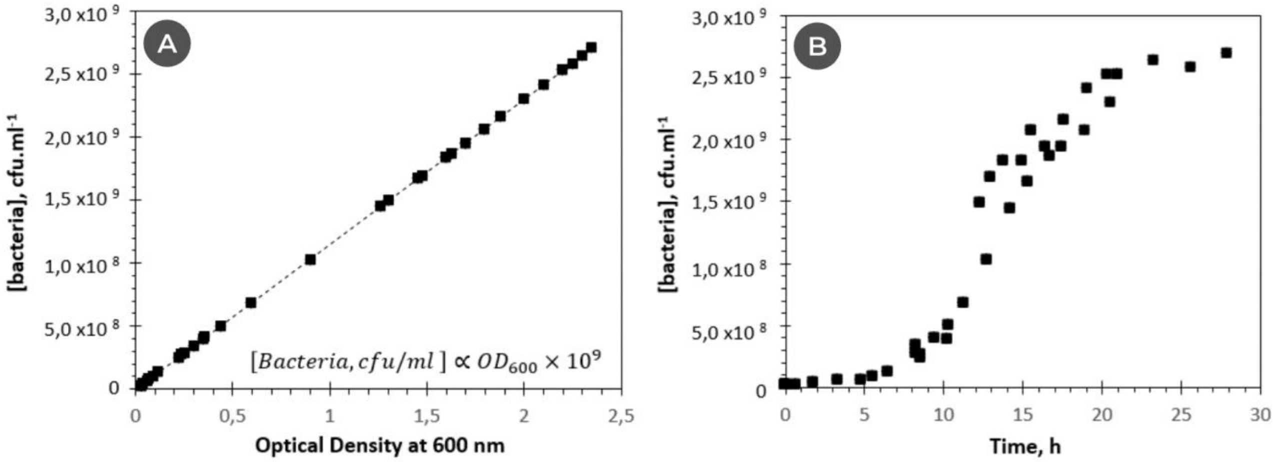

Figure 2.22 – Correlation between the optical density at 600 nm and the concentration of bacteria. (A) Linear correlation between the concentration of viable bacteria (colony-forming unit, cfu) and OD_{600}. (B) Growth curve of *Shewanella oneidensis* in MR-L/F in aerobic conditions at 30°C.

From Pinto *et al.*, 2016

2.3.1.3. MFC integration & electrochemical characterization

Colonization of the electrospun carbon electrodes by electroactive bacteria is required before the microbial fuel cell starts to produce current. This colonization may either be conducted in situ or ex situ. In situ colonization was first performed. A raw sterilized electrospun carbon electrode was mounted into a sterile lab-scale MFC reactor (**Figure 2.23**) (sterilization carried out by autoclaving at 120°C for 20 minutes).

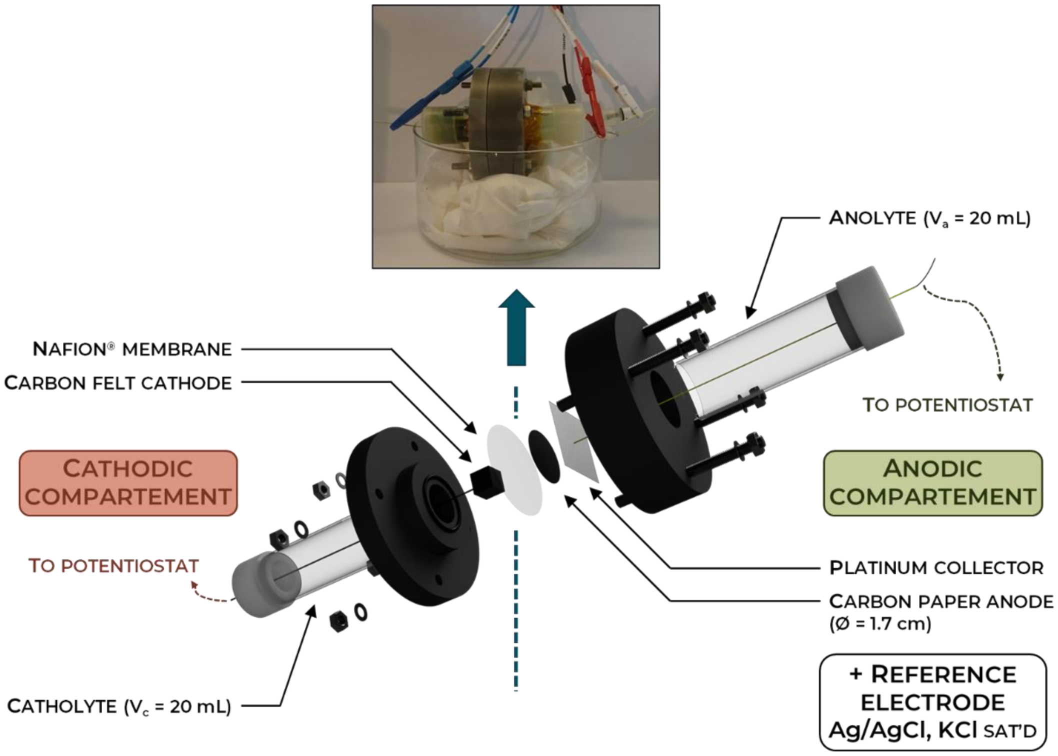
ANOLYTE (V_a = 20 mL)
NAFION® MEMBRANE
CARBON FELT CATHODE
TO POTENTIOSTAT
CATHODIC COMPARTEMENT
ANODIC COMPARTEMENT
TO POTENTIOSTAT
PLATINUM COLLECTOR
CARBON PAPER ANODE
(Ø = 1.7 cm)
+ REFERENCE ELECTRODE Ag/AgCl, KCl SAT'D
CATHOLYTE (V_c = 20 mL)

Figure 2.23 – Lab-scale two-compartment microbial fuel cell setup

The lab-scaled reactor is constituted of two 20 mL anodic and cathodic compartments, separated by a pretreated Nafion® proton exchange membrane (Nafion® NRE-212, 50 µm thick, Sigma-Aldrich) used to prevent catholyte and anolyte to mix up and bacteria to leak to the cathodic side while letting protons flow between the two sides. The Nafion® is pretreated with concentrated HNO_3 overnight and subsequently rinsed with distilled water until its neutralization and is sterilized under UV light for 30 minutes.

The electrospun carbon electrode is sandwiched between the Nafion® membrane and a platinum mesh current collector, while the cathode consists of 1 cm^3 of carbon felt. The catholyte is made up of 150 mM of NaCl (supporting electrolyte) and 100 mM of $K_3[Fe(CN)_6]$. For in situ colonization, the anodic compartment is filled with 20 mL of fresh MR1/L medium inoculated at OD_{600} = 0.7 with *S. oneidensis* from the exponential phase of the bacterial culture as described before (OD_{600} ≈ 1.6). The two compartments are sealed with silicon folding skirt stoppers while ensuring as little air as possible is trapped inside. A sterilized Ag/AgCl, KCl saturated reference electrode is inserted through the stopper of the anodic compartment (careful sterilization with 70 % ethanol). The reactor assembly is conducted under sterile conditions in a biosafety cabinet. Reference electrode, anode (electrospun carbon electrode) and cathode (carbon felt) are connected to a Bio-Logic VSP potentiostat (Claix, France) controlled by the software EC-Lab® respectively as reference, working electrode and counter-electrode.

The anode potential is poised at +0.3 V vs. the reference electrode as it has been shown to favor bacterial development and extracellular electron transfer (EET)[31]–[34]. The resulting current is monitored as a function of time by chronoamperometry (CA). Current density j (µA·cm^{-2}) is then calculated by normalization of the current i at steady state (> 2 hours) to the anode area ($Ø_{anode}$ = 1.7 cm; $A_{anode, geometrical}$ ≈ 2.27 cm^{2}). Cyclic voltammograms (CV) are subsequently recorded in the range -0.7 to +0.7 V vs. the reference electrode (scan rate: 1 mV·s^{-1}) every 24 hours to identify the electron transfers between bacteria and anode through the redox reaction. When a stable maximum in oxidation current due to EET is reached, polarization of the anode is stopped for 16 hours to let the electrode potential stabilize. The working electrode and counter electrode channels are reversed on the software. Polarization and power curves are subsequently recorded by applying an incremental series of negative currents to the cathode, for 20 seconds, while the emf ($\Delta E = E_{cathode} - E_{anode}$) is recorded (at the 10th second). Polarization ($\Delta E = f(j)$) and power (P (mW·cm^{-2}) $= \Delta E \cdot j = j^2 \cdot R_{int} = f(j)$, with R_{int} the internal resistance) curves are then plotted. The anolyte is recharged with 1 mmol of sodium lactate every 4 days to ensure that there is no carbon source shortage for the bacteria. All the experiments are conducted at 21°C.

First of all, the electrochemical behavior of the MFC in abiotic conditions is acquired with sterile MR1-L medium as the anolyte (**Figure 2.24**) as a reference.

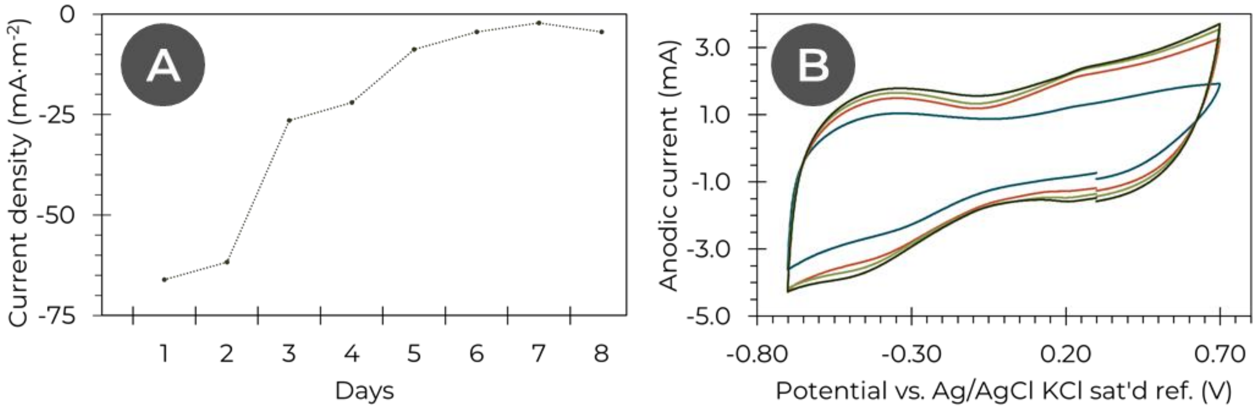

Figure 2.24 – Electrochemical characterization of a control two-compartment MFC including a sterilized electrospun carbon electrode polarized at +0.3 V vs. the reference (electrospun from a 10 wt% PAN in DMF solution, stabilized under air at 280°C, carbonized under argon at 940°C, thickness of 254 µm). (A) Evolution of the average current density. (B) Evolution of cyclic voltammetry as a function of time (– 1st day, – 2nd day, – 3rd day, – 4th day); sweep rate of 1 mV·s^{-1}; 3 cycles are acquired, here is the second one. Current and power are normalized by the geometric surface area of the electrospun carbon electrode ($Ø_{anode}$ = 1.7 cm; $A_{anode, geometrical}$ ≈ 2.27 cm^{2}). The anolyte is MR1-L medium; the catholyte is 150 mM of NaCl (supporting electrolyte) and 100 mM of $K_3[Fe(CN)_6]$.

Only a slightly negative current is measured as a function of time (**Figure 2.24.A**). The cyclic voltammetry (**Figure 2.24.B**) shows a pure capacitive behavior with no electrochemical response corresponding to the oxidation/reduction of the lactate. This is coherent since the electrochemical lactate oxidation requires a catalyst such as a transition metal, enzyme or microorganism. This is linked to the high activation energy for the lactate/pyruvate couple. No polarization curve is measured as the system cannot oxidize any reduced compound in the MR1-L medium.

This experiment will be used as a reference and will be compared to the characterization of the in situ colonized electrospun carbon electrode (**Figure 2.25**).

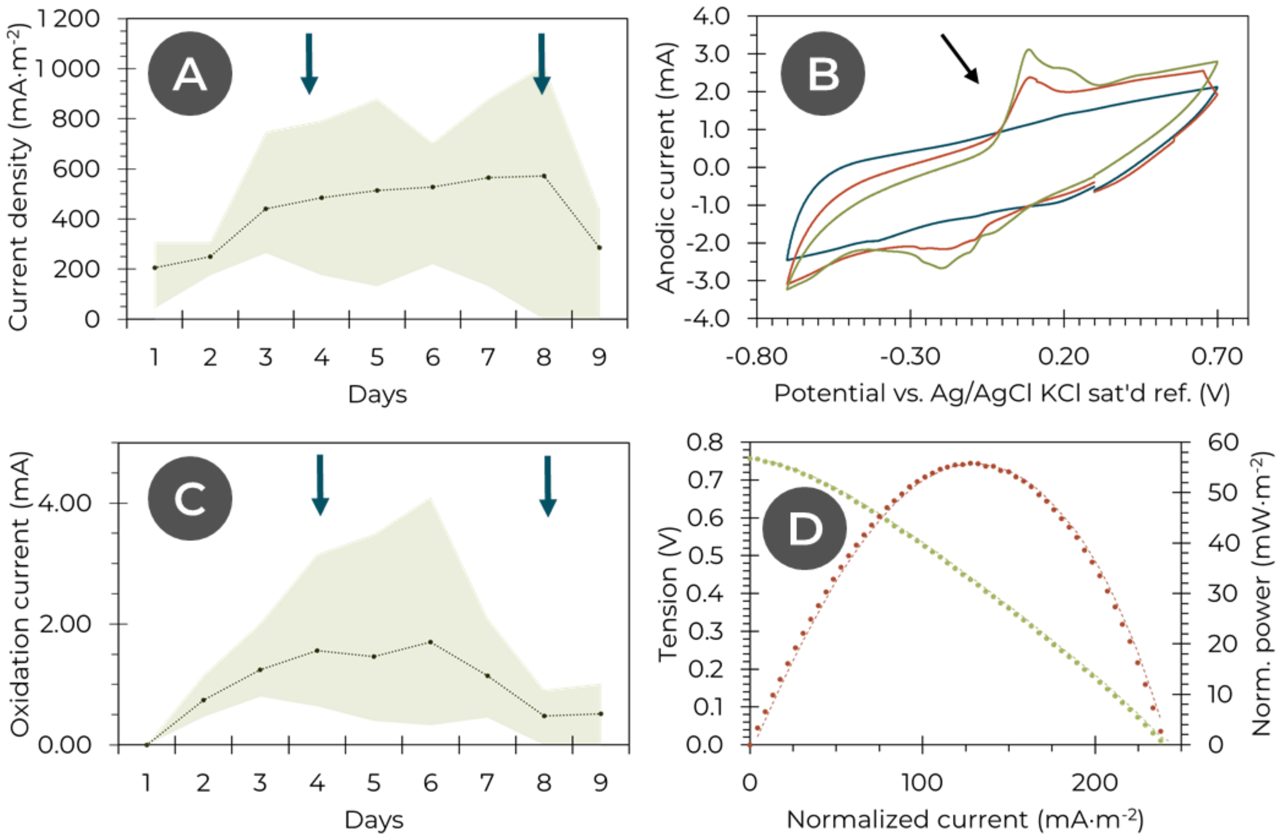

Figure 2.25 – Electrochemical characterization of a two-compartment MFC including an electrospun carbon electrode polarized at +0.3 V vs. the reference (electrospun from a 10 wt% PAN in DMF solution, stabilized under air at 280°C, carbonized under argon at 940°C) colonized in situ as a function of time. (A) Evolution of the average current density; blue arrows indicate addition of 1 mmol of sodium lactate; the green zone represents maximum and minimum values; N = 3. (B) Evolution of cyclic voltammetry as a function of time (– 1st day, – 2nd day, – 3rd day); sweep rate of 1 mV·s^{-1}; 3 cycles are acquired, here is the second one; thickness of 254 µm. (C) Evolution of the average current corresponding to the peak shown by the arrow on the CV; blue arrows indicate addition of 1 mmol of sodium lactate; the green zone represents maximum and minimum values; N = 3. (D) Polarization (•) and power (•) curves of the MFC on the 6th day. Current and power are normalized by the geometric surface area of the electrospun carbon electrode ($Ø_{anode}$ = 1.7 cm; $A_{anode, geometrical}$ ≈ 2.27 cm^2). The anolyte is MR1-L medium; the catholyte is 150 mM of NaCl (supporting electrolyte) and 100 mM of $K_3[Fe(CN)_6]$.

The average current density (**Figure 2.25.A**) starts around 200 mA·m^{-2} on the first day and increases sharply on the third day to a value of 450 mA·m^{-2}. It then stabilizes for a few days at this value before starting to decrease at around day 8.

Cyclic voltammetry (**Figure 2.25.B**) shows a quasi-capacitive response on the first day of experiment, hinting little redox activity of the bacteria. From the second day onwards a wide oxidation peak starts to appear between -0.05 and +0.3 V vs. Ag/AgCl KCl saturated reference (Ref.), with a collection of associated reduction peaks between -0.5 and -0.1 V vs. Ref. All three voltammograms are similar and the second one will be plotted hereafter and in future electrochemical characterization of MFCs. The ΔE between the oxidation and reduction events is very large, demonstrating an irreversibility phenomenon. This could be related to the complexity of the bacterial electron transport pathway[35]. The oxidation peak is very large and could be related to multiple redox species, and in particular to multiple hemes in cytochrome proteins, known to be involved in EET[36],[37]. It occurs in a potential range that is usually associated to direct electron transfer[34],[38]. This oxidation peak seems in particular linked to the MtrC/OmcA multi-heme cytochrome terminal protein complex of the Mtr respiration pathway – used to reduce Fe^{III} oxides in naturally-occurring *Shewanella oneidensis* strains (**Figure 2.26**)[39]–[42].

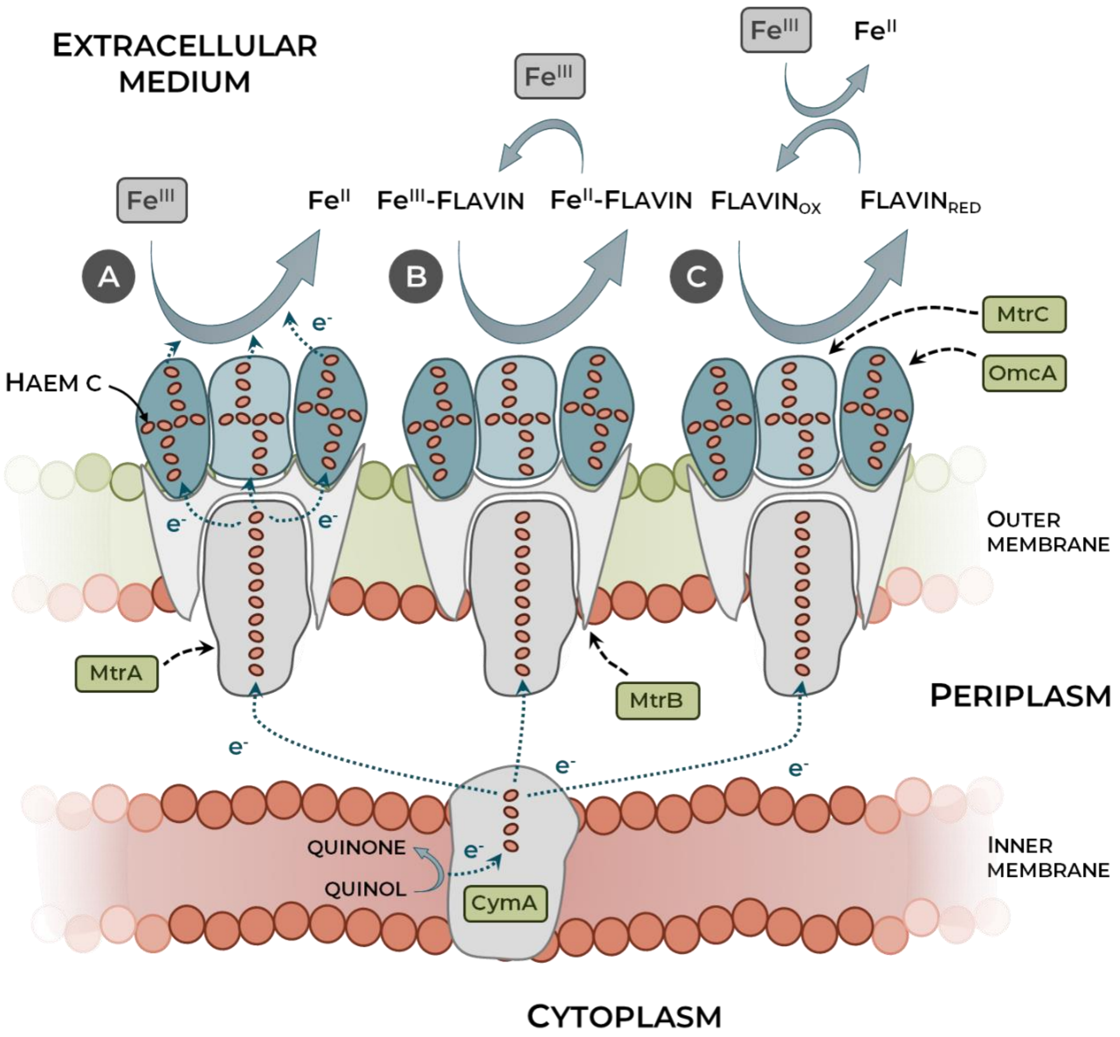
EXTRACELLULAR MEDIUM
Fe^{III}
Fe^{II}
Fe^{III}
Fe^{II}
Fe^{III}
Fe^{III}-FLAVIN
Fe^{II}-FLAVIN
FLAVIN$_{OX}$
FLAVIN$_{RED}$
A
B
C
e$^-$
HAEM C
MtrC
OmcA
OUTER MEMBRANE
MtrA
MtrB
PERIPLASM
QUINONE
QUINOL
CymA
INNER MEMBRANE
CYTOPLASM

Figure 2.26 – Overview of the Mtr respiration pathway in *Shewanella oneidensis* MR-1. Proteins known to be directly involved in the natural extracellular reduction of Fe^{III} oxides – or the anode in an MFC – include (1) the inner membrane tetrahaem cytochrome c (*c*-Cyt) CymA homologue of the NapC/NirT family of quinol deshydrogenases; (2) the periplasmic decahaem *c*-Cyt MtrA; (3) the porin-like outer membrane protein MtrB & (4) the outer membrane decahaem *c*-Cyts MtrC and OmcA mediating the EET. Together they transfer electrons from the quinone/quinol pool in the inner membrane – originating from upstream respiration – to the periplasm and then either directly or through other periplasmic proteins to the outer membrane where the EET is performed by MtrC and OmcA. This two proteins can transfer electrons (A) directly to the surface of the final electron acceptor; (B) by transferring electrons to flavin-chelated Fe^{III} or (C) to oxidized flavin mediators.

Adapted from Shi *et al.*, 2009 & Shi *et al.*, 2012

The MtrABC/OmcA complex is thus believed to be involved in *S. oneidensis* both in direct transmembrane EET and in the pili electrical conductivity and redox behavior. Recent reports henceforth show that these pili might be outer membrane and periplasmic extensions of *S. oneidensis* cells, functionalized with MtrABC/OmcA (**Figure 2.27**)[43]. It is however difficult to assign the electrochemical behavior observed here to either of these transfer mechanisms on the sole basis of cyclic voltammetry. The direct electron transfer reported is most likely a combination of these pathways.

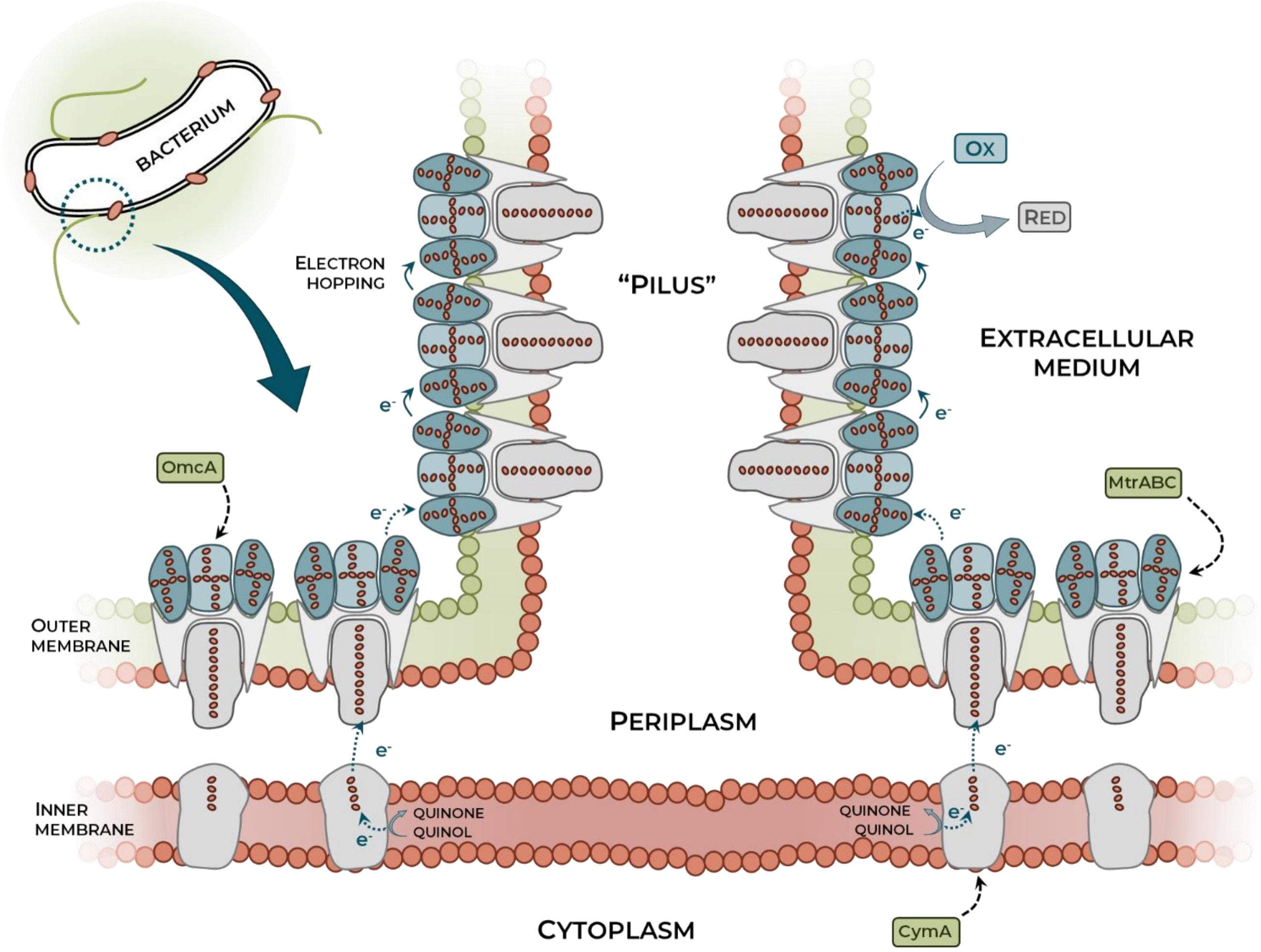

Figure 2.27 – Assumed architecture of the *Shewanella oneidensis* MR-1 conductive pilus. The so-called pilus or nanowire would be an outer membrane and periplasmic extension including the multiheme cytochromes complexes MtrABC/OmcA responsible for direct extracellular electron transfer.

Adapted from Pirbadian *et al.*, 2014

Note that indirect electron transfer through riboflavin redox mediators would have been reported near -0.45 V vs. Ag/AgCl, KCl saturated reference[38]. Additionally, cyclic voltammetry at higher scan rates than 5 $mV \cdot s^{-1}$ show almost clear redox peaks, hinting for a non-diffusion controlled reaction which is coherent with the direct electron transfer mentioned. The intensity of the oxidation peak increases from the first to the sixth day (**Figure 2.25.C**), which is understandable as bacteria continuously grow and adapt to their new environment and use it as an electron acceptor. From the sixth day, cyclic voltammetry start to be difficult to acquire on some setups and the EET-associated oxidative current starts to drop.

We hypothesize that this decrease in electrochemical activity may be linked to two phenomena. Firstly, the bacterial overgrowth may impede the nutrients and bacterial waste diffusion through the biofilm. This putative drop in nutrient diffusion could then be interpreted as a drop in ionic conductivity of the material. Alternatively, this may be linked to the lower electrical conductivity and electrochemical activity of the biofilm compared with the pristine carbon fibers surface.

After stopping anode polarization, the emf of the MFC eventually stabilizes between 700 and 800 mV (the bioanode potential stabilizing around -400 mV). The polarization and power curves are then recorded (**Figure 2.25.D**). A maximum power of 56 mW·m^{-2} and current density of 240 mA·m^{-2} are measured on day 6 in these experimental conditions. From the slope of the polarization curve, we then estimate the internal resistance of the system $R_{int} \approx 14$ kΩ. This value is higher than the typical resistance of the electrospun carbon electrode (R ~ 10^3 Ω) but it is not inconsistent since the reactor architecture is not optimized. Additionally, the maximum current density estimated from the polarization curve is lower than the average current density recorded by chronoamperometry. This may be explained by kinetics differences between the two measurements, as chronoamperometry imposes a potential and reports a steady-phase current while the polarization experiments impose a current while recording the potential of the electrodes.

For comparison, the same experiment carried out with commercial carbon felt as the anode has been reported[14] by Pinto *et al*. The current density output was around 100 mA·m^{-2}, and the polarization and power curves developed maximum power and current densities of respectively 19 mW·m^{-2} and 100 mA·m^{-2}. The performances of the electrospun carbon electrode are clearly higher.

These series of experiments indicate that a few days are necessary for the bacteria to adapt to the MFC reactor environment and to sufficiently colonize the electrospun carbon anode to start producing a stable current output. Cyclic voltammetry results show that the bacterial growth and adaptation to the bioanode as a final electron acceptor triggers a noticeable production of proteins linked to direct electron transfer. Moreover, this increase in EET-associated proteins is tightly linked to the current production of the MFC. The maximum power and current densities exhibited by the system – 56 mW·m^{-2} and 240 mA·m^{-2} respectively – are noticeably better than a conventional commercial carbon felt in the same conditions. However after about a week, the signal starts to decrease, probably due to bacterial overgrowth and electron transfer. This requires to investigate on the rate of the biofilm development.

2.3.1.4. Post-mortem imaging

SEM analysis (Hitachi S-3400N) of the air-dried post-mortem bioanode indeed show a heavy colonization and deposition of matter on the material (**Figure 2.28**), obstructing in some part of the electrode the inter microfibers space. The deposited matter was hinted to be biofilm as bacilli-like shapes consistent with the presence of *S. oneidensis* seemed embedded inside.

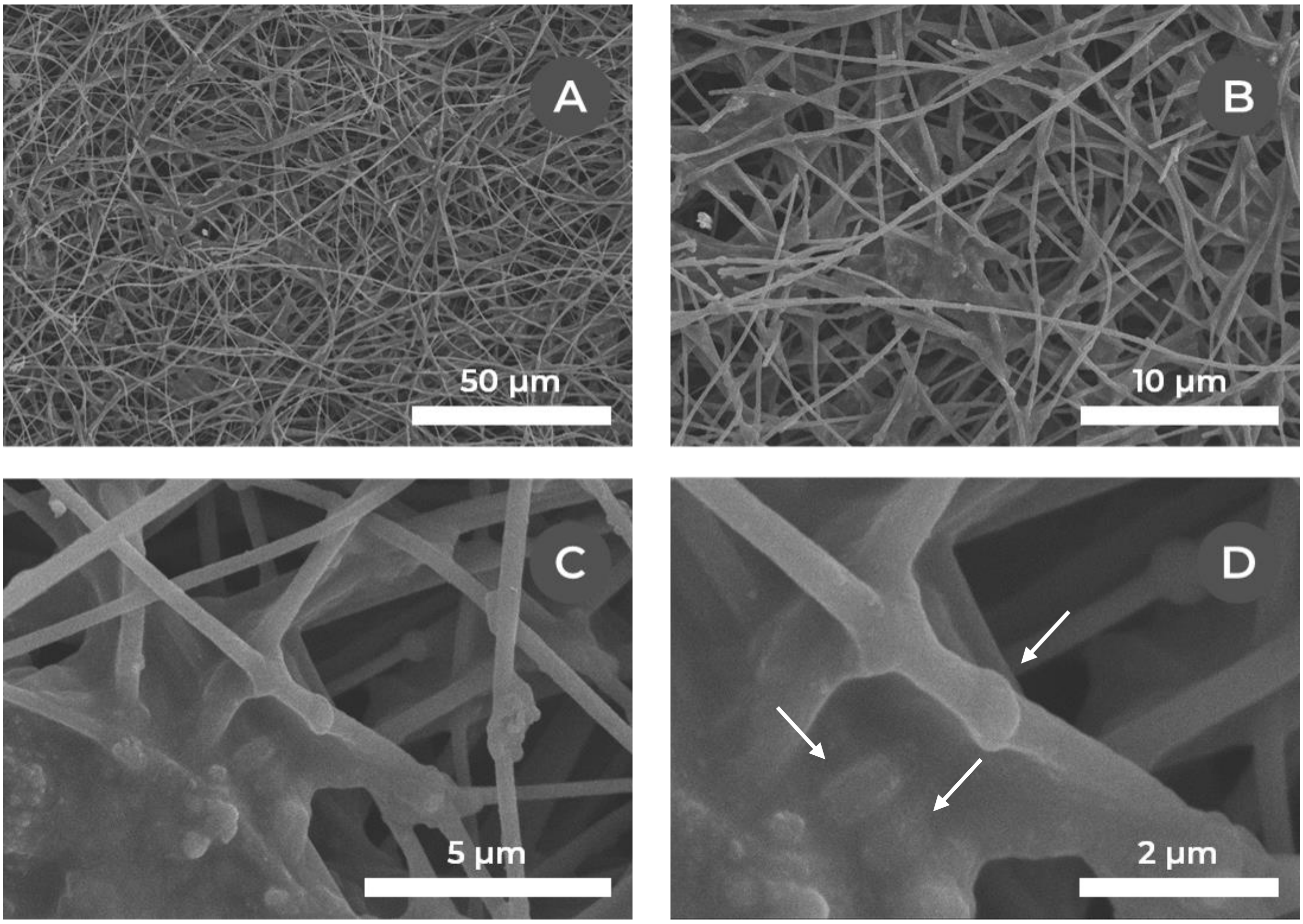

Figure 2.28 – SEM micrographs of an air-dried post-mortem bioanode based on electrospun carbon electrode after 14 days of operation, polarized at +0.3 V vs. Ag/AgCl, KCl saturated reference, coated with 15 nm of gold. The development of a biofilm between the microfibers embedding *S. oneidensis* (arrows) is visible.

Energy-dispersive X-ray spectroscopy (EDX) spectroscopy was used on the colonized electrospun carbon electrode to survey the chemical composition of the matter to verify its supposed biological nature.

Energy-dispersive X-ray spectroscopy[44] is here coupled with scanning electron microscopy and relies on the stimulation of the material by irradiation with a high energy beam of electrons. The resulting excitation of the electronic structure of the present elements triggers an X-ray emission characteristic of each element. Comparison with reference spectra therefore allows identification of the elemental composition of the scanned material.

Elemental mapping of a zone of the colonized carbon electrode showing both bare carbon fibers and deposited matter assumed to be biofilm was acquired with SEM-EDX. The spectrum resulting from the analysis of the accumulated material notably shows the presence of sodium, chlorine, phosphorus, sulfur and potassium in significant quantities (**Figure 2.29.A-B**). Carbon and oxygen are also present but are not herein considered as they are ubiquitous and usually considered uncertainly analyzable with EDX. Phosphorus (**Figure 2.29.C**) is used as a proxy for biological matter as it has no reason to be present on the raw fibers in significant amount and is clearly limited to the extent of the assumed biofilm. Elemental mapping of sulfur and sodium give a similar result, whereas potassium is not restricted to a particular zone. On the other hand, the chlorine mapping pattern (**Figure 2.29.D**) is striking as it seems limited to small patches reminiscent of the size and shape of *S. oneidensis*.

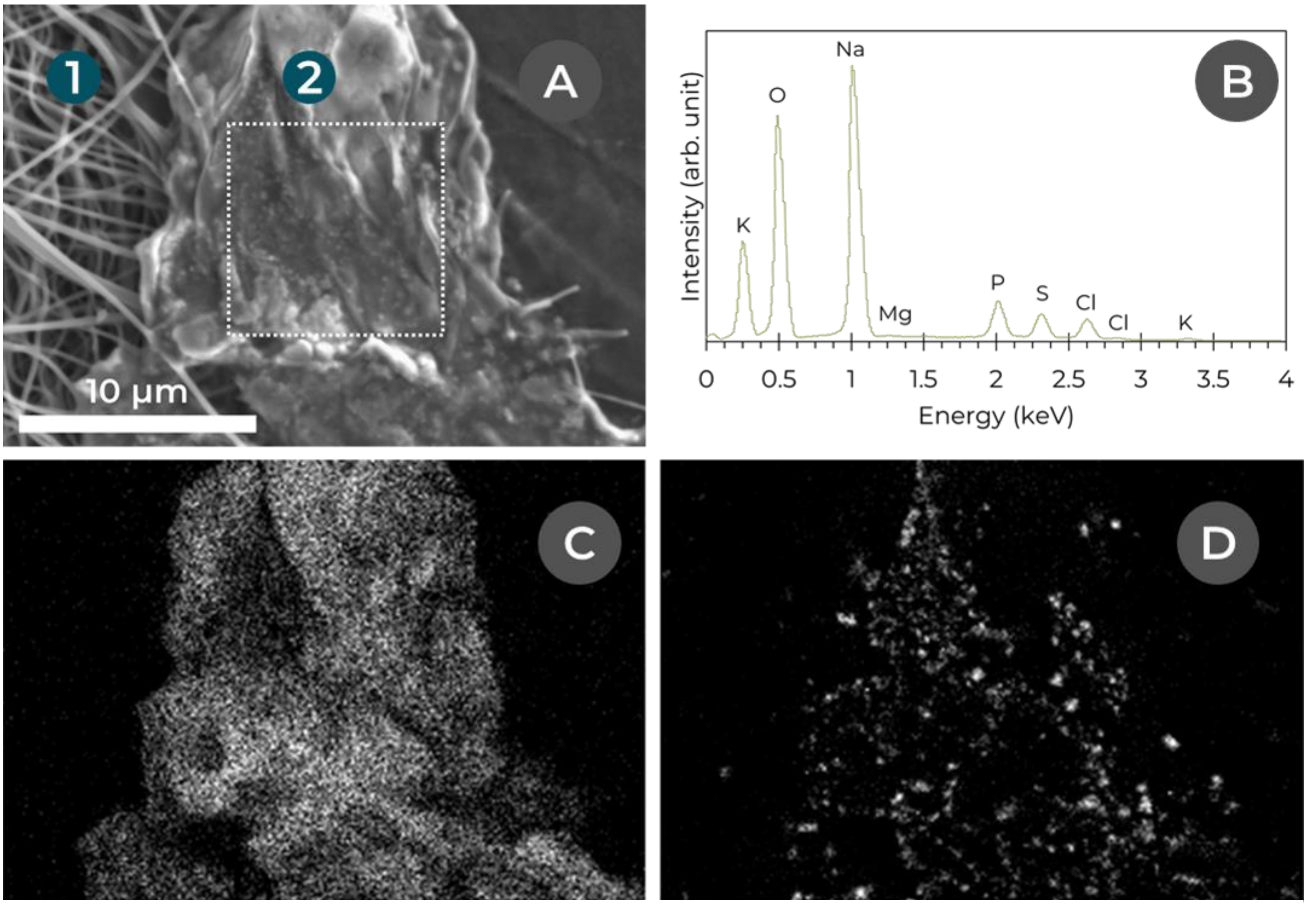

Figure 2.29 – SEM coupled with energy-dispersive X-ray spectroscopy characterization on the biofilm formed at the surface of the colonized electrospun carbon electrode. (A) SEM micrograph of a zone exhibiting both bare fibers (1) & assumed biofilm (2). (B) EDX spectrum of the square zone shown in (A). (C) Elemental mapping of phosphorus. (D) Elemental mapping of chlorine.

This hypothesis seems consistent with the known internal cellular content of prokaryotes, reported to contain a significant fraction of chloride ions[45]. It has been verified by conducting the SEM-EDX analysis of a drop of *S. oneidensis* concentrated culture medium resuspended in phosphate buffered saline and spread and dried on a silicon wafer (**Figure 2.30**). The resulting spectrum reports a strong signal for chlorine (**Figure 2.30.B**), which is strongly localized within the bacterial cells (**Figure 2.30.C**).

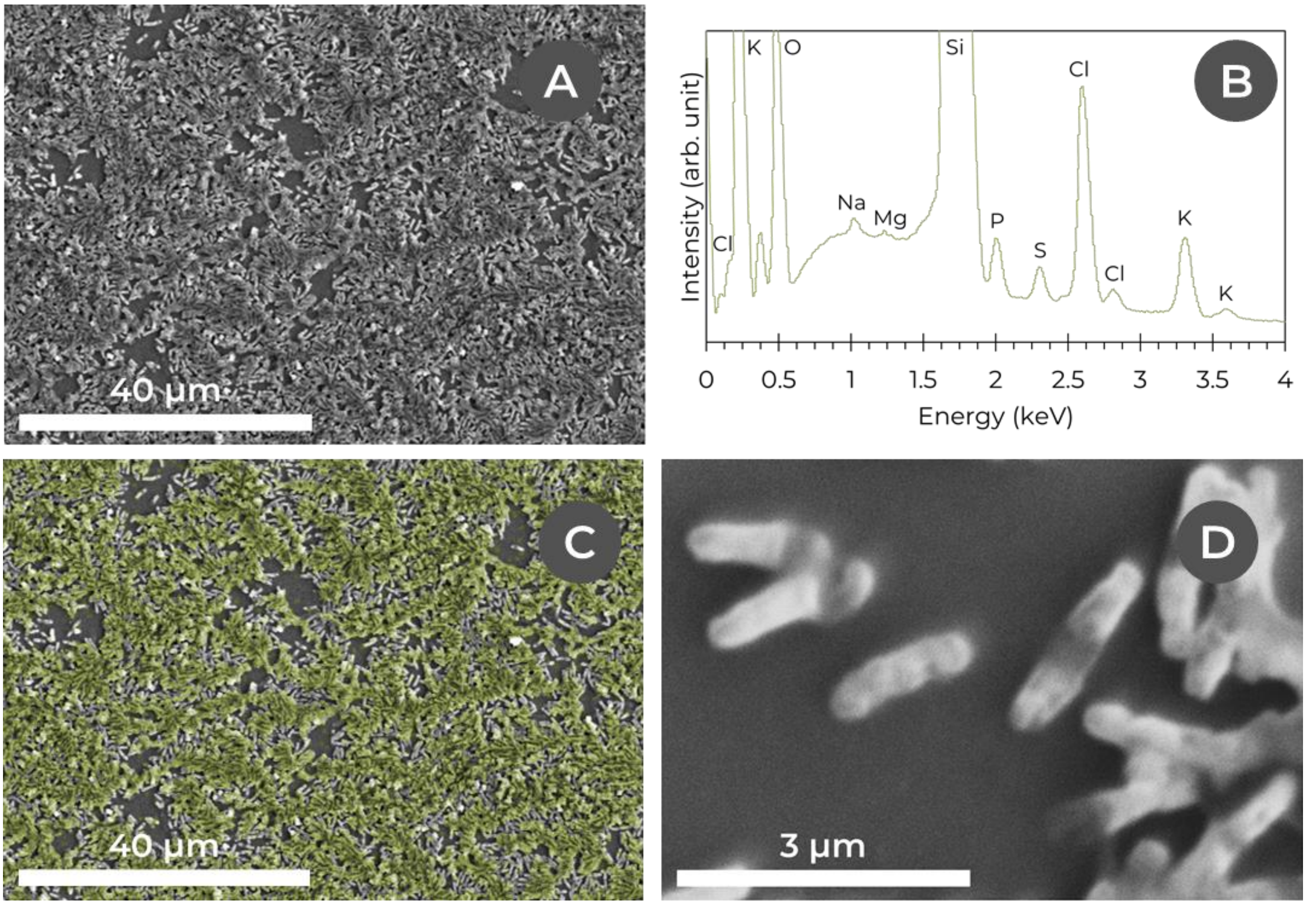

Figure 2.30 – SEM-EDX characterization of air-dried *Shewanella oneidensis* bacteria on a silicon wafer. (A) & (D) SEM micrograph of the bacteria. (B) EDX spectrum of (A). (C) Elemental mapping of chlorine superimposed on (A).

These SEM-EDX analysis of the deposited matter indicate a post-mortem presence of extensive biofilm on the bioanode, as well as the presence of embedded bacteria in this extracellular scaffold.

Eventually the electrospun carbon electrode colonized in situ by *Shewanella oneidensis* appears to be an interesting MFC bioanode. However, to alleviate the lag phase of the first days of current production and designing a ready-to-use electrospun carbon bioanode, precolonization of the membrane by electroactive bacteria will be henceforth considered.

2.3.2. Membrane precolonization & ready-to-use bioanodes

Bacterial growth in the medium surrounding the electrode, bacterial viability as a function of time and biofilm formation were monitored to study the precolonization of the electrospun carbon electrode by *S. oneidensis*.

2.3.2.1. Bacterial growth investigation

The precolonization of the electrospun carbon electrode was conducted by its immersion into diluted MR1/L medium inoculated with *S. oneidensis*. 1 cm^2 of electrospun carbon electrode was immersed in MR-1/L medium set at an optical density of *S. oneidensis* $OD_{600,\ initial} = 0.1$. The temperature was set at 21°C and the medium was agitated at 80 rpm on an orbital shaker. No lactate was added during the experiment.

The optical density of the medium surrounding the electrospun carbon electrode is measured as a function of time and the density of live cells in the electrospun carbon electrode is evaluated with an Invitrogen™ LIVE/DEAD™ *Bac*Light™ Bacterial Viability Kit (Thermo Fisher Scientific) (**Figure 2.31**). The live/dead assay consists of a mix of fluorescent reagents (Syto 9 and Propidium iodide) which bind nucleic acid and allow the quick fluorescent identification of live bacteria with an intact plasma membrane (in green) and dead bacteria with compromised membrane integrity (in red). The test is conducted 15 minutes in PBS buffer with [Syto 9] = 5 µM and [Propidium iodide] = 27 µM, before washing in PBS buffer for 15 minutes and subsequent epifluorescence microscopy.

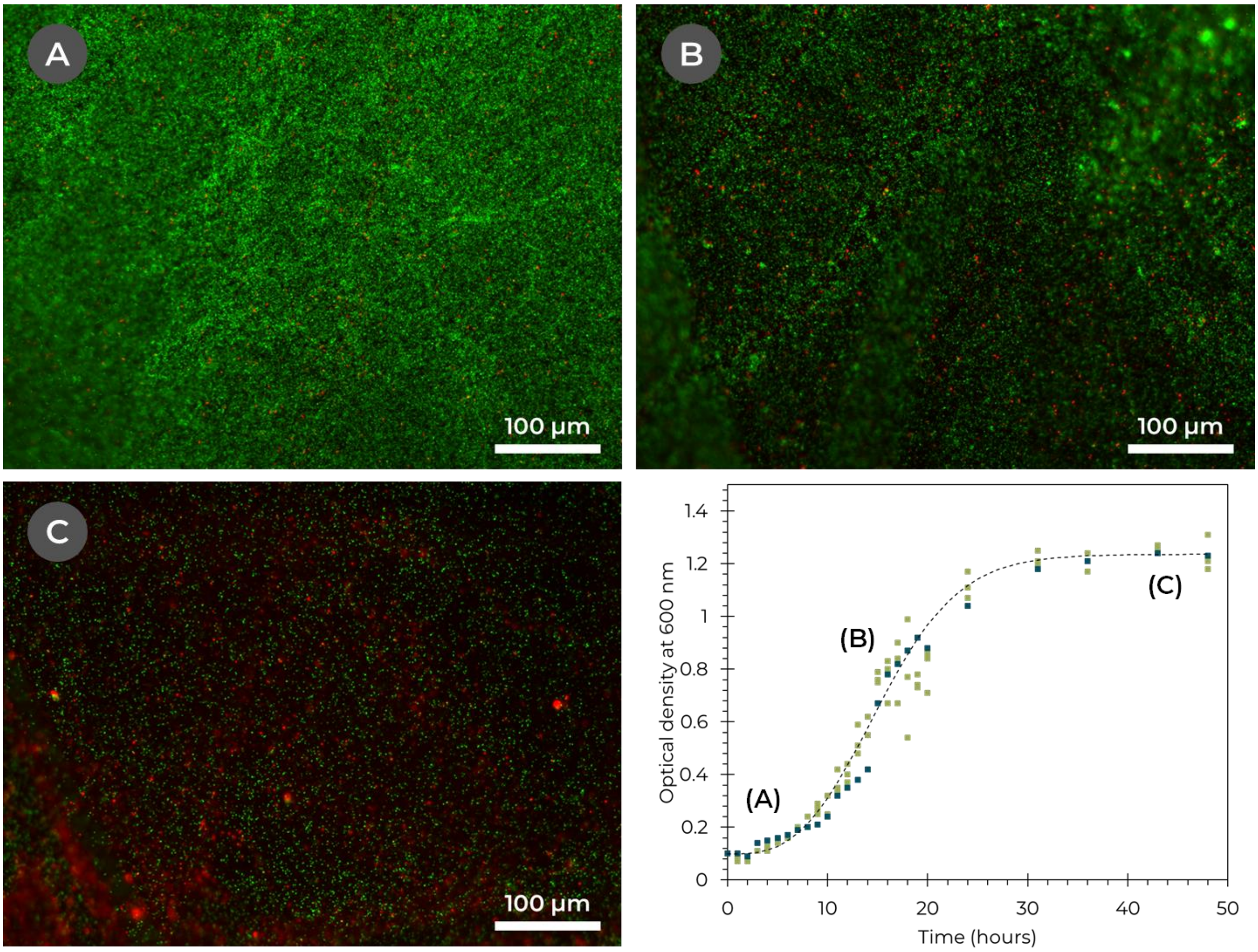

Figure 2.31 – Growth curves of MR-1/L medium inoculated at $OD_{600} = 0.1$ as a function of time in a control medium (•) and a medium with an electrospun carbon membrane (•); conducted at 21°C; N = 3. Epifluorescence microscopy of the electrospun membrane dyed with a live/dead kit (SYTO 9/Propidium iodide) at (A) 1 h, (B) 15 h & (C) 48 h. Green: live cells; red: dead cells.

The growth curves in the electrospun carbon electrode (**Figure 2.31**) follow the typical bacterial growth curve. Following the linear fit of the so-called exponential phase, the time before the start of the exponential phase is $t_{\text{lag-log}} \approx 1$ hour in both cases. The bacteria in the media in which the electrospun carbon electrode is immersed seem to grow a little bit quicker than those in the control medium and eventually reach the stationary phase around 30 hours while the control medium reaches it between 30 and 40 hours. According to the live/dead assay, bacteria impregnate the electrospun carbon electrode from the very first hours, and start to die noticeably only when the stationary phase is reached which is normal as this phase is characterized by the limitation in nutrient supply (here lactate).

By comparing the control and the electrospun carbon electrode growth curves, no inhibitory effect on bacterial growth seems to be attributable to the presence of the electrospun carbon electrode. Moreover, colonization of the electrospun carbon electrode by *S. oneidensis* takes place quickly during the first hours. Nevertheless most of those bacteria may still remain in a planktonic state as thick bacterial biofilm typically takes a few days to develop[55]. Therefore biofilm formation as a function of time must be monitored to determine the best length of bacterial precolonization.

2.3.2.2. Microscopy & biofilm formation evaluation

Biofilm development is important to allow a robust embedment of bacteria in the electrospun carbon electrode and a good electron transfer[46]–[48]. Biofilm formation and growth as a function of time was monitored by electron microscopy.

SEM micrographs were taken every 24 hours from the electrospun carbon electrode immersed in MR-1/L inoculated with *S. oneidensis* to follow the colonization of the electrospun carbon electrode by *S. oneidensis* (**Figure 2.32**). No significant deposition of biofilm was obtained for the first two days (**Figure 2.32.A-B**). On the third day of colonization matter starts to depose in between the fibers of the electrospun carbon electrode (**Figure 2.32.C**). From the fourth to the sixth day no evolution of the deposited matter was observed on the electrospun carbon electrode, and the matter was limited to the fibers interstitial space (**Figure 2.32.D-F**). Furthermore, the deposition of this matter was limited to the first micrometers of the electrospun carbon electrode. However, the two sides of the electrospun carbon membranes were colonized (**Figure 2.32.F**).

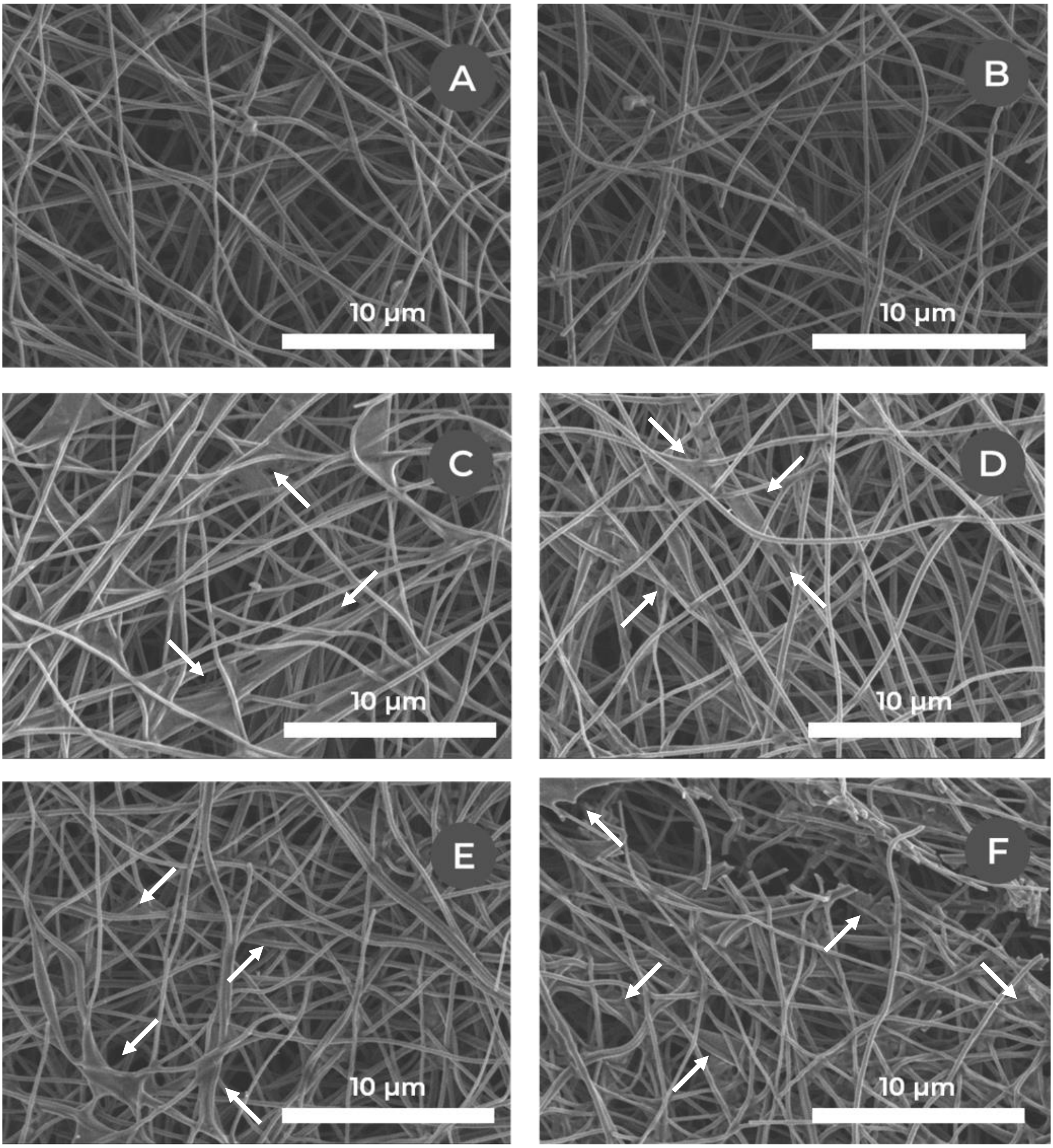

Figure 2.32 – SEM micrographs of air-dried electrospun carbon electrode at different stages of immersion in MR-1/L medium incubated with *S. oneidensis* at OD_{600} = 0.1. (A) 1st day; (B) 2nd day; (C) 3rd day; (D) 4th day; (E) 5th day; (F) 6th day; note the cut performed with a razor blade to estimate the in-depth colonization of the fibers. Samples coated with 15 nm of gold. Arrows show organic matter deposed onto the electrospun fibers.

2.3.2.3. MFC integration & electrochemical characterization

Following this study, it was decided to let the electrospun carbon electrode be immersed in MR-1/L medium set at an optical density of *S. oneidensis* $OD_{600,\ \mathrm{initial}}$ = 0.1 for 4 days to get a good bacterial colonization in the electrospun carbon electrode before integration into an MFC reactor. The temperature is set at 21°C and the setup agitated at 80 rpm on an orbital shaker. No lactate is added until the end of the precolonization. The resulting ex situ colonized electrospun carbon electrode is then integrated as a bioanode into the MFC reactor and the bioanode is poised at +0.3 V vs. Ref. before an electrochemical characterization study similar to the electrospun carbon electrode colonized in situ is conducted (**Figure 2.33**).

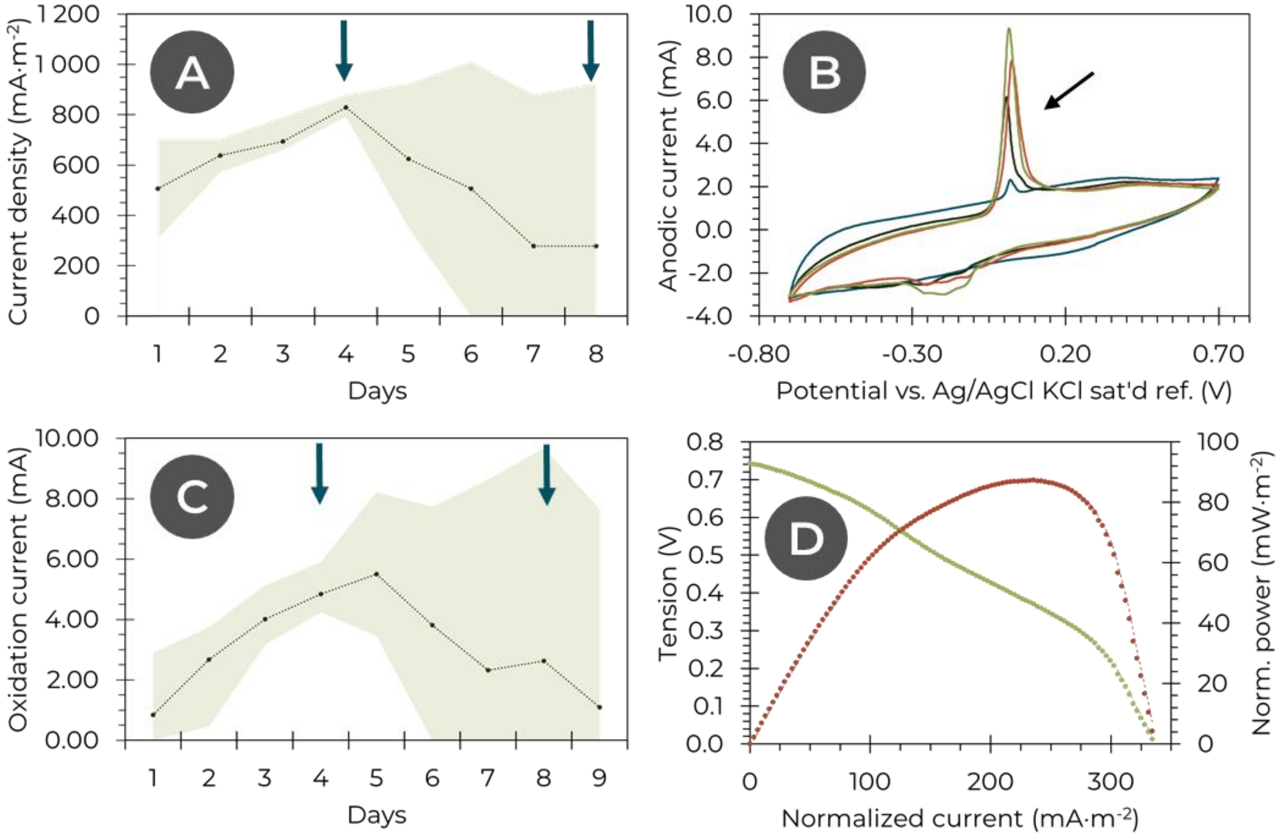

Figure 2.33 – Electrochemical characterization of a two-compartment MFC including an ex situ precolonized electrospun carbon electrode polarized at +0.3 V vs. the reference (electrospun from a 10 wt% PAN in DMF solution, stabilized under air at 280°C, carbonized under argon at 940°C, precolonization as described before) as a function of time. (A) Evolution of the average current density; blue arrows indicate addition of 1 mmol of sodium lactate; the green zone represents maximum and minimum values; N = 6. (B) Evolution of cyclic voltammetry as a function of time (– 1st day, – 4th day before lactate addition, – 4th day after lactate addition, – 5th day); sweep rate of 1 mV·s^{-1}; 3 cycles are recorded, here is the second one; thickness of 205 µm. (C) Evolution of the average current corresponding to the peak shown by the arrow on the CV; blue arrows indicate addition of 1 mmol of sodium lactate; the green zone represents maximum and minimum values; N = 6. (D) Polarization (•) and power (•) curves of an MFC at maximum current density value (here 5th day, thickness of 293 µm). Current and power are normalized by the geometric surface area of the electrospun carbon electrode ($Ø_{anode}$ = 1.7 cm; $A_{anode, geometrical}$ ≈ 2.27 cm^2).

In these experiments, the average current density (**Figure 2.33.A**) starts at around 500 mA·m^{-2}, and increases to 800 mA·m^{-2} on the fourth day. From the fifth day, the average current density decreases as the stability of the system probably starts to be affected by the overgrowth of the bacteria and biofilm.

Cyclic voltammetry (**Figure 2.33.B**) shows from the very first day the presence of an oxidation peak between 0 and +0.05 V vs. Ref., which grows for the next few days. The addition of 1 mmol of sodium lactate (day four) to the MFC reactor maintains the increase in intensity of the oxidation peak. After the fifth day, the oxidation peak maximum current starts to drop (**Figure 2.33.C**). This trend is also observed for the multiple reduction peaks between -0.5 and -0.1 V vs. Ref. As observed with the in situ colonized electrospun carbon electrodes, these multiple peaks highlight the complexity and irreversibility of the proteins and pathways involved in EET. Furthermore, the potentials of the oxidation peaks seem to indicate direct electron transfer.

After stopping anode polarization and waiting for its stabilization, the emf of the MFC reverts between 700 and 800 mV (the bioanode potential stabilizing around -400 mV). In these experimental conditions the power curve (**Figure 2.33.D**) exhibits a maximum power density at around 87 mW·m^{-2} – or 296 W·m^{-3} – which is a bit higher but consistent with the maximum power recorded for the in situ colonization of the bioanode (56 mW·m^{-2}). The polarization curve shows a maximum current at around 335 mA·m^{-2} – or 1.14·10^{3} A·m^{-3} – with a modification of the slope of the polarization curve in the last part of it, attributed to mass transport losses. The estimation of the internal resistance of the MFC is $R_{int} \approx 27$ kΩ which is higher but in the same magnitude than for the in situ colonized anode polarization curve.

2.3.2.4. Post-mortem imaging

Post-mortem SEM imaging of the bioanode has been performed (**Figure 2.34**). The development of a thick biofilm between the fibers similarly to the in situ electrospun carbon anode can be observed.

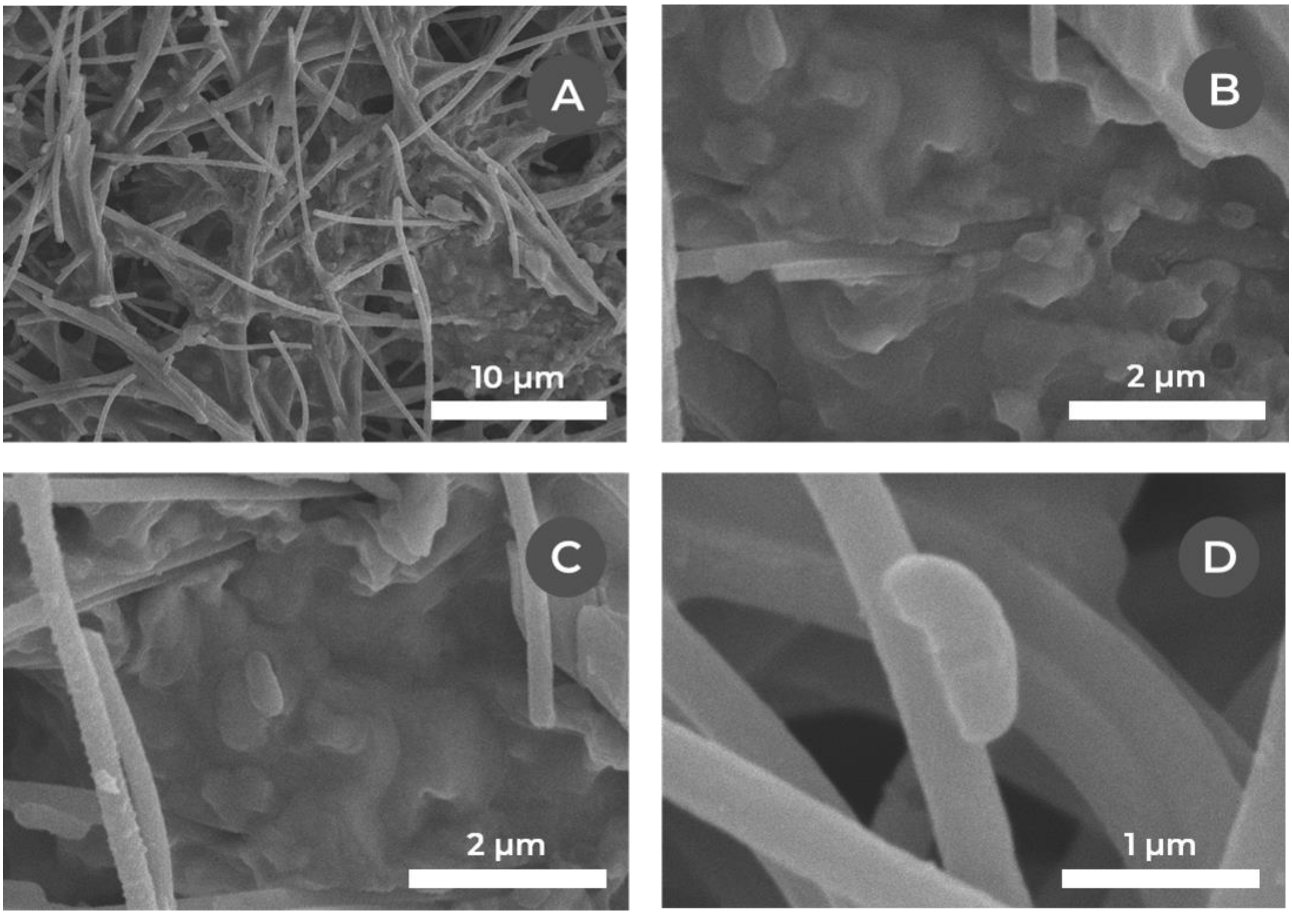

Figure 2.34 – SEM micrographs of an air-dried post-mortem bioanode based on the ex situ precolonized electrospun carbon electrode by *S.* oneidensis after 10 days of operation, polarized at +0.3 V vs. Ag/AgCl, KCl saturated reference, coated with 15 nm of gold. The development of a uniform biofilm between the microfibers is visible.

The electrochemical behavior – polarization and power curves – of an MFC including an ex situ precolonized bioanode is similar to the in situ colonized bioanode setup (maximum power and current densities of respectively 56 mW·m^{-2} and 335 mA·m^{-2} for the former, and 56 mW·m^{-2} and 240 mA·m^{-2} for the latter). The difference is mainly observed on the current output on the first few days of the fuel cell operation. Ex situ electrode colonization reduces the lag phase required to let the bacteria adapt to the electrospun carbon electrode and to colonize it.

In order to improve the performances of the electrospun carbon electrode, it was decided to take advantage of the precolonized membrane (ex situ colonization) relative thinness (200 to 300 µm) to build a thicker, 3D ready-to-use bioanode infused with biofilm through its depth. We hope that such a material would exhibit a higher power and current output while being only limited by nutrient diffusion towards its core and benefiting from the performance of a carbon microfibers-based electrode. Likewise, difficulties with deep penetration of electroactive bacteria and biofilm development limiting the use of 3D materials colonized in situ as reported in the literature[28] would be avoided.

2.4. 3D ready-to-use carbon microfibers bioanode

The preparation of the so-called 3D carbon microfibers bioanode yet requires optimization of its dimensions and assembly process. These parameters are herein explored through electron microscopy and electrochemical characterization before determining the best approach to the fabrication of the 3D bioanode.

2.4.1. Experimental procedure

The individual membranes used for the assembly of a 3D carbon microfibers bioanode are prepared according to the procedure presented in *2.3.2.3. MFC integration & electrochemical characterization*.

Once the membrane are precolonized, they are stacked into the MFC reactor, poised at +0.3 V vs. Ref. and electrochemically characterized as described before. Their thickness is measured post-mortem to account for a possible compression of the fibers in the MFC reactor.

2.4.2. Effect of bioanode stacking & thickness

The electrochemical analyses of the different stacked setups are henceforth compared to understand the effect of the bioanode thickness, as well as to define their optimum.

2.4.2.1. MFC integration & electrochemical characterization

The electrochemical activities of the 2-fold, 3-fold and 5-fold stacks are therefore recorded and compared (**Figure 2.35**).

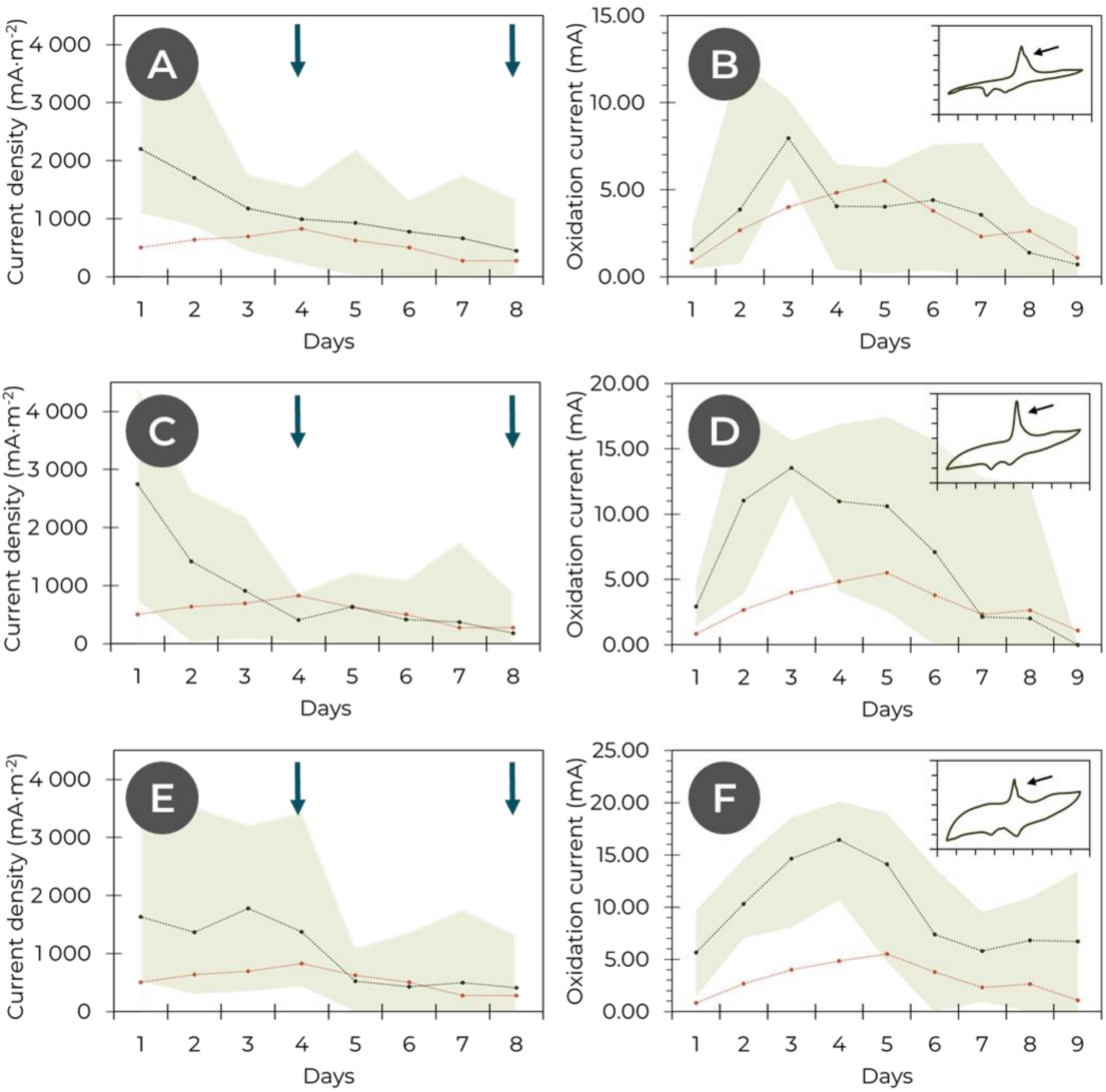

Figure 2.35 – Electrochemical characterization of a two-compartment MFC including a (A-B) 2-fold; (C-D) 3-fold & (E-F) 5-fold stacked precolonized electrospun carbon electrode membrane polarized at +0.3 V vs. the reference (electrospun from a 10 wt% PAN in DMF solution, stabilized under air at 280°C, carbonized under argon at 940°C, precolonization as described before) as a function of time. (A,C,E) Evolution of the average current density (•); blue arrows indicate addition of 1 mmol of sodium lactate; the green zone represents maximum and minimum values. Comparison (•) with a simple precolonized bioanode; N = 6. (B,D,F) Evolution of the average current (•) corresponding to the peak shown by the arrow on the CV; the green zone represents maximum and minimum values. Comparison (•) with a simple precolonized bioanode; N = 6. For the CV shown at top-right: x-axis is the anode potential vs. Ref. (-0.8 to +0.8 V), y-axis is the anode current (-12 to +18 mA). Current and power are normalized by the geometric surface area of the electrospun carbon electrode ($Ø_{anode}$ = 1.7 cm; $A_{anode, geometrical}$ ≈ 2.27 cm^2).

For all the systems, the average current density (**Figure 2.35.A,C,E**) starts at much higher values than the control precolonized membrane, up to around 2750 mA·m^{-2} for the 3-fold stacks. Interestingly, these values are not clearly different from one stack to another through the time, albeit initially better than the control. They then tend to decrease on the first few days to usually plummet to the level of the control precolonized membrane around the fourth day. Here again, the reduction in current output may be attributed to the heavy biofilm development and its effect on the progressive decrease in influx of nutrients to the biofilm as well as on the electron transfer efficiency.

The cyclic voltammetry (**Figure 2.35,B,D,F**) on the other hand shows a strong dependence with the number of stacked electrospun carbon electrodes. First of all the capacitive signal of the voltammograms rises up with the thickness of the system. This is understandable as the surface accessible to the anolyte for the establishment of a double layer increases with the volume of bioanode. For comparison, the capacitive surface area corresponding to the CV recorded on the first day is calculated and compared with the volume of each stack (**Figure 2.36**). The surface area increases as expected with the thickness of the setup. However, the surface-to-volume ratio of the systems seem roughly of the same order of magnitude. Henceforth the totality of the electrode should be accessible to the anolyte in each case.

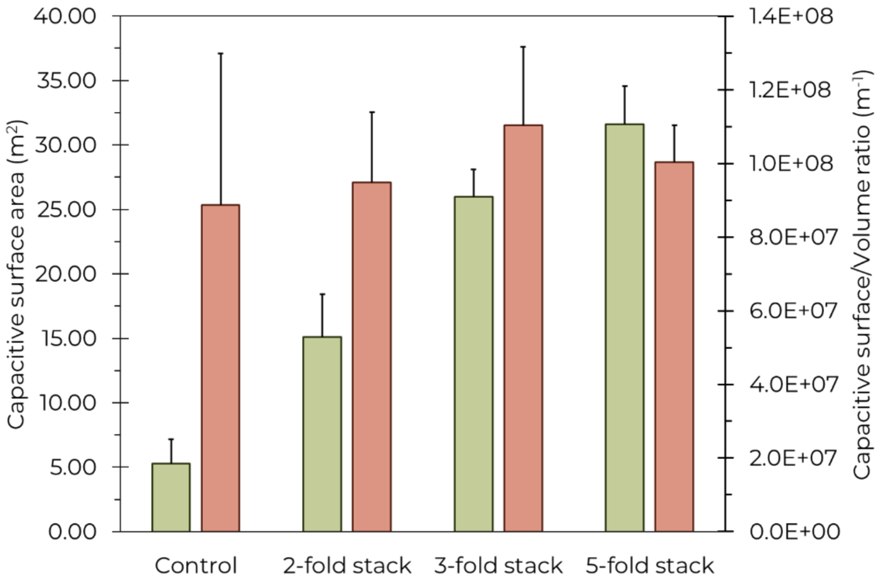

Figure 2.36 – Comparison of the average nominal (◆) or volume normalized (◆) capacitive surface area on the first day between bioanodes composed of stacked precolonized electrospun carbon electrodes (from 1 to 5). N = 6. The capacitive surface area is calculated from the cyclic voltammograms.

Nevertheless, the evolution of the average maximal oxidative current roughly follows the same trend as the control precolonized membrane, decreasing after reaching a maximum. This might again hint that even if the total volume of the anode is accessible to the anolyte, the eventual overgrowth of the biofilm hinders the diffusion of nutrient species to the core of the bioanode.

On the other hand, the average maximum current relative to the main oxidative peak grows higher and higher with the thickness of the system. While approximately equal to the control for the 2-fold setup, it rises up to 4.1 or 3.9 times higher respectively in the case of the 3-fold and 5-fold setups on the third day.

This scaling decorrelation between cyclic voltammetry and chronoamperometry may be attributed to the differences in nature and kinetics between the two measurements. The maximum current in chronoamperometry is measured at steady state, when the current output may be limited by the influx of nutrients to the bacteria, while cyclic voltammetry relies on a more local electrochemical probing of the bacterial redox proteins and mediators.

There is still room for improvement in increasing the current density of thicker electrodes by working on diffusion from the anolyte to the electrospun carbon electrode. Nevertheless these results reflect a strong effect of precolonized layer stacking on increasing the effective surface area of the system and therefore the bacterial electron transfer rate.

The detailed electrochemical characterization of the 5-fold stacks is then presented (**Figure 2.37**).

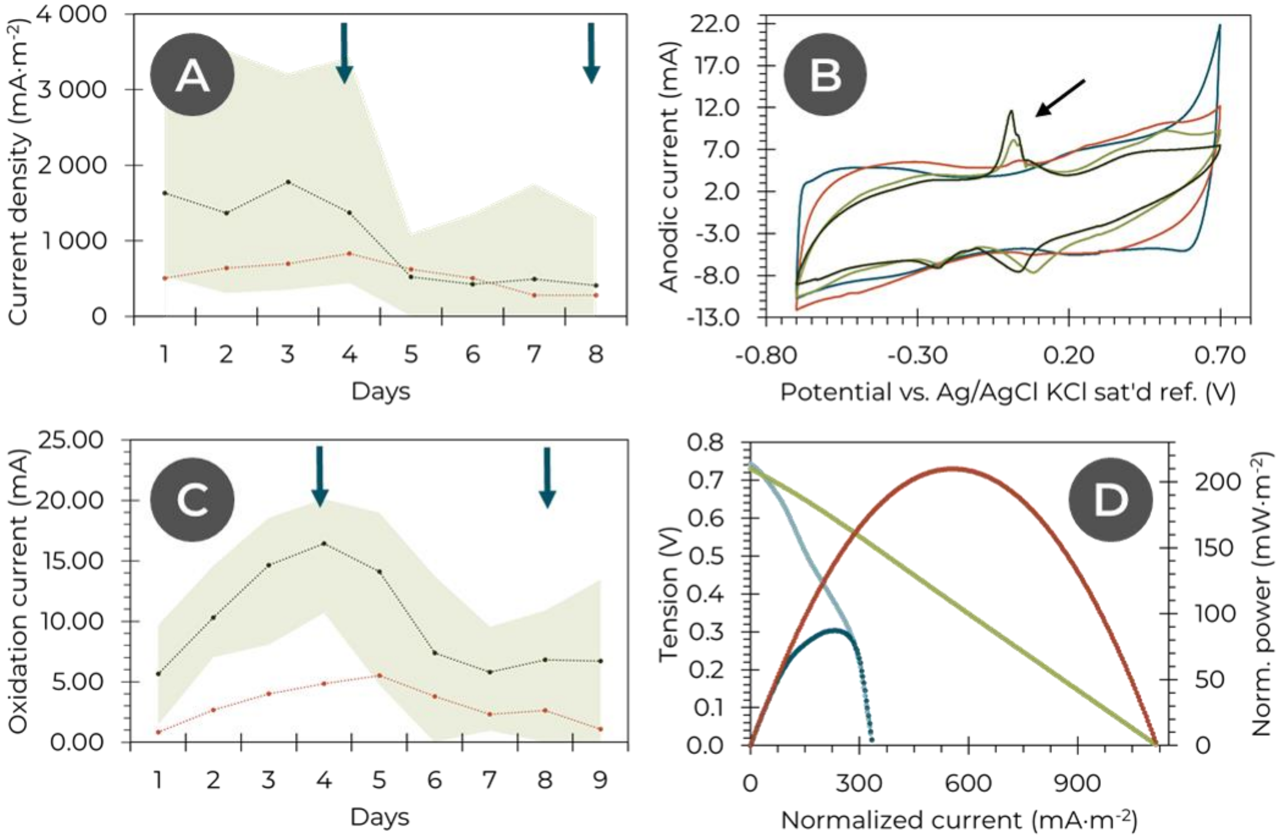

Figure 2.37 – Electrochemical characterization of a two-compartment MFC including a 5-fold stacked precolonized electrospun carbon electrode polarized at +0.3 V vs. the reference (electrospun from a 10 wt% PAN in DMF solution, stabilized under air at 280°C, carbonized under argon at 940°C, precolonization as described before) as a function of time. (A) Evolution of the average current density (•); blue arrows indicate addition of 1 mmol of sodium lactate; the green zone represents maximum and minimum values. Comparison (•) with a simple precolonized bioanode; N = 6. (B) Evolution of cyclic voltammetry as a function of time (– 1st day, – 3rd day, – 6th day, – 8th day after lactate addition); sweep rate of 1 mV·s^{-1}; 3 cycles are acquired, here is the second one; thickness of 1303 µm. (C) Evolution of the average current (•) corresponding to the peak shown by the arrow on the CV; blue arrows indicate addition of 1 mmol of sodium lactate; the green zone represents maximum and minimum values. Comparison (•) with a simple precolonized bioanode; N = 6. (D) Polarization (•) and power (•) curves of an MFC at maximum current density value (here 5th day, thickness of 1359 µm). Comparison with the polarization (•) and power (•) curves of a simple precolonized bioanode (here 5th day, thickness of 293 µm). Current and power are normalized by the geometric surface area of the electrospun carbon electrode ($Ø_{anode}$ = 1.7 cm; $A_{anode,\ geometrical}$ ≈ 2.27 cm^2).

The average current density of the 5-fold stacked bioanode MFC (**Figure 2.37.A**) already starts at around 1700 mA·cm^{-2} and remains at this level until the fourth day. After this point the recorded current density starts to decrease as observed in previous experiments, to finally reach similar levels as the unstacked bioanode from the sixth day onwards. However, currents density up to approximately 7 times the average current density of the control MFC configuration are observed during the first days of experiment. Eventually, the difference between the stacked and control bioanode current output decreases with time. This behavior may be attributed to the growth of a thick biofilm that hinders nutrient diffusion to the bacteria and blocks the electron transfer, especially toward the depths of the 3D bioanode.

Cyclic voltammetry (**Figure 2.37.B-C**) already shows an oxidation peak between 0 and +0.05 V vs. Ref. for the first day in most of the MFC configurations. The intensity of the peak rises until the fourth or fifth day before decreasing as observed in the unstacked precolonized membrane. However, this drop in peak oxidation current stalls after the sixth or seventh day and a stable level higher than the control precolonized membrane is kept until the ninth day. After this point, measurements become difficult as corrosion starts to attack the wires connecting the platinum mesh current collector to the potentiostat.

After stopping the anode polarization and waiting for a stabilization of its potential, emf between 0.7 and 0.8 V were observed. Polarization and power curves were recorded (**Figure 2.37.D**) and show a maximum power density of 210 $mW{\cdot}m^{-2}$, as well as a maximum current density of 1119 $mA{\cdot}m^{-2}$. These values are respectively 2.4 and 3.3 times higher than the control precolonized membrane, for a bioanode thickness of 293 and 1359 µm – or 4.6 times higher. These values are clearly better than those observed for a thinner bioanode. The internal resistance of the MFC can also be evaluated to be $R_{int} \approx 3\ k\Omega$, which is clearly lower than the values reported before. This could be explained by the improvement of the bioanode conductivity due to the compression of the carbon microfibers perpendicular to their plane in the MFC reactor, improving then the contact between them.

The evolution of electronic transfer efficiency between the untacked precolonized control membrane and the stacked bioanodes is evaluated by comparing the maximum cyclic voltammetry oxidative current of each sample (**Figure 2.38**).

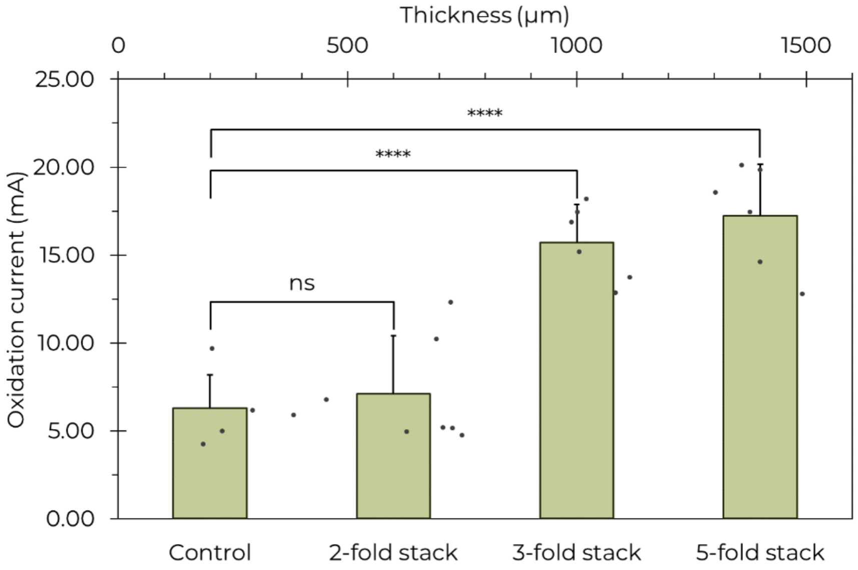

Figure 2.38 – Comparison of the maximum cyclic voltammetry oxidative current corresponding to electron transfer from bacteria to the electrospun carbon electrode between bioanodes composed of stacked precolonized electrospun carbon electrodes. N = 6. Points correspond to the individual measurements. The thickness of the bioanode is measured post-mortem to account for the compression of the fibers. Sets were compared for statistical significance.

The control membranes exhibit an average peak oxidative current of 6.04 ± 1.89 mA, while the 2-fold stack bioanodes show an average current of 7.10 ± 3.30 mA, the 3-fold stack 15.72 ± 2.14 mA and the 5-fold stack 17.23 ± 2.95 mA. The difference between the control and the 2-folds stacks is not clearly significant, but the 3-fold and 5-fold stacks peak oxidative currents are significantly higher than those of the control precolonized membranes. However, the difference between the 3-fold and the 5-fold stacks is not significant either ($p = 0.33$). This behavior may again be explained by the fact that over a certain thickness, the diffusion of nutrients toward the bacteria colonizing the inner layers of the 3D bioanode may be impeded by the fibers and the biofilm of the outer layers.

Eventually, the maximum power and current densities reported for the 5-fold stack – 210 $mW \cdot m^{-2}$ and 1119 $mA \cdot m^{-2}$ respectively for surface normalization, or 155 $W \cdot m^{-3}$ and 823 $A \cdot m^{-3}$ for volume normalization – recorded in a non-optimized bulk MFC reactor can be compared with the literature (**Table 2.2**). In the case of a lactate-fed anodic *S. oneidensis* MFC including a ferricyanide catholyte and with a miniature optimized reactor using a reticulated vitreous carbon anode under carefully anaerobic conditions, Ringeisen *et al.* report performances[49] of 3 $W \cdot m^{-2}$ and 12500 $mA \cdot m^{-2}$, or 500 $W \cdot m^{-3}$ and 2080 $A \cdot m^{-3}$. The surface-normalized values are approximately one order of magnitude higher than those obtained in this work, but the volume power density is merely twice lower, without any optimization. Moreover, the values reported are way higher than those obtained with a simpler and more conventional commercial carbon felt anode in the same conditions – 19 $mW \cdot m^{-2}$ and 100 $mA \cdot m^{-2}$. This shows promising insights for optimized MFC including 3D precolonized bioanodes. Note that the single precolonized electrospun carbon electrode exhibits even slightly higher volume current and power densities – respectively 296 W·m^{-3} and 1140 A·m^{-3} – than the 5-fold stack (but lower surface normalized performances) still without any reactor optimization.

Table 2.2 – Comparison of the surface (◆) & volume (◆) normalized electrochemical performances between the literature and the precolonized electrospun carbon electrode setups, optionally stacked. The performances compare MFCs using a carbon-based anode, *S. oneidensis* as the anodic exoelectrogenic strain with growth medium supplemented with lactate as the anolyte, & a ferricyanide solution as the catholyte.

Setup	Current	Power
Literature optimum (Ringeisen *et al.*)[49]	12.5 A·m^{-2}	3 W·m^{-2}
	2.08·10^{3} A·m^{-3}	500 W·m^{-3}
Commercial carbon felt (Pinto *et al.*)[14]	0.100	19·10^{-3}
	10	1.9
Precolonized electrospun carbon electrode	0.334	0.087
	1.14·10^{3}	296
5-fold stack	1.12	0.210
	0.823·10^{3}	155

2.4.2.2. Post-mortem imaging

The post-mortem colonization of the inner layers of the stacks is therefore evaluated by scanning electron microscopy to identify if the biofilm development may be in cause in the hindrance of the medium diffusion or in electron transfer.

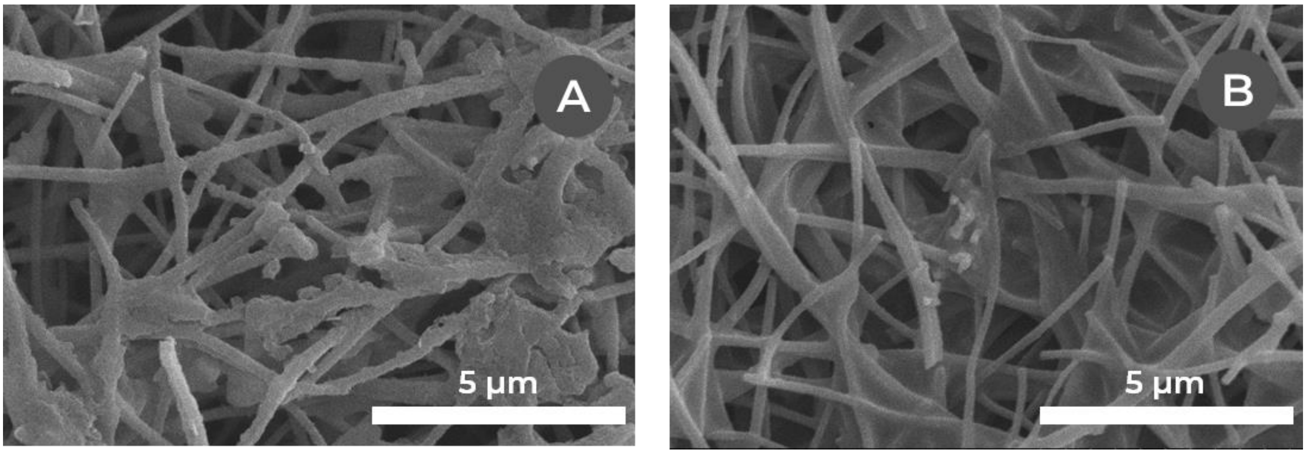

Figure 2.39 – SEM micrographs of the two layers of an air-dried post-mortem bioanode based on 2-fold precolonized electrospun carbon electrode after 10 days of operation, polarized at +0.3 V vs. Ag/AgCl, KCl saturated reference, coated with 15 nm of gold. (A) Layer in contact with the Nafion® membrane; (B) Layer in contact with the anolyte.

The 2-fold stack observation (**Figure 2.39**) shows a proper colonization of the fibers in both the electrospun carbon layers. The biofilm covering is clearly denser after MFC integration than in the ex situ precolonized fibers before MFC integration. On the layer in contact with the Nafion® membrane, the compression of the fibers and biofilm can be clearly seen. On the upper layer, the biofilm development is similar to the unstacked precolonized bioanodes.

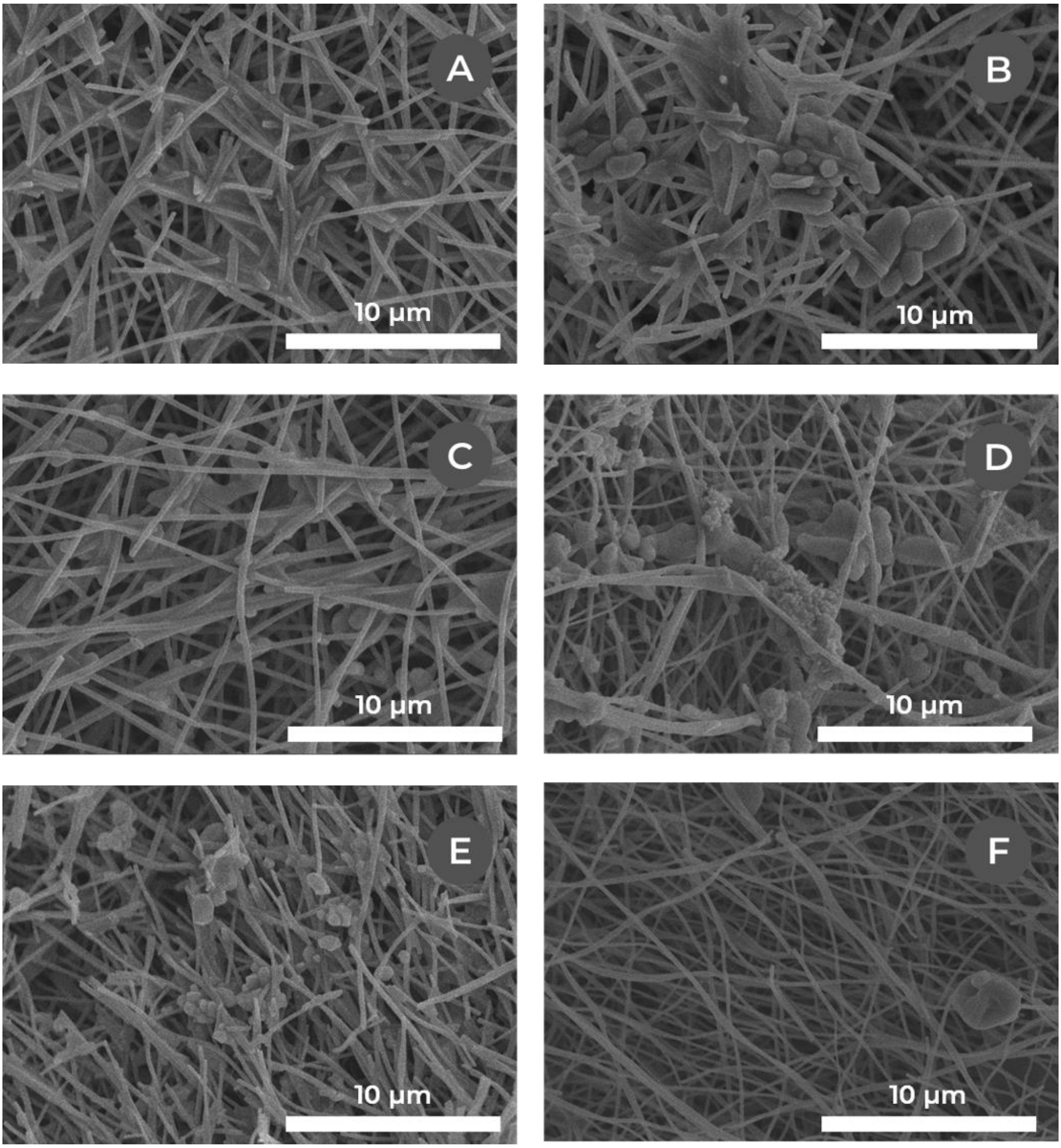

Figure 2.40 – SEM micrographs of the layers of air-dried post-mortem bioanodes based on 3-fold (A-C) & 5-fold (D-F) precolonized electrospun carbon electrode after 10 days of operation, polarized at +0.3 V vs. Ag/AgCl, KCl saturated reference, coated with 15 nm of gold. (A) Layer in contact with the anolyte; (B) Middle layer; (C) Layer in contact with the Nafion® membrane; (D) Layer in contact with the anolyte; (E) Fourth layer; (F) Layer in contact with the Nafion® membrane.

The 3-fold stack SEM analysis (**Figure 2.40.A-C**) also indicates a good colonization of the different layers. The compression of the biofilm and fibers on the two lower layers can be seen. For the 5-fold stack, a good colonization is visible on the upper layer – the one in contact with the current collector – (**Figure 2.40.D**) as well as on the second and third layers. Here the biofilm development is similar as the one observed on the other stacks. The fourth layer (**Figure 2.40.E**) also shows a biofilm development albeit somewhat sparser than on the other layers. However, on the fifth layer – the one in contact with the Nafion® membrane – (**Figure 2.40.F**), no clear development of a biofilm can be seen beyond the precolonization of the membrane.

This trend of a sparser development of bacterial biofilm is seen consistently on the post-mortem layers, even more strikingly on the lower layers of the thickest stacked 3D electrodes, even with the precolonization of the membranes. This trend has been previously reported on the limited in situ colonization of commercial carbon felt by *S. oneidensis* – restricted to the first 100 µm of the material[14]. However, the precolonization of the membrane here allow a deeper development of a consistent biofilm, up to around 1 mm in depth.

It may be hypothesized that nutrient diffusion is hindered by the microfibers network and prevents further growth and development of bacteria and biofilm for thick bioanode (~ 1 mm).

2.4.3. Biofilm overgrowth

As seen previously, the cyclic voltammograms recorded can inform us on the capacitive surface area of the bioanode. By calculating the evolution of the capacitive surface area through the time for one of the MFC configurations (**Figure 2.41**), we can indeed see that it quickly decreases after the first few days from its initial maximum around 10 m^2 to 5 m^2 after 6 days. It then stabilizes at this value for the following days. This diminution of the capacitive surface area can be linked to the growth of the biofilm which isolate the electrode from the anolyte and prevent the formation of the capacitive double-layer. In this case, roughly half of the electrode surface is finally covered by the biofilm. Moreover, both the evolution of the peak oxidative current (**Figure 2.41.A**) and current density (**Figure 2.41.B**) which pass through a maximum around the fourth day – as seen in previous experiments – seems linked to the growth of the biofilm and shows three phases:

(1) During the first two days the oxidative current and current density remain low, and the capacitive surface area is unaffected: the bacteria adapt to the electrospun carbon electrode and do not build up a significant amount of biofilm;
(2) The oxidative current and current densities rise quickly and reach a maximum around the third and fourth days: the bacteria are fully adapted to their environment and transfer a lot of electrons. They therefore grow and secrete biofilm, reducing the available capacitive surface area;
(3) The growth of the biofilm probably limits the diffusion of the organic molecules to the core of the bioanode: the current density and oxidative current decrease, and the biofilm growth end up.

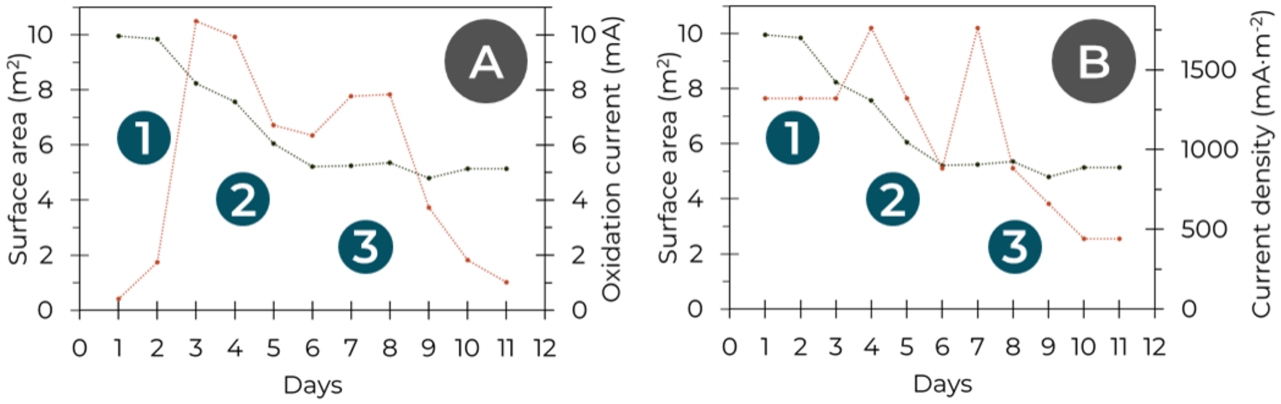

Figure 2.41 – Evolution of the capacitive surface area (•) of a 2-fold stacked precolonized bioanode as a function of the time (thickness of 693 µm). The capacitive surface area is calculated from cyclic voltammetry. The surface area is compared with (A) the maximum current of the main oxidation peak on the CV (•), & (B) the current density output of the MFC, normalized by the geometric surface area of the electrospun carbon electrode ($Ø_{anode}$ = 1.7 cm; $A_{anode,\ geometrical}$ ≈ 2.27 cm^2). This shape is representative of the behaviors observed for electrospun carbon electrodes integrated into an MFC.

This model would account for the "bell curve" appearance of the current densities and oxidative currents, passing through a maximum before plummeting.

2.4.4. Microfibers architecture & diffusion limitations

The stalling of the performances for the thickest 3D electrospun carbon electrodes could also be linked to diffusion hindrance to the core of the bioanode due to the electrospun mat architecture. The possible limitations of mass transport through the electrospun fibers and toward the core of the thickest bioanodes is therefore investigated.

To gain some insights on the rate of static diffusion of soluble redox active species from the surrounding solution to the inner parts of electrospun carbon paper electrodes, a 381 µm thick stack of electrospun carbon paper is integrated into a three-electrode configuration cell (Ag/AgCl, KCl saturated reference (Ref.), Pt wire counter electrode, and electrospun carbon membrane working electrode, Ø = 1.4 cm). The cell is filled with an electrolyte consisting of NaCl 150 mM + 100 mM $K_3[Fe(CN)_6]$ in Milli-Q H_2O, and the carbon membrane is let to impregnate in the electrolyte. After waiting for the stabilization of the cell open-circuit voltage (OCV), a series of cyclic are acquired between -0.8 and +0.28 V vs. Ref. The upper vertex potential at +0.28 V has been chosen to limit the reoxidation of the redox probe while staying in CV conditions, depleting the ferricyanide probe in the fibers. Therefore, the concentration equilibrium in ferricyanide could only be reached by diffusion of the probe from the bulk electrolyte through the depth of the membrane. After the 20th CV, approximately half of the volume of the cell was replenished with fresh electrolyte.

The goal of the study (**Figure 2.42**) is to check if the thickness of the electrode has an impact on the evolution of the reduction peak in these conditions, revealing a quicker consumption of the electroactive species than it is replenished by diffusion. This is thought to mimic the situation with the lactate consumption by bacteria and diffusion from the medium in thick bioanodes.

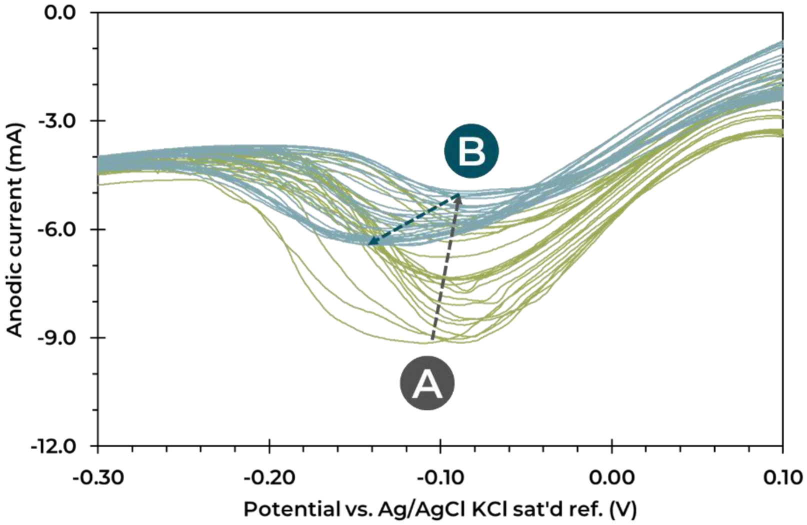

Figure 2.42 – Evolution of the ferricyanide reduction peak intensity for 50 successive cyclic voltammetries (acquired between -0.8 and +0.28 V vs. Ag/AgCl, KCl saturated reference; scan rate of 1 mV·s^{-1}, three electrode setup: Pt wire counter electrode & electrospun carbon membrane working electrode, Ø = 1.4 cm, thickness of 381 μm; electrolyte: NaCl 150 mM + 100 mM $K_3[Fe(CN)_6]$ in Milli-Q H_2O). (A) Decreasing of the peak reduction current; (B) Increasing and stabilization of the peak reduction current after electrolyte replenishment. Note that the peak potential drift is linked to the diffusion of the redox probe through the sintered-glass tip of the reference electrode.

We observe two phases during this experiment. Firstly (**Figure 2.42.A**), the current of the CV peak associated with the ferricyanide reduction decreases. This behavior can be associated both to the decrease in ferricyanide concentration within the mat, as well as from a depletion of ferricyanide within the whole electrolyte. During the first cycles, the former must be dominant, and the latter might become observable after a time. To check for this second effect, the cell is replenished with fresh electrolyte after 20 cycles. Immediately (**Figure 2.42.B**), the current of the reduction peak increases. However, from cycle 30, the reduction current reaches a steady state, with a smaller intensity than for cycle 1. Note that the peak potential drift is linked to the diffusion of the redox probe through the sintered-glass tip of the reference electrode.

The behavior observed can be explained by the fact that the ferricyanide concentration first decreases within the mat, and then in the whole solution. When the electrolyte is replenished, the second effect is compensated and a steady state is reached. However this steady state exhibits less reduction current than at cycle 1 when the mat is fully impregnated with ferricyanide ions. This is linked to a smaller concentration of ferricyanide, as predicted by equation **[2.10]**, probably due to the limited diffusion of the redox probe from the electrolyte to through the depth of the mat.

The redox probe used here – potassium ferricyanide – is however not fully comparable to the lactate consumed by the bacteria in the MFC setup. Additionally, the bio-oxidation of lactate mechanisms and kinetics is more complicated than the contact reduction of ferricyanide into ferricyanide. Albeit preliminary, these results nevertheless show that at the thickness and time scales studied, the electrospun carbon electrodes fibers indeed plays a hindering role in the static diffusion of redox active species toward their depths.

Overall, the ex situ precolonization of electrospun carbon electrodes and their integration into 3D stacked bioanodes shows promising performances for MFC power generation (up to 200 $W \cdot m^{-3}$ to be compared with maximum reported performances of 500 $W \cdot m^{-3}$ for optimized *S. oneidensis* based microbial fuel cells). Moreover, the ex situ colonization guarantees the quick set up of a current output upon MFC integration since the adaptation and growth lag of the electroactive bacteria is limited by the precolonization. The surface power and current densities of these electrodes remain nevertheless somewhat limited (up to 210 $mW \cdot m^{-2}$ and 1119 $mW \cdot m^{-2}$ to be compared with 3 $W \cdot m^{-2}$ and 12500 $mA \cdot m^{-2}$). Eventually, the growth of the bacterial biofilm in between the microfibers tends to also impede diffusion through the depth of the fibers and to limit the stability of the current output as a function of time. In the next paragraphs, the ex situ colonized electrospun carbon electrode will be called the "precolonized bioanode".

2.5. Cryodesiccation & conservation

Besides performances improvements, the development of proper conservation techniques is critical to guarantee the long-term storage and availability of ready-to-use MFC bioanodes. The main challenge is therefore to preserve the bacterial cells colonizing the electrospun carbon scaffold. A wide range of cell conservation techniques have been reported in the literature, such as cryopreservation[50] and cryodesiccation[51],[52]. Freezing and drying may however be noxious to living cells and require a suitable tuning to guarantee a reasonable bacterial surviving rate. Cryodesiccation (or freeze-drying) of bioanodes has in particular been demonstrated[53] as a relevant conservation technique in microbial fuel cells. However, the application of cryodesiccation and its lasting impact on EET performances remains largely unstudied especially for precolonized bioelectrodes and among *Shewanella* spp.

Hence, this part focuses on the design of a cryodesiccation protocol, simple and efficient and providing storable lyophilized electrospun carbon bioanodes precolonized with *Shewanella oneidensis*.

2.5.1. Experimental procedure

The electrospun carbon electrodes are precolonized according to the protocol described in *2.3.2 Membrane precolonization & ready-to-use bioanodes*. They were cut before cryodesiccation to approximately 2 cm x 2 cm in order to be readily mountable into the MFC reactor.

The precolonized bioanodes were first frozen in liquid nitrogen (-195.79°C) in order to freeze the water without forming big ice crystals. It is then placed in a freeze-dryer (Christ Alpha 2-4 LD) under high vacuum. The drying operation was performed at -85°C and 0.12 mbar for 24 hours. During the process, the water contained in the membrane and the bacteria is sublimated (**Figure 2.43**) and the bioanode subsequently dried. It was chosen not to use any exogenous cryoprotectant in order to guarantee the simplicity of the process.

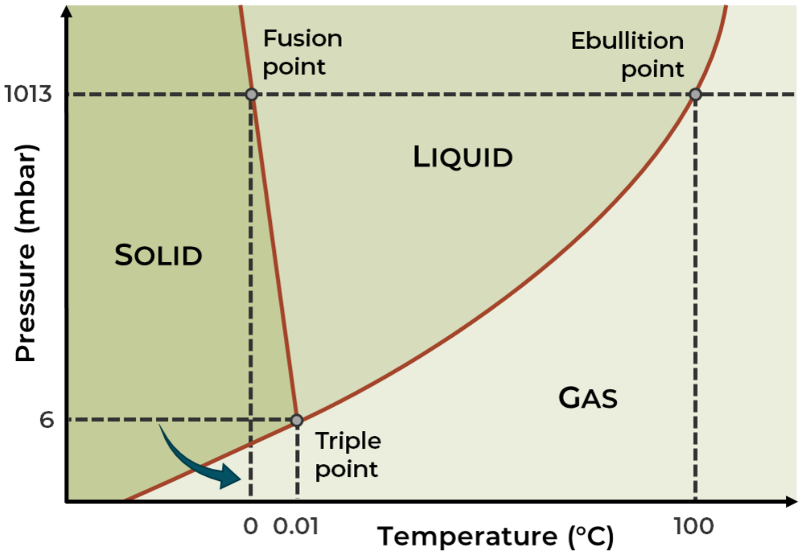
Fusion point
Ebullition point
1013
LIQUID
SOLID
Pressure (mbar)
GAS
6
Triple point
0
0.01
Temperature (°C)
100

Figure 2.43 – Simplified water phase diagram. The blue arrow depicts the sublimation taking place during the cryodesiccation.

After cryodesiccation, the macroscopic aspect of the membranes is unaffected. Possible microscopic changes in architecture are investigated with SEM (**Figure 2.44**), and no major effects relatively to the uncryodesiccated membrane either on the fibers or on the biofilm is visible.

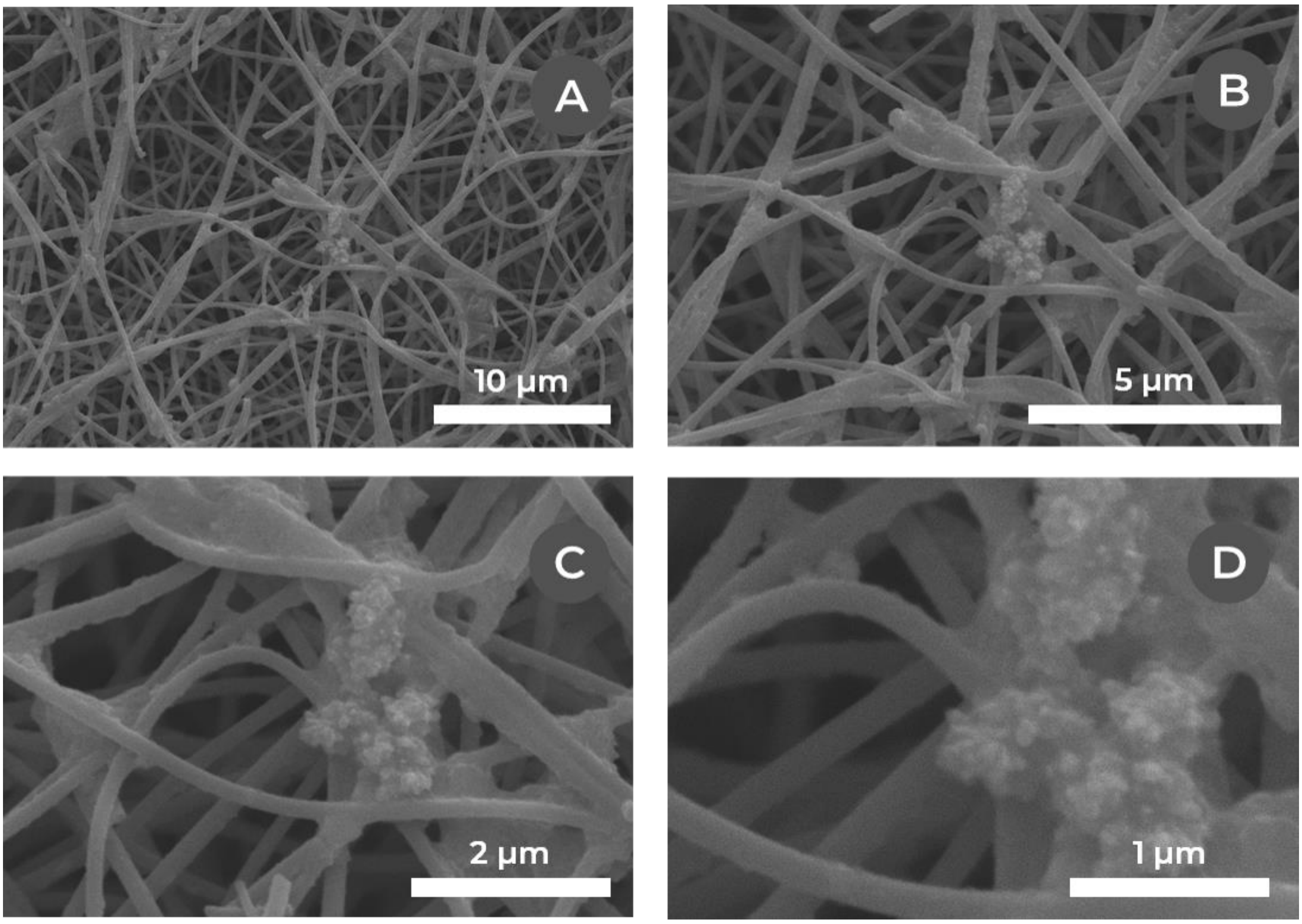
A
10 µm
B
5 µm
C
2 µm
D
1 µm

Figure 2.44 – SEM micrographs of a cryodesiccated precolonized bioanode, coated with 15 nm of gold.

The effect of the cryodesiccation on bacterial viability is subsequently explored to determine if the process is safe to the integrity of *S. oneidensis*.

2.5.2. Bacteria viability & exoelectrogenic activity

As a matter of fact, the cryodesiccation of bacterial cells let them face two stresses – freezing and drying. Although the process is widely reported as a bacterial conservation technique, these two steps may harm the bacteria as ice crystals and osmotic pressure can damage the cell wall[52].

The viability of the bacteria as well as the integrity of its cellular wall can be assessed using live/dead assays. On the other hand, cell function and survival rate may be determined by cultivating cryodesiccated bacteria on agar plate and count them.

Additionally, the integration of the cryodesiccated bioanodes into an MFC will be used to understand the effect of cryodesiccation on the bacteria exoelectrogenic activity and electrochemical performances.

2.5.2.1. Live/dead test

The viability of the bacteria after the cryodesiccation is evaluated with an Invitrogen™ LIVE/DEAD™ *Bac*Light™ Bacterial Viability Kit and observed with an epifluorescence microscope (**Figure 2.45**). The membranes are incubated 15 minutes in a live/dead mix consisting of PBS buffer and approximately [Syto 9] = 5 µm and [Propidium iodide] = 27 µm and washed 15 minutes in PBS buffer before observation.

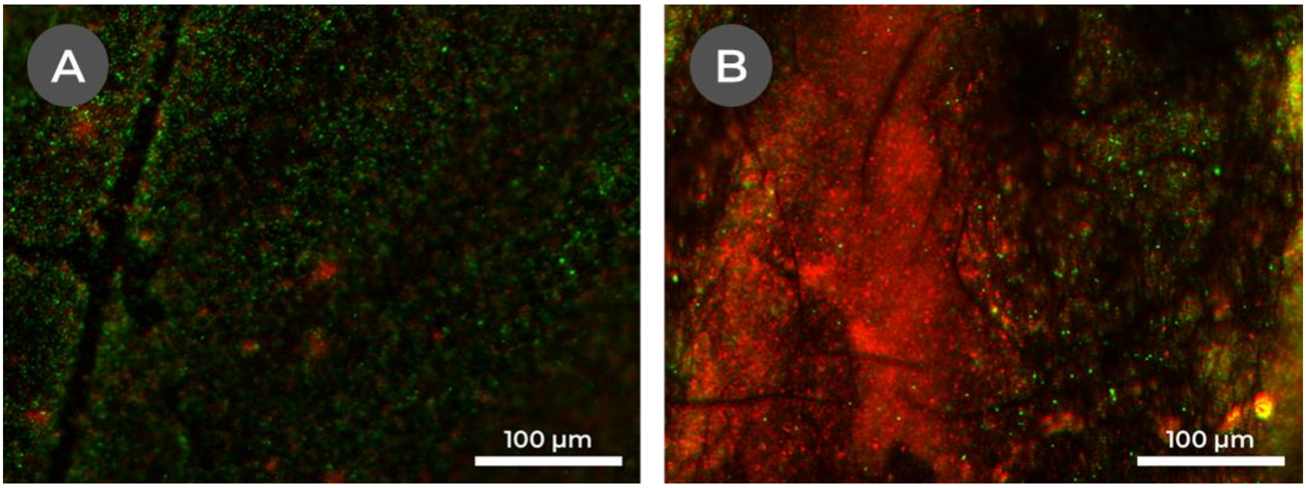

Figure 2.45 – Epifluorescence microscopy of the electrospun carbon electrode dyed with Invitrogen™ LIVE/DEAD™ *Bac*Light™ Bacterial Viability Kit (SYTO 9/Propidium iodide) (A) before & (B) after cryodesiccation. Green highlights live cells while red highlights dead cells.

The control precolonized electrospun carbon electrode (**Figure 2.45.A**) is consistent with the previous results where a balanced mix of live and dead cells is observed. The cryodesiccated membrane (**Figure 2.45.B**) visually shows more dead cells, yet numerous live ones. The cryodesiccation therefore seems to affect the integrity of the bacterial wall sufficiently mildly to let a significant fraction of the bacteria live.

2.5.2.2. Plate count

The cell survival rate after cryodesiccation can also be evaluated by comparing the number of cultivable bacteria in the cryodesiccated membrane.

Sterilized electrospun carbon was precolonized according to the protocol described in *2.3.2.3. MFC integration & electrochemical characterization* ($OD_{600,\text{initial}}$ = 0.1, MR1-L medium, 21°C, 4 days of colonization). Individual samples measured 5.0 x 5.0 mm, and were 0.477 mm thick ($V \approx 12\ mm^3$, $m \approx 1$ mg). After precolonization, half of the samples were cryodesiccated and the others kept as controls.

The bacteria were then extracted from the membranes by breaking them down in sterile conditions before ball-milling it in 5 mL of MR1 medium with glass beads for 1 hour (Ø = 2 mm, 80 rpm). The resulting medium was diluted in the range 10^{-1} to 10^{-6} and 20 µL were spread on LB-agar plates (triplicate) and incubated overnight at 30°C before counting. The number of colonies is compared between control and cryodesiccated samples (**Figure 2.46**).

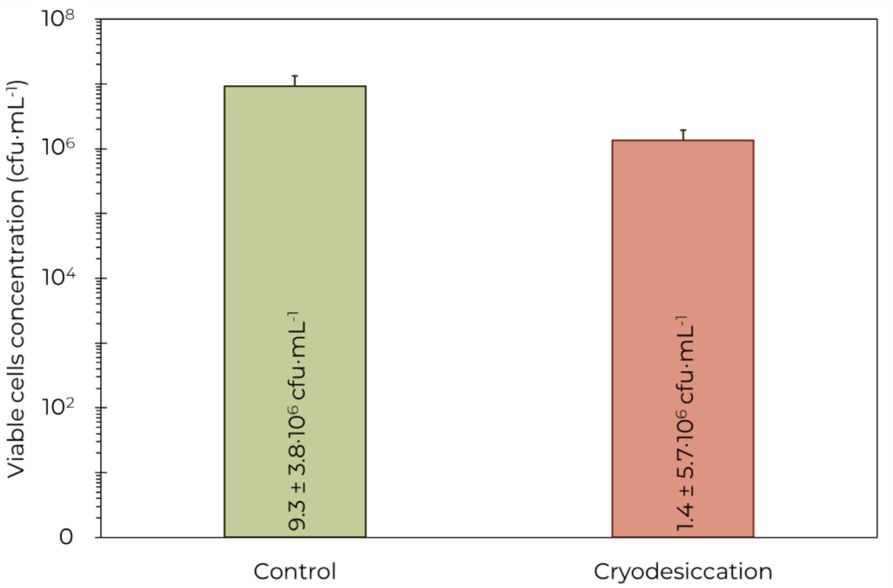

Figure 2.46 – Comparison of the concentrations of cultivable bacteria determined by plate counting on LB-agar between control & cryodesiccated precolonized electrospun carbon membranes after ball-milling of 12 mm^3 of membrane in MR-1; N = 3.

In compliance with visual estimation of the live/dead assay, after cryodesiccation many bacteria were still able to form colonies. A significant fraction of them were however still killed in the process (survival rate ~ 15 %), yet a quick recovery upon MFC integration is expected as about 15 hours are sufficient for the exponential phase of bacterial development to multiply the number of cells by an order of magnitude (**Figure 2.31**). Note that this survival rate to the process is consistent with the survival rate found for other gammaproteobacteria in the literature[54] (about 10-50 %

survival rate depending on the species, yet with the addition of skimmed milk and sodium glutamate for long-term storage). Accordingly, the pre-cryodesiccation cell density is expected to be recovered in less than a day.

2.5.2.3. MFC integration & electrochemical characterization

The cryodesiccated precolonized membrane is then integrated into the MFC reactor, poised at +0.3 V vs. Ref. and electrochemically characterized as described before (**Figure 2.47**).

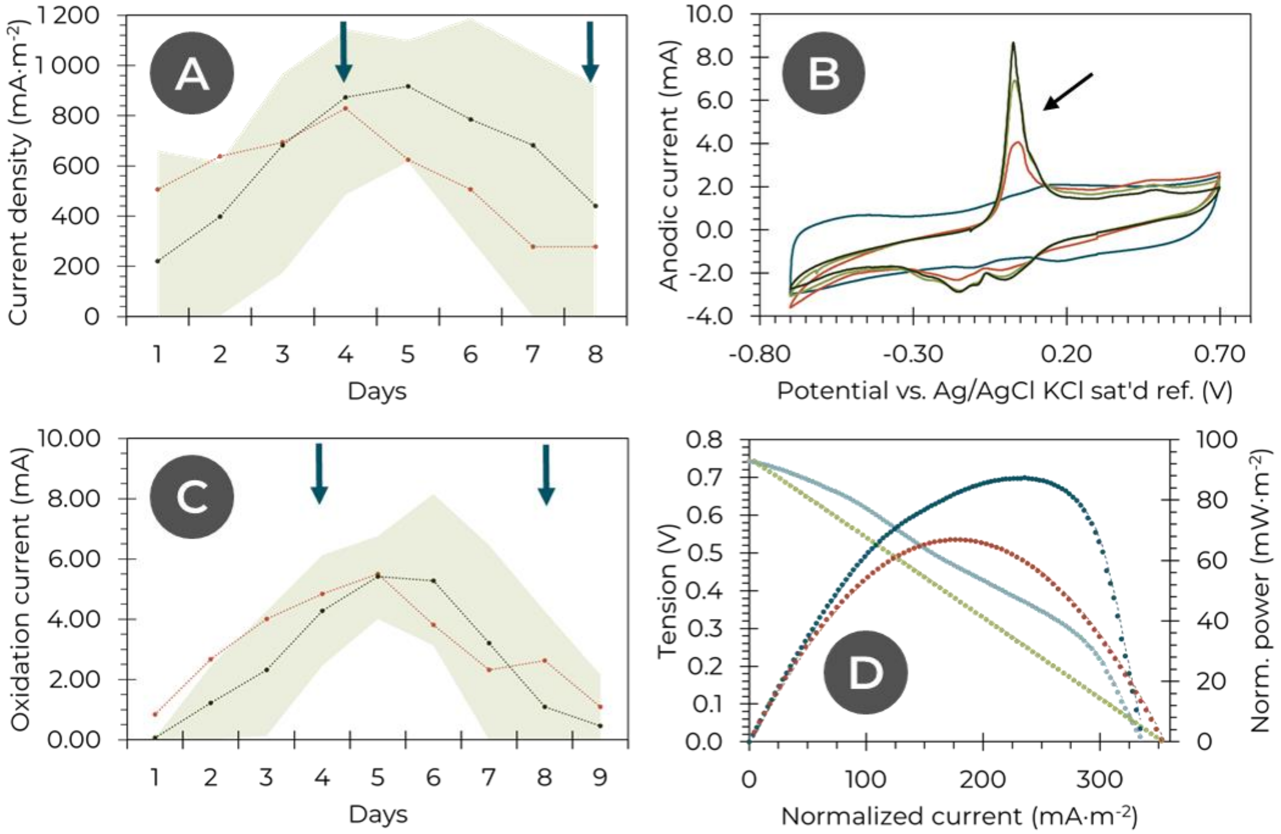

Figure 2.47 – Electrochemical characterization of a two-compartment MFC including a cryodesiccated precolonized electrospun carbon electrode polarized at +0.3 V vs. the reference (electrospun from a 10 wt% PAN in DMF solution, stabilized under air at 280°C, carbonized under argon at 940°C, precolonization & cryodesiccation as described before) as a function of time. (A) Evolution of the average current density (•); blue arrows indicate addition of 1 mmol of sodium lactate; the green zone represents maximum and minimum values. Comparison (•) with a simple precolonized bioanode; N = 6. (B) Evolution of cyclic voltammetry as a function of time (– 1st day, – 4th day, – 5th day, – 6th day); sweep rate of 1 mV·s^{-1}; 3 cycles are acquired, here is the second one; thickness of 354 µm. (C) Evolution of the average current (•) corresponding to the peak shown by the arrow on the CV; blue arrows indicate addition of 1 mmol of sodium lactate; the green zone represents maximum and minimum values. Comparison (•) with a simple precolonized bioanode; N = 6. (D) Polarization (•) and power (•) curves of an MFC at maximum current density value (here 5th day, thickness of 249 µm). Comparison with the polarization (•) and power (•) curves of a precolonized bioanode (here 5th day, thickness of 293 µm). Current and power are normalized by the geometric surface area of the electrospun carbon electrode (Ø$_{anode}$ = 1.7 cm; A$_{anode, geometrical}$ ≈ 2.27 cm^2).

The average current density (**Figure 2.47.A**) already starts at about 200 $mA \cdot m^{-2}$ and grows steadily until the fifth day where it reaches an average value of approximately 900 $mA \cdot m^{-2}$. It then slowly decreases over the next few days. Even if the current density is slightly lower for the first few days, as the cryodesiccated bacteria have to recover before reaching their full exoelectrogenic activity, the difference between the control and cryodesiccated bioanodes is rapidly erased.

Cyclic voltammetry (**Figure 2.47.B**) of the MFC including the cryodesiccated precolonized membrane exhibits almost no noticeable oxidation peak for the first day. However the recovery of a significant oxidation peak occurs after a few days, and this peak keeps on growing to quickly reach the aspect and intensity of the cyclic voltammetry of a non-cryodesiccated membrane (**Figure 2.47.C**). Indeed after 3 or 4 days the peak cyclic voltammetry oxidation current of the cryodesiccated membrane is no different than the control.

The polarization and power curves (**Figure 2.47.D**) acquired show a maximum power density of around 65 $mW \cdot m^{-2}$, and a maximum current density of approximately 350 $mA \cdot m^{-2}$. These values are similar to the one achieved for the control. The internal resistance of the cell can also be evaluated at $R_{int} \approx 47$ kΩ. This value, albeit higher than those calculated for other systems remains coherent. Importantly, the variation observed in internal resistance throughout the various studied MFCs might also result from the architecture of the cells which is not optimized nor finely controlled and may vary between the setups.

The conservation of electronic transfer efficiency between the precolonized control membranes and the cryodesiccated samples is evaluated by comparing the maximum cyclic voltammetry oxidative current of each sample (**Figure 2.48**).

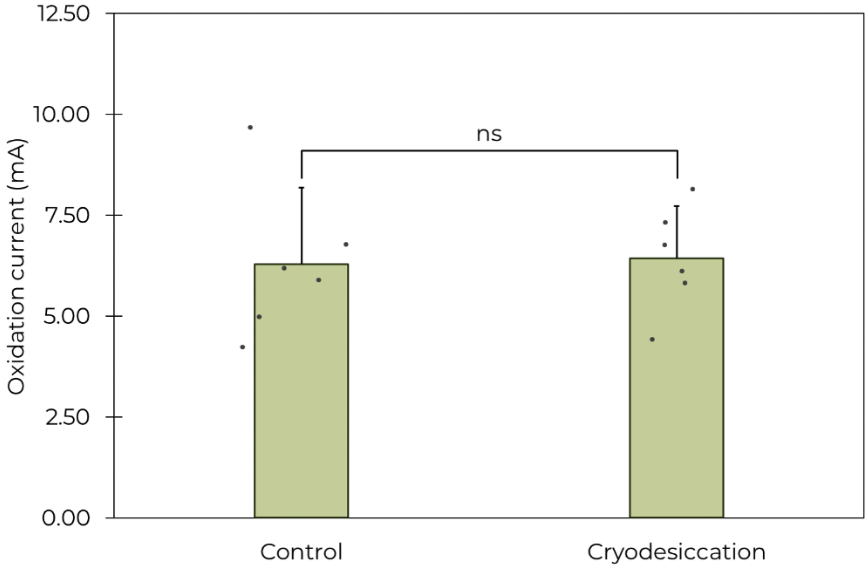

Figure 2.48 – Comparison of the maximum cyclic voltammetry oxidative current corresponding to electron transfer from bacteria to the electrospun carbon electrode between fresh and previously cryodesiccated precolonized electrospun carbon electrodes. N = 6. Points correspond to the individual measurements. Sets were compared for statistical significance.

The control membranes exhibit an average peak oxidative current of 6.04 ± 1.89 mA, while the cryodesiccated bioanodes show an average current of 6.44 ± 1.29 mA. The difference between these two experiments is not significant, therefore confirming that the cryodesiccation of a precolonized electrospun carbon electrode is not damaging to the electron transfer efficiency between *S. oneidensis* and the electrospun carbon electrode.

2.5.2.4. Post-mortem imaging

The colonization of the bioanode is evaluated by post-mortem SEM imaging (**Figure 2.49**). The clear development of a biofilm is noticeable after 10 days of operation, comparable in some extent to the other bioanodes. We may note a modification of the morphology of the biofilm which is probably due to the cryodesiccation process.

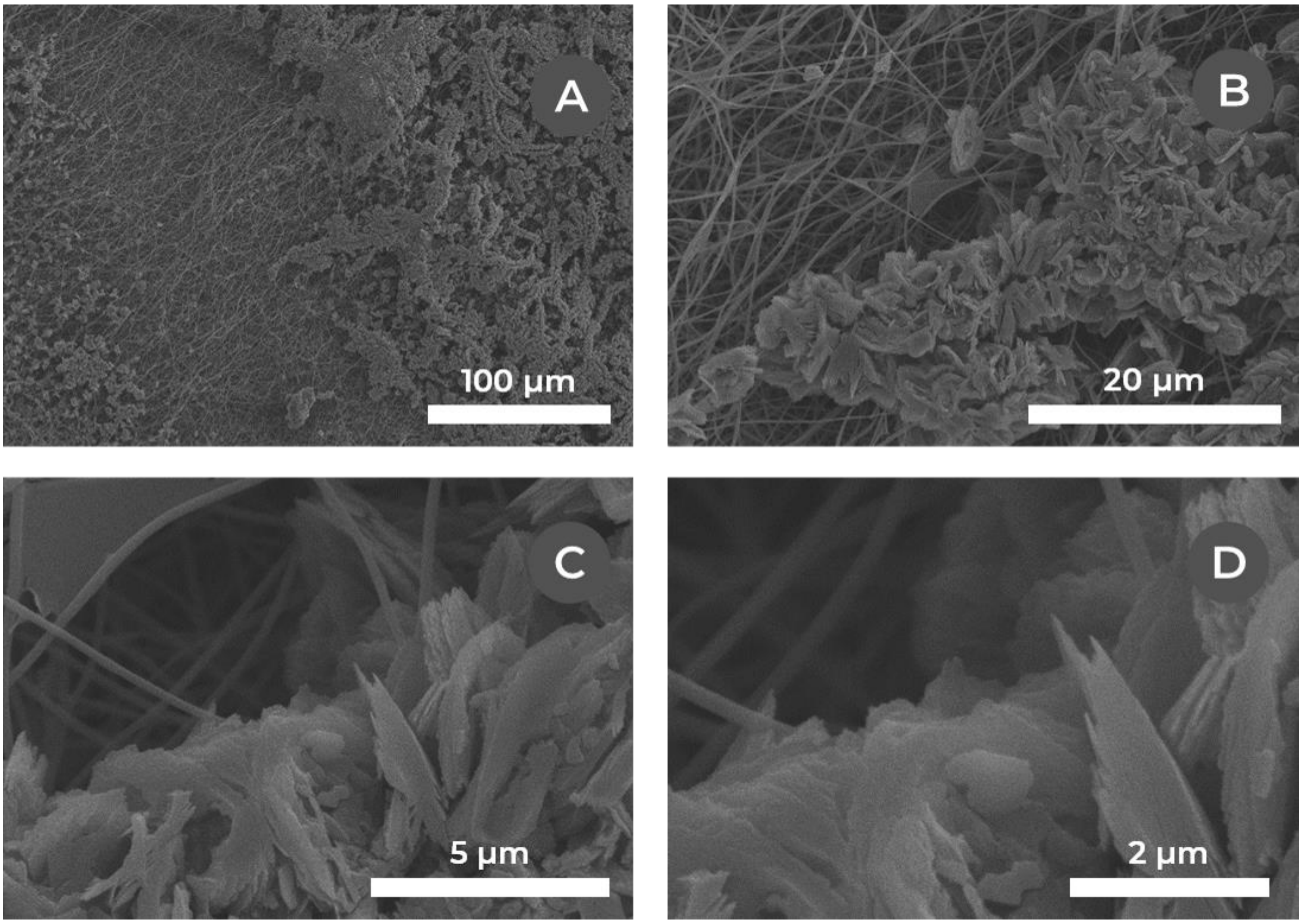

Figure 2.49 – SEM micrographs of an air-dried post-mortem bioanode based on cryodesiccated precolonized electrospun carbon electrode after 10 days of operation, polarized at +0.3 V vs. Ag/AgCl, KCl saturated reference, coated with 15 nm of gold.

Finally, the very straightforward cryodesiccation of the precolonized electrospun carbon electrodes appears as a proper way to preserve its efficiency while ensuring its shelf-life, without introducing the need for any cryoprotectant. In particular, the cryodesiccation of the membrane does not hamper the electrochemical performances of the MFC, apart from introducing a brief lag-phase during the first few days of operation. This approach guarantees the conservation of bioanodes precolonized with *Shewanella oneidensis* for on-demand power generation. Henceforth, it ensures the storage of the bioanodes presented previously, as well as of further *S. oneidensis* based bioanode architectures that may be developed.

2.6. Conclusion

Overall, we successfully synthetized carbon electrospun carbon electrodes and integrated them into a lab-scaled MFC reactor. The impregnation of the membranes by the exoelectrogenic bacteria *Shewanella oneidensis* was conducted either by in situ or ex situ (before MFC integration) colonization.

Electrospun carbon microfibers bioanodes show promising electrochemical performances despite the notable presence of a lag-phase delaying current production linked to the adaptation of the bacteria to the electrode. In situ colonized electrospun carbon membrane hence exhibits power and current densities of about 56 $mW \cdot m^{-2}$ and 240 $mA \cdot m^{-2}$ respectively – which are noticeably better than a conventional commercial carbon felt in the same conditions.

The precolonization of the membrane is efficient in reducing the length of this phase, and lays open the opportunity to design 3D ready-to-use bioanodes by stacking them. Stacked precolonized membranes therefore show better power and current densities up to 210 $mW \cdot m^{-2}$ and 1119 $mA \cdot m^{-2}$ and an even better volume power density of up to 200 to 300 $W \cdot m^{-3}$ which is comparable to the best power densities achieved in the literature for similar conditions but different anodes (~ 500 $W \cdot m^{-3}$)[49], without any reactor optimization. Nevertheless a plateau is reached upon a certain thickness due to the poor diffusion of the nutrients toward their core. This observation gives us an indication of the optimal thickness of an in-depth colonized electrospun bioanode (~ 1 mm). Additionally, the long-term stability of these systems is hampered by bacterial biofilm overgrowth.

Besides, the long-term storage of precolonized bioanodes was explored through cryodesiccation. This technique has been shown to be a simple and robust way to ensure a good conservation of the material architecture and bacteria exoelectrogenic activity, without harming its performances.

However, the major downside of this overall approach lies in its relative complexity. Even if it yields ready-to-use storable MFC bioanodes, a lot of steps are required from the electrospinning of a PAN solution to the final cryodesiccation of a precolonized carbon electrode. Therefore, the next chapters will be dedicated to the development of an electrospinning method able to swiftly produce a conductive – and eventually precolonized – membrane easily integrated into an MFC.

REFERENCES

[1] X. Huang. Fabrication and properties of carbon fibers. *Materials* **2,** 2369–2403 (2009).

[2] Z. Bashir. A critical review of the stabilisation of polyacrylonitrile. *Carbon* **29,** 1081–1090 (1991).

[3] R. C. Houtz. 'Orlon' Acrylic Fiber: Chemistry and Properties. *Text. Res. J.* **20,** 786–801 (1950).

[4] J. Schurz. Discoloration effects in acrylonitrile polymers. *J. Polym. Sci.* **28,** 438–439 (1958).

[5] A. E. Standage & R. Matkowski. Thermal oxidation of polyacrylonitrile. *Eur. Polym. J.* **7,** 775–783 (1971).

[6] A. Konkin. *Properties of carbon fibres and fields of their application*. *Elsevier Science Publishers B. V., Handbook of Composites.* **1,** (1985).

[7] H. N. Friedlander, L. H. Peebles, J. Brandrup & J. R. Kirby. On the Chromophore of Polyacrylonitrile. VI. Mechanism of Color Formation in Polyacrylonitrile. *Macromolecules* **1,** 79–86 (1968).

[8] A. J. Clarke & J. E. Bailey. Oxidation of Acrylic Fibres for Carbon Fibre Formation. *Nature* **243,** 146–150 (1973).

[9] P. J. Goodhew, A. J. Clarke & J. E. Bailey. A review of the fabrication and properties of carbon fibres. *Mater. Sci. Eng.* **17,** 3–30 (1975).

[10] J. E. Bailey & A. J. Clarke. Carbon fibres. *Chem. Br.* **6,** 484 (1970).

[11] M. Yu *et al.* Microstructural evolution in polyacrylonitrile fibers during oxidative stabilization. *J. Polym. Sci. Part B Polym. Phys.* **46,** 759–765 (2008).

[12] M. Ji, C. Wang, Y. Bai, M. Yu & Y. Wang. Structural Evolution of Polyacrylonitrile Precursor Fibers during Preoxidation and Carbonization. *Polym. Bull.* **59,** 527–536 (2007).

[13] M. Jing, C. Wang, Q. Wang, Y. Bai & B. Zhu. Chemical structure evolution and mechanism during pre-carbonization of PAN-based stabilized fiber in the temperature range of 350–600°C. *Polym. Degrad. Stab.* **92,** 1737–1742 (2007).

[14] D. Pinto. Electronic transfer within a microbial fuel cell. Better understanding of Experimental and Structural Parameters at the Interface between Electro-active Bacteria and Carbon-based Electrodes. *École doctorale Physique et chimie des matériaux (Paris)* (Sorbonne Université, 2016).

[15] K. Sakai, S. Iwamura, R. Sumida, I. Ogino & S. R. Mukai. Carbon paper with a high surface area prepared from carbon nanofibers obtained through the liquid pulse injection technique. *ACS Omega* **3,** 691–697 (2018).

[16] C. Kim *et al.* Raman spectroscopic evaluation of polyacrylonitrile-based carbon nanofibers prepared by electrospinning. *J. Raman Spectrosc.* **35,** 928–933 (2004).

[17] D. R. Lide. *CRC handbook of chemistry and physics*. (CRC Press, 1999).

[18] E. Frackowiak & F. Béguin. Carbon materials for the electrochemical storage of energy in capacitors. in (2001).

[19] I. Dahl *et al.* Anomalous Increase in Carbon Capacitance at Pore Sizes Less Than 1 Nanometer. *Science* **313,** 1760–1763 (2006).

[20] B. Trémillon. *Électrochimie analytique et réactions en solution*. (1993).

[21] S. J. Konopka & B. McDuffie. Diffusion coefficients of ferri- and ferrocyanide ions in aqueous media, using twin-electrode thin-layer electrochemistry. *Anal. Chem.* **42,** 1741–1746 (1970).

[22] W. J. Blaedel & R. C. Engstrom. Investigations of the ferricyanide-ferrocyanide system by pulsed rotation voltammetry. *Anal. Chem.* **50,** 476–479 (1978).

[23] Z. Zhang, S. Schwartz, L. Wagner & W. Miller. A Greedy Algorithm for Aligning DNA Sequences. *J. Comput. Biol.* **7,** 203–214 (2000).

[24] E. P. Ivanova, S. Flavier & R. Christen. Phylogenetic relationships among marine Alteromonas-like proteobacteria: emended description of the family Alteromonadaceae and proposal of Pseudoalteromonadaceae fam. nov., Colwelliaceae fam. nov., Shewanellaceae fam. nov., Moritellaceae fam. nov., Ferr. *Int. J. Syst. Evol. Microbiol.* **54,** 1773–1788 (2004).

[25] M. T. MacDonell & R. R. Colwell. Phylogeny of the Vibrionaceae, and Recommendation for Two New Genera, Listonella and Shewanella. *Syst. Appl. Microbiol.* **6,** 171–182 (1985).

[26] E. Marsili *et al.* Shewanella secretes flavins that mediate extracellular electron transfer. *PNAS* **105,** 3968–3973 (2008).

[27] O. Bretschger *et al.* Current production and metal oxide reduction by Shewanella oneidensis MR-1 wild type and mutants. *Appl. Environ. Microbiol.* **73,** 7003–7012 (2007).

[28] B. E. Logan & K. Rabaey. Conversion of Wastes into Bioelectricity and Chemicals by Using Microbial Electrochemical Technologies. *Science* **337,** 686 LP – 690 (2012).

[29] D. Baron, E. LaBelle, D. Coursolle, J. A. Gralnick & D. R. Bond. Electrochemical measurement of electron transfer kinetics by Shewanella oneidensis MR-1. *J. Biol. Chem.* **284,** 28865–28873 (2009).

[30] H. Lodish *et al. Molecular Cell Biology. 4th edition*. *Molecular Cell Biology. 4th edition* (2000).

[31] P. G. Dennis *et al.* Anode potential influences the structure and function of anodic electrode and electrolyte-associated microbiomes. *Sci. Rep.* **6,** 39114 (2016).

[32] S. Ishii *et al.* Microbial population and functional dynamics associated with surface potential and carbon metabolism. *Isme J.* **8,** 963 (2013).

[33] D. A. Finkelstein, L. M. Tender & J. G. Zeikus. Effect of Electrode Potential on Electrode-Reducing Microbiota. *Environ. Sci. Technol.* **40,** 6990–6995 (2006).

[34] D. Pinto, T. Coradin & C. Laberty-Robert. Effect of anode polarization on biofilm formation and electron transfer in Shewanella oneidensis/graphite felt microbial fuel cells. *Bioelectrochemistry* **120,** 1–9 (2018).

[35] P. Mitchell. Coupling of Phosphorylation to Electron and Hydrogen Transfer by a Chemi-Osmotic type of Mechanism. *Nature* **191,** 144–148 (1961).

[36] J. M. Myers & C. R. Myers. Role for outer membrane cytochromes OmcA and OmcB of Shewanella putrefaciens MR-1 in reduction of manganese dioxide. *Appl. Environ. Microbiol.* **67,** 260–269 (2001).

[37] J. M. Myers & C. R. Myers. Role of the tetraheme cytochrome CymA in anaerobic electron transport in cells of Shewanella putrefaciens MR-1 with normal levels of menaquinone. *J. Bacteriol.* **182,** 67–75 (2000).

[38] J. N. Roy *et al.* Applied Electrode Potential Leads to Shewanella oneidensis MR-1 Biofilms Engaged in Direct Electron Transfer. *J. Electrochem. Soc.* **160,** H866–H871 (2013).

[39] C. L. Reardon *et al.* Role of outer-membrane cytochromes MtrC and OmcA in the biomineralization

of ferrihydrite by Shewanella oneidensis MR-1. *Geobiology* **8,** 56–68 (2010).

[40] L. Shi *et al.* Molecular underpinnings of Fe(III) oxide reduction by Shewanella oneidensis MR-1. *Front. Microbiol.* **3,** 1–10 (2012).

[41] L. Shi *et al.* The roles of outer membrane cytochromes of Shewanella and Geobacter in extracellular electron transfer. *Environ. Microbiol. Rep.* **1,** 220–227 (2009).

[42] L. Shi, T. C. Squier, J. M. Zachara & J. K. Fredrickson. Respiration of metal (hydr)oxides by Shewanella and Geobacter: a key role for multihaem c-type cytochromes. *Mol. Microbiol.* **65,** 12–20 (2007).

[43] S. Pirbadian *et al.* Shewanella oneidensis MR-1 nanowires are outer membrane and periplasmic extensions of the extracellular electron transport components. *PNAS* **111,** 12883–8 (2014).

[44] N. Mehrban & J. Bowen. 5 - Monitoring biomineralization of biomaterials in vivo. in (ed. Narayan, R. J. B. T.-M. and E. of B. and their P. I. V.) 81–110 (Woodhead Publishing, 2017).

[45] M. Heldal, S. Norland & O. Tumyr. X-ray microanalytic method for measurement of dry matter and elemental content of individual bacteria. *Appl. Environ. Microbiol.* **50,** 1251–1257 (1985).

[46] G. Reguera *et al.* Biofilm and nanowire production leads to increased current in Geobacter sulfurreducens fuel cells. *Appl. Environ. Microbiol.* **72,** 7345–7348 (2006).

[47] A. P. Borole *et al.* Electroactive biofilms: Current status and future research needs. *Energy Environ. Sci.* **4,** 4813–4834 (2011).

[48] Y. Xiao *et al.* Extracellular polymeric substances are transient media for microbial extracellular electron transfer. *Sci. Adv.* **3,** (2017).

[49] B. R. Ringeisen *et al.* High power density from a miniature microbial fuel cell using Shewanella oneidensis DSP10. *Environ. Sci. Technol.* **40,** 2629–2634 (2006).

[50] S. F. Freeze-Drying and Cryopreservation of Bacteria BT - Cryopreservation and Freeze-Drying Protocols. in (eds. Day, J. G. & Pennington, M. W.) 21–30 (Humana Press, 1995).

[51] S. Wenfeng, R. Gooneratne, N. Glithero, R. J. Weld & N. Pasco. Appraising freeze-drying for storage of bacteria and their ready access in a rapid toxicity assessment assay. *Appl. Microbiol. Biotechnol.* **97,** 10189–10198 (2013).

[52] Y. Miyamoto-Shinohara, J. Sukenobe, T. Imaizumi & T. Nakahara. Survival of freeze-dried bacteria. *J. Gen. Appl. Microbiol.* **54,** 9–24 (2008).

[53] M. Mohammadifar & S. Choi. On-Demand Micro-Power Generation from an Origami-Inspired Paper Biobattery Stack. *Batteries* **4,** 14 (2018).

[54] Y. Miyamoto-Shinohara *et al.* Survival Rate of Microbes after Freeze-Drying and Long-Term Storage. *Cryobiology* **41,** 251–255 (2000).

[55] K. M. Thormann, R. M. Saville, S. Shukla, D. A. Pelletier & A. M. Spormann. Initial Phases of biofilm formation in Shewanella oneidensis MR-1. *J. Bacteriol.* **186,** 8096–8104 (2004).

3

ONE-STEP ELECTROSPUN CONDUCTIVE FIBERS

TABLE OF CONTENTS

Chapter 3. One-step electrospun conductive fibers 169

3.1. Introduction & objectives 169

3.2. Lab-made conductive membrane preparation 170

3.2.1. Electrospinning of a composite carbon–polymer fibers network 170

3.2.2. Lab-made carbon nanofibers load 170

3.2.2.1. SEM imaging 173

3.2.2.2. Electrical conductivity 173

3.2.3. Carbon black load 175

3.2.3.1. SEM imaging 176

3.2.3.2. Electrical conductivity 178

3.2.3.3. Electrochemical characterization 179

3.3. Dual electrospun network & composite carbon–polymer fibers 182

3.3.1. Experimental procedure 182

3.3.2. Dual electrospun mat characterization 184

3.3.2.1. SEM imaging 184

3.3.2.2. Electrical conductivity 185

3.4. Bacteria viability on composite carbon–polymer fibers 187

3.4.1. Live/dead assay 187

3.4.2. Electrochemical activity 188

3.4.2.1. MFC integration & electrochemical characterization 188

3.4.2.2. Post-mortem imaging 192

3.5. Conclusion 194

References 195

CHAPTER 3. ONE-STEP ELECTROSPUN CONDUCTIVE FIBERS

3.1. Introduction & objectives

Chapter 2 has highlighted the promising performances of an MFC bioanode based on electrospun microfibers. Nevertheless, some downsides to this architecture still remain. Among them, the numerous synthesis steps required to convert a PAN solution to a conductive nonwoven carbon microfibers mat is especially inconvenient. Moreover, the required heating stages prevent any incorporation of living cells in the first steps of the process – especially during the electrospinning – as they would subsequently die.

Results recently highlighted in the literature[1]–[3] report the practical application of electrospinning to synthetize composite particle–polymer fibers mats. Amongst the studied fibers, carbon–polymer composites[1],[3] appear as a suitable approach to synthetize electrospun conductive membranes with a minimal number of steps – and in particular without any heat treatment.

Accordingly, this chapter focuses on the development of a process generating a conductive electrospun fibers mat in as little steps as possible, whilst guaranteeing the biocompatibility of the structure. Furthermore, a particular focus will be addressed on paving the way for the latter development of a process able to encapsulate bacteria directly during the electrospinning phase. All these endeavors are undertaken while keeping in mind the simplicity of the process, aiming for a one-step synthesis of the electrospun mat.

Therefore, the synthesis of a composite carbon–polymer fibers mat is first addressed. Two different carbon loads are compared, either commercial carbon black or anisotropic particles prepared from the electrospun carbon membranes prepared in Chapter 2. The architectures and electrical conductivities of the mats are then characterized.

A setup is then developed to simultaneously electrospin two different solutions, one conductive and the other non-conductive. The goal is to provide a platform for the future development of conductive electrodes including a low-conductivity component. The electrical conductivity and architecture of the dual mat is also evaluated.

Both the bacterial survival rate and electrochemical activity are evaluated on those composite electrospun membranes.

3.2. Lab-made conductive membrane preparation

Composite electrospun carbon–polymer fibers mats have been recently reported in the literature[1],[3] as a relevant way to synthetize conductive microfibers without any heat treatment. This part accordingly focuses on the application of this technique to produce electrospun mats appropriate for MFC applications.

3.2.1. Electrospinning of a composite carbon–polymer fibers network

The composite fibers presented will be electrospun from a polymer binder solution – polyacrylonitrile or poly(ε-caprolactone) (**Figure 3.1**) – including either commercial carbon black or anisotropic carbon particles prepared from milled electrospun carbon membranes.

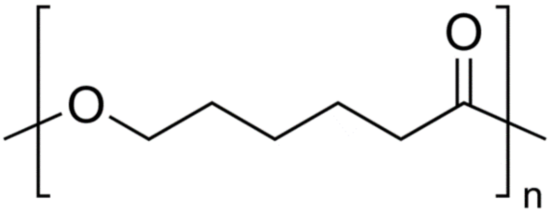

Figure 3.1 – Poly(ε-caprolactone) structure

The polyacrylonitrile (PAN, M_w ~ 150 000), the poly(ε-caprolactone) (PCL, M_w ~ 14 000) and poly(ethylene glycol) (PEG, M_n ~ 3000) were purchased from Sigma-Aldrich (USA). The chloroform (99.0-99.4% stabilized, AnalaR NORMAPUR® ACS, Reag. Ph. Eur. analytical reagent, used as received) and DMF (≥99.8%, AnalaR NORMAPUR® ACS, Reag. Ph. Eur. analytical reagent, used as received) were purchased from VWR. The Vulcan XC-72R Carbon black (CB) purchased from FuelCellStore.

3.2.2. Lab-made carbon nanofibers load

Firstly, we attempted to synthetize a conductive composite carbon–polymer electrospun mat from anisotropic conductive carbon nanorods – a few micrometers in length and a few hundred nanometers in width – obtained by milling the electrospun carbon membranes presented previously.

The goal of this approach was to use a carbon material readily available in the lab to produce a material which would hopefully reach electrical percolation once electrospun to produce a conductive composite mat.

Electrospun carbon membrane milling: The electrospun carbon membranes from Chapter 2 (surface conductivity: $\sigma_S \sim 10^{-1}$ S·cm^{-1}; transverse conductivity: $\sigma_T \sim 10^{-2}$ S·cm^{-1}, pelletized conductivity $\sigma_{bulk} \sim 1$ S·cm^{-1}) were grinded by ball-milling (Ø = 2 cm, 80 rpm, 1 week) to yield a fine black powder hereafter designated as the “milled carbon nanofibers”. SEM imaging of the powder (**Figure 3.2.A-B**) reveals a compact arrangement of short nanofibers. Note (**Figure 3.2.C**) that the milled carbon nanofibers are smaller in diameter (137 ± 27 nm vs. 271 ± 61 nm) than the samples presented in Chapter 2. This variation could either be attributed to a variation relative to the ambient electrospinning conditions or also probably to a loss of mass during the milling process and breakage of the fibers. Nevertheless, the fibers diameter distribution remains remarkably monodisperse. Under those conditions, the milled carbon nanofibers also exhibit a relatively short length of 890 ± 611 nm. The distribution is here again relatively fine, with very few fibers longer than 3 µm.

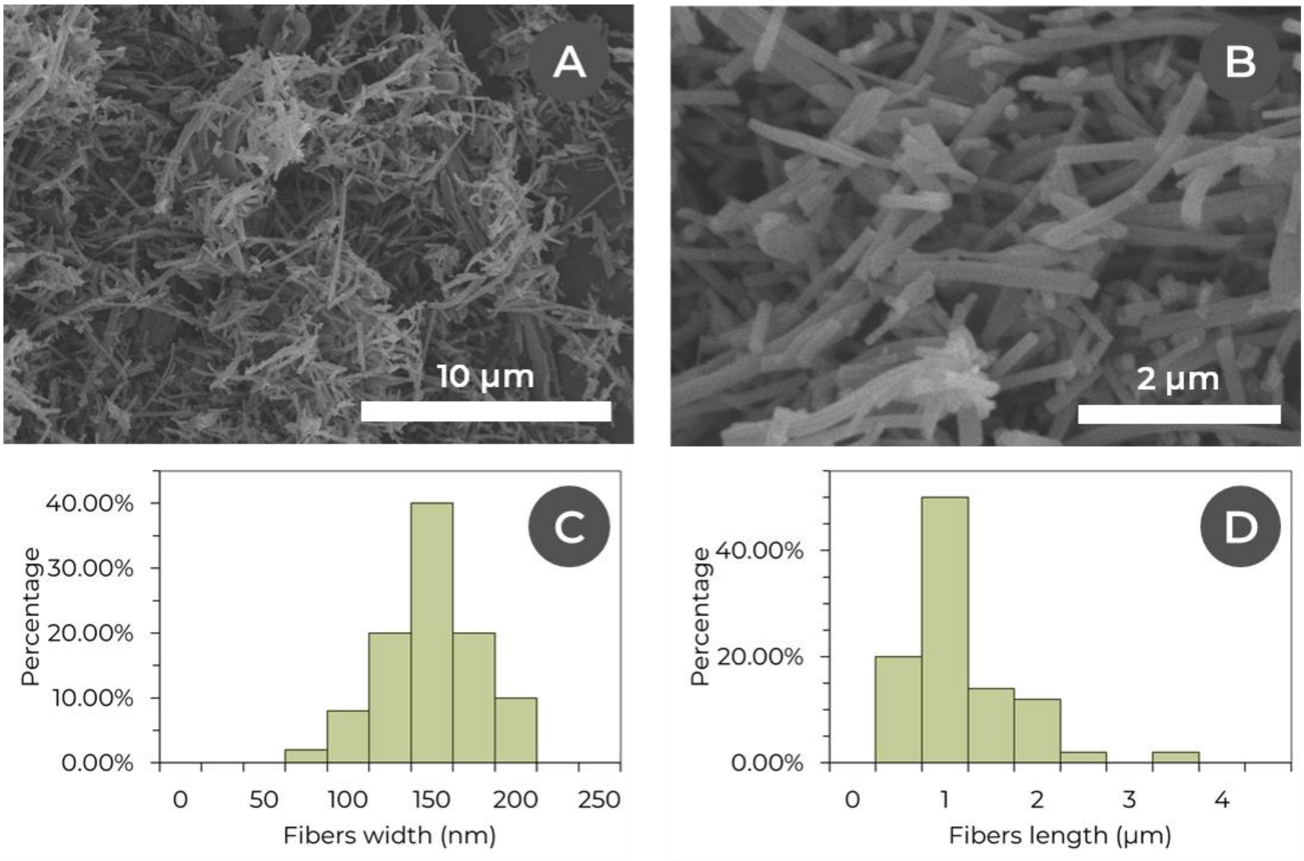

Figure 3.2 – (A), (B) SEM micrographs of the milled carbon nanofibers powder; (C) Fibers width & (D) Fibers length distributions; N = 50.

Solution formulation: Series of formulations with an increasing weight ratio of milled carbon nanofibers versus binder (PCL) were prepared (**Table 3.1**). The milled carbon nanofibers were firstly dispersed in the solvent in an ultrasonic bath (ultrasonic effective power: 75 W) for 30 minutes before adding the PCL polymer binder and PEG (for better carbon dispersion) and stirring overnight at room temperature until full dissolution.

Table 3.1 – Formulations of milled carbon fiber–PCL solutions for composite electrospinning

Carbon proportion in the dry fibers	Milled carbon nanofibers	PCL binder	Solvent	Additives
1.4 %	0.15 wt%	9 wt%	90:10 (w/w) Chloroform & DMF	PEG 2 wt%
6.4 %	0.75 wt%			
12.0 %	1.50 wt%			
15.4 %	2.00 wt%			
21.4 %	3.00 wt%			
27.3 %	3.00 wt%	6 wt%		

These solutions are electrospun on a grounded aluminum foil on a roller using the Electrospinz ES1™ generator and apparatus (**Figure 3.3**). The electrospinning parameters are set as follow:

- **Electric field**: between 1-2kV·cm^{-1} set by tuning the voltage and distance between the spinneret tip and the collector respectively in the range 13-21 kV and 13 cm. Higher carbon loads required higher electric fields. The current never exceeded 9 μA;
- **Injection speed**: 3.5 mL·h^{-1} using a Fisherbrand™ syringe pump and a Terumo® 10cc Eccentric Luer Tip syringe equipped with a blunt-end needle ($Ø_{internal}$ = 0.75 mm);
- **Volume**: up to 3.5 mL were injected, apart for the 50% ratio solution which was difficult to electrospin and collected a far less fibers;
- **Temperature**: 21°C thermostatted by the lab air-conditioner;
- **Relative humidity**: in the range of 30 to 35%. Higher values were avoided by running the setup in a closed poly(methyl acrylate) box connected to the lab dry compressed air outlet;
- **Substrate**: aluminum foil fixed on a roller with a speed set at around 400 rpm.

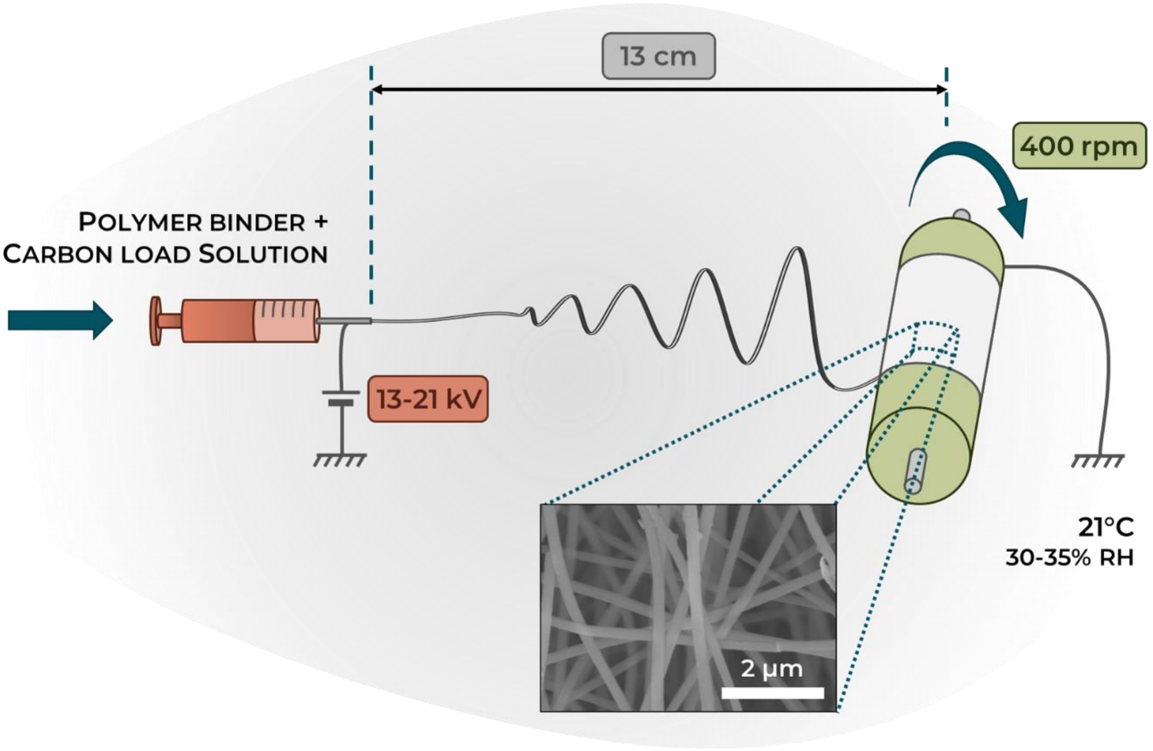

Figure 3.3 – Overview of a composite electrospinning setup.

The resulting membrane is easily peeled of the aluminum foil after the process.

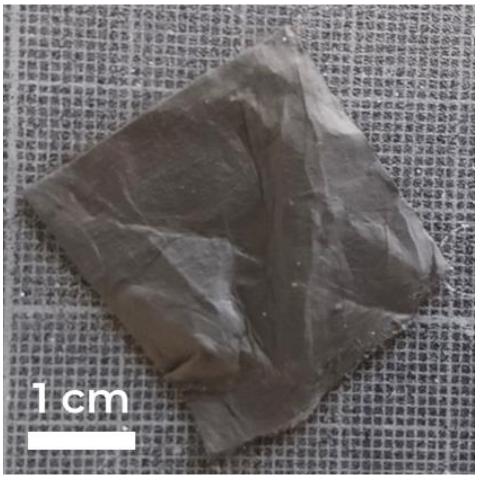

Figure 3.4 – Electrospun PCL 6 wt% + Milled carbon nanofibers 3 wt% + PEG 2 wt% membrane.

The self-standing membranes (thickness up to ~ 300 µm) are grey-black and darker as the carbon content increases. They are easy to handle and resistant to tearing and bending.

3.2.2.1. SEM imaging

The architecture of the electrospun fibers is subsequently characterized by SEM (**Figure 3.5**). The micrographs indeed show an integration of milled carbon nanofibers along the PCL binder fibers. The carbon nanofibers tend to align longitudinally with the binder. However, even at high concentration, the milled carbon nanofibers do not percolate in a satisfying way. Any electrical conductivity will be produced by interfiber contacts and will result in poor performances, even at high carbon loads while the electrospinning process is unstable and difficult.

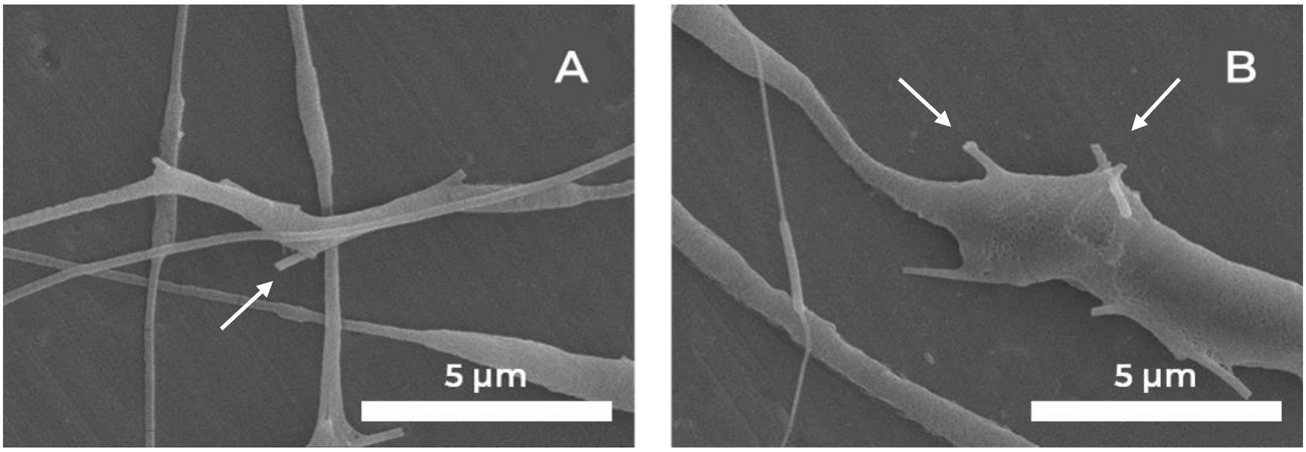

Figure 3.5 – SEM micrographs of composite electrospun fibers (electrospun from a solution of PCL 6 wt% + Milled carbon nanofibers 3 wt% + PEG 2 wt% in 90:10 (w/w) Chloroform & DMF). The milled carbon nanofibers are shown by the arrows.

The electrical conductivity of the mats is therefore evaluated.

3.2.2.2. Electrical conductivity

The surface conductivity of the fibers is measured by a two-electrode setup (**Figure 3.6.A**).

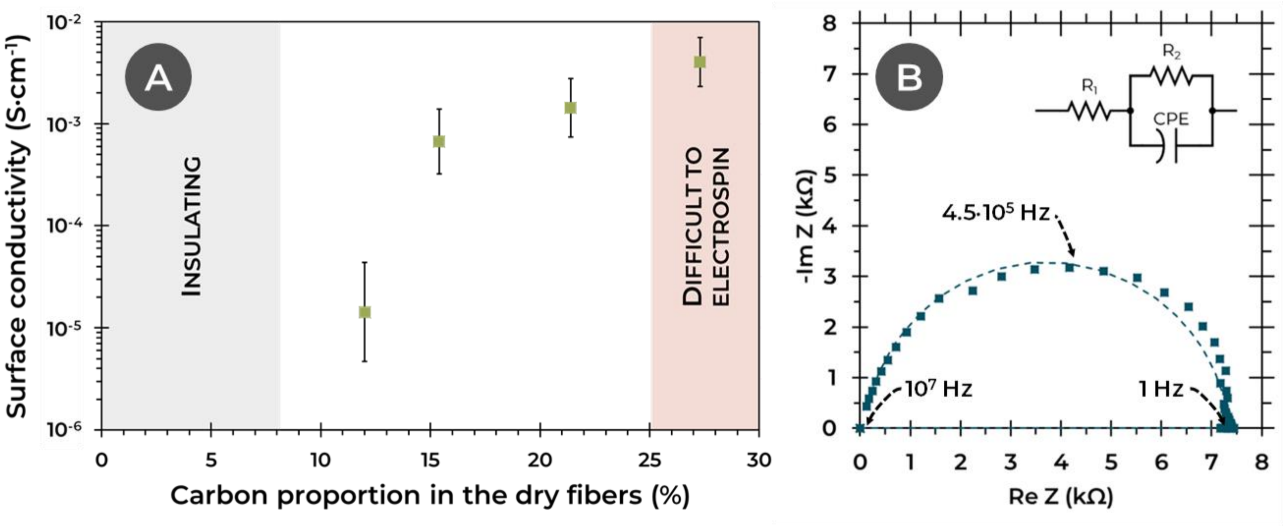

Figure 3.6 – (A) Evolution of the surface conductivity evaluated by a two-electrode setup of a composite PCL/Milled carbon nanofibers electrospun mat against the carbon proportion in the dry fibers calculated from the electrospun solution formulation. (B) Shape of the impedance spectroscopy (amplitude of 100 mV) behavior of a composite PCL/Milled carbon nanofibers electrospun mat (here electrospun from a solution of PCL 6 wt% + Milled carbon nanofibers 3 wt% + PEG 2 wt% in 90:10 (w/w) Chloroform & DMF; thickness of 289 µm). The fit represented by the dotted line corresponds to the equivalent circuit model in the upper right corner with the following parameters: R_1 = 85 ± 7.5 Ω; R_2 = 7273 ± 20 Ω; Constant Phase Element (CPE) of impedance $Z = \frac{1}{Q\cdot(i\omega)^{\alpha}}$ with $Q = 1.13\cdot10^{-10} \pm 0.07\cdot10^{-10}$ $S\cdot s^{\alpha}$ & $\alpha = 0.935 \pm 0.004$.

A measurable surface electrical conductivity (σ_S) is achieved for samples loaded with at least 12 % of carbon nanofibers in the dry mat. As expected, the composite electrospun membranes however exhibit a poor electrical conductivity, at best more than one order of magnitude lower than the electrospun carbon membrane themselves ($4\cdot10^{-3}$ vs. ~ 10^{-1} S·cm^{-1}), at the cost of an unstable and difficult electrospinning process.

The study of the samples by impedance spectroscopy does not exhibits a pure resistance value like for electrospun carbon electrodes but rather a depressed half-circle on the Nyquist plot (**Figure 3.6.B**). The observed behavior can be interpreted as the impedance response of a resistance R_1 in series with a resistance R_2 in parallel with a constant phase element (CPE). The CPE can be understood as a non-perfect capacitor of impedance $Z = \frac{1}{Q\cdot(i\omega)^{\alpha}}$. This shows that the membrane behavior is not purely resistive and also exhibits a capacitive participation, probably due to the complexity of the conductive pathways in the mat. By considering the resistance for this sample equal to the upper intersection of the real axis with the half circle ($R = R_1 + R_2 \approx 7$ kΩ), the transverse conductivity can be evaluated at the very low value of $\sigma_T \sim 10^{-6}$ S·cm^{-1}.

Following these results, it was decided not to select these lab-made milled carbon nanofibers as a proper carbon load for further applications. However, this study demonstrates the possibility to electrospin highly anisotropic conductive materials at high proportions relatively to the polymer binder.

3.2.3. Carbon black load

Commercial Vulcan XC-72R Carbon black (CB) then evaluated as the carbon load. Recent reports[1],[3] indeed show the feasibility of the preparation of composite carbon–polymer nanofibers mats by electrospinning using this carbon powder and various polymer binders.

Solution formulation: Series of formulations with an increasing weight ratio of carbon black against binder were prepared (**Table 3.2**). The carbon black was firstly dispersed in the solvent in an ultrasonic bath (ultrasonic effective power: 75 W) for 30 minutes before adding the PAN polymer binder and stirring overnight at room temperature until full dissolution.

Table 3.2 – Formulations of Carbon black–PAN solutions for composite electrospinning

Carbon proportion in the dry fibers	Carbon black	PAN binder	Solvent
28.6 %	4.0 wt%	10 wt%	DMF
37.5 %	6.0 wt%		
44.4 %	8.0 wt%		
44.4 %	5.6 wt%	7 wt%	
50.0 %	7.0 wt%		

These solutions are electrospun on a grounded aluminum foil on a roller using the Electrospinz ES1™ generator and apparatus (**Figure 3.3**). The electrospinning parameters are set as follow:

- **Electric field**: around 1.5 $kV\cdot cm^{-1}$ set by tuning the voltage and distance between the spinneret tip and the collector respectively in the range 16-21 kV and 13 cm. The electric field was tuned to reach an equilibrium between the injection and extrusion speeds. The current never exceeded 9 µA;
- **Injection speed**: 3.5 $mL\cdot h^{-1}$ using a Fisherbrand™ syringe pump and a Terumo® 10cc Eccentric Luer Tip syringe equipped with a blunt-end needle ($Ø_{internal}$ = 0.75 mm);
- **Volume**: around 3.5 mL of solution is injected to ensure the deposition of a thick self-standing membrane, apart from the PAN 10 wt% + CB 8 wt% which was difficult to electrospin;
- **Temperature**: 21°C thermostatted by the lab air-conditioner;
- **Relative humidity**: in the range of 30 to 35%. Higher values were avoided by running the setup in a closed poly(methyl acrylate) box connected to the lab dry compressed air outlet;
- **Substrate**: aluminum foil fixed on a roller with a speed set at around 400 rpm.

The membranes are easily peeled off the aluminum after the electrospinning.

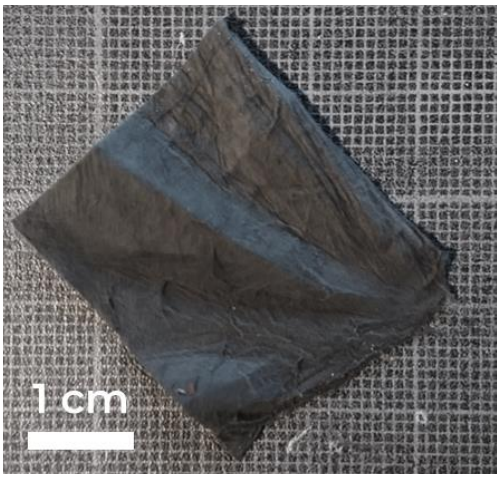

Figure 3.7 – Electrospun PAN 10 wt% + CB 6 wt% membrane.

The self-standing electrospun membrane (thickness up to ~ 300 µm) are dark grey to black as the carbon content increases. They are easy to handle and relatively resistant to tearing and bending.

3.2.3.1. SEM imaging

The architecture of the electrospun fibers is then characterized by SEM (**Figure 3.8**). For the PAN 10 wt% + CB 6 wt% sample, the fibers exhibit a very rough aspect and an average diameter higher than observed for regular electrospun PAN membranes (1.72 ± 0.43 µm vs. 0.45 ± 0.10 µm), which is consistent with the integration of carbon black along the polymer binder. Moreover, the carbon black particles seem to be integrated into the whole length of the fibers and to be homogeneously distributed along it.

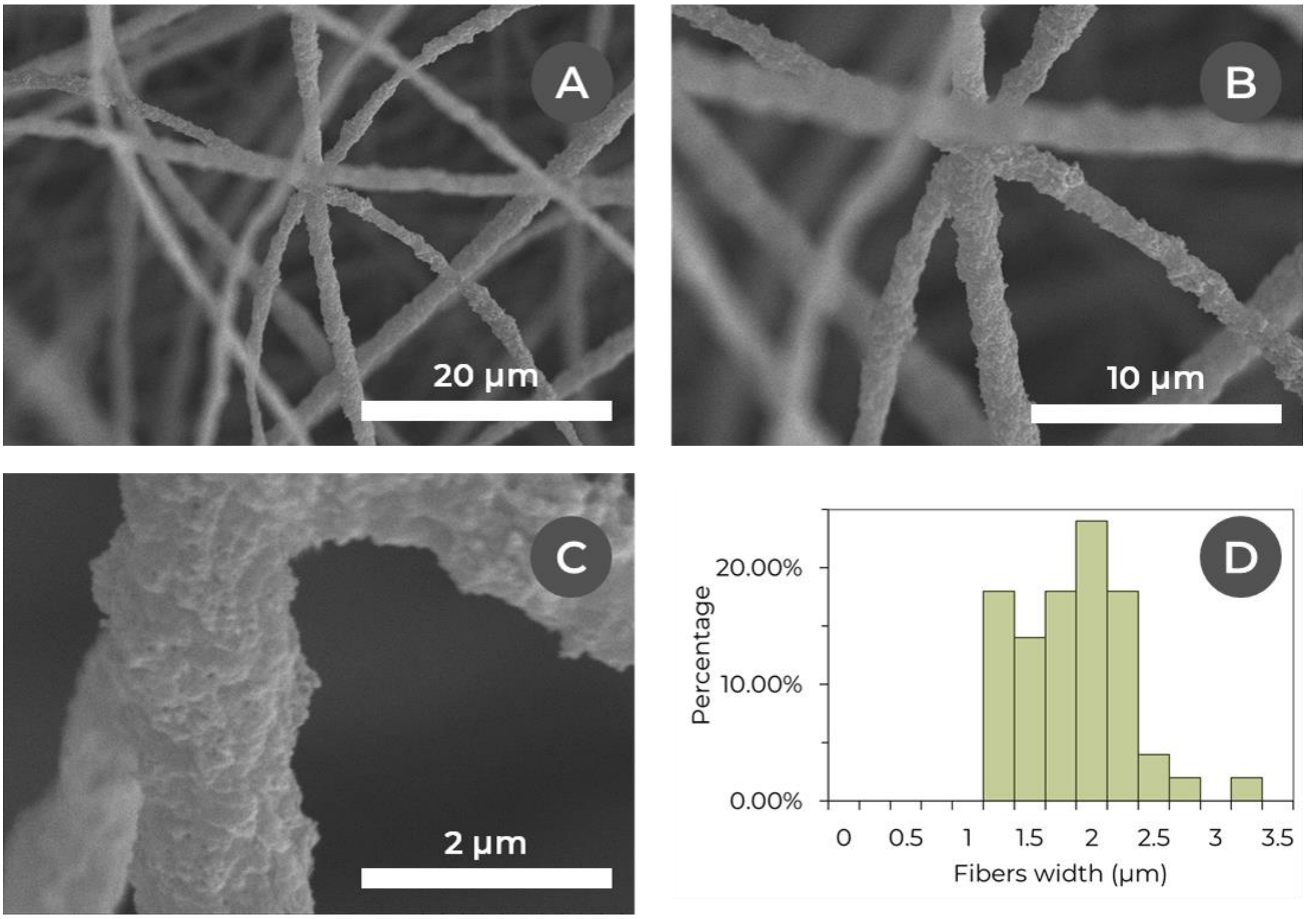

Figure 3.8 – (A), (B), (C) SEM micrographs of composite electrospun fibers (electrospun from a solution of PAN 10 wt% + Vulcan XC-72R Carbon black 6 wt% in DMF) & (D) Diameter distribution of the fibers.

Moreover, imaging of fibers including various concentrations of carbon black (**Figure 3.9**) reveals that a full homogeneous coverage of the polymer fibers already occurs from a 37.5 % proportion of carbon in the dry fibers (PAN 10 wt% + CB 6 wt% in DMF). The PAN 10 wt% + CB 8 wt% formulation is even less homogeneous. However, reducing the binder concentration (the PAN 7 wt% + CB 7 wt%) still lead to fully covered fibers, thinner and with a higher proportion of carbon in the dry fibers (50 %). The porosity of all these mats is visually comparable to those observed until now for other electrospun system (~ 95%).

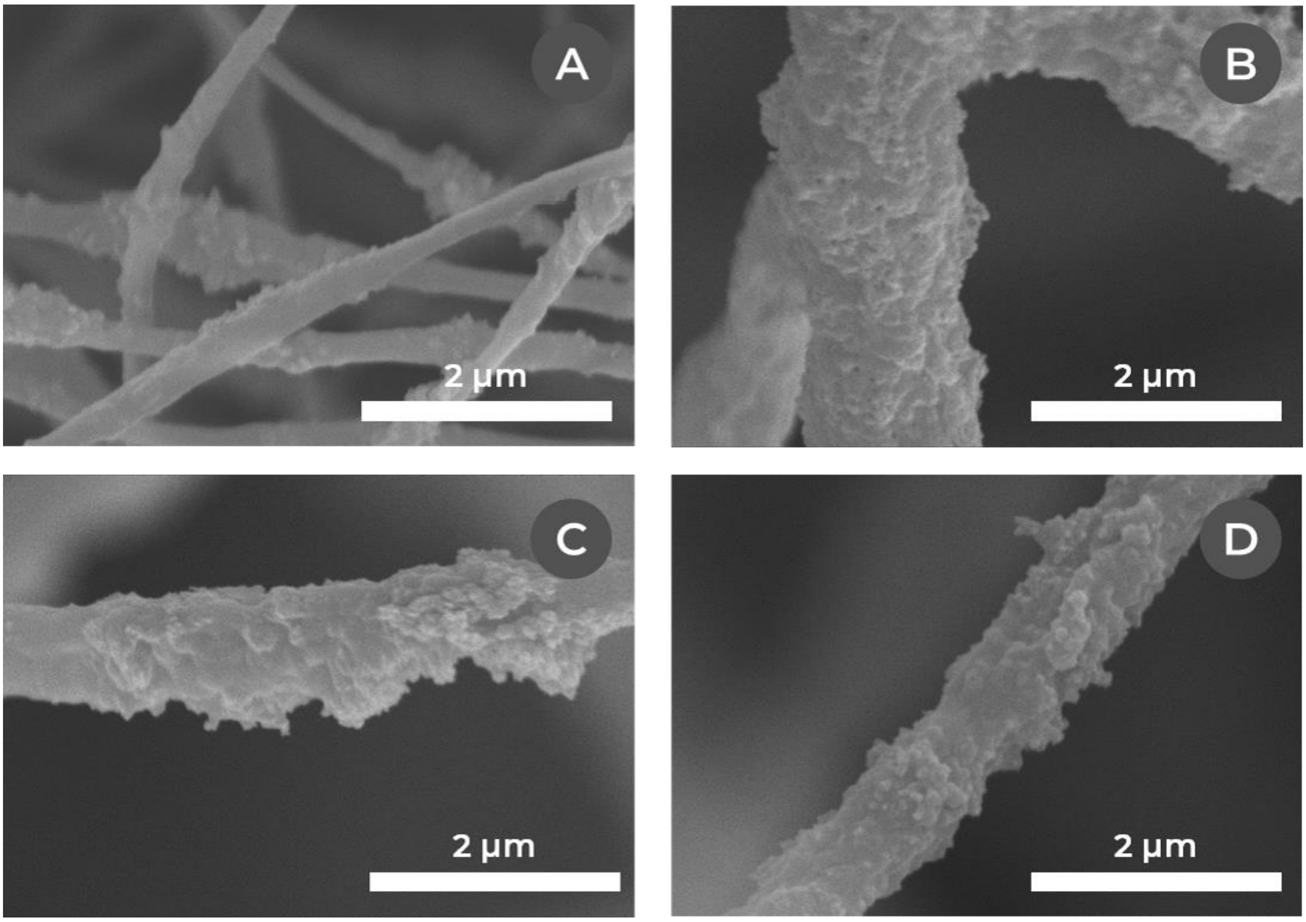

Figure 3.9 – SEM micrographs of electrospun fibers from various Carbon black–PAN formulations. Membranes electrospun from (in DMF): (A) PAN 10 wt% + CB 4 wt%; (B) PAN 10 wt% + CB 6 wt%; (C) PAN 10 wt% + CB 8 wt% & (D) PAN 7 wt% + CB 7 wt%.

Overall, the tested formulations lead to the electrospinning of polymer fibers well-covered in carbon black. Full homogenous coverage of the fibers occurs from a 37.5 % proportion of carbon in the dry fibers, and it is possible to reach up to 50 % of carbon in the dry fibers while keeping a good coverage by reducing the binder concentration in the carbon–polymer solution (PAN 7 wt% + CB 7 wt%). All the electrospun mats are easily handled and are resistant to bending.

3.2.3.2. Electrical conductivity

The electrical conductivity of the fibers is subsequently evaluated (**Figure 3.10**). The surface conductivity (σ_S) and the transverse conductivity (σ_T) are measured by a two-electrode setup, the latter with impedance spectroscopy.

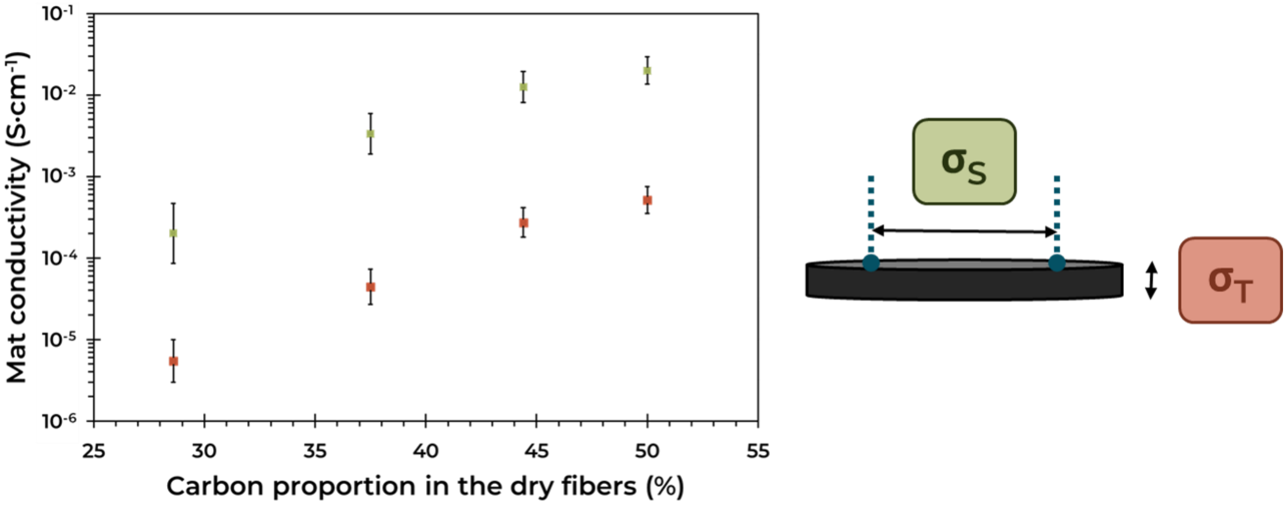

Figure 3.10 – Evolution of the surface σ_S (•) & transverse σ_T (•) conductivities evaluated by respectively a two-electrode setup and impedance spectroscopy of a composite PAN/Carbon black electrospun mat against the carbon proportion in the dry fibers calculated from the electrospun solution formulation.

The Vulcan XC-72R Carbon black has a bulk conductivity upon compression[4] in the range of 0.5-5 S·cm^{-1}. The surface electrical conductivities (σ_S) of the samples increase continuously with the carbon proportion in the dry fibers from $2 \cdot 10^{-4}$ S·cm^{-1} for 28.6 % of carbon black to $2 \cdot 10^{-2}$ S·cm^{-1} for 50 %, i.e., an increase of 2 order of magnitude. The surface conductivity of the highest loaded sample is however lower than the bulk carbon black or electrospun carbon membranes from Chapter 2. This can be explained by the nature of the membrane – intermingled fibers – which allows relatively few electrical contacts between the carbon particles. The transverse conductivities measured by impedance spectroscopy exhibit solely a real impedance value like the electrospun carbon electrodes presented in Chapter 2. Similarly to previous samples, the transverse conductivity (σ_T) is slightly over one order of magnitude lower in these samples than σ_S.

The electrical conductivities of most of the samples (37.5% or PAN 10 wt% + CB 6 wt% and higher) should however still relevant for electrochemical applications.

3.2.3.3. Electrochemical characterization

The capacitive and faradaic behaviors of the PAN 10 wt% + CB 6 wt% are evaluated by cyclic voltammetry (**Figure 3.11**) to verify the suitability of the composite carbon black–polymer electrospun membranes for electrochemical applications. The measurements are conducted in a three electrodes configuration (Ag/AgCl, KCl saturated reference (Ref.), Pt wire counter electrode, and a carbon membrane working electrode), between -0.8 and +0.8 V vs. Ref. at various scan rates between 1 and 100 mV·s^{-1}. The electrode dimensions are Ø = 1.4 cm, h = 421 µm and therefore S = 1.54 cm^2 and V = $9.56 \cdot 10^{-2}$ cm^3.

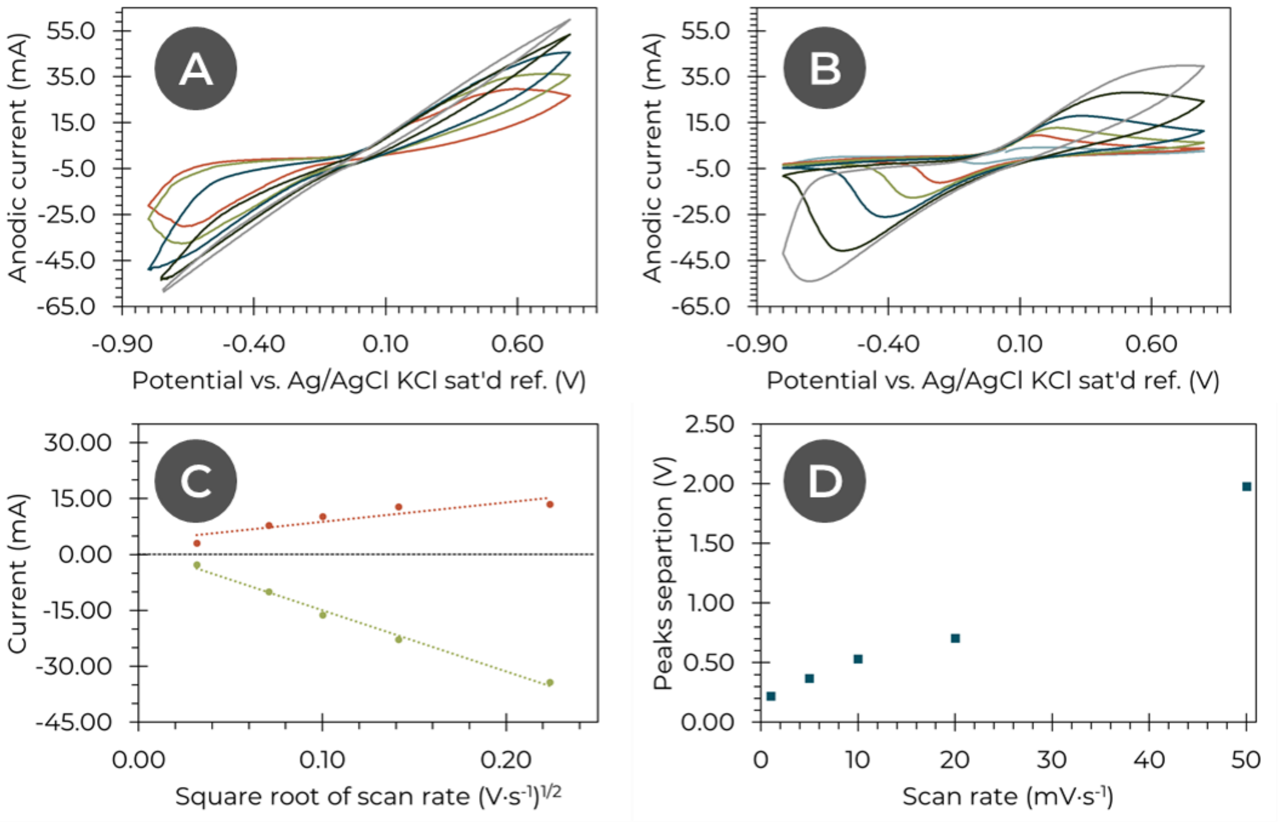

Figure 3.11 – Electrochemical characterization of a composite electrospun membrane (electrospun from a 10 wt% PAN + 6 wt% CB in DMF solution, thickness of 421 μm). (A) Cyclic voltammetry of the capacitive response (NaCl 150 mM in H_2O); (B) Cyclic voltammetry of the faradaic response (NaCl 150 mM + $K_3[Fe(CN)_6]$ 100 mM in H_2O). Scan rate varying from 1 to 100 $mV\cdot s^{-1}$ (– 1 $mV\cdot s^{-1}$, – 5 $mV\cdot s^{-1}$, – 10 $mV\cdot s^{-1}$, – 20 $mV\cdot s^{-1}$, – 50 $mV\cdot s^{-1}$, – 100 $mV\cdot s^{-1}$). (C) Randles–Sevcik plot based on (B) for the $[Fe(CN)_6]^{4-}$ oxidation (•) & $[Fe(CN)_6]^{3-}$ reduction (•); (D) Evolution of the potential difference between oxidation and reduction peaks as a function of the scan rate.

The capacitive response of the electrode is measured in a saline electrolyte (NaCl 150 mM in H_2O) and the faradaic response in the same electrolyte supplemented with 100 mM of $K_3[Fe(CN)_6]$.

The measurement in the saline electrolyte (**Figure 3.11.A**) shows a characteristic capacitive signal as expected. Tabulated values[5] allow the evaluation of the capacitive surface area of the system $A_c \approx 15\ m^2$, or $SSA_c \approx 1.6\cdot10^3\ m^2\cdot g^{-1}$, which is comparable to the surface capacitive area measured for electrospun carbon membrane.

The addition of 100 mM of potassium ferricyanide (**Figure 3.11.B**) shows a faradaic signal of both oxidation and reduction peaks up to 50 $mV\cdot s^{-1}$, corresponding to the redox reaction $[Fe(CN)_6]^{3-} + e^- = [Fe(CN)_6]^{4-}$ (at 100 $mV\cdot s^{-1}$, the oxidation peak is difficult to distinguish in this range of potential).

For this sample, the shape of the cyclic voltammograms accounts for a quasi-irreversible reaction. This is confirmed by the increase of the potential difference between the oxidation and reduction peaks as function of the scan rate from around 0.22 V at 1 $mV\cdot s^{-1}$ up to 1.98 V at 50 $mV\cdot s^{-1}$ (**Figure 3.11.D**). The evolution of the current densities of the oxidation and reduction peaks as a function of the square root of the scan rate is plotted (**Figure 3.11.C**). As for electrospun carbon membranes, this quasi-irreversibility can be linked to the hydrophobicity and tortuosity of the architecture of the electrospun carbon membrane. We then estimate the faradaic surface of the electrospun carbon membrane. A_f is around 0.14 m^2, which represents 0.92 % of the capacitive surface area. A_f is similar than for the electrospun carbon electrode albeit for a higher absolute capacitive surface area. This result may be explained by the diffusion of the redox probe though the carbon electrospun membrane. The electrode is here relatively thick (~ 410 μm) which hinders the diffusion of the probe to the depths of the electrospun mat as seen in Chapter 2.

This electrochemical characterization confirms the suitability of the composite carbon–polymer electrospun membranes as an electrode. Their behavior does not differ significantly compared to electrospun carbon electrodes.

Overall, conductive composite carbon–polymer electrospun membranes were obtained from milled carbon nanofibers as well as commercial carbon black loads in polymer binders. The evaluation of their respective electrical conductivities strongly favors the choice of the commercial Vulcan XC 72R Carbon black as the carbon load (no more than $4\cdot10^{-3}$ $S\cdot cm^{-1}$ and a difficult electrospinning process for the milled carbon nanofibers vs. up to $2\cdot10^{-2}$ $S\cdot cm^{-1}$ and an easy process for carbon black). Moreover, membranes obtained from carbon black–PAN solutions were electrochemically characterized and deemed suitable for further applications. Therefore, composite carbon–polymer electrospun membrane based on PAN + Vulcan XC 72R Carbon black will be used hereafter, with a carbon black proportion in the dry fibers ranging from 28.6 to 50 %.

3.3. Dual electrospun network & composite carbon–polymer fibers

Deeper applications of the electrospinning technique which focus on developing a process for the encapsulation of bacterial cell into an electrospun conductive network without the need of heat treatment will be presented further in this work. Nevertheless, the fibers encapsulating the bacteria cannot be loaded enough with carbon materials to guarantee the proper conductivity of the membrane on their own akin to a reliable electrospinning process. Therefore, we propose to develop a process allowing the simultaneous dual electrospinning of conductive fibers along this primary network. The resulting mat will be composed of an intermingled network of fibers from the two solutions (**Figure 3.12**).

Multi-spinneret electrospinning is widely reported in the literature[6],[7] and will here be applied to the production of a conductive mat including a primary network of low-conductivity fibers. Accordingly, the conductive composite carbon–polymer electrospun fibers hitherto presented will be used as a conductive electrospun scaffold.

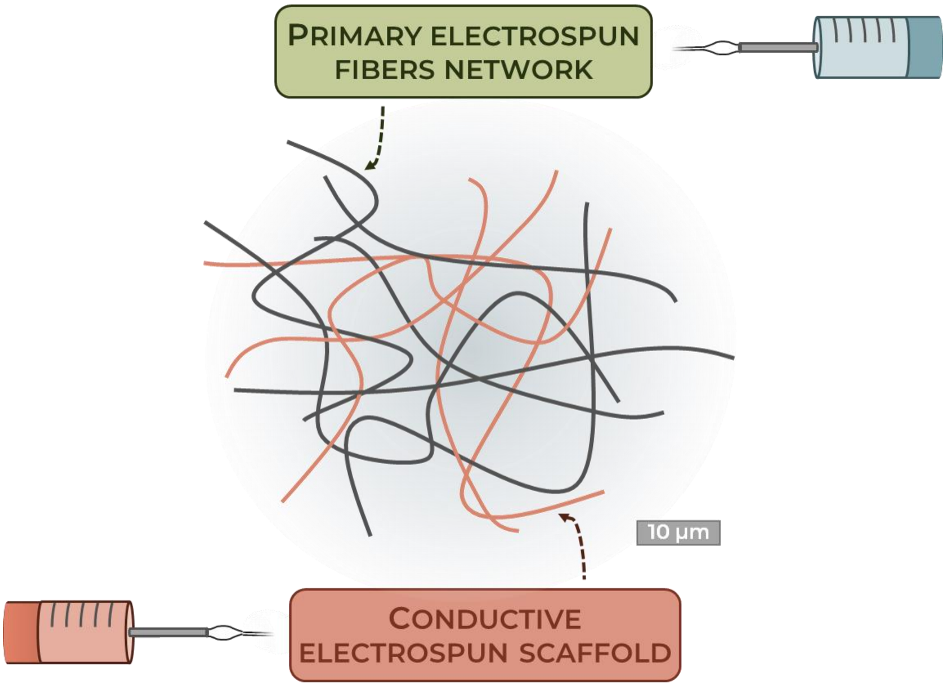
PRIMARY ELECTROSPUN FIBERS NETWORK
10 µm
CONDUCTIVE ELECTROSPUN SCAFFOLD

Figure 3.12 – Architecture of a dual electrospun mat including a conductive fibers scaffold

3.3.1. Experimental procedure

Two electrospinning solutions (**Table 3.3**) are then prepared to evaluate the feasibility of the dual electrospinning process in these conditions. The conductive scaffold solution is prepared by firstly dispersing the carbon black in the solvent in an ultrasonic bath (ultrasonic effective power: 75 W) for 30 minutes. The polymers are then added and stirred overnight at room temperature until full dissolution.

Table 3.3 – Formulations of the primary & conductive scaffold solution for the dual electrospinning.

Solution	Solvent	Polymer	Additives
Primary network	90:10 (w/w) Chloroform & DMF	PCL 9 wt%	–
Conductive scaffold	DMF	PAN 10 wt%	CB 4 wt%

These solutions are dual electrospun on a grounded aluminum foil on a roller using the Electrospinz ES1™ generator and apparatus and two spinnerets symmetrically disposed on each side of the collector (**Figure 3.13**). The electrospinning parameters are defined as follow:

- **Electric field**: around 1.4 kV·cm^{-1} set by tuning the voltage and distance between the spinnerets and collectors respectively at 18.5 kV and 13 cm;
- **Injection speed**: 3.5 mL·h^{-1} using a Fisherbrand™ syringe pump and a Terumo® 10cc Eccentric Luer Tip syringe equipped with a blunt-end needle ($Ø_{internal}$ = 0.75 mm) for each solution;
- **Volume**: around 1.75 mL of each solution are injected to ensure the deposition of a thick self-standing membrane;
- **Temperature**: 21°C thermostatted by the lab air-conditioner;
- **Relative humidity**: kept between 30 and 35% by running the setup in a closed poly(methyl acrylate) box connected to the lab dry compressed air outlet;
- **Substrate**: aluminum foils fixed on a roller with a speed set at around 400 rpm.

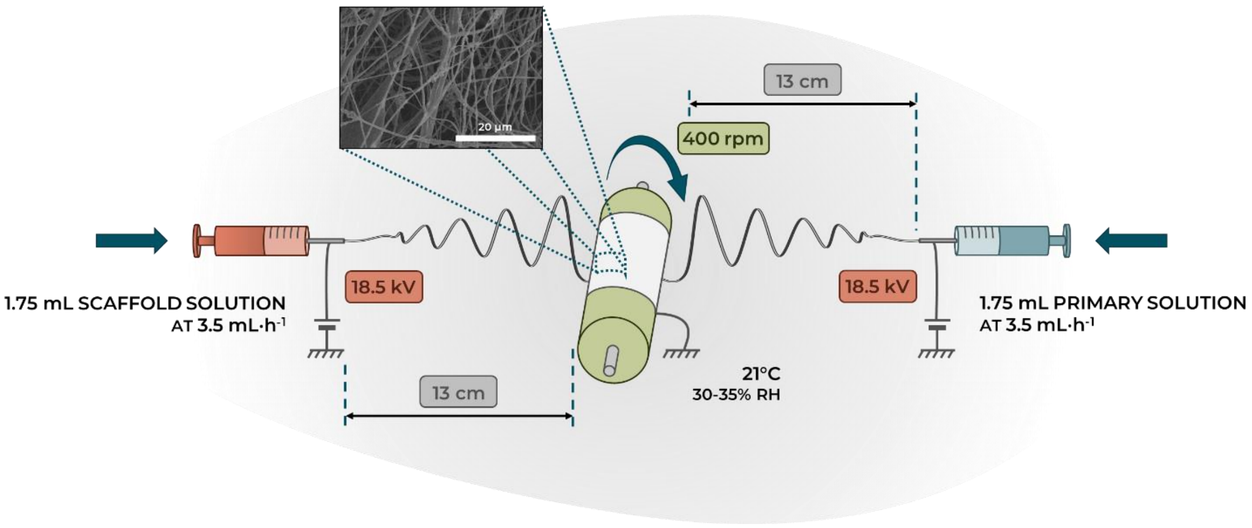

Figure 3.13 – Overview of a dual electrospinning setup.

The resulting self-standing membrane is easily peeled off the aluminum foil.

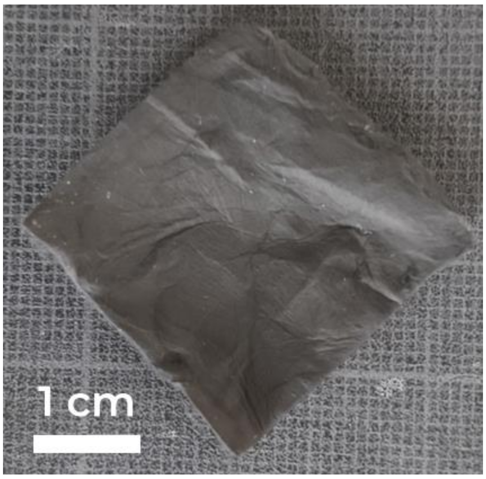

Figure 3.14 – Dual electrospun conductive membrane.

The membrane (thickness of ~ 250 µm) is grey-black and exhibits a good resistance when handled or bent.

3.3.2. Dual electrospun mat characterization

The dual electrospun membrane architecture is then characterized by SEM imaging and its conductivity is evaluated by a two-electrode setup and impedance spectroscopy.

3.3.2.1. SEM imaging

SEM imaging of the fibers (**Figure 3.15**) reveals two intermingled populations of fibers. The PCL primary fibers are highly embedded in a denser conductive scaffold network (**Figure 3.15.B**). These secondary conductive scaffold fibers are well connected together (**Figure 3.15.C**). A close-up on the conductive fibers exhibits the presence of carbon black powder within the fibers (**Figure 3.15.D**).

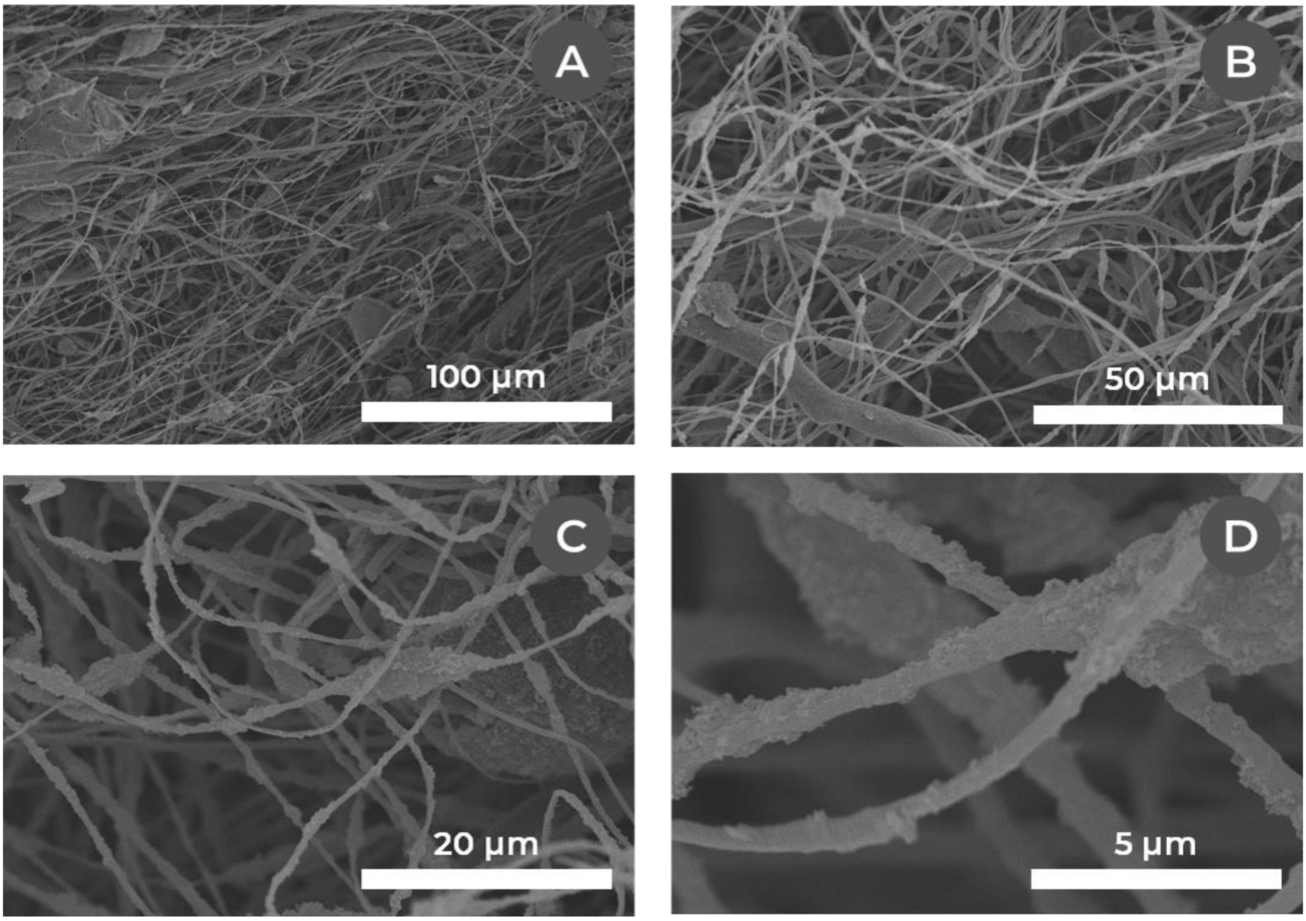

Figure 3.15 – SEM micrographs of a PCL/conductive fibers dual electrospun membrane (dual electrospun from PCL 9 wt% in 90:10 (w/w) chloroform & DMF & PAN 10 wt% + CB 4 wt% in DMF). (A) & (B) Overall aspect of the mat. Note the two intermingled populations of fibers. (C) Conductive scaffold & (D) Close-up on the conductive scaffold fibers.

The general architecture of the dual electrospun mat seems to have reach the goal presented previously. The electrical conductivity of the membrane can now be characterized.

3.3.2.2. Electrical conductivity

The electrical conductivity is studied both by a two-electrode setup and impedance spectroscopy.

The surface two-electrode measurement gives a value varying along the mat in the range of $\sigma_S \sim 10^{-3}$ to 10^{-4} S·cm^{-1} which is consistent with the values measured for a composite electrospun membrane of similar formulation (PAN 10 wt% + CB 4 wt%). Impedance spectroscopy shows solely real values varying along the mat around $\sigma_T \sim 10^{-5}$ to 10^{-6} S·cm^{-1} which is again consistent with previous measurements (**Table 3.4**).

Table 3.4 – Typical electrical conductivities σ_S & σ_T for the electrospun carbon electrode, the composite electrospun membrane & the dual electrospun membrane.

Sample	σ_S ($S \cdot cm^{-1}$)[a]	σ_T ($S \cdot cm^{-1}$)[b]
Electrospun carbon electrode	$\sim 10^{-1}$	$\sim 10^{-1}$ to 10^{-2}
Composite electrospun membrane (PAN 10 wt% + CB 4 wt%)	$2 \cdot 10^{-4}$	$6 \cdot 10^{-6}$
Dual electrospun membrane (PCL 10 wt% / PAN 10 wt% + CB 4 wt%)	$\sim 10^{-3}$ to 10^{-4}	$\sim 10^{-5}$ to 10^{-6}

[a] Calculated from two-electrode setup measurements; maximum sensibility of 40 MΩ. [b] Calculated from impedance spectroscopy measurements; amplitude of 100 mV; maximum sensibility of $\sim 10^{8}$ Ω.

Eventually the dual electrospun mat is conductive as expected.

Altogether, the aimed architecture of the dual electrospun membrane is respected, with the two populations of primary and secondary conductive fibers intermingled together. Furthermore, the resultant mat is conductive, with similar conductivities compared with the composite electrospun membrane from the same formulation (where $\sigma_S \sim 10^{-3}$ to 10^{-4} $S \cdot cm^{-1}$ and $\sigma_T \sim 10^{-5}$ to 10^{-6} $S \cdot cm^{-1}$). The dual electrospun membranes conductivities need to be further improved, however, the feasibility of this process is now demonstrated.

3.4. Bacteria viability on composite carbon–polymer fibers

The viability of electroactive bacteria on the composite carbon–polymer fibers must be evaluated before integrating it into a bioanode or an MFC setup.

The survival and electrochemical activity of *Shewanella oneidensis* will therefore be investigated on a composite electrospun membrane from a 10 wt% PAN + 6 wt% CB in DMF solution, exhibiting homogeneous structure as well as good electrical conductivity (~ 10^{-2}-10^{-3} S·cm^{-1}).

3.4.1. Live/dead assay

The viability of the cells is evaluated with an Invitrogen™ LIVE/DEAD™ *Bac*Light™ Bacterial viability kit (Thermo Fisher Scientific) (**Figure 3.16**).

A piece of composite electrospun membrane of 1 cm^2 was immersed in MR-1/L medium set at an optical density of *S. oneidensis* $OD_{600,\text{initial}} = 0.1$. The medium was agitated at 80 rpm on an orbital shaker for 3 days at 21°C before staining the cells and observing them under an epifluorescence microscope.

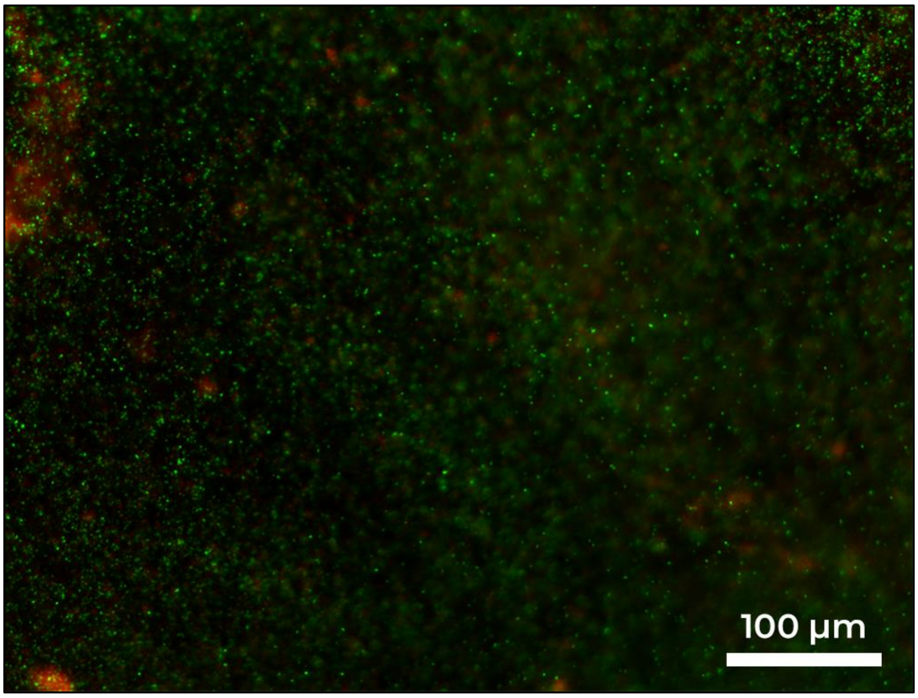

Figure 3.16 – Epifluorescence microscopy of a PAN–Carbon black electrospun membrane (electrospun from a solution of 10 wt% PAN + 6 wt% CB in DMF) colonized for 3 days by *S. oneidensis*, dyed with Invitrogen™ *Bac*Light™ Bacterial Viability Kit. Green highlights live cells while red highlights dead cells.

After 3 days of colonization, a lot of cells have impregnated the membrane and most are still alive. No toxicity of the electrospun mat on the bacteria is therefore noticeable following the live/dead assay.

3.4.2. Electrochemical activity

Furthermore, the electrochemical activity of *S. oneidensis* on the composite carbon–polymer mat was evaluated to verify that the cells were able to perform EET in this environment, akin to evaluate the MFC performances of such electrode colonized in situ.

3.4.2.1. MFC integration & electrochemical characterization

A composite electrospun membrane was subsequently sterilized for 20 minutes at 120°C and integrated into a sterile MFC reactor for in situ colonization under the conditions presented in Chapter 2. The catholyte is made up of 150 mM of NaCl (supporting electrolyte) and 100 mM of $K_3[Fe(CN)_6]$. The anodic compartment is filled with 20 mL of fresh MR1/L medium inoculated at $OD_{600} = 0.7$ with *S. oneidensis* from the exponential phase of a bacterial culture.

The anode potential is potentiostatically poised at +0.3 V vs. Ag/AgCl, KCl saturated reference. The MFC current output is monitored through time with chronoamperometry (CA) and the current density j (μA·cm^{-2}) is calculated ($Ø_{anode} = 1.7$ cm; $A_{anode,geometrical} \approx 2.27$ cm^2). Cyclic voltammograms (CV) are recorded in the range of -0.7 to +0.7 V against Ref. (scan rate: 1 mV·s^{-1}) every 24 hours. On the fifth day, the polarization of the anode is stopped after the cyclic voltammetry for 16 hours to let the electrode potential stabilized and the working and counter electrodes channels are reversed. Polarization and power curves are recorded by applying an incremental series of negative currents to the cathode while the emf is recorded. The anolyte is recharged with 1 mmol of sodium lactate every 4 days to ensure there is no carbon source shortage for the bacteria. All the processes are conducted at 21°C. The electrochemical characterization of the system is then compared to the average in situ colonized electrospun carbon membrane presented in Chapter 2 (**Figure 3.17**).

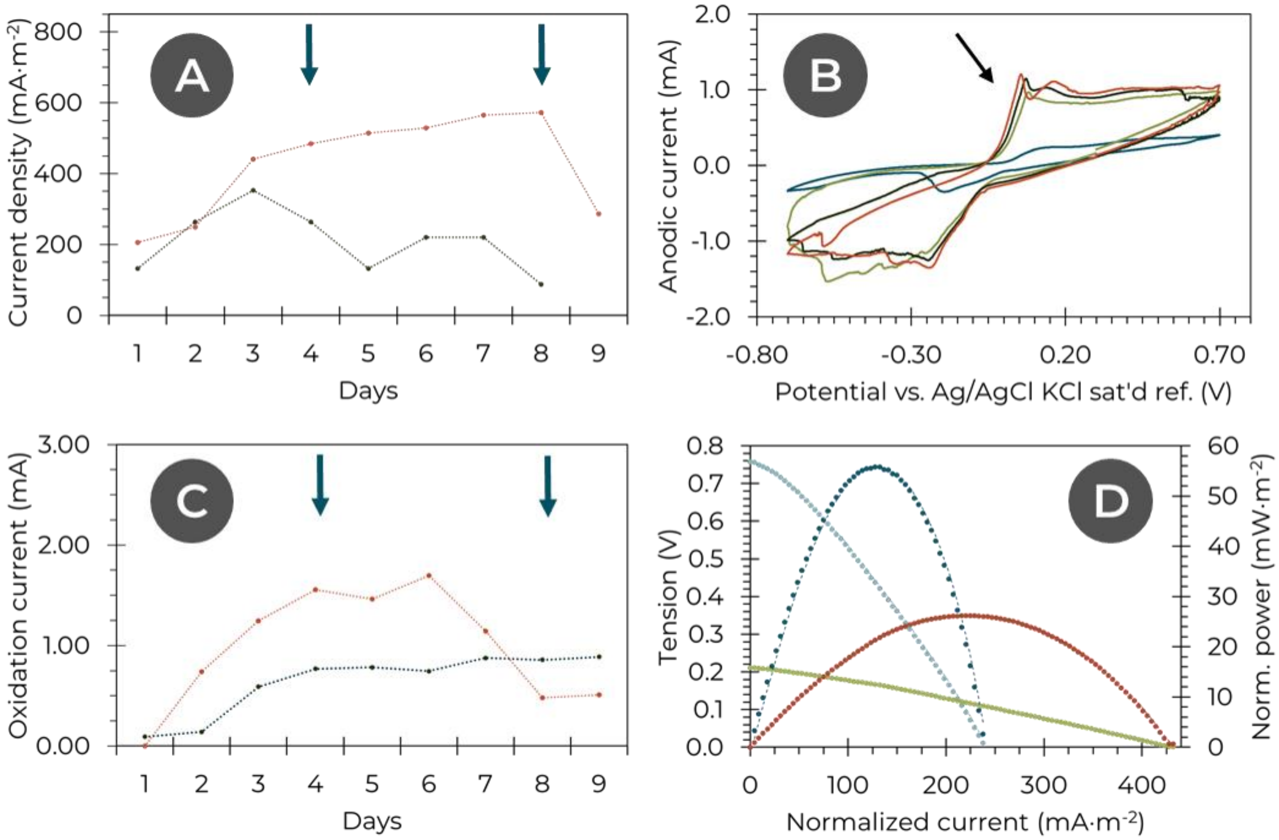

Figure 3.17 – Electrochemical characterization of a two-compartment MFC including a composite electrospun electrode polarized at +0.3 V vs. the reference (electrospun from a 10 wt% PAN + 6 wt% CB in DMF solution, thickness of 115 µm) as a function of time. (A) Evolution of the current density (•); blue arrows indicate addition of 1 mmol of sodium lactate comparison (•) with an in situ colonized electrospun carbon electrode; N = 3. (B) Evolution of cyclic voltammetry as a function of time (– 1st day, – 3rd day, – 5th day, – 7th day); sweep rate of 1 mV·s-^{1}; 3 cycles are acquired, here is the second one. (C) Evolution of the average current (•) corresponding to the peak shown by the arrow on the CV; blue arrows indicate addition of 1 mmol of sodium lactate. Comparison (•) with an in situ colonized electrospun carbon electrode; N = 3. (D) Polarization (•) and power (•) curves of an MFC at maximum current density value (here 5th day, thickness of 115 µm). Comparison with the polarization (•) and power (•) curves of an in situ colonized electrospun carbon electrode (here 6th day, thickness of 293 µm). Current and power are normalized by the geometric surface area of the electrospun electrode (Ø$_{anode}$ = 1.7 cm; A$_{anode,\ geometrical}$ ≈ 2.27 cm^2).

The current density (**Figure 3.17.A**) starts around 135 mA·m^{-2} and increases until the third day when it reaches over 350 mA·m^{-2}. It then slowly decreases and stays around 100-200 mA·m^{-2} until the end of the experiment.

Cyclic voltammetry (**Figure 3.17.B**) shows no significant oxidation peak on the first day and a capacitive response noticeably smaller than for the next days, hinting for a poor in-depth wettability of the fibers at the microscopic level. This is understandable since carbon materials tend to be hydrophobic – contact angle experiments on the membrane showing however a quick absorption of water at the macroscopic level. Oxidation peaks ranging between -0.05 and +0.3 V vs. Ag/AgCl KCl saturated – at the potentials expected for EET through the Mtr pathway[8]–[10] – start to appear on the second day and are clearly visible on the third day. Their intensities remain stable (**Figure 3.17.C**) for the rest of the experiment. Firstly, the presence of these peaks confirms the presence of extracellular electron transfer and thus the suitability of the composite electrospun network for MFC applications. Secondly, a more complex behavior is observed here (presence of two separated oxidation peaks) than observed for the electrospun carbon electrode, where we usually observed only one peak. This behavior will be analyzed more in detail in Chapter 3 where composite electrospun mats will be more widely implemented into bioanodes but already suggests a difference in EET as the environment of *S. oneidensis* changes.

After stopping the polarization of the anode and waiting for its stabilization, the emf of the MFC reverts to 0.21 V (the anode potential stabilizing at 90 mV). This is clearly lower that for electrospun carbon electrodes and may again be linked to the difference in EET between the two systems. The polarization and power curves (**Figure 3.17.D**) recorded show a maximum power and current densities of respectively 26 mW·m^{-2} and 430 mA·m^{-2} respectively. Notice that even if the surface normalized maximum power density is clearly lower than for the electrospun carbon paper (26 vs. 56 mW·m^{-2}), the maximum current density is higher (430 vs. 240 mA·m^{-2}) and the low thickness of the membrane (115 µm) leads to impressive volume normalized performances of 225 W·m^{-2} and 3740 A·m^{-2}, similar or even higher than in the previous electrospun systems. We can estimate the internal resistance of the system $R_{int} \approx 11$ kΩ from the slope of the polarization curve. This value is consistent with previously reported internal resistances and with the typical resistance of the electrospun mat (R ~ 1 kΩ).

Interestingly, the MFC run for 16 days with a better current output stability (**Figure 3.18.A-B**) than the electrospun carbon electrodes (**Figure 3.18.C-D**) **–** the measurements were only eventually stopped due to a prolonged computer crash.

In particular, the performances of the latter tended to exhibit a three-phase “bell curve” appearance where they started at low values (1) before increasing to a maximum (2) and eventually fell (3). In the meantime, the in situ measured anode surface capacitive area followed a trend were it was stable (1), decreased steadily (2) and was stable again at last (3). This evolution was hypothesized to be linked to the growth of the biofilm. First, it allowed an increase in electrochemical performances as it developed before limiting nutrients and organics diffusion, leading then to a low-current density steady phase where most of the bacteria were unable to degrade properly any lactate nor to give up their cellular wastes.

In the case of the composite electrospun electrode however, the capacitive surface area seems to rise quickly the first day (when it is very low due to a bad in-depth wettability of the electrode) and then stabilizes at around 2.5 m^2 from the third and fourth days on until the end of the measurements. The CV-main peak oxidation current (**Figure 3.18.A**) remarkably follows the increase of the electrode surface area. However, the current density output (**Figure 3.18.B**) increases with the electrode surface for the first days and then decreases at day 5.

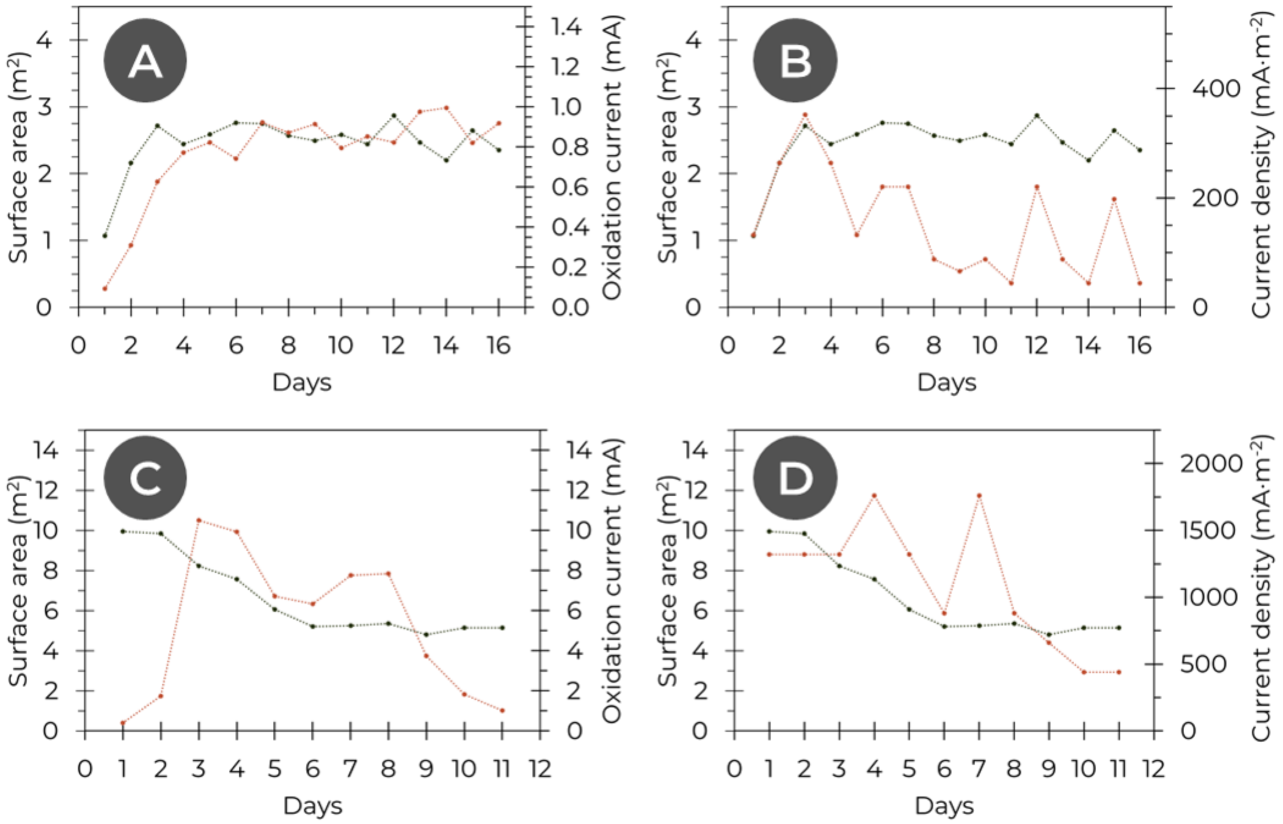

Figure 3.18 – Evolution of the capacitive surface area (•) of a composite electrospun electrode (A-B; electrospun from a 10 wt% PAN + 6 wt% CB in DMF solution, thickness of 115 µm) and a 2-fold stacked precolonized bioanode (C-D; thickness of 693 µm) as a function of the time. The capacitive surface area is calculated from cyclic voltammetry. The surface area is compared with (A-C) the maximum current of the main oxidation peak on the CV (•), & (B-D) the current density output of the MFC, normalized by the geometric surface area of the electrospun carbon electrode ($Ø_{anode}$ = 1.7 cm; $A_{anode,\ geometrical}$ ≈ 2.27 cm^2).

Altogether, even if a decrease in current density is eventually observed, the composite electrospun electrode exhibits better stability than the electrospun carbon electrodes. In particular, a measurable current is generated by the setup after 16 days, and no decrease of the capacitive surface area of the electrode linked to biofilm overgrowth is noticeable. Further improvements still have to be done to improve the output stability of electrospun bioanodes. However, the use of composite carbon black–polymer electrospun fibers in MFCs seems to improve their stability, probably by influencing the biofilm development.

3.4.2.2. Post-mortem imaging

The post-mortem colonization of the composite electrospun electrode is afterward evaluated by SEM (**Figure 3.19**).

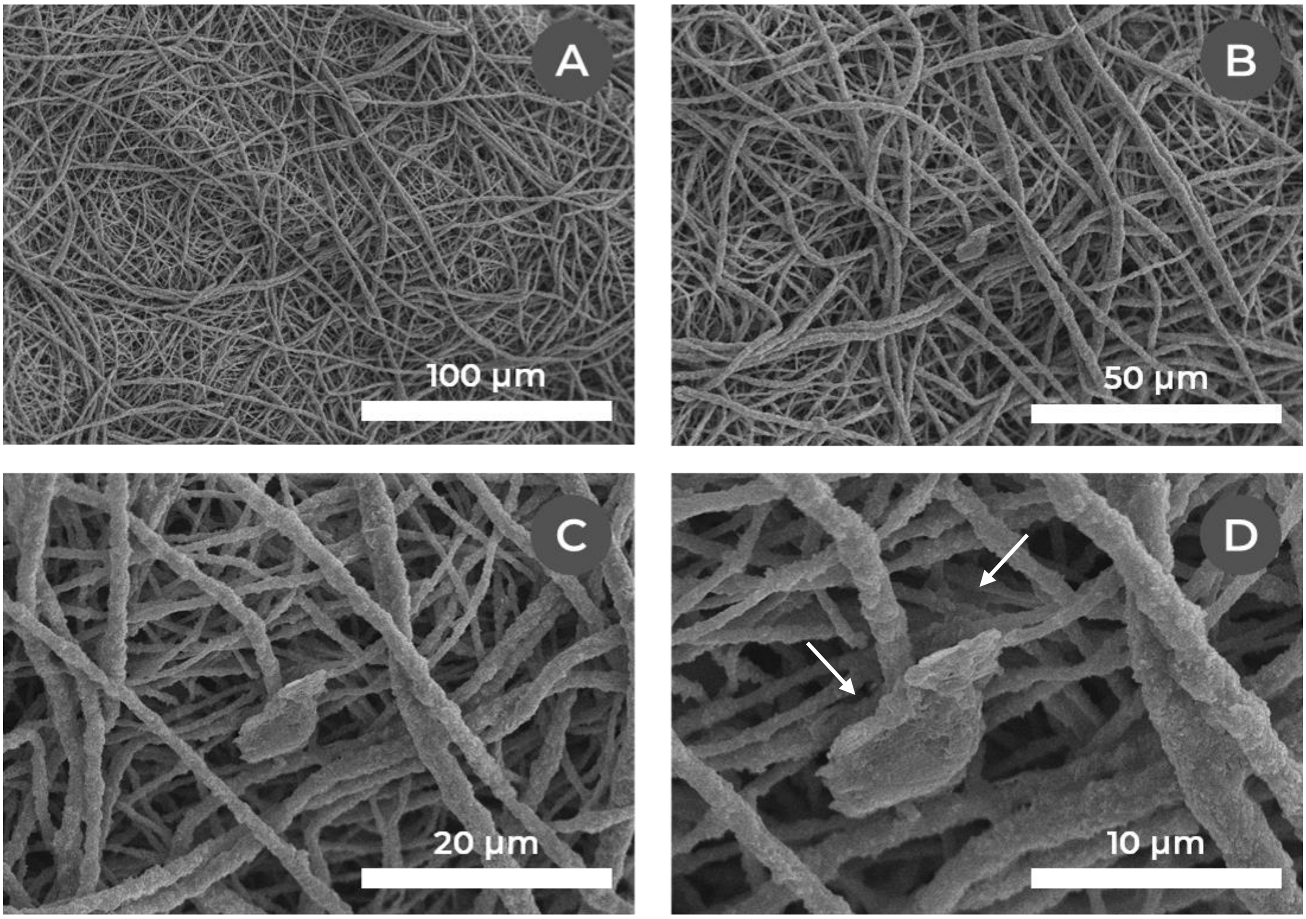

Figure 3.19 – SEM micrographs of the air-dried post-mortem composite electrospun electrode (electrospun from a 10 wt% PAN + 6 wt% CB in DMF solution) after 16 days of operation, polarized at +0.3 V vs. Ag/AgCl, KCl saturated reference, coated with 15 nm of gold. Note the deposition of some matter in between the fibers (arrows).

The SEM observation of the membrane exhibits an architecture relatively conserved between the pristine electrode (**Figure 3.8**) and the post-mortem electrode. However, the interfiber space has clearly decreased after 16 days of operation, and accordingly some biofilm and organic matter not present in the pristine membrane are visible in the post-mortem sample. Interestingly, no biofilm overgrowth clogging the interfiber space is here noticeable, perhaps due to a weaker bacterial adhesion. The difference in bacterial adhesion is probably linked to a combined effect of difference of surface condition, roughness, ζ-potential and surface charge as well as surface chemistry between electrospun carbon fibers and the commercial carbon black embedded in the polymeric binder. Interestingly, the observation tends to show that a wide development of biofilm in not required for the observation of a DET-linked current generation.

Finally, the composite electrospun electrode seems well-suited for bacterial growth, exoelectronic transfer and overall MFC applications. The membrane shows no noticeable toxicity for *Shewanella oneidensis* cells grown on it, and clear EET is seen upon MFC integration. Additionally, the electrochemical performances of a composite electrospun electrode from 10 wt% PAN + 6 wt% carbon black in DMF are quite impressive, exhibiting high volume power and current densities – of 225 $W \cdot m^{-2}$ and 3740 $A \cdot m^{-2}$ – thanks to the thinness of the membrane colonized. Moreover, the post-mortem SEM analysis of the electrode shows little biofilm overgrowth, which is promising for improved long-term stability of the system which ran here for 16 days with less fall in performances than electrospun carbon electrodes.

3.5. Conclusion

We have developed a method to electrospin one-step conductive composite carbon–polymer fibers, aiming for MFC applications. The best formulations tested were based on commercial Vulcan XC-72R Carbon black and a polyacrylonitrile binder, exhibiting a suitable electrical conductivity – up to $2 \cdot 10^{-2}$ $S \cdot cm^{-1}$ for planar (surface) conductivity – and electrochemical behavior.

Afterwards, a process based on a dual electrospinning approach was developed to fabricate a fiber mat consisting of a primary low-conductivity mat intermingled with a conductive carbon–polymer scaffold. The formulations were based on those previously developed. This architecture was intended to pave the way for further electrospun bioanodes where bacterial cells are directly encapsulated into the primary mat. This design will be presented in the next chapter. The architecture and conductivity of the dual mat were characterized and subsequently corresponded to this goal (fibers of ~1 µm, porosity of ~ 95 %, conductivities $\sigma_S \sim 10^{-3}$ to 10^{-4} $S \cdot cm^{-1}$ & $\sigma_T \sim 10^{-5}$ to 10^{-6} $S \cdot cm^{-1}$).

The survival and electrochemical activity of *Shewanella oneidensis* on a composite carbon black–polymer electrospun mat was surveyed. Firstly, the mat showed no toxicity to the cells under a live/dead assay. Additionally, the integration of a composite electrospun membrane into an MFC reactor demonstrated an electrochemical activity intensity similar to other bioanode, albeit with different oxidation peaks shapes on cyclic voltammetry curves. Remarkably, the long-term stability of the corresponding MFC was far better than observed for electrospun carbon electrode-based reactors. In particular, no decrease in electrode capacitive surface area linked to a biofilm overgrowth was detectable. This was confirmed by SEM imaging. An eventual decrease in current output was nevertheless observed. Nevertheless, the performances exhibited by the bioanode were still impressive – volume current and power densities of $3.74 \cdot 10^3$ $A \cdot m^{-3}$ & 225 $W \cdot m^{-3}$ were achieved – and encouraging for further applications of composite carbon–polymer electrospun fibers in MFCs.

To be used in an MFC setup, these membranes however still need to be colonized before producing a stable current output. Accordingly, in the next chapter, the integration of electroactive cells directly during the electrospinning process in core-shell fibers dual electrospun with composite electrospun fibers will be undertaken.

REFERENCES

[1] E. C. Self, E. C. McRen & P. N. Pintauro. High Performance Particle/Polymer Nanofiber Anodes for Li-ion Batteries using Electrospinning. *ChemSusChem* **9,** 208–215 (2016).

[2] W. Zhang & P. N. Pintauro. High-performance nanofiber fuel cell electrodes. *ChemSusChem* **4,** 1753–1757 (2011).

[3] E. C. Self *et al.* High Areal Capacity Si/LiCoO2Batteries from Electrospun Composite Fiber Mats. *ChemSusChem* **10,** 1823–1831 (2017).

[4] D. Pantea, H. Darmstadt, S. Kaliaguine & C. Roy. Electrical conductivity of conductive carbon blacks: influence of surface chemistry and topology. *Appl. Surf. Sci.* **217,** 181–193 (2003).

[5] E. Frackowiak & F. Béguin. Carbon materials for the electrochemical storage of energy in capacitors. in (2001).

[6] S. Kidoaki, I. K. Kwon & T. Matsuda. Mesoscopic spatial designs of nano- and microfiber meshes for tissue-engineering matrix and scaffold based on newly devised multilayering and mixing electrospinning techniques. *Biomaterials* **26,** 37–46 (2005).

[7] M. Sun, X. Li, B. Ding, J. Yu & G. Sun. Mechanical and wettable behavior of polyacrylonitrile reinforced fibrous polystyrene mats. *J. Colloid Interface Sci.* **347,** 147–152 (2010).

[8] J. N. Roy *et al.* Applied Electrode Potential Leads to Shewanella oneidensis MR-1 Biofilms Engaged in Direct Electron Transfer. *J. Electrochem. Soc.* **160,** H866–H871 (2013).

[9] J. M. Myers & C. R. Myers. Role of the tetraheme cytochrome CymA in anaerobic electron transport in cells of Shewanella putrefaciens MR-1 with normal levels of menaquinone. *J. Bacteriol.* **182,** 67–75 (2000).

[10] J. M. Myers & C. R. Myers. Role for outer membrane cytochromes OmcA and OmcB of Shewanella putrefaciens MR-1 in reduction of manganese dioxide. *Appl. Environ. Microbiol.* **67,** 260–269 (2001).

4

CORE-SHELL ARCHITECTURE: DESIGNING A ONE-STEP BACTERIA ENCAPSULATING BIOANODE

TABLE OF CONTENTS

Chapter 4. Core-shell architecture: Designing a one-step bacteria-encapsulating bioanode....... 201
- 4.1. Introduction & objectives 201
- 4.2. Lab-made core-shell coelectrospun fibers..... 202
  - 4.2.1. Design of a coelectrospinning apparatus..... 202
  - 4.2.2. Experimental procedure 203
  - 4.2.3. Core-shell architecture characterization 206
    - 4.2.3.1. Optical microscope..... 207
    - 4.2.3.2. SEM imaging 207
    - 4.2.3.3. Focused ion beam milling..... 209
- 4.3. Bacteria encapsulation 211
  - 4.3.1. Bacterial culture 211
  - 4.3.2. Core-shell coextrusion 211
  - 4.3.3. Bacteria encapsulation characterization 212
    - 4.3.3.1. Epifluorescence microscope 212
    - 4.3.3.2. Confocal microscope..... 213
    - 4.3.3.3. SEM imaging 214
    - 4.3.3.4. Bacteria survival..... 215
- 4.4. Dual electrospun core-shell/conductive fibers scaffold network..... 216
  - 4.4.1. Dual electrospinning setup..... 216
  - 4.4.2. Network characterization 219
    - 4.4.2.1. SEM imaging 219
    - 4.4.2.2. Electrical conductivity..... 221
- 4.5. Integrated one-step conductive bioanode encapsulating electroactive bacteria 223
  - 4.5.1. Electrospinning setup..... 223
  - 4.5.2. Bioanode characterization..... 225
    - 4.5.2.1. SEM imaging 225
    - 4.5.2.2. Confocal microscopy & bacteria viability..... 226
    - 4.5.2.3. Electrical conductivity..... 227
    - 4.5.2.4. MFC integration & electrochemical characterization..... 228
    - 4.5.2.5. Post-mortem imaging..... 232

4.5.3. Integrated bioanode cryodesiccation 232
4.5.3.1. MFC integration & electrochemical characterization 234
4.5.3.2. Post-mortem imaging 239
4.6. Conclusion 242
References 244

CHAPTER 4. CORE-SHELL ARCHITECTURE: DESIGNING A ONE-STEP BACTERIA-ENCAPSULATING BIOANODE

4.1. Introduction & objectives

Electrospun carbon microfibers bioanodes have demonstrated promising performances for current generation in an MFC setup[1], stemming from their high surface area as well as their scale well-suited for bacterial adhesion and electron transfer. Nevertheless they still suffer from some drawbacks, highlighted in Chapter 2, and in particular require numerous synthesis steps and tend to show a drop in performances as the bacterial biofilm development is eventually detrimental to the long-term stability of the system.

The first of those impairments – the length of the heat treatment phases – was addressed in Chapter 3 in which the synthesis of carbon–polymer composite fibers was explored. A process was designed to produce a conductive double mat of electrospun fibers, formed by a conductive scaffold as well as a second network of carbon–polymer composite fibers. The goal of this design was to provide a framework for the encapsulation of bacterial cells in the latter network, while ensuring the overall electrical conductivity of the system thanks to the former.

Based on these results and on the advances on the production of electrospun core-shell fibers[2]–[4], this chapter focuses on the synthesis of a fully-integrated one-step bioanode. Without neither heat treatment nor precolonization stage, the objective of this work is to provide a conclusive process for the production of a conductive bacteria-encapsulating electrospun mat able to produce a current upon its integration into an MFC reactor. Furthermore, the encapsulation of bacterial cells inside electrospun fibers is envisioned to tune the biofilm growth and the related diffusion impairment through the fibers network.

A coaxial electrospinning setup is therefore developed to allow the production of lab-made core-shell coelectrospun fibers, whose architectures are subsequently characterized.

This setup is thereafter applied to the encapsulation of the electroactive *Shewanella oneidensis* cells, and their survival through the process as well as the architecture of the resulting network are characterized.

The results from Chapter 3 are further refined to allow the production of a dual conductive network formed by core-shell electrospun fibers integrating carbon into their shell to connect them to the composite conductive scaffold.

The previous results are combined into a one-step bacteria encapsulating bioanode, optionally cryodesiccated, which is integrated into an MFC reactor while its electrochemical behavior and stability are investigated.

4.2. Lab-made core-shell coelectrospun fibers

Coaxial electrospinning has been first described to yield core-shell microfibers by Sun *et al.* in 2003[5]. With this approach, two different polymer solutions are coelectrospun simultaneously with the help of a of two-capillary coaxial spinneret (**Figure 4.1**). This spinneret produces a compound drop and Taylor cone which is extruded into a core-shell fiber.

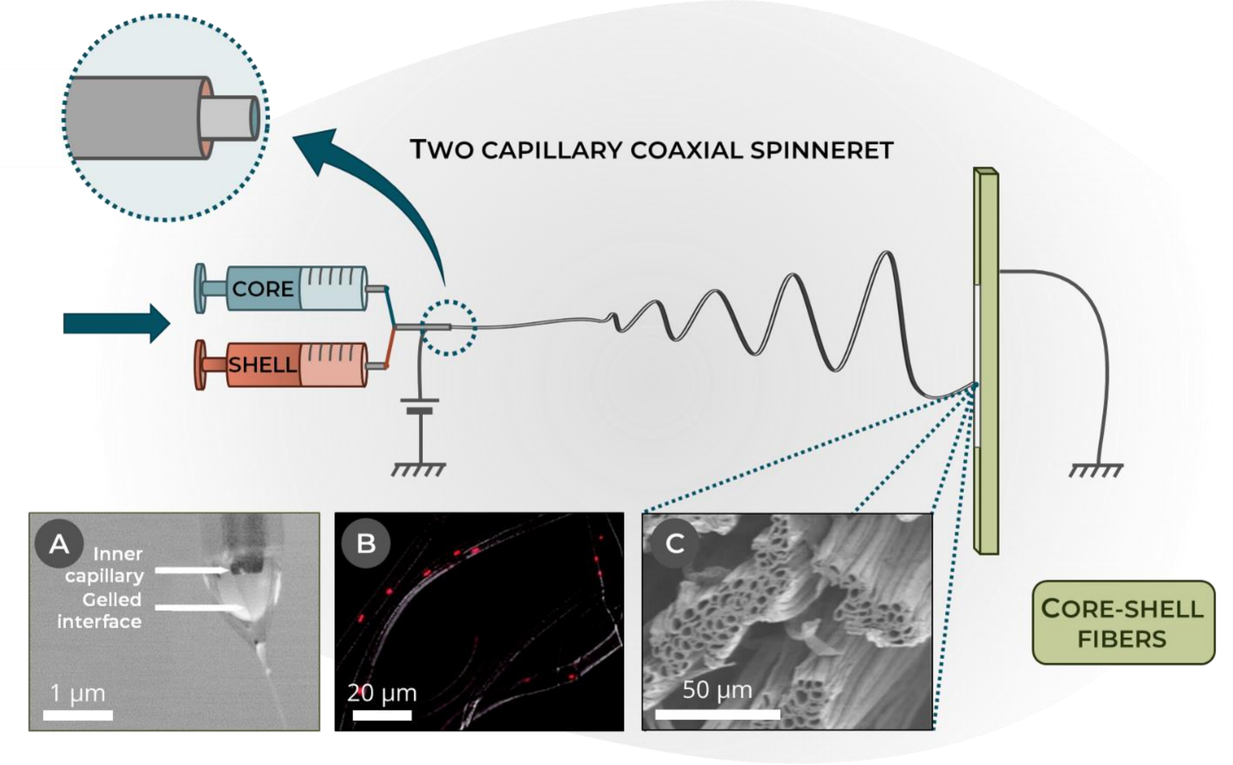

Figure 4.1 – Production of core-shell nanofibers by a coaxial two-capillary spinneret. (A) Compound pendant drop containing a PCL shell and PEO core solution. The protrusion of the inner capillary outside the shell capillary and the gelled interface between the solutions are seen. (B) Fluorescent microscopy of DsRed-expressing *Pseudomonas putida* S12 encapsulated in PCL-shell–PEO-core fibers & (C) High Resolution SEM micrographs of hollow PCL-shell–PEO-core fibers.

This technique has been further refined to produce polymeric, polymer-metal hybrid, ceramic or metal filled or hollow fibers, as well as encapsulating bacteria[2]–[4],[6].

4.2.1. Design of a coelectrospinning apparatus

In order to produce core-shell electrospun fibers, a coaxial electrospinning apparatus adapted to the laboratory electrospinning platform was developed. The spinneret (**Figure 4.2**) polymer parts were designed on Autodesk® Fusion 360 and printed on a Formlabs Form 2 3D-printer in the FLGPGR04 photopolymer resin. The resin is easily cleanable and resistant to the usual electrospinning solvents.

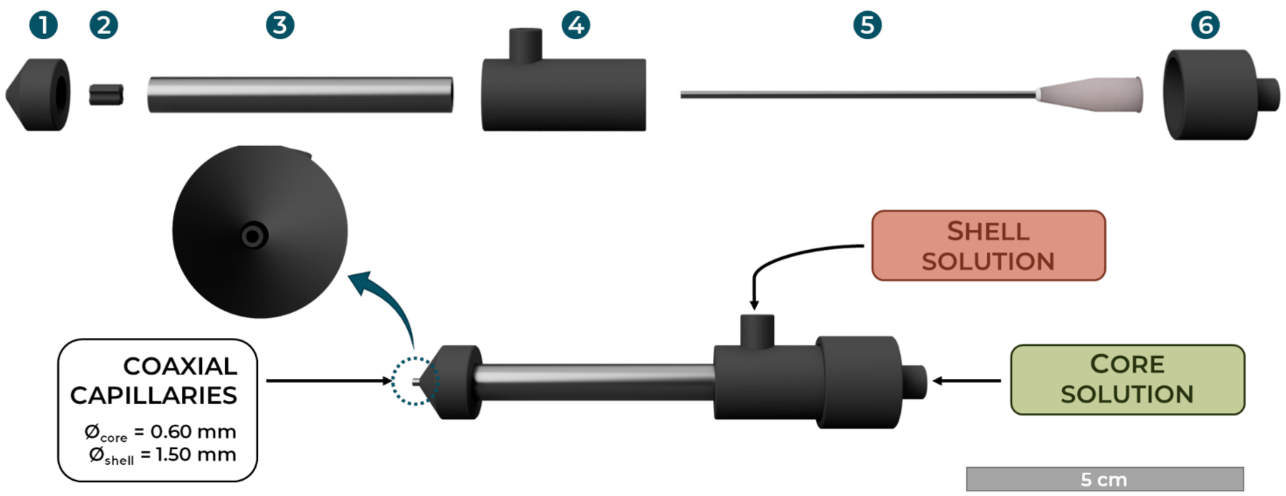

Figure 4.2 – 3D-printed coaxial electrospinning spinneret.

The spinneret is composed of 5 pieces:

1. 3D-printed nozzle (Ø$_{\text{shell}}$ = 1.50 mm);
2. 3D-printed fluted centering piece;
3. Steel tube (Ø = 6 mm);
4. 3D-printed main body with shell solution entry;
5. Blunt-end needle (Ø$_{\text{core}}$ = 0.60 mm);
6. 3D-printed cap with core solution entry.

During its assembly, the various parts were sealed together and electrically isolated with tape. The internal needle is set to slightly protrude from the external nozzle in order to improve the electrospinning stability[2].

4.2.2. Experimental procedure

Due to the targeted application of the core-shell polymer fibers presented in this chapter, the chosen materials should cover the following characteristics:

- An insolubility of the shell in water to ensure the structural integrity of the fibers once immersed in a water-based electrolyte;
- A water soluble core polymer to allow the future adjunction of bacterial cell into this phase while ensuring their survival;
- A biocompatibility of the previous polymers;
- An easy coelectrospinning of the system.

Based on the literature[2],[3], the coextrusion of a poly(ε-caprolactone) shell dissolved in a 9:1 by weight mix of chloroform and DMF and of a poly(ethylene oxide) core dissolved in water (**Figure 4.3**) were hereafter chosen. Due to the immiscibility of the two solutions and difference of solvent affinities of the two polymers, a gelled interface should form between them and stabilize the process.

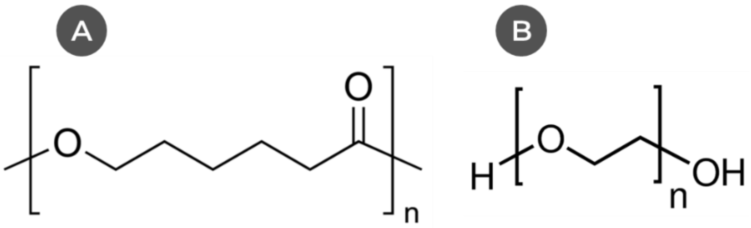

Figure 4.3 – (A) Poly(ε-caprolactone); (B) Poly(ethylene oxide)/Poly(ethylene glycol) structures.

The poly(ε-caprolactone) (PCL, M_w ~ 14 000), the poly(ethylene oxide) (PEO, M_v ~ 600 000) and the poly(ethylene glycol) (PEG, M_n ~ 3000) were purchased from Sigma-Aldrich (USA). The chloroform (99.0-99.4 % stabilized, AnalaR NORMAPUR® ACS, Reag. Ph. Eur. analytical reagent, used as received) and DMF (≥99.8 %, AnalaR NORMAPUR® ACS, Reag. Ph. Eur. analytical reagent, used as received) were purchased from VWR.

The polymer solutions (**Table 2.1**) were stirred overnight at room temperature to ensure their complete dissolution.

Table 4.1 – Formulations of the core and shell solutions for the coelectrospinning.

Solution	Solvent	Polymer	Additives
Core	Milli-Q water	PEO 5 wt%	–
Shell	90:10 (w/w) Chloroform & DMF	PCL 9 wt%	PEG 1 wt%

These solutions are coelectrospun on a grounded aluminum foil fixed on a roller using the Electrospinz ES1™ generator and apparatus and the coaxial electrospinning spinneret (**Figure 4.4**). The spinneret is positioned vertically straight up the roller to avoid gravitational deformation of the double droplet and connected to the generator with copper tape and a high voltage cable. The electrospinning parameters are set as follow[2]:

- **Electric field**: around 2kV·cm^{-1} set by tuning the voltage and distance between the spinneret tip and the collector respectively at 22 kV and 11 cm. The current never exceeded 9 μA;
- **Injection speed**: 3.5 mL·h^{-1} for the shell solution using a Fisherbrand™ syringe pump and a IPAS 20cc glass syringe connected to the shell inlet of the spinneret with a polyethylene tube. 0.5 mL·h^{-1} for the core solution using a Fisherbrand™ syringe pump and a Terumo® 10cc Eccentric Luer Tip syringe connected to the core inlet of the spinneret using a silicone tube;
- **Volume**: 3.5 mL of shell solution & 0.5 mL of core solution are injected to ensure the deposition of a thick self-standing membrane;
- **Temperature**: 21°C thermostatted by the lab air-conditioner;

- **Relative humidity**: in the range of 30 to 60 %. Higher values were avoided by running the setup in a closed poly(methyl acrylate) box connected to the lab dry compressed air outlet;
- **Substrate**: aluminum foil fixed on a roller with a speed set at around 400 rpm.

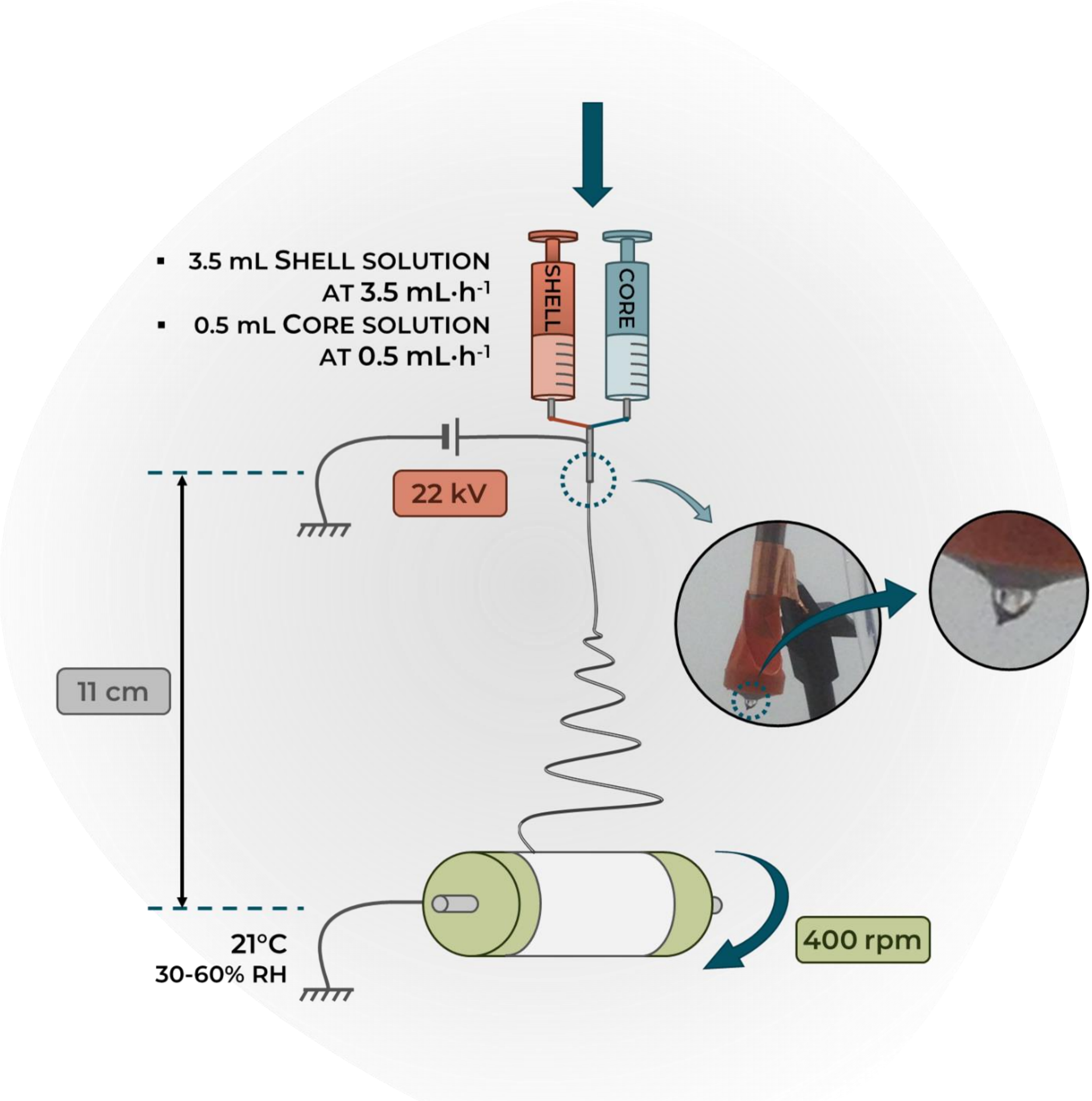
3.5 mL SHELL SOLUTION AT 3.5 mL·h-1
0.5 mL CORE SOLUTION AT 0.5 mL·h-1
SHELL
CORE
22 kV
11 cm
21°C
30-60% RH
400 rpm

Figure 4.4 – Overview of the core-shell coelectrospinning setup used in this study. Note the compound pendant drop and Taylor cone with a gelled interface between the two solutions.

The compound pendant droplet is overall fairly stable. A gelling of the shell solution sometimes occurs. A simple cleaning of the gelled drop with an insulating rod is sufficient to let the process go on.

The resulting deposited fibers are dried overnight at ambient temperature to let the residual solvent evaporate. The self-standing membrane (thickness ~ 100 µm) is easily peeled off the aluminum substrate (**Figure 4.5**).

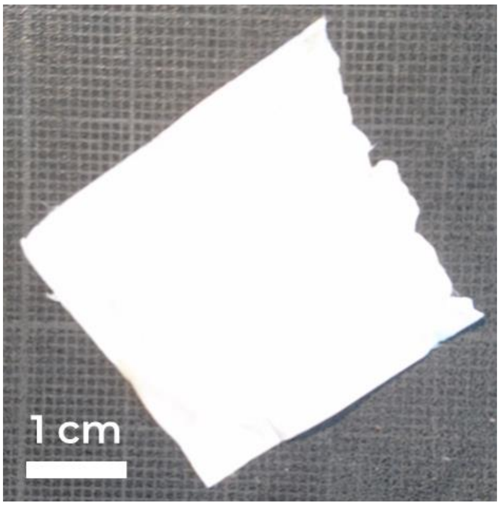

Figure 4.5 – Coelectrospun PCL/PEO membrane.

The coelectrospun membrane is easy to handle, and robust to tearing or bending.

4.2.3. Core-shell architecture characterization

While the coelectrospinning process and the compound droplet are fairly stable and hint for a conclusive core-shell electrospinning, the microscopic architecture of the fibers must be characterized. The coelectrospun mat is then investigated by optical microscope and SEM imaging coupled with focused ion beam (FIB) milling.

4.2.3.1. Optical microscope

Firstly, optical microscopy was performed on a freshly coelectrospun membrane to quickly assess the overall architecture of the membrane (**Figure 4.6**).

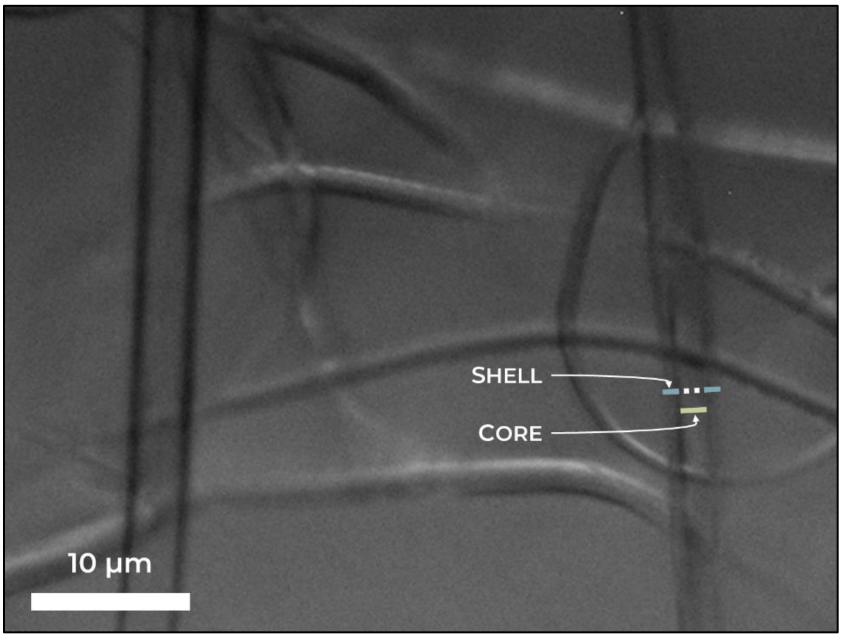

Figure 4.6 – Optical micrographs of coelectrospun fibers (shell: PCL 9 wt% + PEG 1 wt% in 90:10 (w/w) chloroform & DMF; core: PEO 5 wt% in H_2O); Note the presence of a double-walled structure.

The observed fibers indeed seem to longitudinally exhibit a double wall structure, which could be compatible with a core-shell architecture. The width of the outer wall seems to span 3-4 µm, while the inner part has a diameter of 1-2 µm. This technique obviously lacks precision, however it shows an overall structure compatible with a successful core-shell coextrusion.

4.2.3.2. SEM imaging

Furthermore, scanning electron microscopy (Hitachi S-3400N) of the same formulation shows a blend of round-section fibers and of ribbon-like structures with an important porosity (**Figure 4.7**).

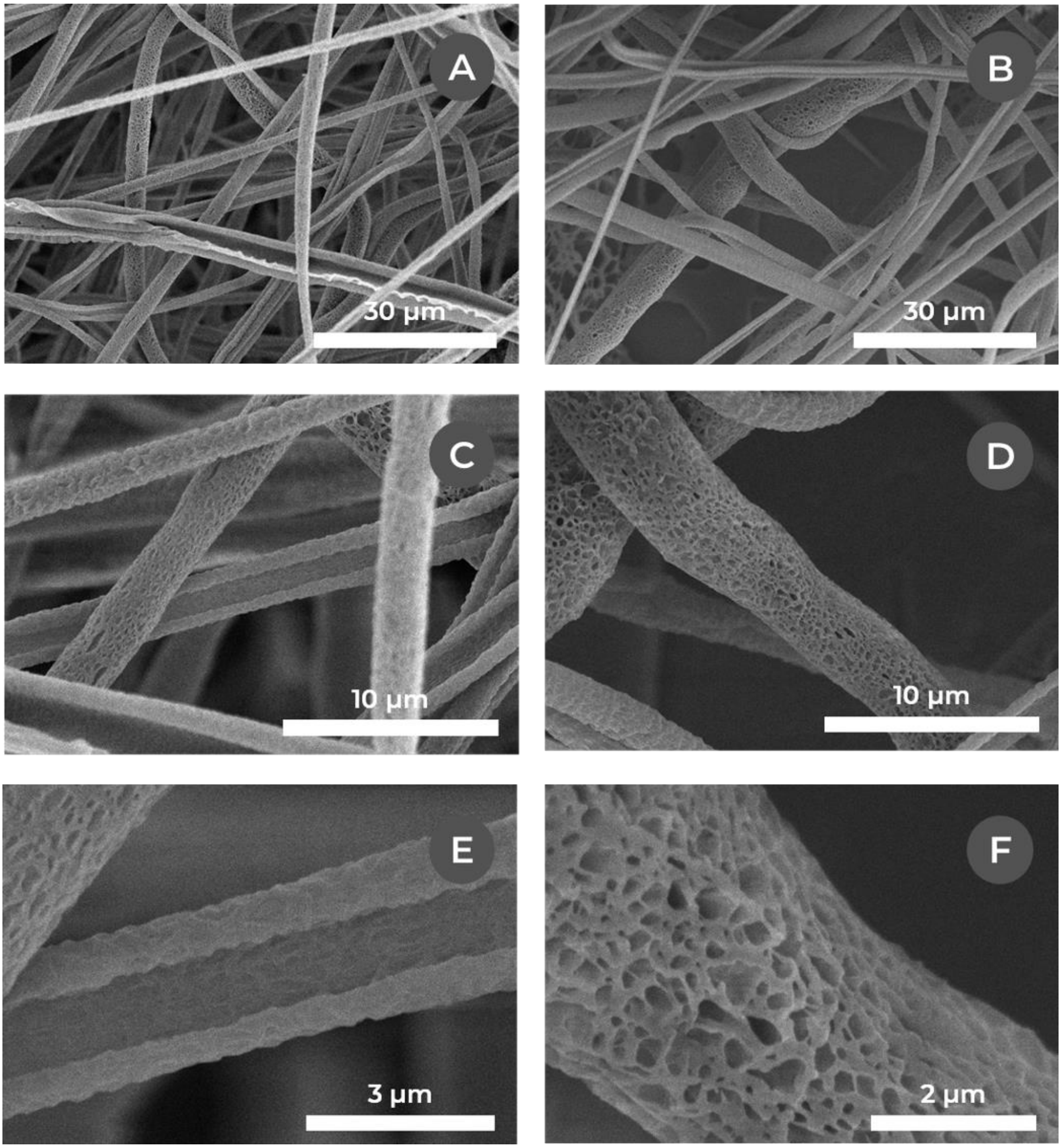

Figure 4.7 – SEM micrographs of coelectrospun fibers (shell: PCL 9 wt% + PEG 1 wt% in 90:10 (w/w) chloroform & DMF; core: PEO 5 wt% in H_2O). (A), (C) & (E) Ribbon-like structure; (B), (D) & (F) Round-section fibers. Membrane coated with 15 nm of gold.

The porosity is expected and resulting of the presence of poly(ethylene glycol) in the shell solution[3]. These pores (~ 200 nm in size) are important for the forecasted encapsulation of bacterial cells to let the surrounding electrolyte diffuse through the walls of the fibers. The presence of ribbon like-structures can be explained by the adsorption of the PEO core onto the inner surface of the shell polymer[2], resulting in the radial collapse of these hollow-fibers[7],[8]. These ribbon-like structures are an important indicator of the inner structure of the fibers, as only successfully coelectrospun core-shell fibers are expected to show this behavior. The round-section fibers cannot be unequivocally attributed to a core-shell architecture at this point. However, their comparable size ($Ø_{ribbon}$ = 2.98 ± 0.90 µm and $Ø_{filled}$ = 3.58 ± 1.61 µm) (**Figure 4.8**) and the even repartition of the two populations inside the mat hint for a similar inner structure. However, their round section might be attributed to a filled core-shell structure which has also been reported for such formulations in the literature[2]. The microtomy or radial milling of the fibers should inform us on their architecture.

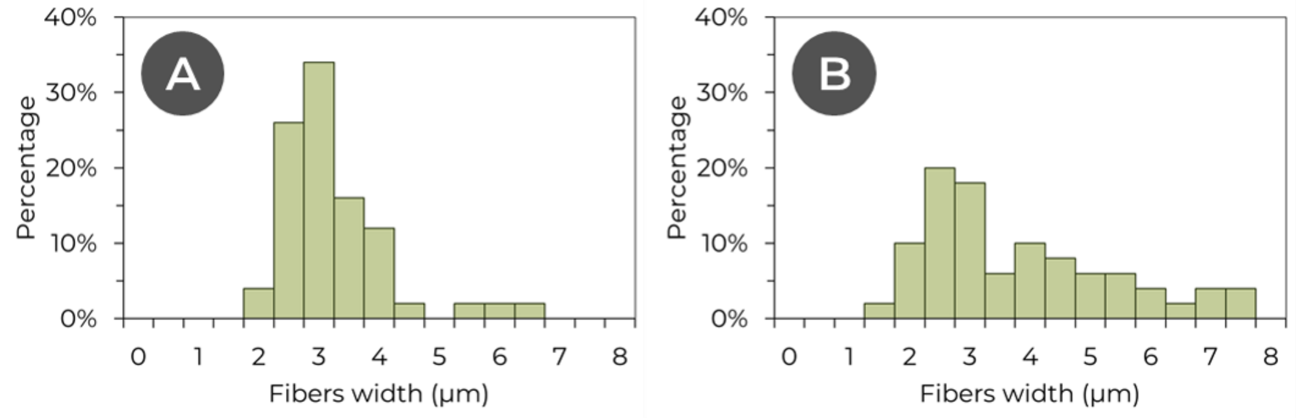

Figure 4.8 – Size distribution of (A) ribbon-like structures & (B) round-section fibers from the SEM micrographs.

4.2.3.3. Focused ion beam milling

Field emission scanning electron microscope (FE-SEM) imaging coupled with focused ion beam (FIB) was performed at the *Institut de Physique du Globe de Paris* with Stephan Borensztajn (Zeiss AURIGA CrossBeam Focused Ion Beam Electron Microscope). The sample was covered with 15 nm of platinum before imaging, and a round-section fiber was radially milled by the focused ion beam (**Figure 4.9**).

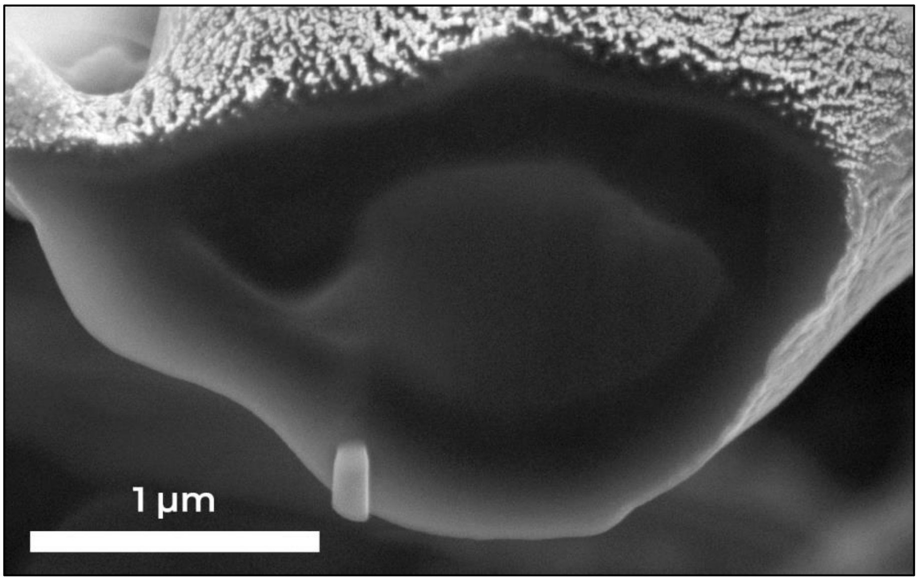

Figure 4.9 – SEM-FEG micrograph of a round-section PCL-PEO coelectrospun fiber radially milled with focused ion milling. Sample covered in 15 nm of Pt; accelerating voltage: 4 kV; FIB milling probe: 30 kV & 240 pA.

The milling of the fibers reveals a radial core-shell structure, with a core of diameter of about 1 µm. The density difference between the two coelectrospun polymers seems sufficient to distinguish them. However, the longitudinal cut of the fibers tends to exhibit an inhomogeneity of the core throughout the fiber, probably due to a compound jet instability.

Overall, the lab-made coelectrospinning spinneret seems fit to produce a core-shell fibers electrospun membrane. The architecture of the resulting fibers varies from collapsed ribbons with hollow core to round-section filled fibers with variable core homogeneity. The outcome of these different structures may mainly depend on ambient parameters and on the stability of the compound droplet during the long electrospinning processes but consistently yields core-shell fibers compatible with the eventual encapsulation of bacteria in their core.

4.3. Bacteria encapsulation

Electrospun core-shell fibers can be used to encapsulate bacteria[3],[4]. Bacterial survival rate to the electrospinning is usually high without any major cellular damage[9],[10]. However, encapsulation of electroactive microorganisms is not widely reported in the literature, and the survival rate of *Shewanella oneidensis* upon coaxial electrospinning was so far unknown.

4.3.1. Bacterial culture

The coaxial electrospinning of two non-electroactive fluorescent proteins-expressing strains (GFP-expressing *Dickeya dadantii* 3937[11] & mCherry-expressing *Pseudomonas fluorescens* PCL1701[12]) as well as *Shewanella oneidensis* CRBIP17.141 was conducted. The fluorescent strains were selected as a mean to characterize the encapsulation of the bacteria inside the fibers.

D. dadantii 3937 were provided by the *Laboratoire Physiologie Cellulaire et Végétale* (LPCV). They were grown overnight on LB-agar[13], then cultivated overnight in LB medium at 30°C and sampled at $OD_{600} \approx 2$. The cells were centrifuged at 5000 g for 20 minutes at 4°C before resuspending them in phosphate buffered saline (PBS; 137 mM NaCl, 2.7 mM KCl, 10 mM Na_2HPO_4, 1.76 mM KH_2PO_4) at the same optical density.

P. fluorescens PCL1701 were provided by the *Institut de Biologie Paris-Seine* (IBPS). They were grown on LB-agar with gentamycin (8 $\mu g{\cdot}mL^{-1}$) for 48 hours, then cultivated overnight in 5 mL of LB medium with gentamycin (8 $\mu m{\cdot}mL^{-1}$). The cells were centrifuged at 5000 g for 20 minutes at 4°C before resuspending them in PBS at $OD_{600} \approx 2$.

The culture protocol of *S. oneidensis* CRBIP17.141 is identical to the one presented in Chapter 2. The bacteria are sampled from the exponential phase at $OD_{600} \approx 1.6$, centrifuged at 5000 g for 20 minutes at 4°C before resuspending them in PBS at $OD_{600} = 1.4$.

4.3.2. Core-shell coextrusion

The core pre-mix and shell solutions (**Table 4.2**) are prepared in sterile conditions and stirred overnight at room temperature to ensure the complete dissolution of the polymers. The final core solution is prepared by blending the core pre-mix in 50:50 (v/v) proportions with a fresh suspension of bacterial cells in PBS in sterile conditions and stirring for 30 minutes – resulting in a final cell optical density of around 1 for *D. dadantii* and *P. fluorescens*, and 0.7 for *S. oneidensis*, and a concentration by weight of 5 % of PEO.

Table 4.2 – Formulations of the core and shell solutions for the coelectrospinning & bacteria encapsulation.

Solution	Solvent	Polymer	Additives
Core pre-mix	Milli-Q water	PEO 10 wt%	–
Shell	90:10 (w/w) Chloroform & DMF	PCL 9 wt%	PEG 1 wt%

These solutions are electrospun in the same conditions as presented in *4.2.2 Experimental procedure*. The mat is air-dried for about 4 hours and yield a self-standing membrane (thickness ~ 100 µm) easily peeled off the aluminum foil (**Figure 4.10**).

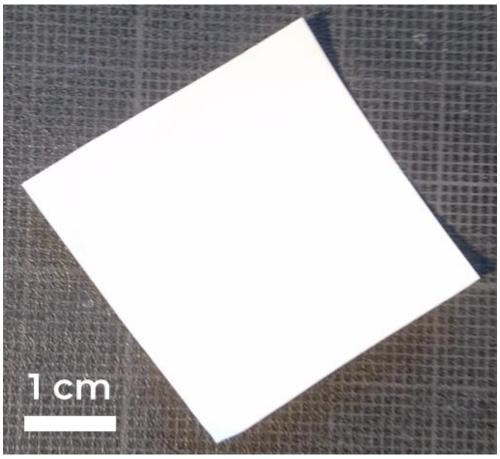

Figure 4.10 – Coelectrospun PCL/PEO membrane encapsulating *Shewanella oneidensis*.

The bacteria adjunction to the system does not affect the mechanical properties of the membrane which is still robust and easily handled.

4.3.3. Bacteria encapsulation characterization

In order to verify the proper encapsulation and survival rate of the bacteria, the coelectrospun mats were characterized by epifluorescence and confocal microscopy and SEM.

4.3.3.1. Epifluorescence microscope

A coelectrospun membrane is prepared from the previous formulations (**Table 4.2**) and the core pre-mix is blended with GFP-expressing *D. dadantii* suspended in PBS 1X at $OD_{600} \approx 1$.

The fibers are collected on a clean microscope slide and imaged under an epifluorescence microscope (Zeiss Axio Imager D1) in brightfield and for GFP fluorescence (**Figure 4.11**).

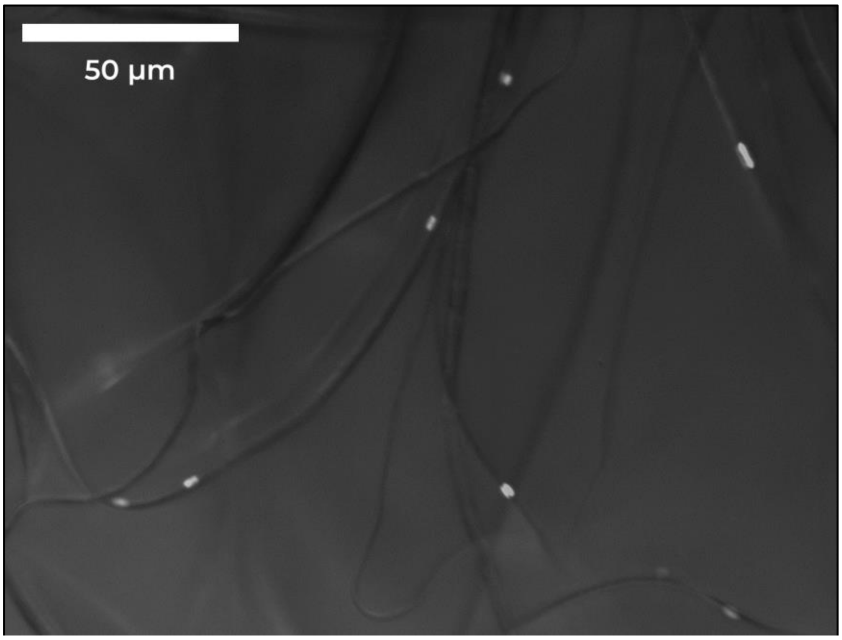

Figure 4.11 – Epifluorescence micrograph of coelectrospun fibers (shell: PCL 9 wt% + PEG 1 wt% in 90:10 (w/w) chloroform & DMF; core: PEO 5 wt% in PBS 0.5X + GFP-expressing *D. dadantii* at OD_{600} ≈ 1). The image is a composite of the brightfield and of GFP channels (the bacteria appear as the white dots).

These observations confirm the colocalisation of the bacteria with the electrospun core-shell fibers. Better information on the encapsulation of the cells will however need a higher resolution.

4.3.3.2. Confocal microscope

The encapsulation is henceforth more finely investigated by adding Coumarin 6 (Sigma-Aldrich, 1 mM) into the shell solution right before the electrospinning, and mCherry-expressing *P. fluorescens* PCL1701 into the core solution. The coelectrospun membrane is then imaged by confocal microscopy (**Figure 4.12**) with the help of France Lam at the IBPS (Leica TCS SPE).

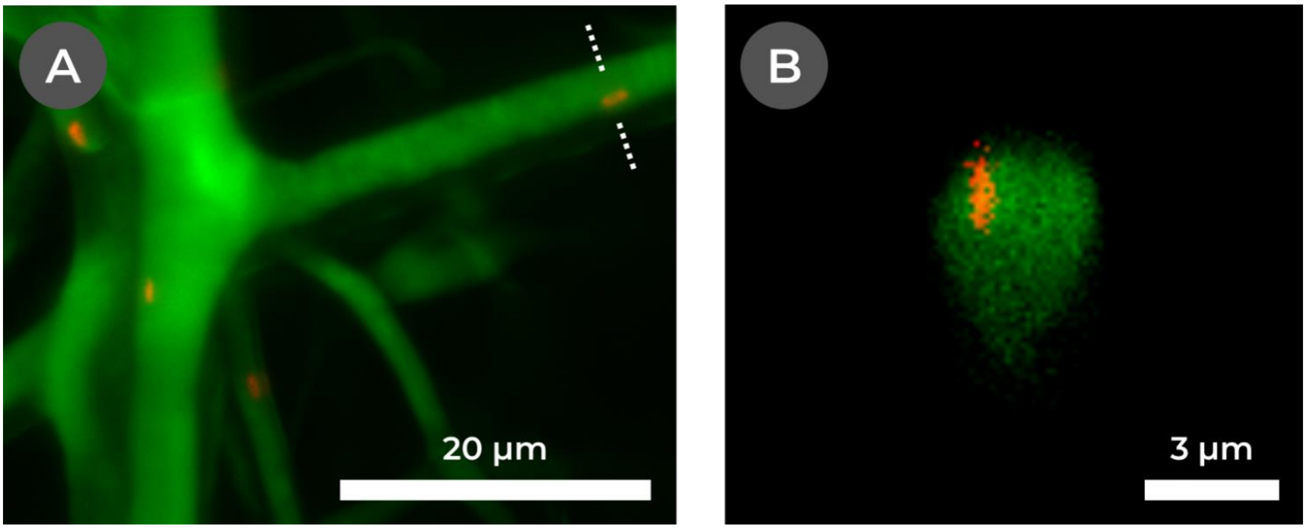

Figure 4.12 – Confocal microscopy of the coelectrospun membrane (shell: PCL 9 wt% + PEG 1 wt% in 90:10 (w/w) chloroform & DMF; core: PEO 5 wt% in PBS 0.5X + mCherry-expressing *P. fluorescens* at OD_{600} ≈ 1). Green highlights the Coumarin 6 signal, red the mCherry signal expressed by the bacteria. (A) Micrograph of the coelectrospun fibers colocalized with *P. fluorescens*; (B) Radial cut of one of the fibers and a bacterium along the white dots line.

Bacteria are again clearly seen colocalized within the coelectrospun fibers (**Figure 4.12.A**). Note that they are longitudinally aligned with the fibers. A radial cut along the axis of the fibers supposedly encapsulating a bacterium clearly show that the cell is indeed inside the fiber (**Figure 4.12.B**).

4.3.3.3. SEM imaging

SEM imaging (**Figure 4.13**) shows an overall structure similar to what was observed previously. The coelectrospun mat is a mix of ribbons and round-section fibers, with an average diameter slightly bigger than before (3.88 ± 1.52 µm). Likewise, the fibers exhibit an analogue porosity on their surface.

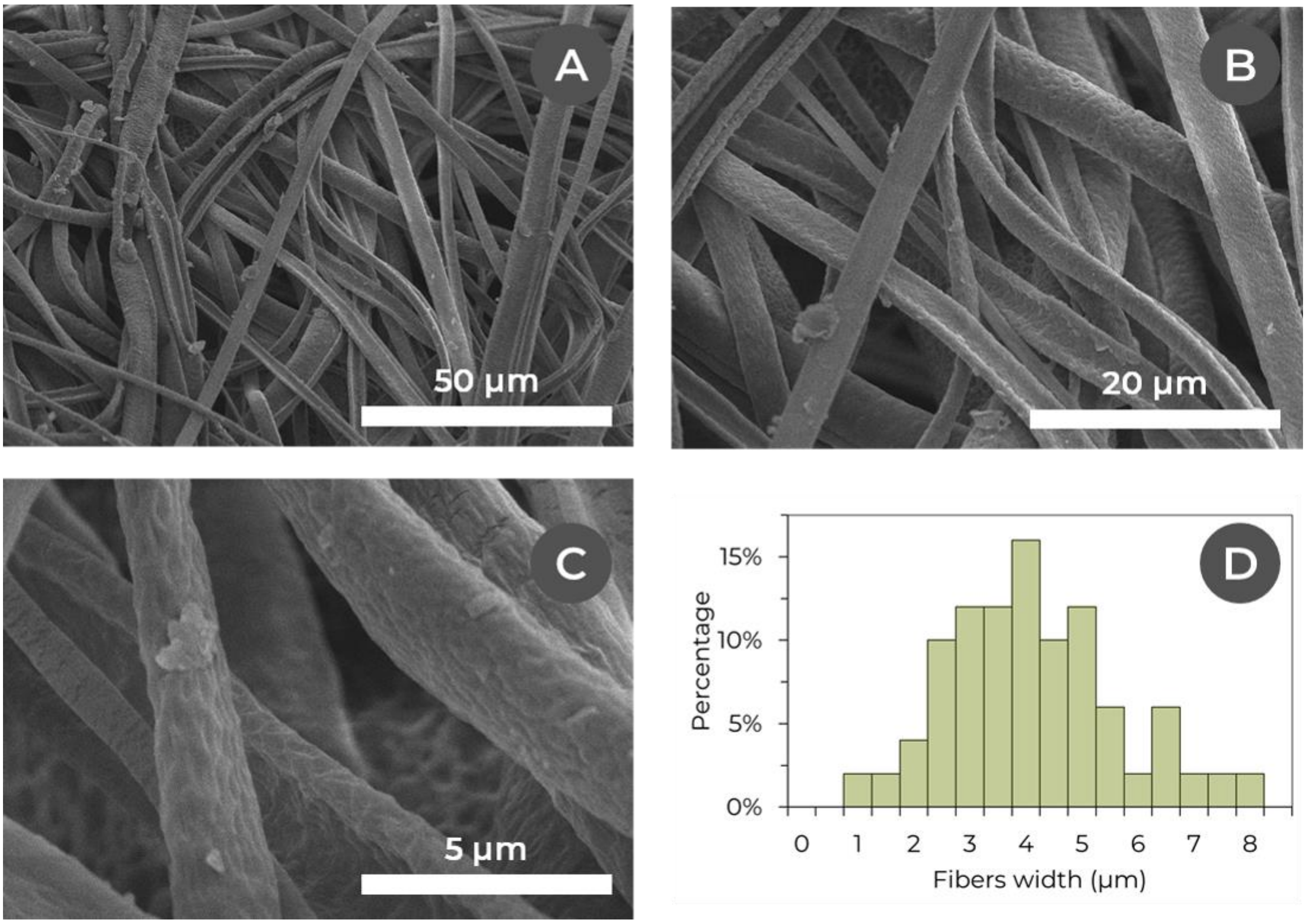

Figure 4.13 – (A), (B), (C) SEM micrographs of coelectrospun fibers encapsulating *S. oneidensis* (shell: PCL 9 wt% + PEG 1 wt% in 90:10 (w/w) chloroform & DMF; core: PEO 5 wt% in PBS 0.5X + *S. oneidensis* at OD_{600} ≈ 0.7) & (D) fibers size distribution; N = 50. Membranes coated with 15 nm of gold.

The core-shell structure observed previously does not seem affected by the adjunction of the bacteria and PBS. The fibers are big enough to encapsulate properly the cells, which are not widely found outside them.

4.3.3.4. Bacteria survival

LIVE/DEAD assay and electroactivity evaluation of the encapsulated cells will be conducted for the final bioanode formulation on *Shewanella oneidensis*. However at this stage, the detectability of the GFP and mCherry fluorophores expressed respectively by the *D. dadantii* and *P. fluorescens* cells encapsulated within the coelectrospun fibers combined to the reported survival of bacteria under similar conditions is deemed sufficient to ensure their survival[3],[14].

The coelectrospinning setup developed previously is henceforth able to encapsulate bacteria in the core of the fibers. Moreover, no major damage seems to affect the encased cells, as expected under these electrospinning conditions.

4.4. Dual electrospun core-shell/conductive fibers scaffold network

The use of a material as an electrode indeed requires a good electronic conductivity. The coelectrospun networks described previously in this chapter are nonetheless insulating and their design therefore require modifications before being used for electrochemical applications. Direct integration of large quantities of carbon black into the core-shell fibers to turn the mat conductive has been tried out but however leads to a highly instable and difficult electrospinning.

Hereafter, we present the development of a dual electrospun core-shell/conductive scaffold network (**Figure 4.14**) enhancing the electrical conductivity of the electrospun mat while integrating core-shell fibers throughout a polymer–carbon scaffold. This architecture is based on the dual conductive network design presented in Chapter 3. Conductive carbon is also added to the shell of the coelectrospun fibers to connect them to the secondary conductive network.

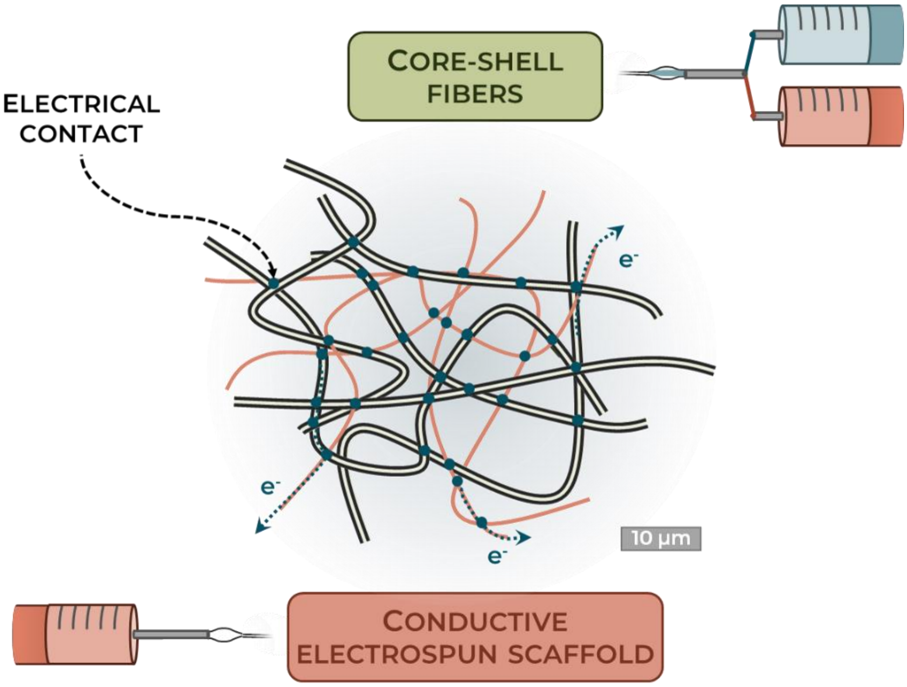

Figure 4.14 – Architecture of the dual electrospun core-shell/conductive fibers scaffold.

4.4.1. Dual electrospinning setup

The formulations of the solutions (**Table 4.3**) for the electrospinning of the dual electrospun electrode are prepared according to the results of Chapter 3 and of *4.3.2 Core-shell coextrusion* after optimization of the process. In particular, the proportion of PCL was gradually reduced and replaced with carbon black until a stable co-electrospinning process was reached.

The scaffold microfibers solution is henceforth based on a mix of polyacrylonitrile (PAN, M_w ~ 150 000) purchased from Sigma-Aldrich (USA) and Vulcan XC-72R Carbon black (CB) purchased from FuelCellStore.

The core solution is stirred overnight at room temperature to ensure the complete dissolution of the polymer. The shell and conductive scaffold solutions are prepared by firstly dispersing the carbon black in the solvents in an ultrasonic bath (ultrasonic effective power: 75 W) for 30 minutes before adding the polymers and stirring overnight at room temperature until full dissolution.

Table 4.3 – Formulations of the core, shell & conductive scaffold solutions for the dual electrospinning of the core-shell/conductive fibers scaffold membrane.

Solution	Solvent	Polymer	Additives
Core	Milli-Q water	PEO 5 wt%	–
Shell	90:10 (w/w) Chloroform & DMF	PCL 6 wt%	PEG 1.5 wt% + CB 2 wt%
Conductive scaffold	DMF	PAN 7 wt%	CB 7wt%

These solutions are electrospun on a grounded aluminum foil fixed on a roller using the Electrospinz ES1™ generator and apparatus, the coaxial electrospinning spinneret and a second spinneret for the conductive scaffold solution (**Figure 4.15**). The spinneret is positioned vertically straight up the roller while the second spinneret is set horizontally. The electrospinning parameters are defined as follow:

- **Electric field**: around 1.4 kV·cm^{-1} set by tuning the voltage and distance between the spinnerets and collector respectively at 18.5 kV and 13 cm;
- **Injection speed**: 3.5 mL·h^{-1} for the shell solution using a Fisherbrand™ syringe pump and a IPAS 20cc glass syringe connected to the shell inlet of the spinneret with a polyethylene tube. 0.5 mL·h^{-1} for the core solution using a Fisherbrand™ syringe pump and a Terumo® 10cc Eccentric Luer Tip syringe connected to the core inlet of the spinneret using a silicone tube. 3.5 mL·h^{-1} for the scaffold solution using a Fisherbrand™ syringe pump and a Terumo® 10cc Eccentric Luer Tip syringe equipped with a blunt-end needle ($Ø_{internal}$ = 0.75 mm);
- **Volume**: around 1.5 mL of shell solution, 0.2 mL of core solution & 1.5 mL of the conductive scaffold solution are injected to ensure the deposition of a thick self-standing membrane;
- **Temperature**: 21°C thermostatted by the lab air-conditioner;
- **Relative humidity**: kept between 30 and 60 % by running the setup in a closed poly(methyl acrylate) box connected to the lab dry compressed air outlet;
- **Substrate**: aluminum foil fixed on a roller with a speed set at around 400 rpm.

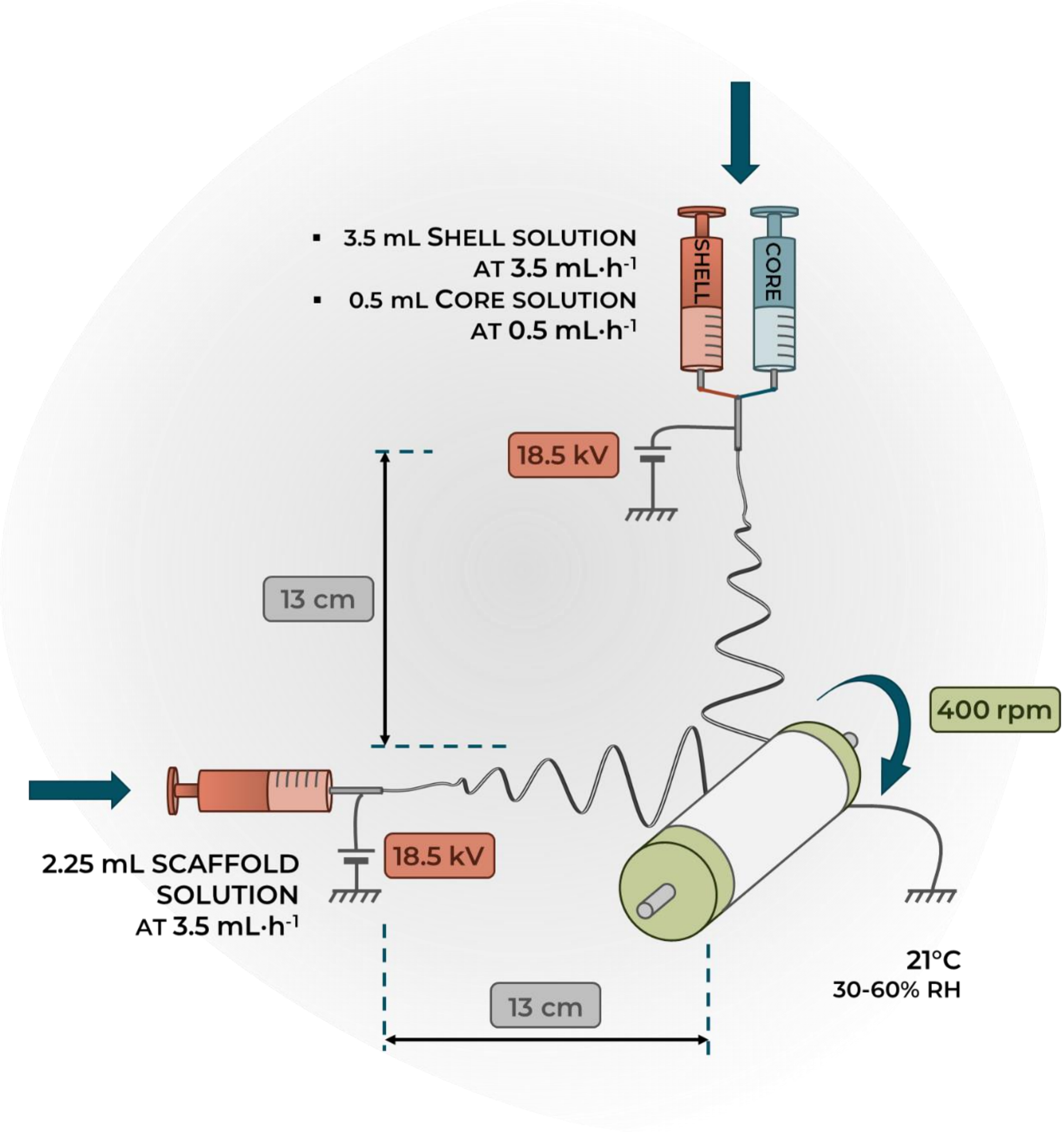
▪ 3.5 mL SHELL SOLUTION
AT 3.5 mL·h⁻¹
▪ 0.5 mL CORE SOLUTION
AT 0.5 mL·h⁻¹
SHELL
CORE
18.5 kV
13 cm
400 rpm
2.25 mL SCAFFOLD
SOLUTION
AT 3.5 mL·h⁻¹
18.5 kV
21°C
30-60% RH
13 cm

Figure 4.15 – Overview of a dual coelectrospinning/secondary mat electrospinning setup.

The resulting self-standing membrane (thickness ~ 100 µm) is air-dried for about 4 hours and easily peeled off the aluminum foil (**Figure 4.16**).

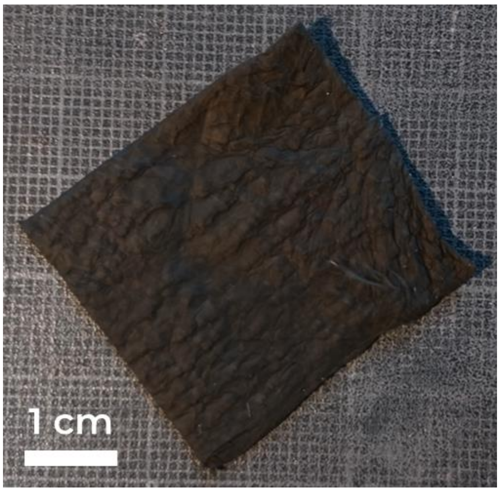

Figure 4.16 – Dual electrospun core-shell/conductive fibers scaffold membrane.

The electrospun membrane handling is overall similar to the previous coelectrospun samples. The adjunction of carbon black modifies its color which turns black. Furthermore, it does not seem to affect its macroscopic mechanical properties.

4.4.2. Network characterization

The dual electrospun core-shell/conductive fibers scaffold membrane architecture is subsequently characterized by SEM imaging and its conductivity by a two-electrode setup and impedance spectroscopy.

4.4.2.1. SEM imaging

SEM imaging of the dual electrospun core-shell/conductive fibers scaffold membrane (**Figure 4.17**) exhibits two populations of intermingled fibers. The coelectrospun network is a mix of ribbon-like collapsed and round-section fibers. The presence of carbon black in their walls is clearly noticeable from their rough surface, as well as their porosity (**Figure 4.17.B**). The secondary conductive scaffold surrounds the core-shell fibers and seems well interconnected (**Figure 4.17.C**). A close-up on these fibers shows continuous and homogeneous presence of carbon black along them (**Figure 4.17.D**). Overall, the aimed architecture of the dual electrospun mat seems to have been reached.

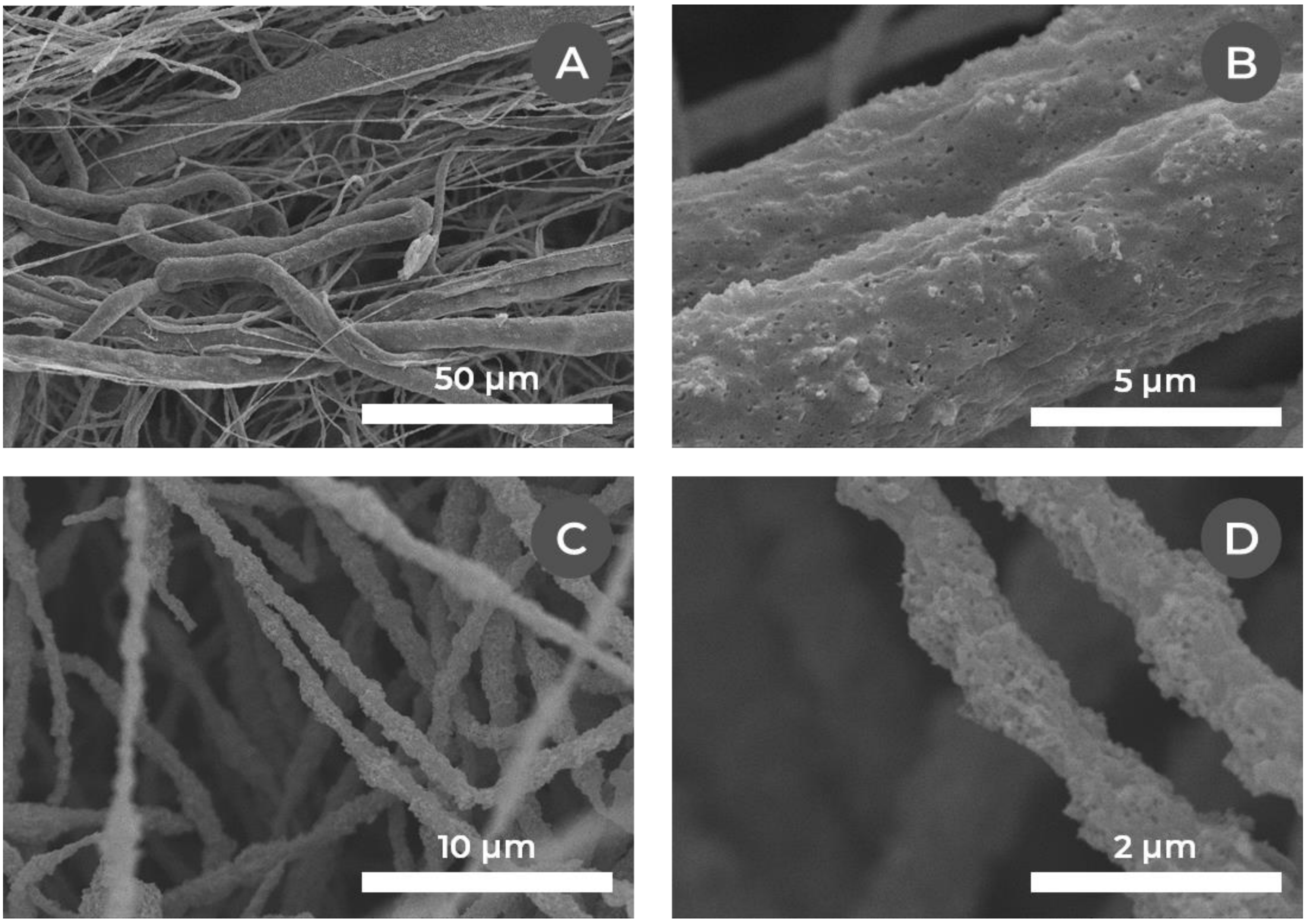

Figure 4.17 – SEM micrographs of the core-shell/conductive fibers scaffold dual electrospun membrane. (A) Overall aspect of the mat. Note the two intermingled populations of fibers; (B) Close-up on the core-shell fibers (coelectrospun from the following solutions; shell: PCL 6 wt% + PEG 1.5 wt% + CB 2 wt% in 90:10 (w/w) chloroform & DMF; core: PEO 5 wt% in H_2O), coated with 15 nm of gold; (C) Conductive scaffold (electrospun from PAN 7 wt% + CB 7 wt% in DMF); (D) Close-up on the conductive scaffold fibers.

The size distribution of the two fibers populations ($Ø_{\text{core-shell}} = 5.67 \pm 2.60$ µm and $Ø_{\text{scaffold}} = 0.986 \pm 0.259$ µm) is less homogenous, but still consistent with the results obtained for the previous systems (**Figure 4.18**). Note that the two previously observed populations of coelectrospun fibers – ribbon-like collapsed structures and round-section fibers – are visible again here.

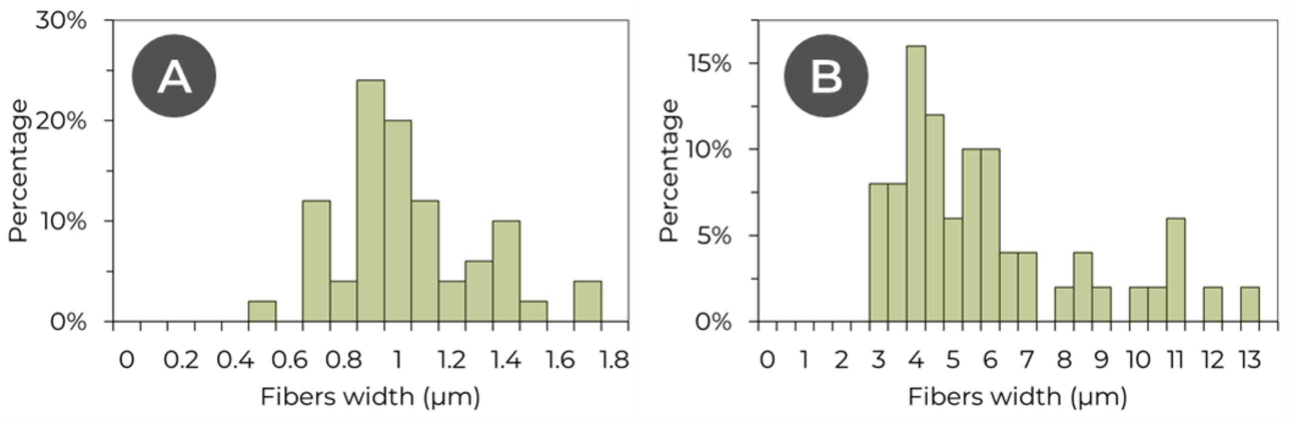

Figure 4.18 – Size distribution of (A) conductive scaffold fibers & (B) coelectrospun fibers from the SEM micrographs.

The volumetric mass density of the fibers is evaluated by weighting a piece of electrospun membrane of known dimensions at around $\rho \approx 0.1$ g·cm^{-3}, which is similar to the electrospun carbon membrane. Its total porosity is evaluated by mercury porosimetry to about 95 % which is consistent with the SEM observations. The interfiber space is around 1 µm.

4.4.2.2. Electrical conductivity

The electrical conductivity of the dual electrospun membrane is studied both by a two-electrode setup and impedance spectroscopy. The two-electrode setup allows the determination of the surface conductivity σ_S, while the transverse conductivity σ_T is evaluated by coupling it with a Swagelok® cell configuration and impedance spectroscopy.

The two-electrode surface measurement gives values that are relatively inhomogeneous along the dual electrospun membrane, but typical values are about $\sigma_S \sim 10^{-2}$ S·cm^{-1}. Impedance spectroscopy exhibits solely a real impedance value. Furthermore, the typical transverse conductivity is about $\sigma_T \sim 10^{-2}$ to 10^{-3} S·cm^{-1}. These values are one order of magnitude smaller than the electrospun carbon electrodes presented in Chapter 2 but still suitable for electrochemical applications (**Table 4.4**). This difference is probably explained by the lower carbon fraction in the dual electrospun fibers than in the electrospun carbon electrodes. Indeed, XPS measurements on electrospun carbon electrodes show a carbon proportion in the fibers of around 84 wt%, while the dual electrospun membrane carbon is added in the form of percolating particles at around 33 wt% in the final dry mat. Note that the dual electrospun core-shell/conductive scaffold membrane has however a better conductivity than the dual mat tested in Chapter 3. This is easily explained by the higher fraction of carbon black in the conductive fibers (50 % vs. 28.5 %). Note that a mat obtained from the core-shell fibers only is highly resistive ($\sigma_S \sim 10^{-5}$ S·cm^{-1}).

Table 4.4 – Typical electrical conductivities σ_S & σ_T for the electrospun carbon electrode & the dual electrospun core-shell/conductive scaffold membrane.

Sample	σ_S (S·cm^{-1})[a]	σ_T (S·cm^{-1})[b]
Electrospun carbon electrode	~ 10^{-1}	~ 10^{-1} to 10^{-2}
Dual electrospun PCL 9wt%/PAN 10 wt% + CB 4 wt% (Chapter 3)	~10^{-3} to 10^{-4}	~10^{-5} to 10^{-6}
Dual electrospun core-shell/conductive scaffold membrane	~ 10^{-2}	~ 10^{-2} to 10^{-3}

[a] Calculated from two-electrode setup measurements; maximum sensibility of 40 MΩ. [b] Calculated from impedance spectroscopy measurements; amplitude of 100 mV; maximum sensibility of ~ 10^8 Ω.

Overall the addition of the polymer–carbon scaffold provides a reliable way to attain a conductive electrospun membrane without heat treatment.

The dual electrospun core-shell/conductive scaffold membrane aimed to provide a conductive electrospun membrane including core-shell coelectrospun fibers. After process optimization, an electrospun mat meeting the previous requirements was eventually obtained (thickness of ~ 100 µm). Core-shell fibers with carbon black included in their wall are intermingled with polymer–carbon conductive scaffold fibers, exhibiting a high porosity of around 95 %. Additionally, the electrical conductivity of the fibers electrospun mat is measured to be ~ 10^{-2} to 10^{-3} S·cm^{-1}.

4.5. Integrated one-step conductive bioanode encapsulating electroactive bacteria

Once a satisfactory electrospun core-shell/conductive scaffold network membrane production protocol is determined, the encapsulation of electroactive bacteria inside the coelectrospun fibers can be addressed.

We then investigate a novel dual electrospun core-shell/conductive scaffold network (**Figure 4.19**) encapsulating the exoelectrogenic *Shewanella oneidensis* CRBIP17.141, based on the dual conductive network design presented in *4.4. Dual electrospun core-shell/conductive fibers scaffold network*. Its architecture and their performances in an MFC reactor electrospun electrode will then be studied. This design will thereafter be referred to as the “Integrated bioanode”.

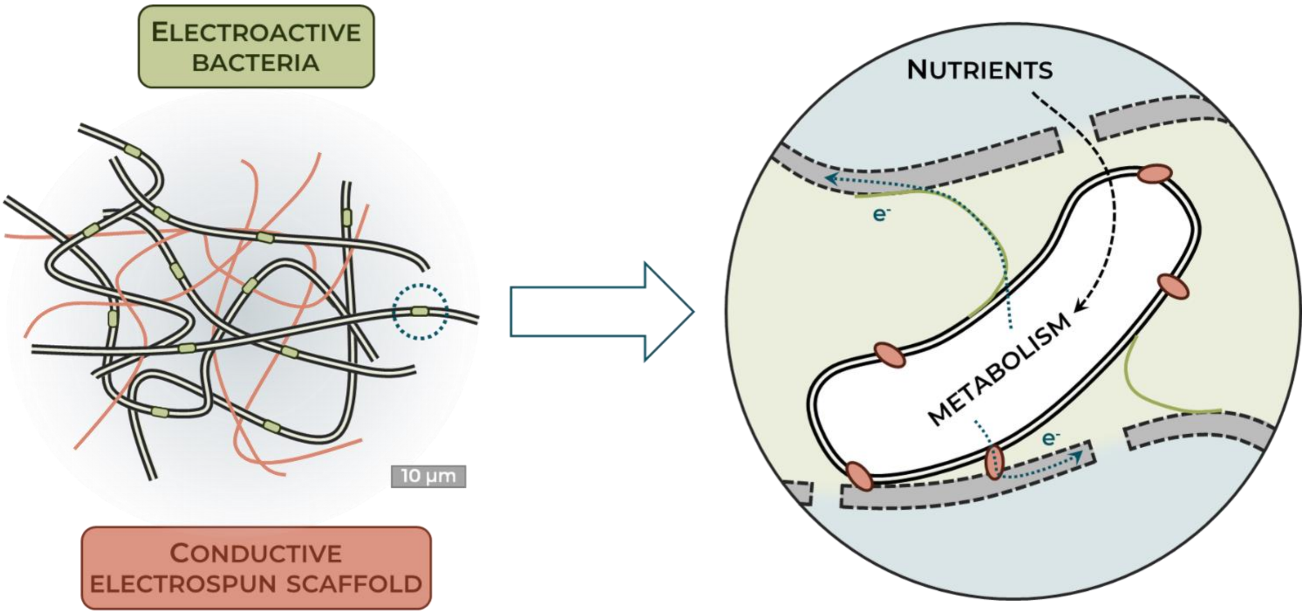

Figure 4.19 – Architecture of the dual electrospun core-shell/conductive fibers scaffold encapsulating bacteria – the “Integrated bioanode”

4.5.1. Electrospinning setup

The formulations of the solutions (**Table 4.5**) for the dual electrospinning of the integrated bioanode are prepared according to the results of *4.4. Dual electrospun core-shell/conductive fibers scaffold network*. The core pre-mix solution is prepared in sterile conditions and stirred overnight at room temperature to ensure the complete dissolution of the polymer. The core solution is prepared by blending the core pre-mix in 50:50 (v/v) proportions with a fresh suspension of *S. oneidensis* in PBS at OD_{600} = 2 in sterile conditions and stirring for 30 minutes – resulting in a final cell optical density of ~ 1 and a concentration by weight of 5 % of PEO.

The shell and conductive scaffold solutions are prepared by dispersing the carbon black in the solvents in an ultrasonic bath for 30 minutes (ultrasonic effective power: 75 W) and then adding the polymers and stirring overnight at room temperature until full dissolution.

Table 4.5 – Formulations of the core, shell & conductive scaffold solutions for the dual electrospinning of the integrated bioanode.

Solution	Solvent	Polymer	Additives
Core pre-mix	Milli-Q water	PEO 10 wt%	–
Shell	90:10 (w/w) Chloroform & DMF	PCL 6 wt%	PEG 1.5 wt% + CB 2 wt%
Conductive scaffold	DMF	PAN 7 wt%	CB 7wt%

These solutions are electrospun on a grounded aluminum foil on a roller using the Electrospinz ES1™ generator and apparatus, the coaxial electrospinning spinneret and a second spinneret for the conductive scaffold solution as presented previously. The core solution is more conductive than before due to the adjunction of PBS – the PBS 1X has a ionic conductivity of around 16 mS·cm^{-1}, while PEO 5 wt% in H_2O has a conductivity of 13 µS·cm^{-1} – which may affect the architecture of the fibers[2],[15]. The electrospinning parameters are then slightly tweaked as follow:

- **Electric field**: around 1 kV·cm^{-1} set by tuning the voltage and distance between the spinnerets and collector respectively at 13 kV and 13 cm;
- **Injection speed**: 3.5 mL·h^{-1} for the shell solution using a Fisherbrand™ syringe pump and a IPAS 20cc glass syringe connected to the shell inlet of the spinneret with a polyethylene tube. 0.5 mL·h^{-1} for the core solution using a Fisherbrand™ syringe pump and a Terumo® 10cc Eccentric Luer Tip syringe connected to the core inlet of the spinneret using a silicone tube. 3.5 mL·h^{-1} for the scaffold solution using a Fisherbrand™ syringe pump and a Terumo® 10cc Eccentric Luer Tip syringe equipped with a blunt-end needle ($Ø_{internal}$ = 0.75 mm);
- **Volume**: around 2.3 mL of shell solution, 0.3 mL of core solution & 1.2 mL of the conductive scaffold solution are injected to ensure the deposition of a thick self-standing membrane;
- **Temperature**: 21°C thermostatted by the lab air-conditioner;
- **Relative humidity**: kept between 30 and 60 % by running the setup in a closed poly(methyl acrylate) box connected to the lab dry compressed air outlet;
- **Substrate**: aluminum foil fixed on a roller with a speed set at around 400 rpm.

The resulting self-standing membrane (thickness ~100 µm) is air-dried for about 4 hours and easily peeled off the aluminum foil (**Figure 4.20**).

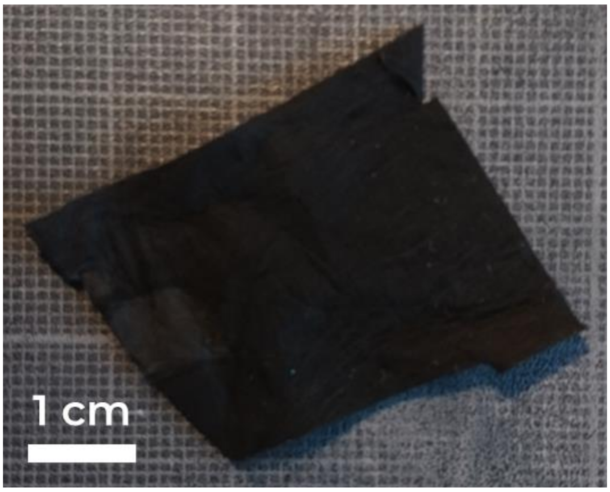

Figure 4.20 – Dual electrospun core-shell/conductive fibers scaffold encapsulating *Shewanella oneidensis* – the "Integrated bioanode"

Like the previous samples, the obtained membrane is robust and easily handled.

4.5.2. Bioanode characterization

The integrated bioanode architecture, bacteria survival rate are henceforth characterized by SEM and confocal microscopy imaging. Its conductivity is measured by a two-electrode setup and impedance spectroscopy.

4.5.2.1. SEM imaging

SEM imaging of the integrated bioanode (**Figure 4.21**) shows as expected the two populations of intermingled fibers portrayed in *4.4. Dual electrospun core-shell/conductive fibers scaffold network*. The overall architectures are similar, and very few bacteria can be spotted outside the fibers.

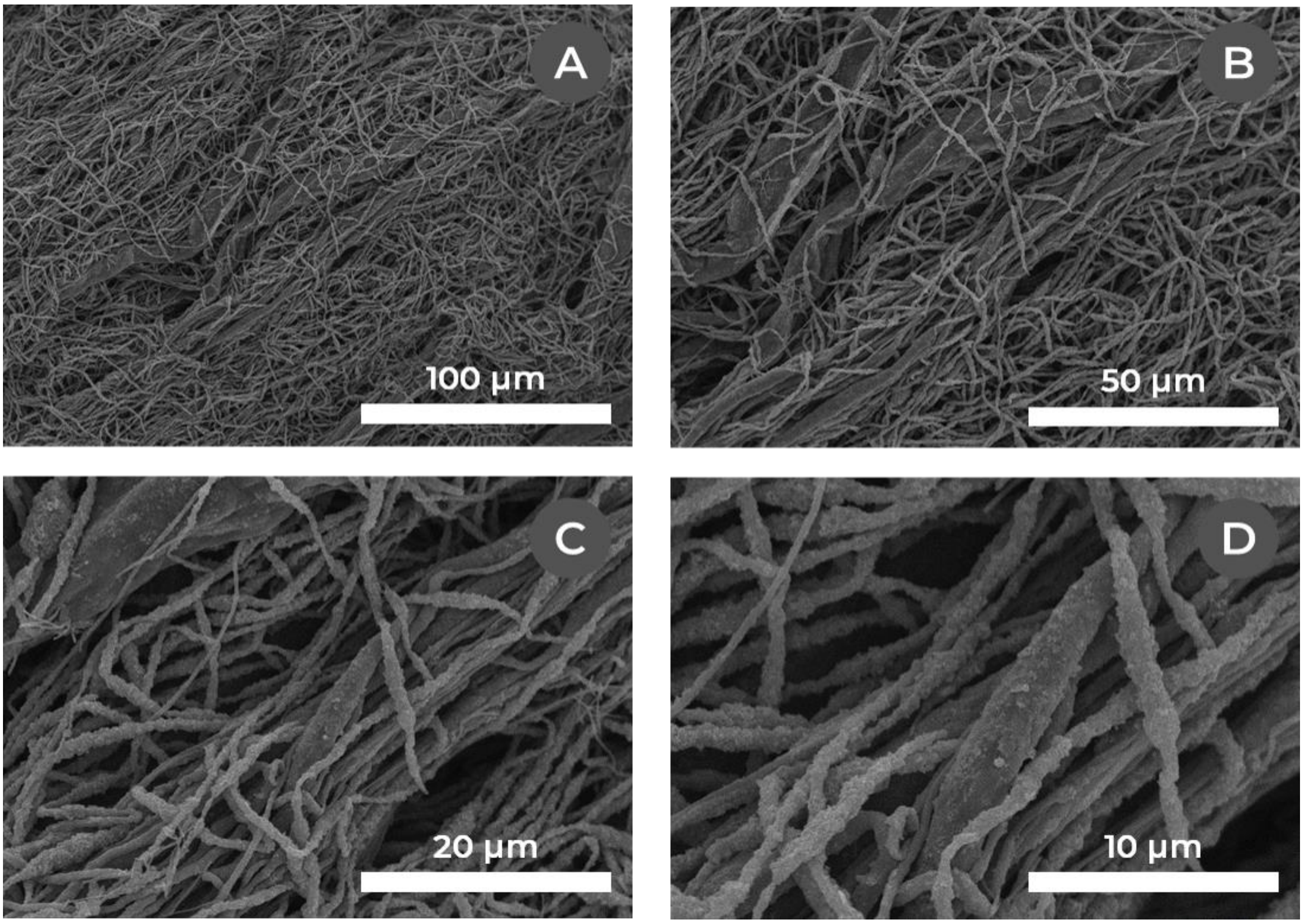

Figure 4.21 – SEM micrographs of the integrated bioanode membrane (dual electrospun from the following solutions; shell: PCL 6 wt% + PEG 1.5 wt% + CB 2 wt% in 90:10 (w/w) chloroform & DMF; core: PEO 5 wt% in PBS 0.5X + *S. oneidensis* at OD_{600} ≈ 1; conductive scaffold: PAN 7 wt% + CB 7 wt% in DMF), coated with 15 nm of gold. Note the two intermingled populations of fibers.

The aimed architecture of the integrated bioanode fibers therefore seem to have been reached.

4.5.2.2. Confocal microscopy & bacteria viability

The survival rate as well as the successful encapsulation of the bacteria after electrospinning of the integrated bioanode is evaluated with an Invitrogen™ LIVE/DEAD™ *Bac*Light™ Bacterial Viability Kit. The dual coelectrospun membrane is immersed 15 minutes in PBS buffer with [Syto 9] = 5 µM and [Propidium iodide] = 27 µM, before washing in PBS buffer for 15 minutes. The membrane has then been imaged with a confocal microscope (**Figure 4.22**) with the help of France Lam at the IBPS (Leica TCS SP5).

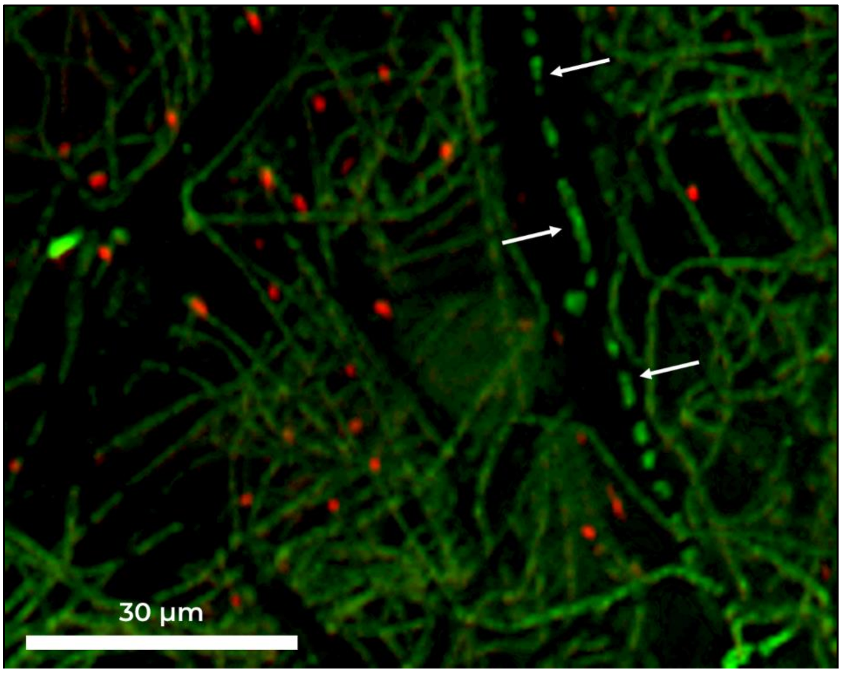

Figure 4.22 – Confocal microscopy of the integrated membrane dyed with Invitrogen™ LIVE/DEAD™ *Bac*Light™ Bacterial Viability Kit (SYTO 9/Propidium iodide). Green highlights live cells while red highlights dead cells. The white arrows show the alignment of live cells along the axis of a coelectrospun fiber (black background; diameter of approximately 9 µm).

The micrograph clearly shows the presence of both live and dead bacteria. The green fluorescence also seems colocalized with the PAN/Carbon black conductive scaffold where it must have adsorbed. Wider core-shell fibers exhibit no fluorescence and can be visualized as black ribbons which stand out the green background. In particular, an alignment of live bacteria can be seen along the axis of one of those fibers (white arrows). Moreover, live bacteria are exclusively found inside the core-shell fibers, while the red ones seem randomly dispersed outside. The latter may be dead because of the presence of toxic organic solvents (chloroform and DMF) in the formulation of the scaffold and shell solutions while the former must have been protected by the core solution and gelled interface in the compound Taylor cone formed during the electrospinning process.

Overall, the encapsulation and survival rate of the bacteria are satisfactory in the integrated bioanode.

4.5.2.3. Electrical conductivity

The surface (σ_S) and transverse (σ_T) conductivities are measured respectively by a two-electrode setup and impedance spectroscopy. As in the case of the dual electrospun core-shell/conductive fibers scaffold, the Nyquist plot of the sample indicates a pure resistive response. Again, the mat conductivity is relatively inhomogeneous along the membrane. The typical conductivities values are also similar to those achieved without bacteria (**Table 4.6**).

Table 4.6 – Typical electrical conductivities σ_S & σ_T for the electrospun carbon electrode, the dual electrospun core-shell/conductive scaffold membrane & the integrated bioanode.

Sample	σ_S ($S \cdot cm^{-1}$)[a]	σ_T ($S \cdot cm^{-1}$)[b]
Electrospun carbon electrode	~ 10^{-1}	~ 10^{-1} to 10^{-2}
Dual electrospun core-shell/conductive scaffold membrane	~ 10^{-2}	~ 10^{-2} to 10^{-3}
Integrated bioanode	~ 10^{-2}	~ 10^{-2} to 10^{-3}

[a] Calculated from two-electrode setup measurements; maximum sensibility of 40 MΩ. [b] Calculated from impedance spectroscopy measurements; amplitude of 100 mV; maximum sensibility of ~ 10^8 Ω.

This behavior is expected as the formulation of the two systems are the same apart from the adjunction of bacteria in the integrated bioanode.

4.5.2.4. MFC integration & electrochemical characterization

Before characterizing the electrochemical performances of the integrated bioanode, a control run is performed by monitoring the behavior of a sterilized electrode under the same conditions. Therefore, a 2 cm x 2 cm integrated bioanode is exposed to UV light for 30 minutes on each side and thoroughly rinsed with sterilized Milli-Q water. Under the conditions presented in Chapter 2, the sterilized electrode is then set up in a sterilized MFC reactor with an anolyte consisting of sterile MR1-L. The anode potential is potentiostatically poised at +0.3 V against an Ag/AgCl, KCl saturated reference electrode. The MFC current output is monitored through time with chronoamperometry (CA) and the current density j ($\mu A \cdot cm^{-2}$) is calculated ($Ø_{anode}$ = 1.7 cm; $A_{anode,geometrical} \approx 2.27$ cm^2). Cyclic voltammograms (CV) are recorded in the range of -0.7 to +0.7 V against Ref. (scan rate: 1 $mV \cdot s^{-1}$) every 24 hours. On the fifth day, the polarization of the anode is stopped after the cyclic voltammetry for 16 hours to let the electrode potential stabilize and the working and counter electrodes channels are reversed. Polarization and power curves are recorded by applying an incremental series of negative currents to the cathode while the emf is recorded. The anolyte is recharged with 1 mmol of sodium lactate every 4 days to ensure there is no carbon source shortage for the bacteria. All the processes are conducted at 21°C. The electrochemical behavior of the MFC in abiotic conditions is then used as a reference (**Figure 4.23**).

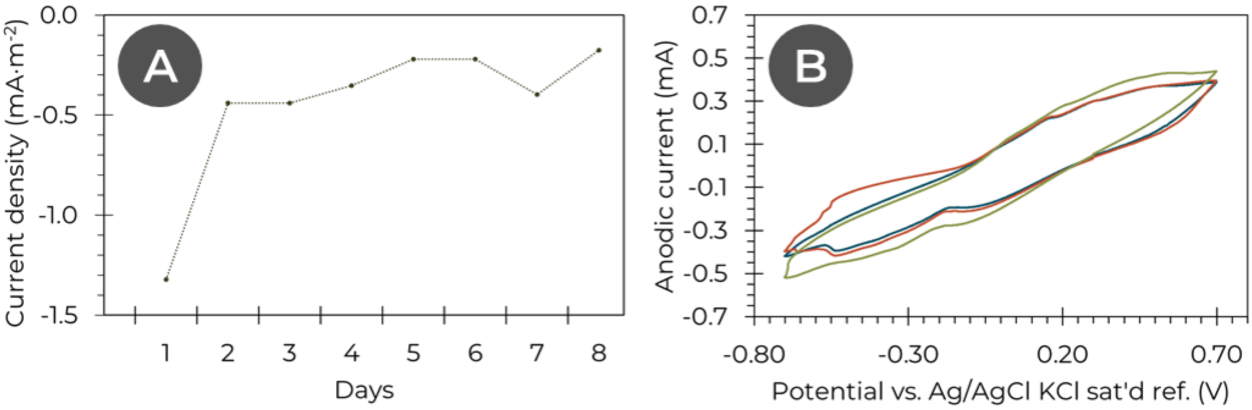

Figure 4.23 – Electrochemical characterization of a control two-compartment MFC including a UV-sterilized integrated bioanode polarized at +0.3 V vs. the reference (electrospun from a dual setup of core-shell fibers – core: PEO 5 wt% + *S. oneidensis* at OD_{600} = 1 in PBS 0.5X; shell: PCL 9 wt% + PEG 1.5 wt% + CB 2 wt% in chloroform/DMF 90:10 (w/w) – & scaffold fibers – from PAN 7 wt% + CB 7 wt% in DMF, sterilized under UV light for 1 hour and rinsed with sterile Milli-Q water, thickness of 81 µm). (A) Evolution of the average current density. (B) Evolution of cyclic voltammetry as a function of time (– 1st day, – 2nd day, – 3rd day); sweep rate of 1 $mV \cdot s^{-1}$; 3 cycles are acquired, here is the second one. Current and power are normalized by the geometric surface area of the electrospun carbon electrode ($Ø_{anode}$ = 1.7 cm; $A_{anode, geometrical} \approx 2.27\ cm^2$). The anolyte is MR1-L medium; the catholyte is 150 mM of NaCl (supporting electrolyte) and 100 mM of $K_3[Fe(CN)_6]$.

As expected, only a slightly negative current is measured as a function of time (**Figure 4.23.A**), and the cyclic voltammetry (**Figure 4.23.B**) exhibits no reliable redox peaks associated to bacterial EET. A few residual redox peaks are visible but they remain very faint. They must be associated with persisting bacterial redox proteins as they appear in the 0-0.3 V vs. Ref. range.

A 410 µm thick integrated bioanode is then set up in a sterilized MFC reactor and likewise electrochemically characterized. This thick electrode architecture is easily achieved by stacking together several layers of freshly electrospun integrated bioanode as each of them encapsulate bacteria – in a similar fashion as 3D carbon microfibers bioanode from Chapter 2. The electrochemical performances of the integrated bioanode is then compared with the precolonized carbon paper membrane presented in Chapter 2 (**Figure 4.24**).

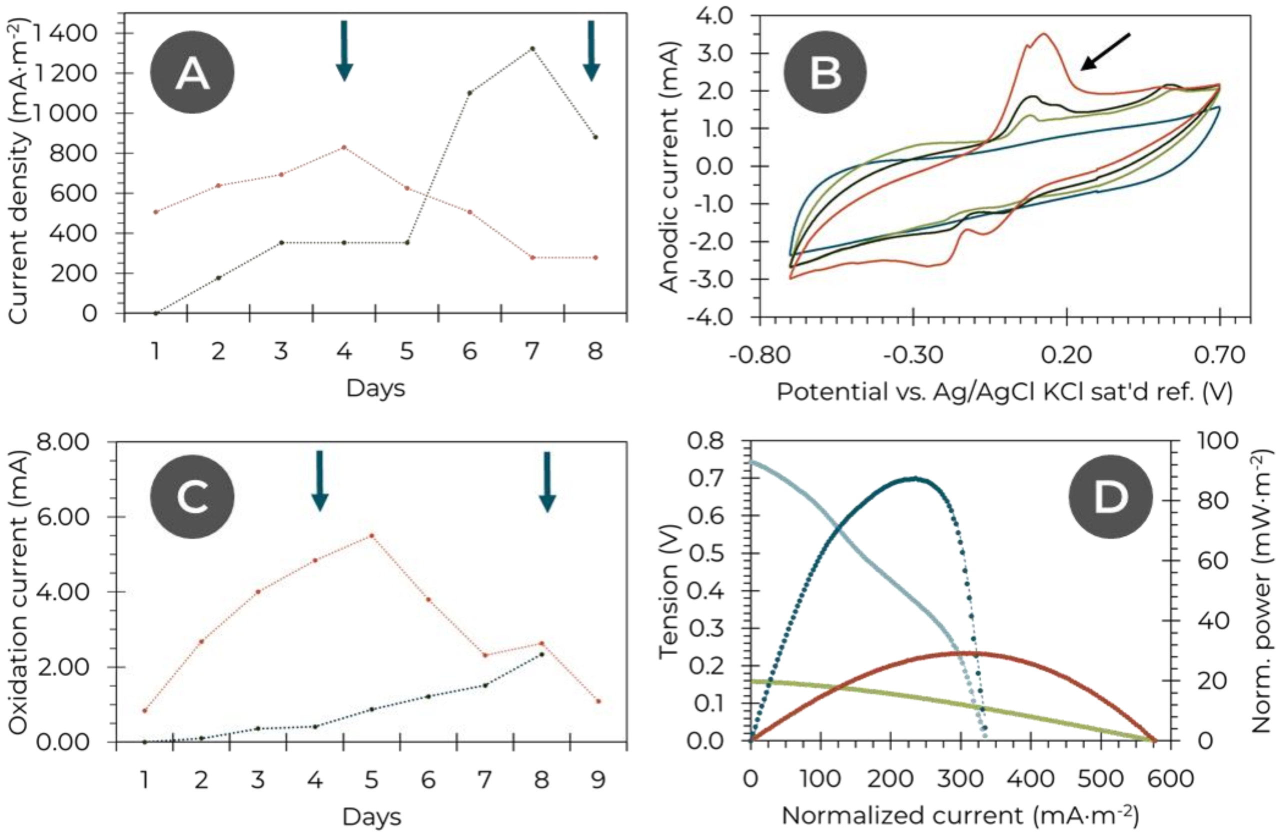

Figure 4.24 – Electrochemical characterization of a two-compartment MFC including an integrated bioanode polarized at +0.3 V vs. the reference (electrospun from a dual setup of core-shell fibers – core: PEO 5 wt% + *S. oneidensis* at OD_{600} = 1 in PBS 0.5X; shell: PCL 9 wt% + PEG 1.5 wt% + CB 2 wt% in chloroform/DMF 90:10 (w/w) – & scaffold fibers – from PAN 7 wt% + CB 7 wt% in DMF, thickness of 410 µm) as a function of time. (A) Evolution of the current density (•); blue arrows indicate addition of 1 mmol of sodium lactate. Comparison (•) with a simple precolonized bioanode; average of N = 6 for the control. (B) Evolution of cyclic voltammetry through time (– 1st day, – 3rd day, – 5th day, – 8th day after lactate addition); sweep rate of 1 mV·s^{-1}; 3 cycles are acquired, here is the second one. (C) Evolution of the current (•) corresponding to the peak shown by the arrow on the CV; blue arrows indicate addition of 1 mmol of sodium lactate. Comparison (•) with a simple precolonized bioanode; average of N = 6 for the reference. Measurements stopped on the 8th day due to a computer crash. (D) Polarization (•) and power (•) curves of an MFC (5th day, thickness of 410 µm). Comparison with the polarization (•) and power (•) curves of a simple precolonized bioanode (here 5th day, thickness of 293 µm). Current and power are normalized by the geometric surface area of the carbon paper (Ø$_{\text{anode}}$ = 1.7 cm; $A_{\text{anode, geometrical}}$ ≈ 2.27 cm^2).

The current density of the setup (**Figure 4.24.A**) is almost zero in the beginning, but slowly increases in the first few days to reach around 350 mA·m^{-2} on the fifth day. It then quickly increases and reaches up to 1350 mA·m^{-2} on the eight day. Afterwards, the computer acquisition stopped due to a hardware problem and could not be resumed for a week when the corrosion of the electrical contacts made it impossible to start again the measurements.

Cyclic voltammetry (**Figure 4.24.B**) shows a quasi-capacitive response with almost no oxidation peak on the first day. However, a peak centered on 0.08 V vs. Ref. appears on the second day and then steadily grows for until the end of the measurements (**Figure 4.24.C**). Furthermore, a non-reversible peak centered on 0.54 V vs. Ref. appears on the second day and then decreases until it is almost unnoticeable on the eight day. Finally, from the fifth day onwards a third oxidation peak centered on 0.2 V vs. Ref. appears until it becomes the dominant one and merge into a double peak with the one at 0.08 V vs. Ref. Firstly, like in the previous electrospun carbon electrodes systems presented in Chapter 2, no redox signal associated with redox mediators – expected at -0.45 V vs. Ref. – is noticeable. The much more complex behavior exhibited here – compared with the usually merged oxidation peak widely recorded in Chapter 2, and even with the two peaks observed for the composite bioanode in Chapter 3 – may be triggered by the encapsulation of the bacteria as well as their contact with carbon particles. All the oxidation potentials reported may be associated to direct electron transfer[16] probably through the Mtr respiration pathway[17],[18] considering the redox potential involved (≥0 V vs. Ag/AgCl, KCl saturated reference). Henceforth the multiple peaks might be attributable to diverse direct EET mechanisms associated with the constraints applied by the core-shell encapsulation on the bacteria.

After stopping the polarization on the fifth day the open-circuit voltage (emf) of the MFC eventually stabilizes at about 0.16 V (the bioanode potential stabilizing around 150 mV), which is clearly lower than reported for electrospun carbon electrodes in Chapter 2, and even different from the composite electrode presented in Chapter 3. The polarization and power curves (**Figure 4.24.D**) recorded show a maximum power and current densities of 30 $mW{\cdot}m^{-2}$ and 577 $mA{\cdot}m^{-2}$ respectively, or volume densities of 70 $W{\cdot}m^{-3}$ and 1400 $A{\cdot}m^{-3}$. From the slope of the polarization curve, we estimated the internal resistance of the system $R_{int} \approx 6\ k\Omega$. This value is of the same order of magnitude than the one of the previously studied MFCs and consistent with the typical resistance value for the bioanode ($R \sim 10^3\ \Omega$).

Interestingly, the difference in open-circuit emf and in the appearance of the polarization curves may be linked to the difference in bacteria environment and EET between the systems. Indeed, the nature of the electrode differs, as the conductive carbon involved in electron conduction is not the same – either carbonized PAN or carbon black. Moreover, the polymer–carbon scaffold does not exhibit the same conduction pathways than plain electrospun carbon fibers. On top of this, the encapsulated bacteria are confined either inside a collapsed ribbon or in a filled PEO environment of about 1 µm in diameter. In both cases, the bacteria may be mechanically constrained, and probably cannot secrete and thrive in as much biofilm as free bacteria. Because of that, the EET performed by the bacteria may be different, and the redox states of the proteins and/or mediators involved in these transfer may vary, thus affecting the Nernst potential of the system. The difference in the redox species involved in EET is indeed verified by comparing the different peaks found in the cyclic voltammograms of the integrated bioanode or the electrospun carbon membrane. The precise interpretation of these peaks remains unclear up to now, but they still inform us on the difference in nature of the electron transfer pathways performed by the bacteria in both cases.

4.5.2.5. Post-mortem imaging

SEM analysis of the air-dried post-mortem integrated bioanode (**Figure 4.25**) shows little alteration of the architecture of the fibers. The integrity of the core-shell fibers seems well preserved, and few deposition of organic matter is observed on the fibers. Overall, no major obstruction of the inter microfibers space is detectable as opposed to the post-mortem analysis of the electrospun carbon electrodes from Chapter 2. Henceforth, the electroactive bacteria responsible for the current output seem restricted to the inside of the core-shell fibers as planned.

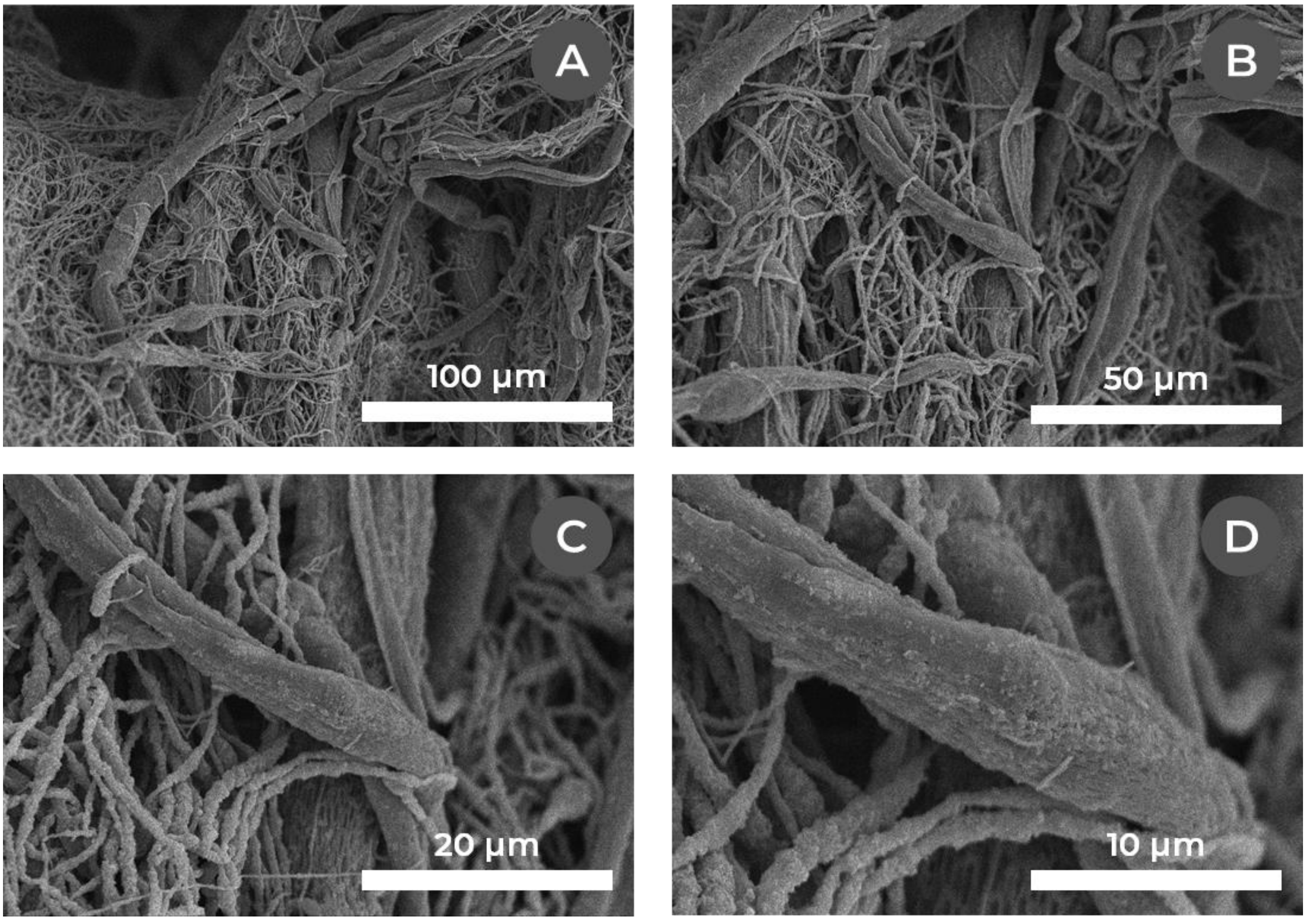

Figure 4.25 – SEM micrographs of an air-dried post-mortem integrated bioanode (shell: PCL 6 wt% + PEG 1.5 wt% + CB 2 wt% in 90:10 (w/w) chloroform & DMF; core: PEO 5 wt% in PBS 0.5X + *S. oneidensis* at OD_{600} ≈ 1; conductive scaffold: PAN 7 wt% + CB 7 wt% in DMF) after 14 days of operation, polarized at +0.3 V vs. Ag/AgCl, KCl saturated reference, coated with 15 nm of gold.

4.5.3. Integrated bioanode cryodesiccation

According to the protocol developed in Chapter 2 for the long-term storage of precolonized electrospun carbon membranes, the integrated bioanode was cryodesiccated and the resulting electrodes electrochemical performances were evaluated.

The integrated bioanode was cut to approximately 2 cm x 2 cm, frozen in liquid nitrogen and then placed in a Christ Alpha 2-4 LD freeze-dryer. The drying operation was performed at -85°C and 0.12 mbar for 24 hours.

After cryodesiccation, the macroscopic aspect and mechanical properties of the membranes seem unaffected. The effect of the cryodesiccation on the electrochemical performances of the integrated bioanode is then investigated.

4.5.3.1. MFC integration & electrochemical characterization

The cryodesiccated integrated bioanode is then mounted into the MFC reactor, poised at +03 V vs. Ref. and electrochemically characterized as described before (**Figure 4.26**).

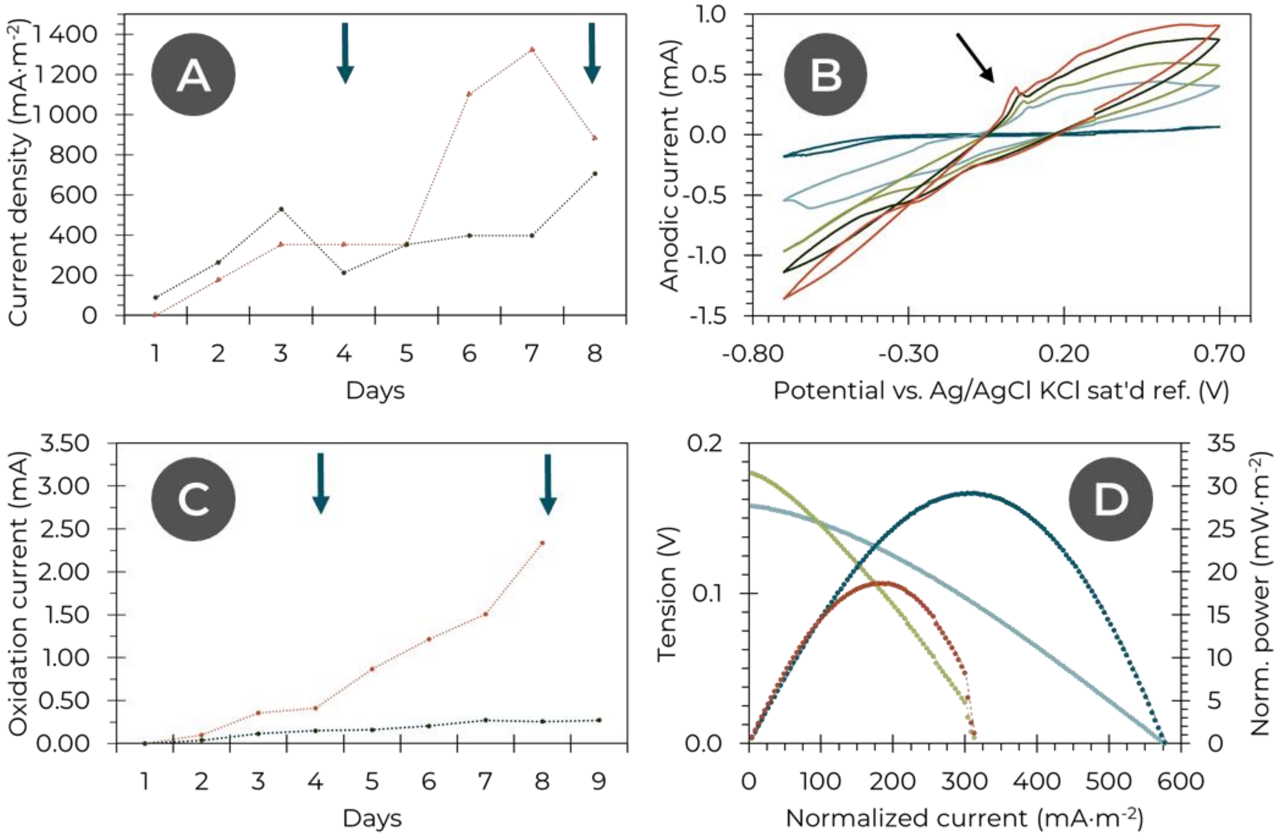

Figure 4.26 – Electrochemical characterization of a two-compartment MFC including a cryodesiccated integrated bioanode polarized at +0.3 V vs. the reference electrospun from a dual setup of core-shell fibers – core: PEO 5 wt% + *S. oneidensis* at OD$_{600}$ = 1 in PBS 0.5X; shell: PCL 9 wt% + PEG 1.5 wt% + CB 2 wt% in chloroform/DMF 90:10 (w/w) – & scaffold fibers – from PAN 7 wt% + CB 7 wt% in DMF, precolonization & cryodesiccation as described before, thickness of 87 µm) as a function of time. (A) Evolution of the current density (•); blue arrows indicate addition of 1 mmol of sodium lactate. Comparison (•) with a fresh integrated bioanode. (B) Evolution of cyclic voltammetry as a function of time (– 1st day, – 2nd day, – 3rd day, – 5th day, – 8th day after lactate addition); sweep rate of 1 mV·s^{-1}; 3 cycles are acquired, here is the second one. (C) Evolution of the current (•) corresponding to the peak shown by the arrow on the CV; blue arrows indicate addition of 1 mmol of sodium lactate. Comparison (•) with a fresh integrated bioanode. (D) Polarization (•) and power (•) curves of an MFC at maximum current density value (here 5th day, thickness of 87 µm). Comparison with the polarization (•) and power (•) curves of a fresh integrated bioanode (here 5th day, thickness of 410 µm). Current and power are normalized by the geometric surface area of the electrospun carbon electrode (Ø$_{anode}$ = 1.7 cm; A$_{anode, geometrical}$ ≈ 2.27 cm^2).

The current density (**Figure 4.26A**) already starts at about 90 mA·m^{-2} on the first day and then rises to the 250 to 700 mA·m^{-2} – or 3000 to 8000 A·m^{-3} – range from the second day on. By comparison, the fresh integrated bioanode never exhibited volume current densities higher than

3220 A·m^{-3} – however up to 1320 mA·m^{-2} when surface normalized. These values are nevertheless of the same order of magnitude and show as expected no negative impact of the cryodesiccation step on the current output of the MFC, which is still largely more stable than in the case of electrospun carbon electrodes.

Cyclic voltammetry (**Figure 4.26.B**) of the MFC including the cryodesiccated integrated bioanode shows no noticeable peak on the first day, and a very low capacitive surface area probably due to a bad wetting in the electrode depth as exhibited by composite electrospun membranes in Chapter 3. However, this issue is overcome and the apparition of oxidation peaks at potentials similar to those observed in the fresh bioanode is noticeable from the second day. They then continue to grow for the next days (**Figure 4.26.C**). This evolution is similar in shape to the fresh integrated bioanode, albeit with smaller currents because of the thinner membrane. Note that the cyclic voltammograms also seem to exhibit an increasing ohmic drop with time. This drop also tend to be seen on other system but is here far more noticeable due to the increase in capacitive surface.

After stopping the polarization on the fifth day, the emf of the MFC stabilizes at about 0.18 V (the bioanode potential stabilizing at around 106 mV) which is similar to the fresh integrated bioanode. The power curve (**Figure 4.26.D**) shows a maximum of around 20 mW·m^{-2}, and the polarization curve exhibits a maximum current density of 315 mA·m^{-2} – or respectively 230 W·m^{-3} and 3620 A·m^{-3}, in the same range as precolonized electrospun carbon electrodes. These values are slightly lower in surface normalization but interestingly better for the volume normalization than for the fresh integrated bioanode. A poor in-depth wettability of the integrated bioanode (410 µm) may be in cause, reducing the benefits of having a thick bioanode when aiming at high volume power or current densities. This observation however has to be mitigated by the fact that in both cases, the bioanode still remains relatively thin i.e. less than 500 µm. Additionally, a sharp decrease in tension is observed at higher current densities due to diffusion limitations. The internal resistance of the cell is also evaluated at $R_{int} \approx 13$ kΩ, which is again in the range expected for these systems albeit higher than in the fresh integrated bioanode. This may however be linked to the higher thickness of the fresh bioanode which have been reliably seen to increase conductivity in previous systems.

The evolution of the capacitive surface area of the cryodesiccated integrated bioanode along twelve days of experiment (**Figure 4.27.A-B**) shows a clearly different behavior compared to the precolonized electrospun carbon electrodes (**Figure 4.27.C-D**), much more similar to the evolution seen for composite electrospun electrodes in Chapter 3 (**Figure 4.27.E-F**).

As seen previously, the performances of the electrospun carbon electrodes tended to exhibit a three-phase “bell curve” probably linked to the growth of the biofilm which allowed an increase in electrochemical performances as it developed before hindering nutrients and organics diffusion, leading to a low-current density steady phase in the end.

In the case of the integrated bioanode however, the capacitive surface seems to rise quickly from the first day (when it is very low due to a bad in-depth wettability of the electrode, as observed for polymer–carbon membranes in Chapter 3) until it stabilizes at around 2.5 m^2 from the fourth and fifth days until the end of the measurements. This is much more similar to the behavior observed with the composite electrospun electrode presented in Chapter 3. The CV-main peak oxidation current (**Figure 4.27.A**) as well of the current density output (**Figure 4.27.B**) here follow the same growth trend: no clear drop can be seen until the corrosion of the contacts make it difficult to keep on the measurements around the twelfth day. In contrast with the composite electrospun electrode from Chapter 3 however, the output of the MFC here follows the increase of the electrode surface and no clear decrease in current density is eventually observed.

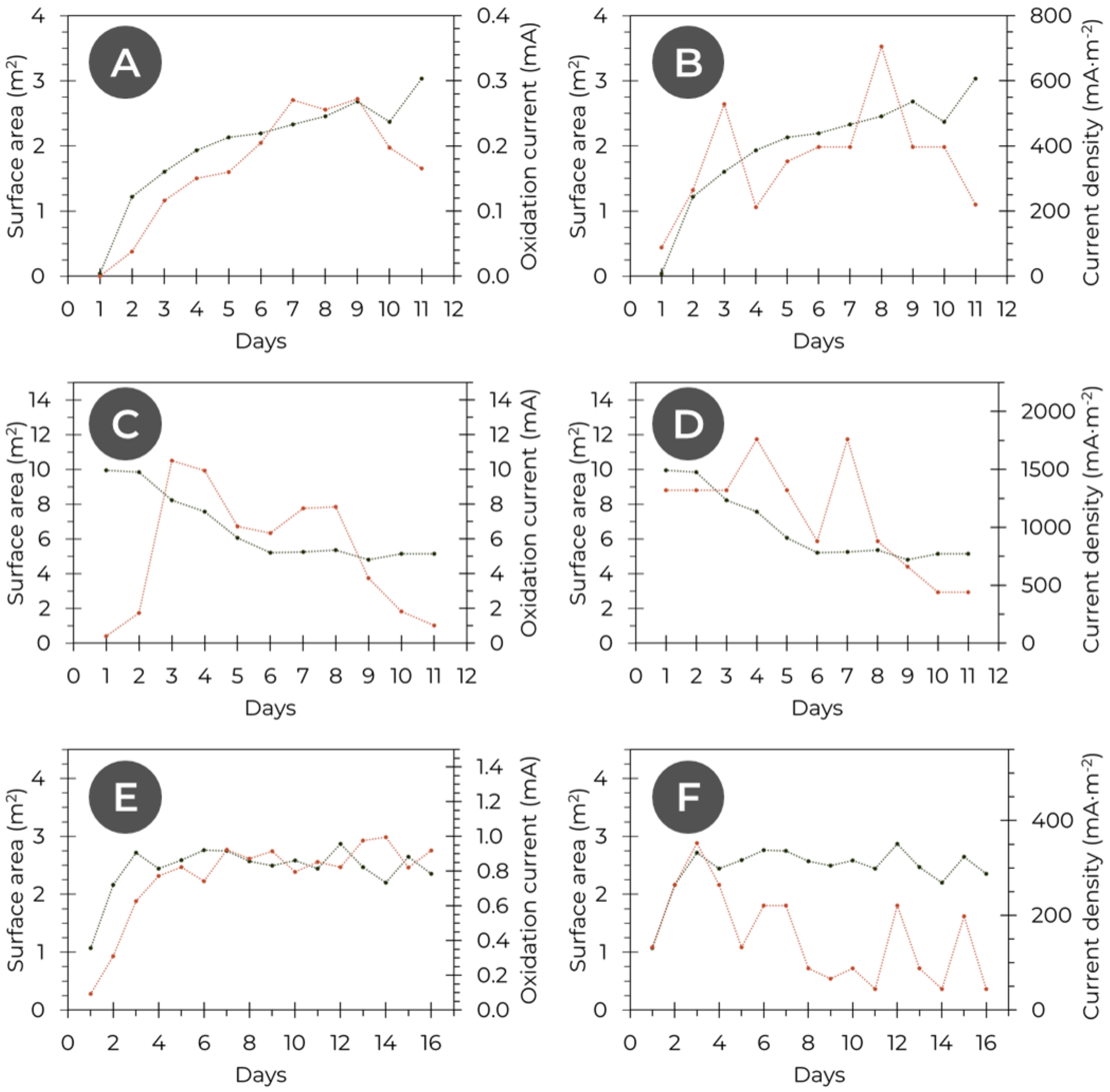

Figure 4.27 – Evolution of the capacitive surface area (•) of a cryodesiccated integrated bioanode (A-B; thickness of 87 µm) and a 2-fold stacked precolonized bioanode (C-D; thickness of 693 µm) as a function of the time. The capacitive surface area is calculated from cyclic voltammetry. The surface area is compared with (A-C) the maximum current of the main oxidation peak on the CV (•), & (B-D) the current density output of the MFC, normalized by the geometric surface area of the electrospun carbon electrode ($Ø_{anode}$ = 1.7 cm; $A_{anode,\ geometrical}$ ≈ 2.27 cm^2).

As no clear decrease in performances is observed during this timeframe, these observations underline a better long-term stability of the integrated bioanode system compared with the precolonized electrospun carbon electrode. The stability of the current output is even better than for the composite electrospun electrode from Chapter 3, which was already better than the electrospun carbon electrode. The improved stability may then be linked to several factors. Firstly, the presence of carbon black in the shell of the coelectrospun fibers may reduce overgrowth of the biofilm as observed in composite electrospun electrodes. Secondly, the better stability observed may be attributed to the encapsulation of the bacteria in core-shell fibers. Then, to the presence of the secondary conductive composite scaffold may reduce the development of biofilm from bacteria that would have leaked outside the fibers, consistently with results observed in composite electrospun electrodes in Chapter 3. Altogether, the objective of this encapsulation which was to postpone the biofilm overgrowth in order to maintain high performances through time, as it will be expected for practical applications, seems reached.

Moreover, the observed increase in capacitive surface area of the anode might be explained by the participation of the inner shell surface as the core PEO slowly dissolves into the electrolyte surrounding the fibers through their pores. The free space inside the fibers due to PEO dissolution may then facilitate the diffusion of nutrients toward the bacteria in the core, increasing their yield until a steady state is reached while their overgrowth is prevented by their encapsulation. More experiments and replicas are nevertheless needed to verify this mechanism.

Additionally, the initial capacitive surface area of the integrated bioanodes tested was evaluated and compared with the precolonized electrospun carbon electrodes previously tested (**Table 4.7**)

Table 4.7 – Comparison of the volume normalized capacitive surface area between the average precolonized electrospun carbon electrode (on the 1st day) & different setups of integrated bioanodes (on the 2nd day to account for a lower in-depth wettability of the fibers). The capacitive surface area is calculated from the cyclic voltammograms.

Sample	Volume normalized capacitive surface area (m^{-1})
Precolonized electrospun carbon electrode (N = 6)	$8.9 \cdot 10^7 \pm 4.1 \cdot 10^7$
Integrated bioanode	$5.2 \cdot 10^7$
Cryodesiccated integrated bioanode	$6.2 \cdot 10^7$
Sterilized integrated bioanode	$5.4 \cdot 10^7$

The volume normalized capacitive surface areas reported are consistent between the three integrated bioanode setup tested. They are slightly lower than the average normalized capacitive surface area of the precolonized electrospun carbon electrodes on the first day albeit of the same order of magnitude – which is coherent with the visual aspects of the microstructure of the electrospun mats (porosity). This mild difference may be explained by the presence of bigger core-shell fibers in the integrated bioanodes which slightly reduce the total surface area. Nevertheless, as observed in the case of the cryodesiccated bioanode (**Figure 4.27.A-B**), this difference eventually closes as the participation of the inner wall of the shell of the fibers becomes more important after a few days of experiment.

Overall, the performances recorded for the integrated bioanodes can be compared with those of the precolonized electrospun carbon electrodes as well as the literature (**Table 4.8**). The surface normalized current densities of the two integrated bioanodes – fresh or cryodesiccated – are clearly higher than for the electrospun carbon electrode, albeit the power density is lower. Nevertheless, as observed before, the volume densities of the electrodes are again remarkably high. In particular, the exhibited current densities of the systems are higher than the precolonized electrospun carbon electrode. Moreover, in the case of the thin cryodesiccated integrated bioanode, the current density exhibited – $3.26 \cdot 10^3$ A·m^{-3} is even higher than the value reported in the literature.

Table 4.8 – Comparison of the surface (◆) & volume (◆) normalized electrochemical performances between the literature, the precolonized electrospun carbon electrode & the integrated bioanodes. The performances compare MFCs using a carbon-based anode, *S. oneidensis* as the anodic exoelectrogenic strain with growth medium supplemented with lactate as the anolyte, & a ferricyanide solution as the catholyte.

Setup	Current	Power
Literature optimum (Ringeisen *et al.*)[19]	12.5 A·m^{-2}	3 W·m^{-2}
	$2.08 \cdot 10^3$ A·m^{-3}	500 W·m^{-3}
Precolonized electrospun carbon electrode	0.334	0.087
	$1.14 \cdot 10^3$	296
Fresh integrated bioanode	0.577	0.030
	$1.40 \cdot 10^3$	70
Cryodesiccated integrated bioanode	0.315	0.020
	$3.26 \cdot 10^3$	230

4.5.3.2. Post-mortem imaging

The post-mortem cryodesiccated bioanode is then imaged with SEM (**Figure 4.28**). No overwhelming deposition of organic matter is observed in between the fibers (**Figure 4.28.A-B**), even if a few core-shell fibers seem covered with biofilm (**Figure 4.28.C-D**). This low development of biofilm on the fibers seems consistent with the previous findings hinting that the capacitive surface area of the system was not significantly reduced through the experiment.

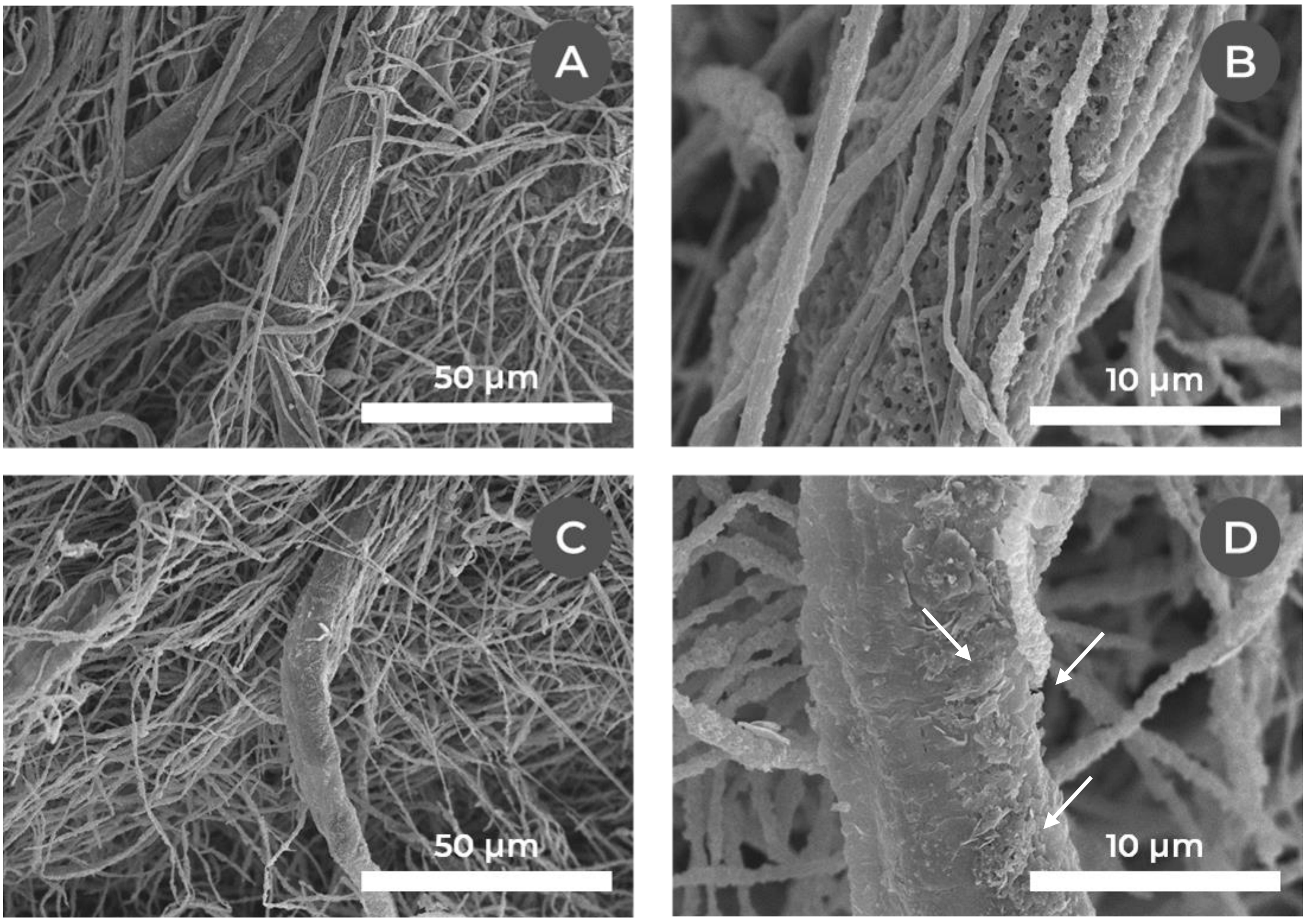

Figure 4.28 – SEM micrographs of an air-dried post-mortem cryodesiccated integrated bioanode after 14 days of operation, polarized at +0.3 V vs. Ag/AgCl, KCl saturated reference, coated with 15 nm of gold. (A-B) Core-shell fibers clean of deposited matter, found overwhelmingly throughout the sample. (C-D) Core-shell fiber surface covered in biofilm, hiding the shell porosity (arrows).

The overall architecture of the bioanode is nevertheless preserved: most of the bacteria seem trapped in the fibers. However, the cryodesiccation step may still have weakened a fraction of the core-shell fibers. If so, some bacteria may not be well encapsulated anymore and would have leaked outside the fibers. This would account for the presence of biofilm on some fibers. However, no heavy biofilm overgrowth similar to the one present on electrospun carbon electrodes can be seen on this post-mortem sample. In particular, the space in between the secondary network fibers is still largely open and should not hinder any diffusion, preventing the performance fall seen in electrospun carbon electrodes.

We have reached the intended architecture for the integrated bioanode. *Shewanella oneidensis* have been encapsulated inside coelectrospun core-shell fibers. These fibers are dual electrospun and intermingled with a secondary conductive scaffold network which guarantees a suitable conductivity for the membrane (~ 10^{-2} to 10^{-3} S·cm^{-1}). The resultant electrode is easily stacked together without any additional treatment to get a bioanode of the desired thickness. Once mounted into an MFC reactor it generates electricity. The obtained integrated bioanode can also be cryodesiccated, and the resulting membrane still exhibits a suitable power generation activity once mounted into an MFC reactor. The current and power densities are similar to those of the precolonized electrospun carbon membrane (volume current density of 3620 A·m^{-3} and power density of 230 W·m^{-3} compared with up to 1140 A·m^{-3} and 296 W·m^{-3} for the precolonized carbon membranes). Additionally, the open-circuit emf of the cell is lower for the integrated bioanode than for the electrospun carbon electrode (0.18 V vs. 0.73 V) and the polarization curves differ, probably due to different dominant EET mechanisms and dynamics. Furthermore, the long-term stability of the integrated bioanode seems better than in the case of the electrospun carbon electrodes, apparently due to a reduced anarchic biofilm development in the interfiber space thanks to the bacteria encapsulation.

4.6. Conclusion

Altogether, we have developed a lab-made electrospinning apparatus and setup to coelectrospin core-shell fibers. The architecture of the fibers varies from collapsed ribbons with hollow core to round-section filled fibers, and the core-shell nature of the fibers has been verified with FE-SEM–FIB. A porosity of a few hundred nanometers is also observed on the wall of the fibers.

Afterwards, bacteria were successfully encapsulated inside the fibers core and their location was tracked with fluorescent markers. Additionally, a process providing a dual electrospun network of core-shell fibers intermingled with a conductive polymer–carbon scaffold was developed. The electrical conductivity of the resulting membrane (~ 10^{-2} to 10^{-3} $S{\cdot}cm^{-1}$) was deemed satisfactory and the two processes were combined together.

Therefore, an integrated bioanode consisting of a dual electrospun network of core-shell fibers encapsulating *Shewanella oneidensis* and a conductive polymer–carbon scaffold was designed and synthetized. These fibers efficiently encapsulate the bacteria, and exhibit a suitable electrical conductivity for electrochemical applications – similar to the previous dual electrospun membranes. Because they already encapsulate bacteria, their thickness can be easily tuned by stacking electrospun layers together similarly to the 3D carbon microfibers bioanode presented in Chapter 2.

The integrated bioanode was then included into an MFC and exhibited electricity generation. In accordance with the results of Chapter 2, this electrode can be cryodesiccated and will still exhibit an electrochemical activity once integrated into the MFC reactor. Its volume current and power densities were similar to those recorded for the electrospun carbon membrane up to 3260 $A{\cdot}m^{-3}$ and 230 $W{\cdot}m^{-3}$ for the thin cryodesiccated bioanode, compared with 1140 $A{\cdot}m^{-3}$ and 296 $W{\cdot}m^{-3}$ for the precolonized carbon membranes. This volume normalized power is still honorable compared with the maximum reported in the literature (~ 500 $W{\cdot}m^{-3}$)[19] considering the fact that the architecture of the cell was not optimized. However, the open-circuit emf was significantly lower (0.18 V vs. 0.73 V), hinting for a different EET behavior probably due to the encapsulation and different environment of the bacteria. Upon MFC integration, the long-term stability of the electrode is also markedly better than for the electrospun carbon electrode. Such impressive volume current densities for thin electrospun systems may be for instance envisioned to be applied to wearable or paper-based MFCs which require a certain flexibility.

However, this design could still be optimized by trying to reduce the amount of polymer–carbon scaffold fibers compared with the core-shell fibers. In the meantime, an increase of electrical conductivity may be considered in order to improve the output of the cell. Eventually, the use of this design in a more applied situation, using wastewater effluents as a fuel can be considered. This last situation will be investigated and presented in the next chapter.

A more thorough analysis of the bacteria behavior encapsulated in the integrated bioanode would also be needed to better understand the EET mechanisms involved, as well as their development in a confined environment.

REFERENCES

[1] D. Pinto. Electronic transfer within a microbial fuel cell. Better understanding of Experimental and Structural Parameters at the Interface between Electro-active Bacteria and Carbon-based Electrodes. *École doctorale Physique et chimie des matériaux (Paris)* (Sorbonne Université, 2016).

[2] Y. Dror *et al.* One-Step Production of Polymeric Microtubes by Co-electrospinning. *Small* **3,** 1064–1073 (2007).

[3] S. Klein *et al.* Encapsulation of bacterial cells in electrospun microtubes. *Biomacromolecules* **10,** 1751–1756 (2009).

[4] E. Zussman. Encapsulation of cells within electrospun fibers. *Polym. Adv. Technol.* **22,** 366–371 (2011).

[5] Z. Sun, E. Zussman, A. L. Yarin, J. H. Wendorff & A. Greiner. Compound Core-Shell Polymer Nanofibers by Co-Electrospinning. *Adv. Mater.* **15,** 1929–1932 (2003).

[6] S. Klein *et al.* Encapsulation of pseudomonas sp. ADP cells in electrospun microtubes for atrazine bioremediation. *J. Ind. Microbiol. Biotechnol.* **39,** 1605–1613 (2012).

[7] A. Arinstein & E. Zussman. Postprocesses in tubular electrospun nanofibers. *Phys. Rev. E* **76,** 56303 (2007).

[8] A. Arinstein, R. Avrahami & E. Zussman. Buckling behaviour of electrospun microtubes: a simple theoretical model and experimental observations. *J. Phys. D. Appl. Phys.* **42,** 15507 (2008).

[9] W. Salalha, J. Kuhn, Y. Dror & E. Zussman. Encapsulation of bacteria and viruses in electrospun nanofibres. *Nanotechnology* **17,** 4675–4681 (2006).

[10] M. Gensheimer *et al.* Novel biohybrid materials by electrospinning: Nanofibers of poly (ethylene oxide) and living bacteria. *Adv. Mater.* **19,** 2480–2482 (2007).

[11] B. Asselbergh, A. E. Achuo, M. Höfte & F. Van Gijsegem. Abscisic acid deficiency leads to rapid activation of tomato defence responses upon infection with Erwinia chrysanthemi. *Mol. Plant Pathol.* **9,** 070925014357003-??? (2007).

[12] E. L. Lagendijk, S. Validov, G. E. M. Lamers, S. De Weert & G. V Bloemberg. Genetic tools for tagging Gram-negative bacteria with mCherry for visualization in vitro and in natural habitats, biofilm and pathogenicity studies. *FEMS Microbiol. Lett.* **305,** 81–90 (2010).

[13] E. Chapelle *et al.* A straightforward and reliable method for bacterial in planta transcriptomics: application to the Dickeya dadantii / Arabidopsis thaliana pathosystem. *Plant J.* **82,** 352–362 (2015).

[14] M. Lowder *et al.* Effect of Starvation and the Viable-but-Nonculturable State on Green Fluorescent Protein (GFP) Fluorescence in GFP-TaggedPseudomonas fluorescens A506. *Appl. Environ. Microbiol.* **66,** 3160–3165 (2000).

[15] S. A. Theron, E. Zussman & A. L. Yarin. Experimental investigation of the governing parameters in the electrospinning of polymer solutions. *Polymer (Guildf).* **45,** 2017–2030 (2004).

[16] J. N. Roy *et al.* Applied Electrode Potential Leads to Shewanella oneidensis MR-1 Biofilms Engaged in Direct Electron Transfer. *J. Electrochem. Soc.* **160,** H866–H871 (2013).

[17] L. Shi *et al.* The roles of outer membrane cytochromes of Shewanella and Geobacter in extracellular electron transfer. *Environ. Microbiol. Rep.* **1,** 220–227 (2009).

[18] L. Shi, T. C. Squier, J. M. Zachara & J. K. Fredrickson. Respiration of metal (hydr)oxides by Shewanella and Geobacter: a key role for multihaem c-type cytochromes. *Mol. Microbiol.* **65,** 12–20 (2007).

[19] B. R. Ringeisen *et al.* High power density from a miniature microbial fuel cell using Shewanella oneidensis DSP10. *Environ. Sci. Technol.* **40,** 2629–2634 (2006).

5

TOWARD ELECTRICITY GENERATION FROM WASTEWATERS

TABLE OF CONTENTS

Chapter 5. Toward electricity generation from wastewaters 251
- 5.1. Introduction & objectives 251
- 5.2. Wastewaters characterization 253
  - 5.2.1. Sample properties & organic matter content 253
  - 5.2.2. Microbiome diversity analysis 254
    - 5.2.2.1. 16S rRNA gene sequencing 254
    - 5.2.2.2. Microbial community profiling 255
- 5.3. Electrospun carbon electrode 257
  - 5.3.1. MFC integration & electrochemical characterization 257
  - 5.3.2. Post-mortem imaging 261
  - 5.3.3. Effect on microbial diversity 262
- 5.4. Integrated bioanode 264
  - 5.4.1. MFC integration & electrochemical characterization 264
  - 5.4.2. Post-mortem imaging 266
- 5.5. Conclusion 269

References 270

CHAPTER 5. TOWARD ELECTRICITY GENERATION FROM WASTEWATERS

5.1. Introduction & objectives

Throughout this work, two main electrospun electrode systems used as an anode in a microbial fuel cell have been studied. In Chapter 2, electrospun carbon electrodes have been synthetized a multi-step process from polyacrylonitrile electrospun fibers. In contrast in Chapter 4, an integrated bioanode system encapsulating *Shewanella oneidensis* in a dual electrospun core-shell/conductive scaffold network based on the composite carbon–polymer fibers developed in Chapter 3 have been obtained.

All the electrodes studied so far were integrated into a MFC two-compartment lab-scale reactor. Potassium ferricyanide was used as a catholyte and reduced on a carbon felt cathode. On the anode side, all oxidation reactions were carried out by the model electroactive bacterium *Shewanella oneidensis* CRBIP17.141 – closely related to *Shewanella oneidensis* MR-1 – provided by the *Centre de Ressources Biologiques de l'Institut Pasteur.* The anode was either colonized in situ or ex situ in the case of electrospun carbon electrodes from Chapter 2, while the integrated bioanode developed in Chapter 4 encapsulates the strain from its one-step synthesis. Consequently, the selected anolyte for these experiments was the minimal culture medium MR-1, adapted to the strain[1]–[3], enriched with 30 mM of sodium lactate to be used as a carbon source by the bacteria. **The lactate, electron donor, was henceforth the fuel of the microbial fuel cell, and *S. oneidensis* its catalyst.**

This model bacterium was shown to exhibit as expected an electrochemical activity leading to a current output for the MFC in all the systems studied. Under these conditions, our electrospun bioanodes were in particular shown to produce volume current and power densities rivaling with the best levels references in the literature[4] – $2.08 \cdot 10^3$ $A \cdot m^{-3}$ & 500 $W \cdot m^{-3}$ for Ringeisen *et al*. vs. up to $1.14 \cdot 10^3$ $A \cdot m^{-3}$ & 296 $W \cdot m^{-3}$ for precolonized electrospun carbon anodes, $3.74 \cdot 10^3$ $A \cdot m^{-3}$ & 225 $W \cdot m^{-3}$ for a composite carbon–polymer electrospun anode or $3.26 \cdot 10^3$ $A \cdot m^{-3}$ & 230 $W \cdot m^{-3}$ for an integrated bioanode. At last, it was shown that the cryodesiccation of these electrodes to allow their long-term conversation was not detrimental to the electroactivity of *S. oneidensis* and that a power output was restored upon integration into an MFC reactor. In particular, this last point was envisioned as a mean to eventually use our bioanodes for a more practical application.

Among Chapter 1 was thus presented the main effective implementations of current-producing MFCs up to this day. Apart from environmental sensors and other low-power remote sensors, the main relevant application of microbial fuel cells remains energy harvesting from wastewaters. Additionally, wastewaters remain a non-negligible source of energy expense. In 2014, according to the International Energy Agency[5], 4 % of the global electricity consumption was linked to the extraction, distribution and water treatment. Wastewater treatment alone represented 25 %

of the total, or about 120 Mtoe of electricity demand. However, wastewaters are usually rich in organic matter and therefore represent a largely unexploited source of energy. Logan and Rabaey actually calculated that it contains 9.3-fold the amount of energy required to treat it[6]–[8]. Microbial fuel cells are indeed the relevant way to extract this untapped power source as many electroactive strains are able to degrade this organic matter for nutrients, and a fraction of this energy can then be collected by the MFC.

Therefore, this chapter focuses on the application of the electrospun bioanodes presented so far to energy production from actual wastewaters. The wastewaters used hereafter have been provided by the *Syndicat Interdépartemental pour l'Assainissement de l'Agglomération Parisienne* (SIAAP).

Firstly, the properties of the wastewaters used and their content in organic matter are characterized, as well as the naturally-occurring bacterial flora present in the samples, determined by 16s rRNA sequencing.

An abiotic electrospun carbon electrode synthetized in Chapter 2 are then be mounted in an MFC fed with these raw wastewaters as the anolyte. The electrochemical behavior and performances of the system are then reported, and compared with the performances observed with an MR-1/L medium anolyte. Moreover, the effect of the process on the bacterial diversity is reported.

A cryodesiccated integrated bioanode developed in Chapter 4 is in turn mounted in an MFC reactor under the same conditions. Its electrochemical behavior and performances are also characterized. The effect of exposing the electrode to a non-sterile anolyte containing a complex blend of organic components is discussed. The difference in behavior between the abiotic electrospun carbon electrode and the *Shewanella oneidensis*-encapsulating integrated bioanode is evaluated.

Eventually, the overall effect of this application to power generation from actual wastewaters is talked through, and future prospects for this endeavor are considered.

5.2. Wastewaters characterization

The wastewaters used hereafter have been collected at the *Seine Centre* plant of the SIAAP (Colombes) by Véronique Brémont and Sam Azimi. They were stored at 4°C and used within the 72 hours following their sampling.

5.2.1. Sample properties & organic matter content

The wastewater sample appears as a slightly turbid yellowish suspension (**Figure 5.1**) of particles of various sizes (up to ~ 1 mm), of pH ≈ 7.

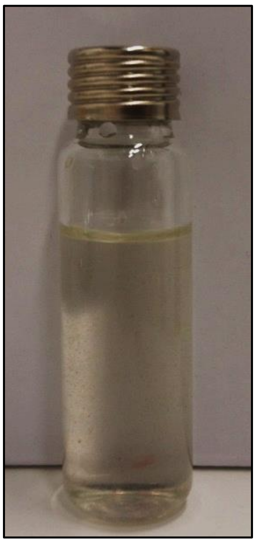

Figure 5.1 – Detail of the used wastewater

The dry residue mass of the wastewater sample was estimated by evaporating the water for 48 hours at 80°C at m_{dry} = 440 ± 22 mg for 1 L of water. This mass includes most non-volatile content of the sample, organic and inorganic together[9]. Thermogravimetric Analysis (TGA) (**Figure 5.2.A**) of the dry residue under air at 5°C·min^{-1} shows a linear decrease in mass between 20 and 600°C where the loss of mass reaches around 15 % of the sample. Between 600 and 725°C, a steep decrease in mass is observed which correlates with an endothermic heat flow in Differential Scanning Calorimetry (DSC) (**Figure 5.2.B**). Afterwards, the sample mass keeps stable at around 54 % of the initial mass. The complete dehydration of the sample should take place up to 180°C[10] where only 3 % of the sample mass has been lost. Up to 800°C, the observed mass loss can be attributed to the combustion and pyrolysis of organic matter[10] and at 800°C it only remains the inorganic fraction of the dry mass. The organic content of the considered wastewater can therefore be estimated at ~ 200 ± 16 mg·L^{-1} with this technique. For comparison, the average biochemical oxygen demand – corresponding to the amount of dissolved oxygen required by aerobes to oxidize the organic molecules, here during 5 days at 20°C in the dark (BOD_5) – measured by the SIAAP on the sampling day was of 263 mg_{O_2}·L^{-1} which is consistent with the value determined by TGA.

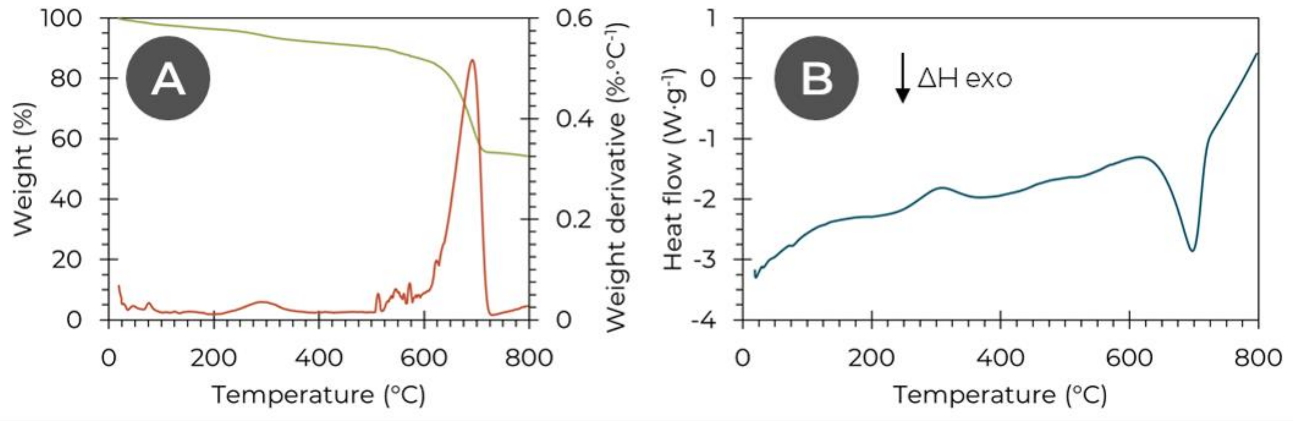

Figure 5.2 – Thermal investigation of the dry residue at 80°C of the wastewater provided by the SIAAP. (A) Thermogravimetric analysis (TGA) of the dry residue. Weight conservation (–) & its derivative (–) against the temperature. (B) Differential scanning calorimetry (DSC) against the temperature. Temperature ramp of 5°C·min^{-1}.

Overall, this simple analysis of the wastewater content gives us insights on the content of the used wastewater. A more thorough analysis of the wastewaters could also be undertaken, but is not necessary for our purpose. The dry mass and organic content of the samples is in the range of wastewaters characteristics reported in the literature[23]. It is additionally one order of magnitude lower than the mass concentration of the lactate in the MR-1/L medium (30 mM, or 2.7 g·L^{-1}).

5.2.2. Microbiome diversity analysis

The microbial diversity and the species profiling of the wastewaters provided was evaluated by 16S rRNA gene amplicon libraries sequencing. The resulting study is expected to give insights on the ability of the naturally-occurring consortium to perform EET in MFC conditions. Furthermore, these results will be compared with a post-mortem microbial diversity analysis to evaluate the evolution of the consortium composition upon MFC operation.

5.2.2.1. 16S rRNA gene sequencing

The 16S ribosomal RNA (16S rRNA) is a subunit of the prokaryotic ribosome that binds to the Shine–Dalgarno sequence. The corresponding gene contains nine hypervariable regions in between highly conserved sequences of the gene (labelled V1 to V9) than are varyingly conserved between bacterial and archaeal species (**Figure 5.3**). Their sequencing and comparison can be used to assess the phylogenetic proximity between species[11]. Closer species exhibit less variability between their sequences than less related taxa. Additionally, the sequencing and comparison of the more conserved hypervariable regions helps to identify higher-level taxonomy levels (kingdom, class and family), while less conserved regions discriminated lower levels (genus and species)[12].

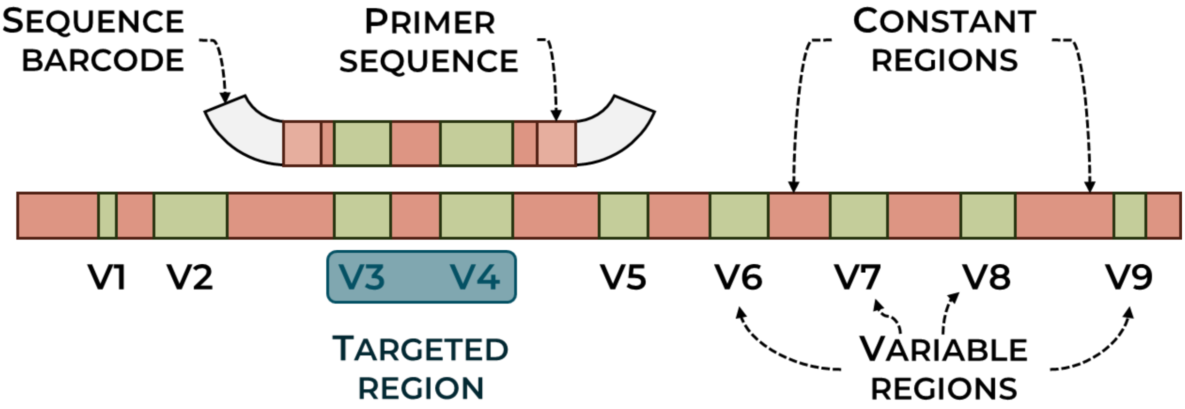

Figure 5.3 – Overview of the prokaryotic 16S rRNA gene, exhibiting the 9 hypervariable regions & the targeted V3-V4 barcoded amplification.

Prior to DNA extraction and sequencing, 3x50 mL of fresh raw wastewaters were centrifuged for 20 minutes at 5000 g and 4°C. The supernatant was discarded and the remaining pellets were freeze-dried by freezing them in liquid nitrogen and drying them at -85°C and 0.12 mbar for 24 hours (Christ Alpha 2-4 LD). They were stored at -80°C until DNA extraction.

DNA extraction was performed using the ZR Fecal DNA Kit (Zymo Research) and quantified fluorometrically at 260 nm using an Invitrogen™ Qubit™ dsDNA HS Assay Kit ([DNA] = 18.5 ± 1.0 ng·µL^{-1}, N = 3). Extracts were frozen at -20°C and shipped on dry ice to MR DNA (Shallowater, Texas, USA) for the barcoded amplicon sequencing of the V3-V4 region of the 16S rRNA gene (primers 341F and 785R). Data processing was performed using a proprietary analysis pipeline. Diversity coverage was however not optimized, therefore the following profiling remains preliminary.

5.2.2.2. Microbial community profiling

The microbial diversity of the sample is thereafter presented regarding the classes (**Figure 5.4.A**) and genera (**Figure 5.4.B**) corresponding to the extracted DNA.

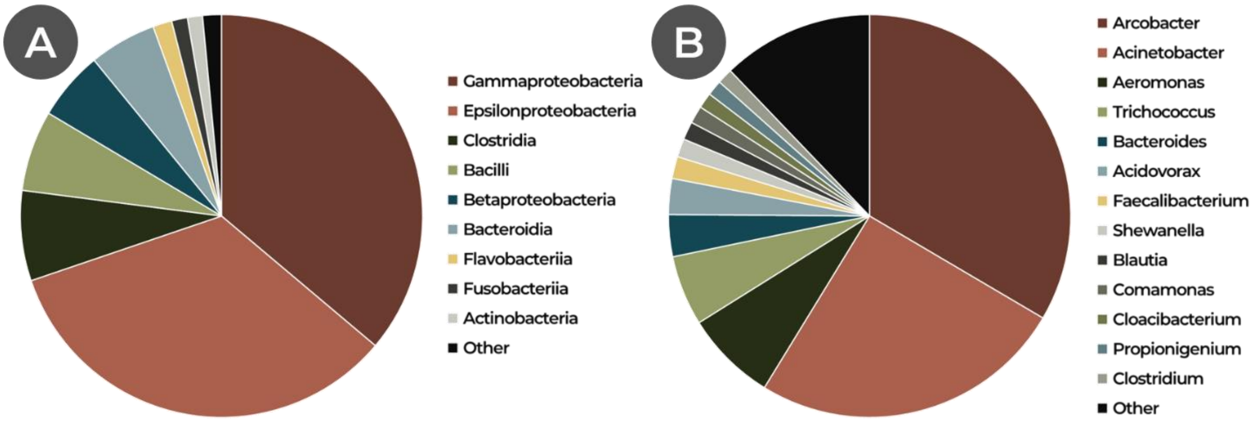

Figure 5.4 – Overview of the total microbiome diversity in the wastewaters provided by the SIAAP. (A) Relative abundance of the bacterial classes; (B) Relative abundance of the bacterial genera. Clades containing less than 1 % of sequences were grouped under "Other".

The bacteria identified in the sample belong mainly to the gammaproteobacteria (36.1 %) and epsilonproteobacteria (33.7 %), followed by clostridia (7.3 %), bacilli (6.5 %), betaproteobacteria (5.6 %), bacteroidia (5.4 %), and some flavobacteriia (1.5 %), fusobacteriia (1.3 %), actinobacteria (1.2 %) as well as other classes accounting each for less than 1 % of the DNA extracted. A finer analysis of the populations reveals an overwhelming presence of species belonging to the genera *Arcobacter* (epsilonproteobacteria, 33.5 %) and *Acinetobacter* (gammaproteobacteria, 25.3 %). Significant populations of *Aeromonas* (gammaproteobacteria, 7.4 %), *Trichococcus* (bacilli, 5.6 %), *Bacteroides* (bacteroidia, 3.4 %), *Acidovorax* (betaproteobacteria, 2.9 %). *Faecalibacterium* (clostridia, 1.8 %), *Shewanella* (gammaproteobacteria, 1.5 %), *Blautia* (clostridia, 1.5 %), *Comamonas* (betaproteobacteria, 1.4 %), *Cloacibacterium* (flavobacteriia, 1.3 %), *Propionigenium* (fusobacteriia, 1.2 %) and *Clostridium* (clostridia, 1.2 %) are also present.

Many of these genera are reported to contain aerotolerant exoelectrogenic species. For instance, *Arcobacter* – here mainly *A. cryaerophilus* – is widely found in wastewater-based MFCs in the literature[13],[14]. *Acinetobacter* – mainly *A. johnsonii* – is not exoelectrogenic but often found associated with electroactive species in MFCs anodic biofilms[15]. *Cloacibacterium* is also reported in other wastewaters-based MFCs[15]. Most *Shewanella* species are also able to perform EET. Additionally, some of the species reported can use exogenous redox shuttles to perform EET, shuttles that can be synthetized by other bacteria of the consortium – for instance, *Faecalibacterium* sp. can use flavins to perform EET[16], and such flavins are produced by *Shewanella* spp. for MET[1]. Synergetic behavior between the species is therefore expected in this consortium[17].

Overall, the ecology of the wastewaters is complex and exhibits many synergies between species to perform EET. These species can also influence themselves positively over nutrient availability, metabolism or biofilm formation (syntrophy). Interestingly, the sample mainly exhibits aerobes or aerotolerant species, probably due to the aerobic conditions in the wastewater plant. Despite the non-optimized diversity coverage, the dominant electroactive bacteria in these wastewaters belong to the genus *Arcobacter*, while many other exoelectrogenic species are present.

5.3. Electrospun carbon electrode

Firstly, the abiotic electrospun carbon electrodes synthetized and electrochemically characterized upon MFC integration and colonization by *Shewanella oneidensis* in Chapter 2 are tested with the raw wastewater as an anolyte.

5.3.1. MFC integration & electrochemical characterization

Three electrospun carbon electrodes prepared from PAN after subsequent heat treatments as described in Chapter 2 are sterilized at 120°C for 20 minutes. They are then integrated into a sterile MFC reactor. The catholyte is made up of 150 mM of NaCl (supporting electrolyte) and 100 mM of $K_3[Fe(CN)_6]$. The anodic compartment is filled with 20 mL of the raw wastewater provided by the SIAAP.

The anode potential is potentiostatically poised at +0.3 V vs. Ag/AgCl, KCl saturated reference. The MFC current output is monitored through time with chronoamperometry (CA) and the current density j ($\mu A \cdot cm^{-2}$) is calculated ($Ø_{anode}$ = 1.7 cm; $A_{anode, geometrical} \approx 2.27\ cm^2$). Cyclic voltammograms (CV) are recorded in the range of -0.7 to +0.7 V against Ref. (scan rate: 1 $mV \cdot s^{-1}$) every 24 hours. On the fifth day, the polarization of the anode is stopped after the cyclic voltammetry for 16 hours to let the electrode potential stabilized and the working and counter electrodes channels are reversed. Polarization and power curves are recorded by applying an incremental series of negative currents to the cathode while the emf is recorded. No further addition of nutrients is conducted during the experiment. All the processes are conducted at 21°C. The electrochemical characterization of the system is then compared to the average in situ colonized electrospun carbon membrane presented in Chapter 2 (**Figure 5.5**).

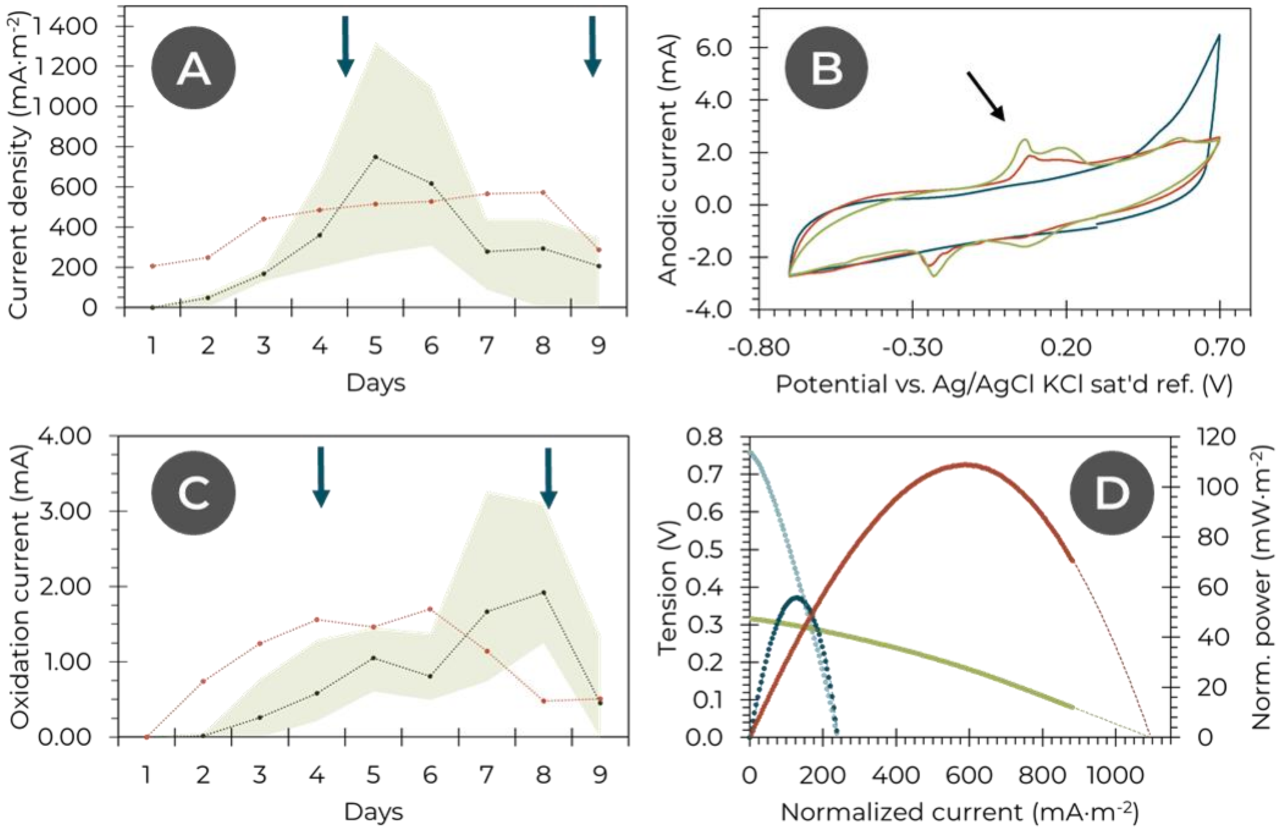

Figure 5.5 – Electrochemical characterization of a two-compartment MFC including an electrospun carbon electrode in wastewater anolyte polarized at +0.3 V vs. the reference (electrospun from a 10 wt% PAN in DMF solution, stabilized under air at 280°C, carbonized under argon at 940°C) as a function of time. (A) Evolution of the average current density (•); blue arrows indicate addition of 1 mmol of sodium lactate only for the *S. oneidensis* setup; the green zone represents maximum and minimum values. Comparison (•) with an in situ colonized electrospun carbon electrode; N = 3. (B) Evolution of cyclic voltammetry as a function of time (– 1st day, – 3rd day, – 5th day); sweep rate of 1 $mV·s^{-1}$; 3 cycles are acquired, here is the second one; thickness of 251 µm. (C) Evolution of the average current (•) corresponding to the peak shown by the arrow on the CV; blue arrows indicate addition of 1 mmol of sodium lactate only for the *S. oneidensis* setup; the green zone represents maximum and minimum values. Comparison (•) with an in situ colonized electrospun carbon electrode; N = 3. (D) Polarization (•) and power (•) curves of an MFC at maximum current density value (here 5th day, thickness of 251 µm). No data was not recorded for current densities over 880 $mA·m^{-2}$ & the dashed line is a linear extrapolation of the data. Comparison with the polarization (•) and power (•) curves of a simple precolonized bioanode (here 5th day, thickness of 293 µm). Current and power are normalized by the geometric surface area of the electrospun carbon electrode ($Ø_{anode}$ = 1.7 cm; $A_{anode, geometrical}$ ≈ 2.27 cm^2).

No current (**Figure 5.5.A**) is observed on the first day. However, the average current density quickly rises from the second day at 48 $mA·m^{-2}$ to the fifth day with a maximum at 750 $mA·m^{-2}$. It then slowly decreases and stays around 200-300 $mA·m^{-2}$ until the end of the experiment.

Cyclic voltammetry (**Figure 5.5.B**) shows no noticeable peak on the first day and a capacitive response similar to the one observed in MR1 medium in Chapter 2. On the second cyclic voltammogram as reported with *S. oneidensis*, two oxidation peaks appear between -0.05 and +0.3 V vs. Ag/AgCl KCl saturated. They are probably attributable to direct electron transfer in metabolic pathways probably homologous to those exhibited by *S. oneidensis.* An extra peak similar to the response exhibited by *S. oneidensis* in composite and core-shell electrospun electrodes is also observed around +0.6 V vs. Ref. The intensity of the peak centered around +0.1 V vs. Ref. like the one studied before starts to be noticeable from day 2 (**Figure 5.5.C**). Its intensity overall increases continuously until the eighth day when it sharply decreases. Interestingly and unlike previously, the 3 acquired cyclic voltammetry were not all similar in this setup. In particular (**Figure 5.6**), an oxidation peak attributable to direct electron transfer[18],[19] was consistently found on the first cyclic voltammetry of the experiment, which was never observed for *S. oneidensis* under the conditions investigated. Altogether, the presence of all these oxidations peaks and their relative correlation with the measured current densities confirms the suitability of the electrospun carbon electrode for electricity generation from wastewaters. The observed electron transfers are obviously more complex than with a pure *S. oneidensis* culture, but they interestingly share a lot in common, and especially the nature and evolution of the direct electron transfer-associated oxidation peaks.

After stopping the polarization of the anode and waiting for its stabilization, the emf of the MFC reverts to 0.32 V (the anode potential stabilizing at 90 mV vs. Ref.). This value is different than observed for *S. oneidensis* but it is understandable since the nature of the bacterial consortium colonizing the electrode and its EET behavior differ from the pure culture. The polarization and power curves (**Figure 5.5.D**) recorded show a maximum power and current densities of respectively 110 $mW{\cdot}m^{-2}$ and 1100 $mA{\cdot}m^{-2}$ (the latter being extrapolated from an incomplete set of data), or 438 $W{\cdot}m^{-3}$ and $4.4{\cdot}10^3$ $A{\cdot}m^{-3}$. These are clearly better values than observed for *S. oneidensis* used as a pure strain, – 56 $mW{\cdot}m^{-2}$ and 240 $mA{\cdot}m^{-2}$ – and this behavior was expected[20]. We can also estimate the internal resistance of the system $R_{int} \approx 7$ kΩ from the slope of the polarization curve. This value is consistent with previously reported internal resistances and with the typical resistance of the electrospun mat ($R \sim 10^3$ Ω).

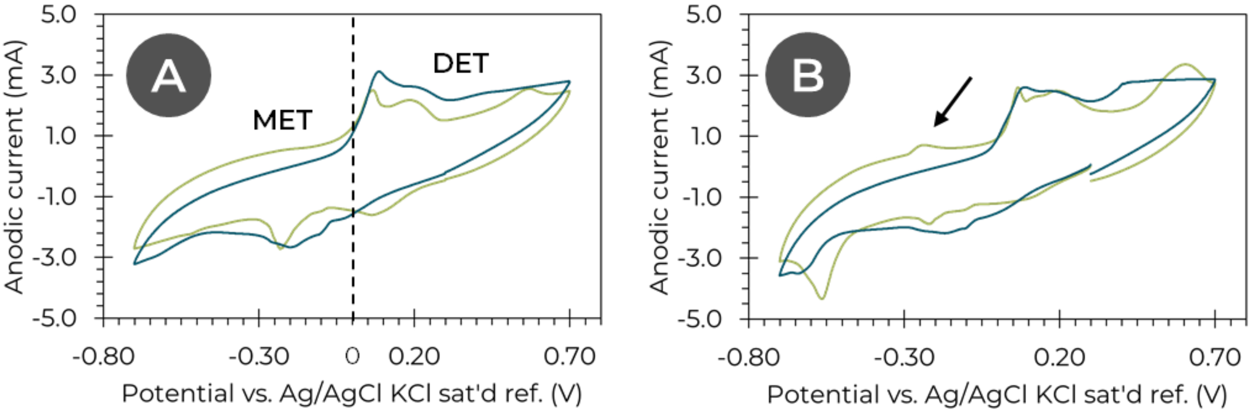

Figure 5.6 – Evolution of the first 2 cycles of cyclic voltammetry as a function of time (sweep rate of 1 mV·s^{-1}) for an electrospun carbon electrode integrated in an MFC using for anolyte either MR-1/L medium colonized with *Shewanella oneidensis* CRBIP17.141 at day 3 (–) or wastewater provide by the SIAAP in otherwise sterile conditions at day 5 (–). (A) Cycle 1; (B) Cycle 2. The black arrow points out the presence of a Mediated Electron Transfer (MET) associated oxidation peak in the wastewater setup while only Direct Electron Transfer (DET) was exhibited in the other setup.

The evolution of the surface capacitive area of the system was also evaluated and averaged between the 3 electrodes tested (**Figure 5.7**). The behavior observed previously with *S. oneidensis* is here also noticeable: the performances exhibit a three-phase "bell curve" appearance where they started at low values (1) before increasing to a maximum (2) and eventually fell (3), akin to the diminution of the capacitive surface area as organic matter deposes on the fibers. However here, the bell curve was shifted to a few days later as the consortium exhibits a lag-phase in order to adapt to its new environment.

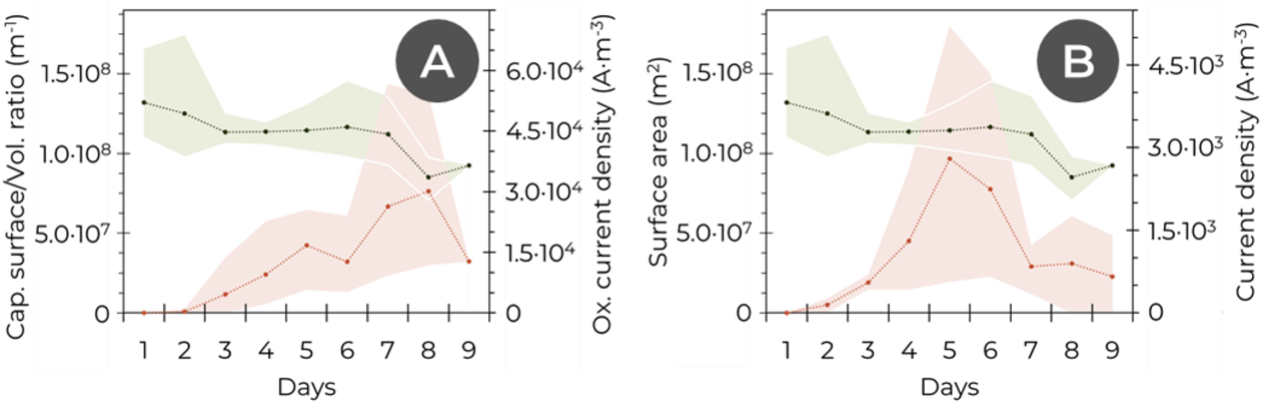

Figure 5.7 – Evolution of the volume normalized capacitive surface area (•) of an electrospun carbon electrode used with a wastewater anolyte as a function of the time; N = 3. The capacitive surface area is calculated from cyclic voltammetry. The surface area is compared with (A) the maximum current density of the main oxidation peak on the CV (•), & (B) the current density output of the MFC, normalized by the volume of the electrospun carbon electrode (Ø$_{\text{anode}}$ = 1.7 cm; A$_{\text{anode, geometrical}}$ ≈ 2.27 cm^2).

Overall, the electrospun carbon electrode shows a similar behavior evolution when using raw wastewater as an anolyte or MR1-L colonize with *Shewanella oneidensis* CRBIP17.141. However, the performances exhibited by the system are clearly better than when using the pure strain *S. oneidensis* as the electroactive species, albeit with an additional lag-phase at the beginning of the measurements linked to the adaptation of the bacterial consortium to the MFC conditions.

5.3.2. Post-mortem imaging

The post-mortem colonization of the electrospun carbon electrode is afterward evaluated by SEM (**Figure 5.8**).

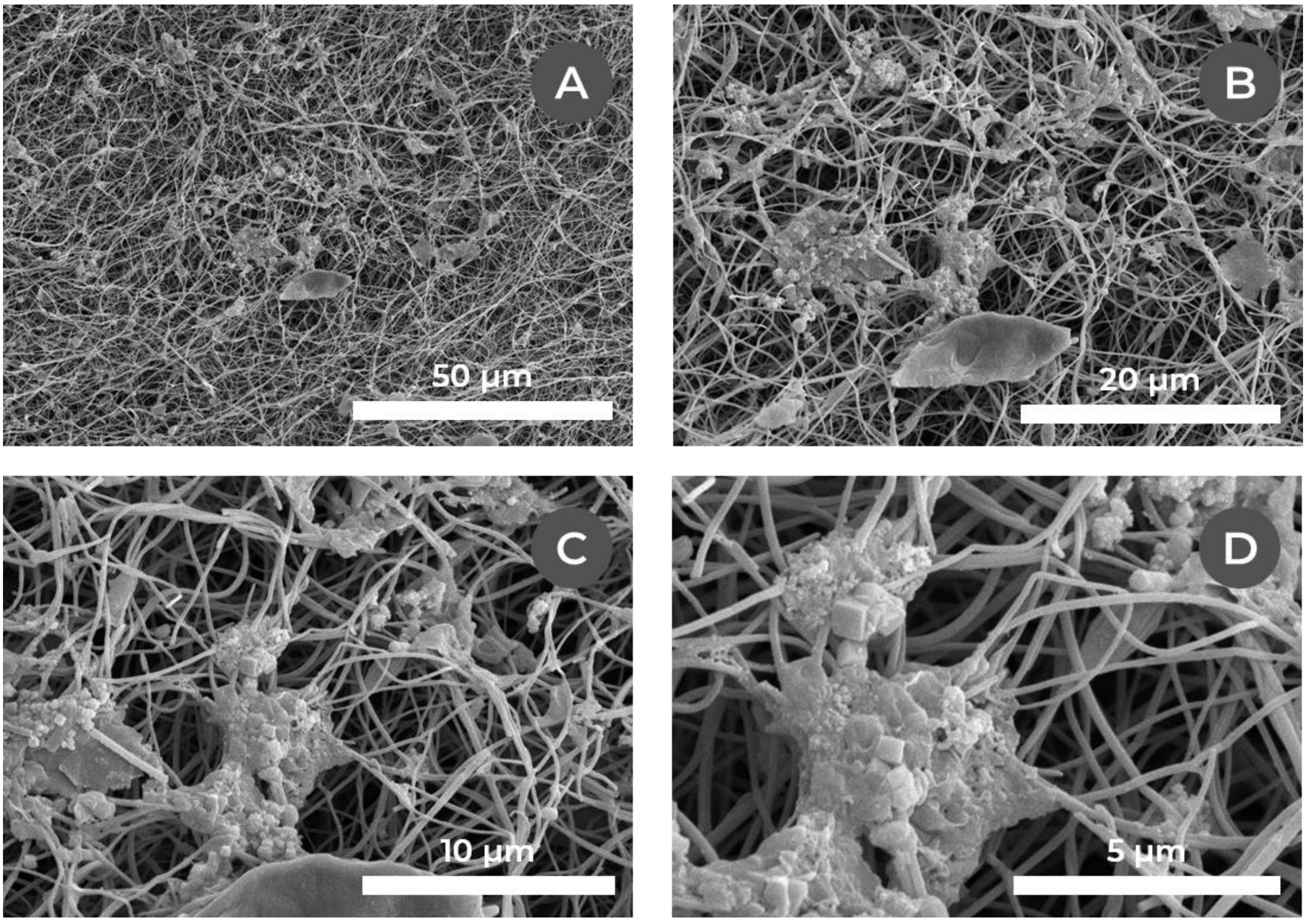

Figure 5.8 – SEM micrographs of an air-dried post-mortem electrospun carbon electrode after 9 days of operation with a wastewater anolyte, polarized at +0.3 V vs. Ag/AgCl, KCl saturated reference, coated with 15 nm of gold.

The SEM observation of the electrode reveals a clear development of biofilm in between the fibers. Additionally, the presence of various shape reminiscent of crystals – maybe metal oxides – can be spotted embedded in the deposited matter. Compared to the previous studies, different biofilm architectures can be seen along the fibers. The variability and diversity of the matter architecture deposed onto the fibers may be linked to the complexity of microorganisms populations present in wastewaters.

5.3.3. Effect on microbial diversity

DNA extraction and 16S rRNA gene sequencing is then carried out on the post-mortem anode and anolyte. The electrode and anolyte are first sonicated for 5 minutes until the electrospun carbon paper is broken down in order to liberate the bacteria. The resulting medium is then centrifuged for 20 minutes at 5000 g and 4°C, and the supernatant is discarded. Bacterial DNA is then extracted from the remaining pellet as described before, purified by ethanol purification, and quantified using the Qubit dsDNA HS Assay Kit ([DNA] ≈ 1.5 ng·μL^{-1}).

Extracts were frozen at -20°C and shipped on dry ice to MR DNA (Shallowater, Texas, USA) for the barcoded amplicon sequencing of the V3-V4 region of the 16S rRNA gene (primers 341F and 785R), and the data was analyzed by a proprietary pipeline. The microbial population profiling is then compared with the raw wastewaters (**Figure 5.9**).

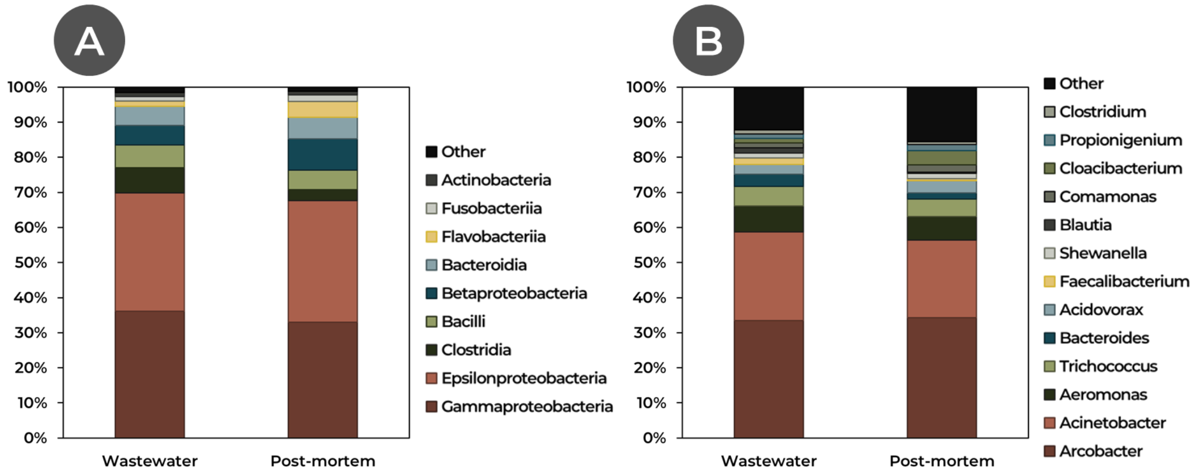

Figure 5.9 – Comparison of the total microbiome diversity between the raw wastewaters provided by the SIAAP & in the post-mortem anolyte after 9 days of MFC operation (anode electrospun from a 10 wt% PAN in DMF solution, stabilized under air at 280°C, carbonized under argon at 940°C, polarized at +0.3 V vs. Ag/AgCl, KCl saturated reference); (A) Relative abundance of the bacterial classes; (B) Relative abundance of the bacterial genera. Clades containing less than 1 % of sequences were grouped under "Other".

After 9 days of MFC operation, the system underwent a modification of the distribution of its microbiome. In particular, the proportion of gammaproteobacteria decreased by 8.7 %, epsilonproteobacteria increased by 2.8 %, bacilli and clostridia saw a sharp decrease – 12.8 % and 56.9 % respectively – and betaproteobacteria and flavobacteriia increased – 58.7 % and 202 %. More precisely, *Arcobacter* species stayed roughly stable (+2.4 %), while the *Acinetobacter* proportion slightly decreased (-12.3 %) and *Cloacibacterium* dramatically increased (+223 %). Most of the non-electroactive genera ubiquitous in wastewaters saw a significant fall in proportions – *Bacteroides* (-47.9 %), *Faecalibacterium* (-70 %), *Blautia* (-73.5 %). Additionally, the *Shewanella* genus stayed stable (-1.5 %), and some other electroactive species found in small proportions in raw wastewaters saw a dramatic increase after MFC operation (e.g. *Pseudomonas*; +554.2 %).

Overall, most of the exoelectrogenic species saw in increase in proportion, while the non-electroactive wastewater-occurring bacteria proportion mainly decreased. This is understandable since species better suited to electron transfer and electricity generation are expected to thrive in MFC conditions[21].

Additionally, the main genus and species found in wastewater – *Arcobacter cryaerophilus* –, albeit less studied than model bacteria such as *Shewanella oneidensis* or *Geobacter sulfurreducens* is reported to perform at least IET, and probably DET through flagellin-associated appendages[13]. Even if it is difficult to decorrelate the participation and synergy of all the species present on the previously reported cyclic voltammograms, these bacteria could be responsible at least in part for the observed DET oxidation waves. More investigation on isolated and pure strains would however be required to confirm this hypothesis.

Altogether, the electrospun carbon electrode exhibits clearly better performances when using raw wastewater as an anolyte than MR1-L colonized with *Shewanella oneidensis* CRBIP17.141 – 438 $W{\cdot}m^{-3}$ and $4.4{\cdot}10^{3}$ $A{\cdot}m^{-3}$ vs. 191 $W{\cdot}m^{-3}$ and $0.8{\cdot}10^{3}$ $A{\cdot}m^{-3}$. Moreover, their general behavior evolutions are similar, following the “bell curve” evolution, albeit with an additional lag-phase at the beginning of the measurements linked to the adaptation of the bacterial consortium to the MFC conditions. The development of biofilm along the carbon fibers has also been verified by SEM imaging. In the meantime, the anodic bacterial microbiome underwent an enrichment in exoelectrogenic species, while most of the non-electroactive bacteria found in wastewaters saw their proportion decrease, sometimes dramatically. *Arcobacter* stayed the main EET genus present after MFC operation.

5.4. Integrated bioanode

A cryodesiccated integrated bioanode developed in Chapter 4 is then evaluated when using wastewater as the anolyte.

5.4.1. MFC integration & electrochemical characterization

A cryodesiccated integrated bioanode is therefore integrated into a sterile MFC reactor. The catholyte is made up of 150 mM of NaCl (supporting electrolyte) and 100 mM of $K_3[Fe(CN)_6]$. The anodic compartment is filled with 20 mL of the raw wastewater provided by the SIAAP. The bioanode is then poised at +0.3 V vs. Ref. and electrochemically characterized as described before (**Figure 5.10**).

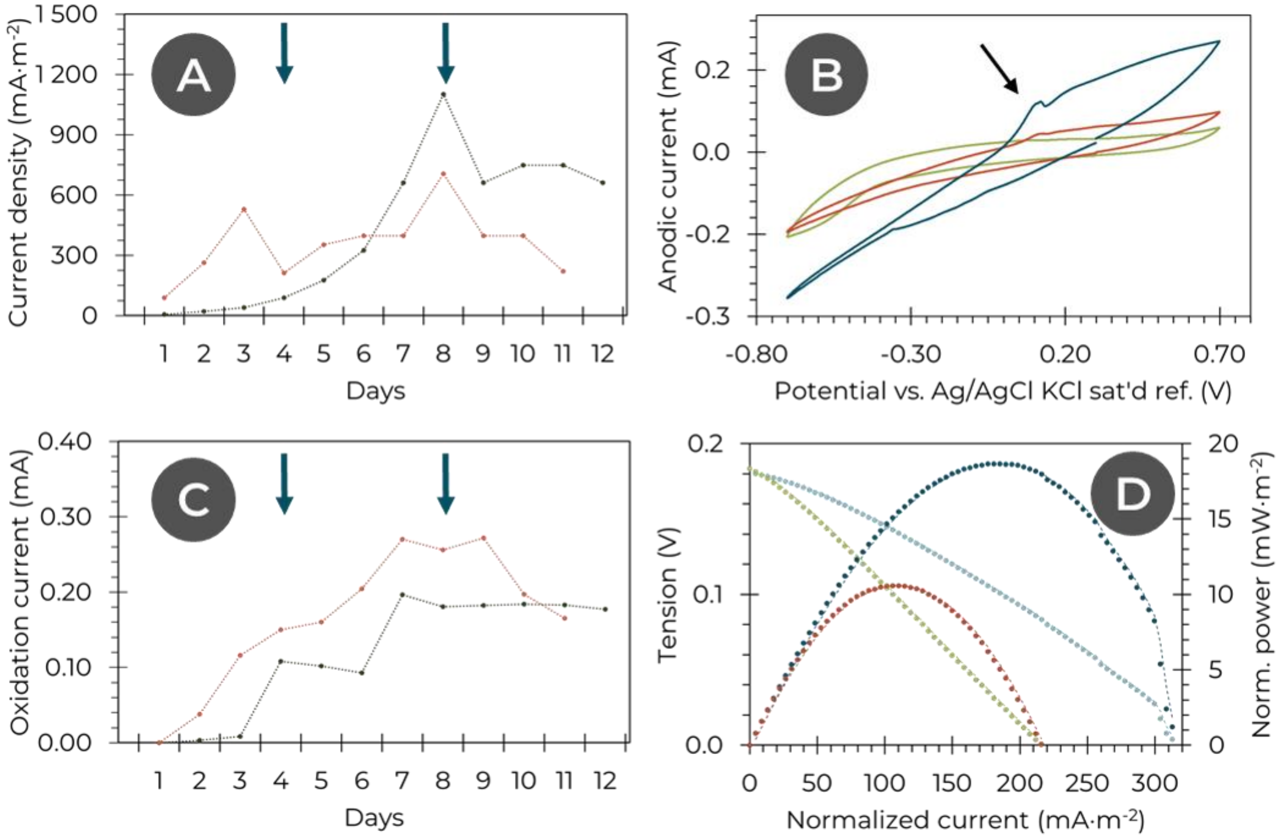

Figure 5.10 – Electrochemical characterization of a two-compartment MFC including a cryodesiccated integrated bioanode in wastewater anolyte polarized at +0.3 V vs. the reference as a function of time. (A) Evolution of the current density (•). Comparison (•) with a cryodesiccated integrated bioanode in MR-1/L medium anolyte; blue arrows indicate addition of 1 mmol of sodium lactate only for the MR-1/L setup. (B) Evolution of cyclic voltammetry as a function of time (– 1st day, – 3rd day, – 5th day); sweep rate of 1 mV·s^{-1}; 3 cycles are acquired, here is the second one; thickness of 87 µm. (C) Evolution of the current (•) corresponding to the peak shown by the arrow on the CV. (•) with a cryodesiccated integrated bioanode in MR-1/L medium anolyte; blue arrows indicate addition of 1 mmol of sodium lactate only for the MR-1/L setup. (D) Polarization (•) and power (•) curves of an MFC at day 5 (thickness of 87 µm). Comparison with the polarization (•) and power (•) curves of a cryodesiccated integrated bioanode in MR-1/L medium anolyte (here 5th day, thickness of 87 µm). Current and power are normalized by the geometric surface area of the electrospun carbon electrode ($Ø_{\text{anode}}$ = 1.7 cm; $A_{\text{anode, geometrical}}$ ≈ 2.27 cm^2).

No current output is observed on the first day of experiment (**Figure 5.10.A**). From the second day onwards, the current density starts to rise up, beginning at the low value of 20 mA·m^{-2}, to rise up to 1100 mA·m^{-2} on day 8 (and even over 1500 mA·m^{-2} on the first few hours of the eighth day). The current density output then stabilizes around 750 mA·m^{-2} until the end of the experiment.

Cyclic voltammetry (**Figure 5.10.B**) shows no noticeable peak on the first day like the cryodesiccated bioanode in MR-1/L medium. From the second day, a behavior very similar to the one observed in the MR-1/L setup is confirmed. A peak centered on 0.08 V vs. Ref. appears and steadily grows for the rest of the experiment (**Figure 5.10.C**). This redox response is however probably due to the superposition of the *S. oneidensis* and a consortium DET, which seem to both happen around this potential. Remarkably, no other peak linked to the consortium is here observed – including the MET. This behavior is interestingly very different from the response observed with the electrospun carbon electrode. Even if it is difficult to decorrelate the EET participation of *S. oneidensis* from the probable electron transfer from the wastewater-borne microorganisms because of the superposition of their DET peak around 0.08 V vs. Ref. and the non-observation of other peaks, the current densities observed in this setup hint for a synergetic participation of the two populations. In particular, even if there is less organic nutrients in wastewaters than in MR-1/L, the current densities observed with the former are better than with the latter. We can hypothesize than the EET participation of *S. oneidensis* is dominant in our system – because of the similarity of the CVs between a cryodesiccated bioanode used with MR-1/L or wastewaters – but that the wastewater-borne microorganisms develop in synergy with them. For instance, the secretion of molecules or the breaking-up of unusable organic molecules into nutrients by the wastewater microorganisms may improve the electroactivity and EET of the encapsulated *S. oneidensis*. Obviously, more studies will be needed to confirm this hypothesis, but it seems consistent with most reports of improved MFC performances when using complex microbial ecosystems[21],[22].

After stopping the polarization of the anode and waiting for its stabilization on the fifth day, the emf of the MFC reverts to 0.18 V (the bioanode potential stabilizing at around 153 mV), which is very similar to the behavior found in the MR-1/L setup. The power and polarization curve are recorded (**Figure 5.10.D**). The power curve shows a maximum of around 12 mW·m^{-2} and the polarization curve exhibits a maximum current density of 216 mA·m^{-2} – or respectively 138 W·m^{-3} and 2.5·10^{3} A·m^{-3} which are still good values. Regrettably, no power and polarization curves were recorded on the current output optimum of the MFC on day 8, but the similar behavior spotted between the two setups and the even better current output of the MFC powered with wastewaters hint that these performances would have been similar if not even better.

Eventually, the performances recorded for the cryodesiccated integrated bioanode used with a wastewater anolyte are very encouraging – especially the volume performances as noted for other electrospun systems. This setup is worthwhile being studied further in these conditions, and its long-term performances must be more thoroughly assessed.

5.4.2. Post-mortem imaging

The post-mortem cryodesiccated bioanode is then imaged with SEM (**Figure 5.11**). More matter seems to have deposed onto the network than in the MR-1/L setup presented in the previous chapter. (**Figure 5.11.A,C**). However, a close-up on each of the fibers shows that actually most of the deposited matter is found on the conductive scaffold fibers (**Figure 5.10.D**) rather than on the core-shell fibers (**Figure 5.10.B**) that are left relatively clean. The good performances observed previously may therefore be attributed to this optimum use of the electrode fibers – *S. oneidensis* staying inside the fibers as observed before, while the water-borne consortium develops on the secondary network. Moreover, a synergetic effect between the two-populations may be at work to explain the observed surge in performances. Either way, more experiments will be needed to confirm this hypothesis, as well as to control that in the long run the colonization of the secondary network by the consortium does not hamper the performances as observed in all the other setups.

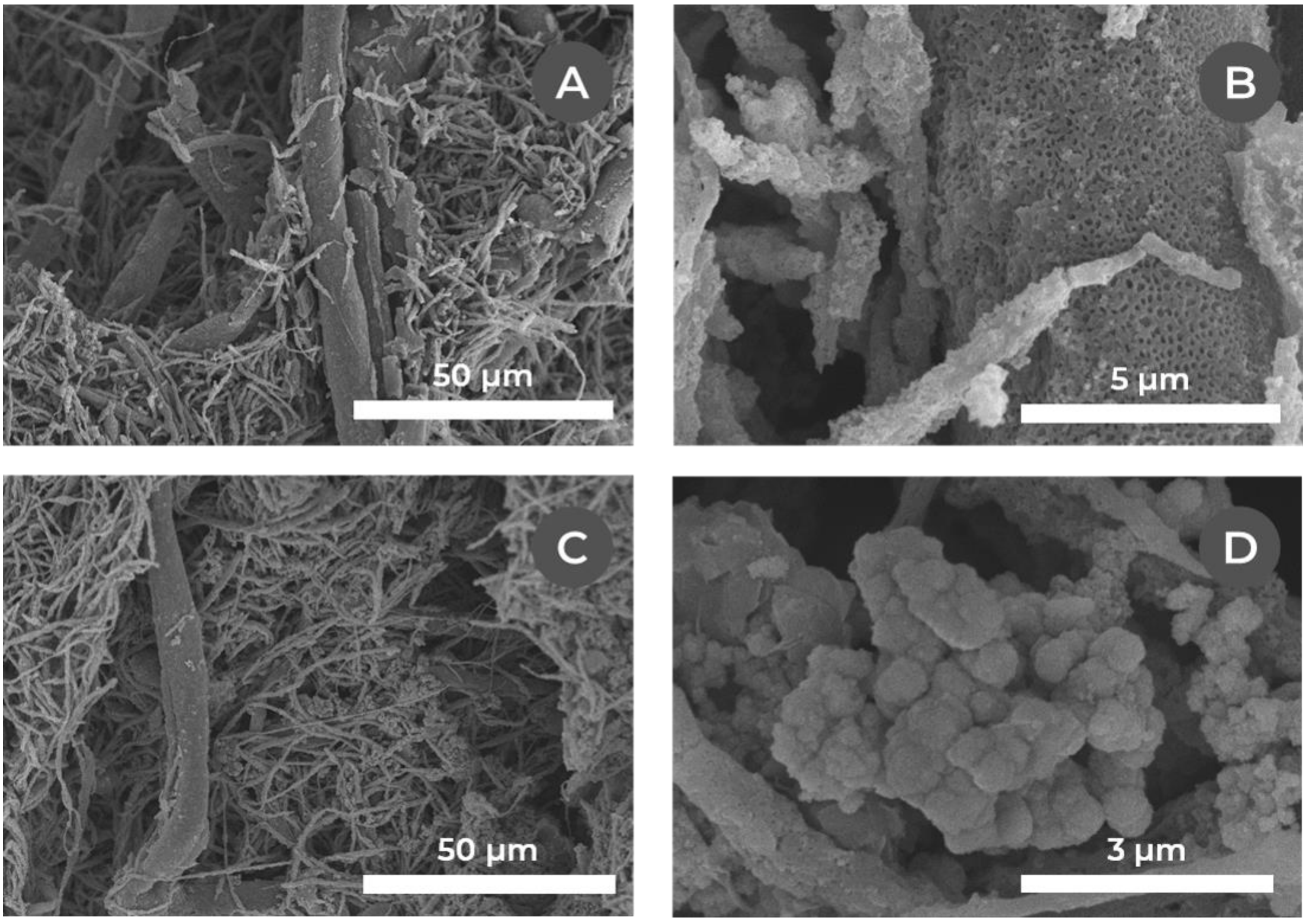

Figure 5.11 – SEM micrographs of an air-dried post-mortem cryodesiccated integrated bioanode after 12 days of operation with a wastewater anolyte, polarized at +0.3 V vs. Ag/AgCl, KCl saturated reference, coated with 15 nm of gold. (A,C) Overview of the post-mortem membrane; (B) Close-up on a core-shell fiber; (D) Close-up on the conductive scaffold.

Overall, the performances recorded for the electrospun bioanodes using wastewater as the anolyte can be compared with those of the same electrodes in MR-1/L medium anolyte as well as with the literature (**Table 5.1**).

Table 5.1 – Comparison of the surface (◆) & volume (◆) normalized electrochemical performances between the literature and different electrospun bioanodes setups, in MR-1/L and wastewater conditions. The performances compare MFCs using a carbon-based anode & a ferricyanide solution as the catholyte.

Setup	Current	Power
Literature optimum (Ringeisen *et al.*)[4]	12.5 A·m^{-2}	3 W·m^{-2}
MR-1/L anolyte	$2.08 \cdot 10^{3}$ A·m^{-3}	500 W·m^{-3}
Precolonized electrospun carbon electrode	0.334	0.087
MR-1/L anolyte	$1.14 \cdot 10^{3}$	296
Cryodesiccated integrated bioanode	0.315	0.020
MR-1/L anolyte	$3.26 \cdot 10^{3}$	230
Electrospun carbon electrode	$1.10 \cdot 10^{3}$	0.110
Wastewater anolyte	$4.4 \cdot 10^{3}$	438
Cryodesiccated integrated bioanode	0.216	0.012
Wastewater anolyte – recorded in suboptimal conditions	$2.5 \cdot 10^{3}$	138

For the in situ colonized electrospun carbon electrode, the performances are clearly higher using the wastewater anolyte – $4.4 \cdot 10^{3}$ A·m^{-3} & 438 W·m^{-3} vs. $1.14 \cdot 10^{3}$ A·m^{-3} & 296 W·m^{-3}. Without reactor optimization, these performances are comparable (power) or higher (current) than the optimized *S. oneidensis*/MR-1/L medium anolyte setup reported by Ringeisen *et al.* this increase in performance using a water-borne consortium was expected[20], but is still outstanding. For the cryodesiccated integrated bioanode, even if the power and polarization curves were not recorded at the best moment, the comparison of the current density output between the two setups strongly hints for a similar improvement in performances – from 700 to 1100 mA·m^{-2} for the same membrane thickness – probably thanks to a synergetic interaction between the encapsulated *S. oneidensis* and the wastewater consortium.

Eventually, the cryodesiccated integrated bioanode exhibits encouraging performances when using wastewater as an anolyte. The current density output recorded surged up to 1500 mA·m^{-2} with a steady maximum output of 1100 mA·m^{-2} while the same electrode used with an MR-1/L medium anolyte exhibited a maximum current density of 700 mA·m^{-2}. The better performances recorded may be attributed to a synergetic interaction between *S. oneidensis* encapsulated in the fibers and the wastewater consortium. Interestingly, the EET behavior exhibited on the CVs is similar to the electrode used in MR-1-L medium, without any extra oxidation peak despite the presence of other bacteria in the system. Finally, more experiments will be needed to explore the interactions between the two populations, as well as to control the long run stability of the integrated bioanode under these conditions.

5.5. Conclusion

Altogether, we have evaluated the performances of the two main electrospun bioanodes designs developed in this work using actual wastewaters as a fuel and microorganisms source.

Abiotic electrospun carbon electrodes from Chapter 2 were shown to exhibit clearly better performance when used with this anolyte rather than with MR-1/L medium colonized with *S. oneidensis* only (current and power densities of respectively $4.4 \cdot 10^{3}$ $A \cdot m^{-3}$ & 438 $W \cdot m^{-3}$ vs. $1.14 \cdot 10^{3}$ $A \cdot m^{-3}$ & 296 $W \cdot m^{-3}$). The overall stability of the setup was nevertheless similar to the one reported in Chapter 2, with a progressive increase in performances after a lag-phase induced by the adaptation of the wastewater consortium to the electrode, before reaching a maximum and eventually falling due to a biofilm overgrowth hindering the system.

A cryodesiccated integrated bioanode from Chapter 4 was then mounted into a similar setup, and was shown to exhibit a better current density output – up to 1500 $mA \cdot m^{-2}$ with a steady maximum output of 1100 $mA \cdot m^{-3}$ vs. a maximum 700 $mA \cdot m^{-2}$. This result may be attributed to a synergy between the encapsulated *S. oneidensis* and the wastewater consortium, but will require further investigation. Additionally, the long-term stability of the system seems to also be better than the electrospun carbon electrode in these conditions, but would also need more studies especially considering than the development of biofilm on the secondary conductive scaffold has been seen in SEM post-mortem imaging.

A 16S rRNA sequencing of the DNA extracted from the bacteria in the raw wastewaters as well as in the post-mortem MFC anolytes and anodes has additionally been conducted. It revealed the complex microbial ecology of the wastewaters, underlining the presence of many electroactive bacteria from various prokaryotic species. The exoelectrogenic strains were enriched by the MFC cycling while the non-electroactive tended to be depleted. In particular, the main electroactive strains detected belonged to the genus *Arcobacter.* This genus is reported to perform IET as well as probably DET exoelectronic transfer, in concordance with the cyclic voltammograms recorded. The synergetic effects all the species may have together could also explain the good performances seen for the electrospun anodes used with a wastewater anolyte.

Eventually, the systems developed in this work show a remarkable potential for their application towards electricity generation from wastewaters, even if further studies will be required to confirm this behavior.

REFERENCES

[1] E. Marsili *et al.* Shewanella secretes flavins that mediate extracellular electron transfer. *PNAS* **105,** 3968–3973 (2008).

[2] O. Bretschger *et al.* Current production and metal oxide reduction by Shewanella oneidensis MR-1 wild type and mutants. *Appl. Environ. Microbiol.* **73,** 7003–7012 (2007).

[3] D. Baron, E. LaBelle, D. Coursolle, J. A. Gralnick & D. R. Bond. Electrochemical measurement of electron transfer kinetics by Shewanella oneidensis MR-1. *J. Biol. Chem.* **284,** 28865–28873 (2009).

[4] B. R. Ringeisen *et al.* High power density from a miniature microbial fuel cell using Shewanella oneidensis DSP10. *Environ. Sci. Technol.* **40,** 2629–2634 (2006).

[5] International Energy Agency. *World Energy Outlook 2016*. (OECD, 2016).

[6] Y. Ahn & B. E. Logan. Altering anode thickness to improve power production in microbial fuel cells with different electrode distances. *Energy and Fuels* **27,** 271–276 (2013).

[7] L. Huang, S. Cheng & G. Chen. Bioelectrochemical systems for efficient recalcitrant wastes treatment. *J. Chem. Technol. Biotechnol.* **86,** 481–491 (2011).

[8] R. A. Rozendal, H. V. M. Hamelers, K. Rabaey, J. Keller & C. J. N. Buisman. Towards practical implementation of bioelectrochemical wastewater treatment. *Trends Biotechnol.* **26,** 450–459 (2008).

[9] T. R. Crompton. *Analysis of Seawater*. (Springer-Verlag, 2006).

[10] A. Magdziarz & S. Werle. Analysis of the combustion and pyrolysis of dried sewage sludge by TGA and MS. *Waste Manag.* **34,** 174–179 (2014).

[11] C. R. Woese, O. Kandlert & M. L. Wheelis. Towards a natural system of organisms : Proposal for the domains. *Proc. Natl. Acad. Sci.* **87,** 4576–4579 (1990).

[12] B. Yang, Y. Wang & P.-Y. Qian. Sensitivity and correlation of hypervariable regions in 16S rRNA genes in phylogenetic analysis. *BMC Bioinformatics* **17,** 135 (2016).

[13] A. G. Pereira-Medrano *et al.* Quantitative proteomic analysis of the exoelectrogenic bacterium Arcobacter butzleri ED-1 reveals increased abundance of a flagellin protein under anaerobic growth on an insoluble electrode. *J. Proteomics* **78,** 197–210 (2013).

[14] V. Fedorovich *et al.* Novel Electrochemically Active Bacterium Phylogenetically Related to Arcobacter butzleri, Isolated from a Microbial Fuel Cell. *Appl. Environ. Microbiol.* **75,** 7326–7334 (2009).

[15] T. Pepè Sciarria, S. Arioli, G. Gargari, D. Mora & F. Adani. Monitoring microbial communities' dynamics during the start-up of microbial fuel cells by high-throughput screening techniques. *Biotechnol. Reports* **21,** e00310 (2019).

[16] M. T. Khan *et al.* The gut anaerobe Faecalibacterium prausnitzii uses an extracellular electron shuttle to grow at oxic–anoxic interphases. *ISME J.* **6,** 1578–1585 (2012).

[17] M. Burmølle, D. Ren, T. Bjarnsholt & S. J. Sørensen. Interactions in multispecies biofilms: do they actually matter? *Trends Microbiol.* **22,** 84–91 (2014).

[18] D. Pinto, T. Coradin & C. Laberty-Robert. Effect of anode polarization on biofilm formation and electron transfer in Shewanella oneidensis/graphite felt microbial fuel cells. *Bioelectrochemistry* **120,** 1–9 (2018).

[19] J. N. Roy *et al.* Catalytic biofilm formation by Shewanella oneidensis MR-1 and anode characterization by expanded uncertainty. *Electrochim. Acta* **126,** 3–10 (2014).

[20] K. Rabaey, N. Boon, S. D. Siciliano, M. Verhaege & W. Verstraete. Biofuel cells select for microbial consortia that self-mediate electron transfer. *Appl. Environ. Microbiol.* **70,** 5373–82 (2004).

[21] B. H. Kim *et al.* Enrichment of microbial community generating electricity using a fuel-cell-type electrochemical cell. *Appl. Microbiol. Biotechnol.* **63,** 672–681 (2004).

[22] P. Parameswaran, C. I. Torres, H.-S. Lee, R. Krajmalnik-Brown & B. E. Rittmann. Syntrophic interactions among anode respiring bacteria (ARB) and Non-ARB in a biofilm anode: electron balances. *Biotechnol. Bioeng.* **103,** 513–523 (2009).

[23] J. Chouler, Á. Cruz-Izquierdo, S. Rengaraj, J. L. Scott & M. Di Lorenzo. A screen-printed paper microbial fuel cell biosensor for detection of toxic compounds in water. *Biosens. Bioelectron.* **102,** 49–56 (2018).

GENERAL CONCLUSION & PROSPECTS

GENERAL CONCLUSION

Since the first report of bioelectroactivity in *Saccharomyces cerevisiae* by Michael Cressé Potter in 1911[1], a lot of progress in understanding the biology foundations of this phenomenon have been made. At the turn of the 21st century, the work of Kim *et al.*[2]–[4] and Rabaey *et al.*[5],[6] laid the ground for in increasing interest in the practical application of electricity generation from microorganisms. Up to this day, the widespread adoption of this technology is nevertheless still hampered by the limited current and power outputs of most of the prototypes developed.

However, the potential low-cost and robustness of an electrochemical system powered by autonomous microorganisms are appealing in this era of energy transition. Improving the efficiency of MFCs must rely on the synergetic participation of numerous fields. Progress can be made by better understanding the biology of exoelectrogenic microorganisms. Improvements must also be made on understanding the specific underpinning of bacteria/electrode electron transfer. On this topic, the development of new materials to optimize the bacterial colonization as well as the electron transfer efficiency has to be proposed. Finally, efforts should be made on optimizing the architecture of full-scale microbial fuel cells in industrial conditions.

In this context, this work has focused on developing several MFC bioanodes designs and synthesis processes based on the electrospinning technique – electrospun carbon microfibers, composite carbon–polymer and core-shell fibers membranes. The electrospun electrodes were first colonized by the model electroactive bacterial strain *Shewanella oneidensis* CRBIP17.141. This facultative anaerobe is able to perform both mediated and direct electron transfer and is closely phylogenetically related to *Shewanella oneidensis* MR-1 which has been extensively studied for its EET abilities. The different electrodes design limitations were identified and their respective performances evaluated. Finally, the developed electrodes were studied using actual wastewater for fuel, in order to gain insight on their behavior under real conditions.

Firstly, the electrospinning technique was used to synthetize **a carbon microfibers bioanode** from polyacrylonitrile through a multi-step approach. The colonization of the membranes by *S. oneidensis* was conducted either in situ or ex situ, the latter reducing the required lag-phase induced by the bacteria adaptation to the electrode. The stacking of precolonized bioanodes was also exploited in order to design thick 3D ready-to-use bioanodes. In situ colonized electrospun carbon membrane exhibited power and current densities of about 56 mW·m^{-2} and 240 mA·m^{-2} respectively – which are noticeably better than a conventional commercial carbon felt tested in the same conditions (19 mW·m^{-2} and 100 mA·m^{-2}). Stacked precolonized electrodes showed even better power and current densities up to 210 mW·m^{-2} and 1119 mA·m^{-2} or **volume power density of up to 200 to 300 W·m^{-3} which is comparable to the best power densities achieved in the literature for similar conditions and conventional anodes (~ 2.1·10^{3} A·m^{-3} & 500 W·m^{-3})**[7], without any reactor optimization. However, the performances of the thickest 3D bioanodes tend to stall over around

1 mm in thickness due to the poor diffusion of the nutrients toward their core. The long-term stability of these systems is hampered by bacterial biofilm overgrowth. Additionally, the synthesis of the electrospun carbon electrode remains relatively complex, and require a lot of steps.

In parallel, the **long-term storage of precolonized bioanodes was achieved by cryodesiccation**, which ensures a good conservation of the material architecture and bacteria exoelectrogenic activity, without harming its performances past the quick lag-phase to reach its peak output.

The bypass of the impractical heat treatments was then attempted by electrospinning **one-step conductive composite carbon–polymer fibers**. Formulations exhibiting electrical conductivities up to $2{\cdot}10^{-2}$ $S{\cdot}cm^{-1}$ were obtained and **exhibited suitable electrochemical performances**. This process was then adapted with a dual electrospinning approach to fabricate a fiber mat made of a primary low-conductivity mat – such as the core-shell fibers subsequently presented – intermingled with a conductive carbon–polymer scaffold. The survival and electrochemical activity of Shewanella oneidensis on a composite carbon black–polymer electrospun mat was then studied and showed no toxicity to the cells. Additionally, the integration of a composite electrospun membrane into an MFC reactor demonstrated an electrochemical activity intensity similar to other bioanode, albeit with different oxidation peaks shapes on cyclic voltammetry curves. The long-term stability of the corresponding MFC was far better than observed for electrospun carbon electrode-based reactors, with no biofilm overgrowth detectable. The performances exhibited by the bioanode were impressive – **volume current and power densities of $3.74{\cdot}10^{3}$ $A{\cdot}m^{-3}$ & 225 $W{\cdot}m^{-3}$**, respectively. An eventual decrease in current output was nevertheless observed and the electrospun membranes still required a subsequent bacterial colonization.

A one-step process to directly electrospin electroactive bacteria encapsulated into core-shell fibers embedded in a conductive network was then developed. Because they already encapsulate bacteria, their thickness can be easily tuned by stacking electrospun layers together similarly to the 3D carbon microfibers bioanode presented previously, and can be cryodesiccated for long-term storage. Altogether, we have developed a lab-made electrospinning apparatus and setup to coelectrospin core-shell fibers which varied from collapsed ribbons with hollow core to round-section filled fibers. Bacteria were also successfully encapsulated inside the fibers core and a process providing a dual electrospun network of core-shell fibers intermingled with a conductive polymer–carbon scaffold was developed. The electrical conductivity of the resulting membrane (~ 10^{-2} to 10^{-3} $S{\cdot}cm^{-1}$) was satisfactory for a bioelectrode. The integrated bioanode was then included into an MFC and **exhibited current and power densities similar to those of the precolonized electrospun carbon membrane (volume current density of 3620 $A{\cdot}m^{-3}$ and power density of 230 $W{\cdot}m^{-3}$** compared with 1140 $A{\cdot}m^{-3}$ and 296 $W{\cdot}m^{-3}$ for the precolonized carbon membranes). Additionally, the open-circuit emf of the cell is lower for the integrated bioanode than for the electrospun carbon electrode (0.18 V vs. 0.73 V) and the polarization curves differ, probably due to different dominant EET mechanisms and dynamics observed in the case of composite carbon–polymer bioanodes. **Additionally, the long-term stability of the integrated bioanode seems better than in the case of the electrospun carbon electrodes, apparently due to a reduced anarchic biofilm development in the interfiber space thanks to the bacteria encapsulation.**

The performances of the **two main electrospun bioanodes designs developed in this work using actual wastewaters as a fuel** and microorganisms source were evaluated. In particular, abiotic **electrospun carbon electrodes** from Chapter 2 were shown to exhibit clearly better performance when used with this anolyte rather than with MR-1/L medium colonized with solely *S. oneidensis* (**current and power densities of respectively $4.4 \cdot 10^3$ $A \cdot m^{-3}$ & 438 $W \cdot m^{-3}$ vs. $1.14 \cdot 10^3$ $A \cdot m^{-3}$ & 296 $W \cdot m^{-3}$**), with similar long-term stability. **Cryodesiccated integrated bioanode** from Chapter 4 was shown to exhibit a better current density output – **up to 1500 $mA \cdot m^{-2}$** with a steady maximum output of **1100 $mA \cdot m^{-3}$ vs. a maximum 700 $mA \cdot m^{-2}$** – than its MR-1 counterpart. Additionally, the long-term stability and performances of the system seem to also be better than the electrospun carbon electrode in these conditions, but would also need more investigations. Eventually, 16S rRNA sequencings of the DNA extracted from wastewater and bioanodes before and after MFC operation were performed. They revealed the complex microbial ecology of the wastewaters, underlining the presence of many electroactive bacteria. The exoelectrogenic strains were enriched by the MFC cycling while the non-electroactive tended to be depleted. In particular, the main electroactive strains detected belonged to the genus *Arcobacter*, reported to perform IET as well as probably DET exoelectronic transfer[8].

PROSPECTS

Overall, the electrospun bioanodes designed, synthetized and characterized in this work show promising performances for further MFC applications. All the electrodes presented exhibit in particular remarkable volume-normalized current and power densities either when colonized by the model bacterium *Shewanella oneidensis* or when used with an actual wastewater anolyte. Moreover, the biofouling seen in electrospun carbon or composite membranes has mostly been addressed with the encapsulation of the bacteria in core-shell fibers, and the long-term storage of the bioanodes is guaranteed by a simple and robust cryodesiccation protocol. Nevertheless, it still exists room for the improvement of the presented designs, and their further integration into actual MFC devices may be considered.

- The improvement of the composite electrospun electrode as well as the integrated bioanode may be undertaken by trying to reduce the proportion of polymer binder used in the formulations. The main downside of these designs is that they are still relatively little conductive when compared with the electrospun carbon electrode. However, their promising performances in MFC as well as their better long-term stability justifies their usefulness, and reducing this last drawback would make them a very interesting platform, event with non-biological loading which could be explored.

- The most outstanding performances of the presented electrospun bioanode is their high volume current and power density. This remarkable performances may not be best highlighted in the bulky lab-scale reactors used for their convenience in this work. A particularly adapted platform for this technology would be the integration into paper-based MFCs[9],[10], which are cheap, miniaturized, on the rise, and particularly well adapted to the dimensions of electrospun electrodes.
- The last chapter of this work was focused on the application of the developed electrospun bioanodes for electricity generation from wastewaters. This attempt to use our systems in more actual conditions has been mainly successful and encouraging. Nevertheless, more work on this matter would be welcome, especially concerning the long-term stability of the setups and their interaction with the wastewater bacterial consortia (especially in the case of the integrated bioanode). Additionally, it would be interesting to integrate the electrospun design into other bioelectrochemical systems than MFCs, such as microbial electrolysis, microbial desalination cells, or bioremediation setups.

Eventually, electrospinning appears as a promising technique for the development of microscopically controlled architectures. Its application to the design and synthesis of electrodes for microbial fuel cells applications is however largely underexplored, and more work on this matter can assuredly lead to further interesting progresses.

REFERENCES

[1] M. C. Potter. Electrical Effects Accompanying the Decomposition of Organic Compounds. *Proc. R. Soc. B Biol. Sci.* **84,** 260–276 (1911).

[2] B. H. Kim, D. H. Park, P. K. Shin, I. S. Chang & H. J. Kim. Mediator-less biofuel cell. (1999).

[3] H. Joo *et al.* A mediator-less microbial fuel cell using a metal reducing bacterium , Shewanella putrefaciens. *Enzyme Microb. Technol.* **30,** 145–152 (2002).

[4] B. H. Kim *et al.* Enrichment of microbial community generating electricity using a fuel-cell-type electrochemical cell. *Appl. Microbiol. Biotechnol.* **63,** 672–681 (2004).

[5] K. Rabaey, N. Boon, M. Höfte & W. Verstraete. Microbial phenazine production enhances electron transfer in biofuel cells. *Environ. Sci. Technol.* **39,** 3401–3408 (2005).

[6] K. Rabaey, N. Boon, S. D. Siciliano, M. Verhaege & W. Verstraete. Biofuel cells select for microbial consortia that self-mediate electron transfer. *Appl. Environ. Microbiol.* **70,** 5373–82 (2004).

[7] B. R. Ringeisen *et al.* High power density from a miniature microbial fuel cell using Shewanella oneidensis DSP10. *Environ. Sci. Technol.* **40,** 2629–2634 (2006).

[8] A. G. Pereira-Medrano *et al.* Quantitative proteomic analysis of the exoelectrogenic bacterium Arcobacter butzleri ED-1 reveals increased abundance of a flagellin protein under anaerobic growth on an insoluble electrode. *J. Proteomics* **78,** 197–210 (2013).

[9] J. Chouler, Á. Cruz-Izquierdo, S. Rengaraj, J. L. Scott & M. Di Lorenzo. A screen-printed paper microbial fuel cell biosensor for detection of toxic compounds in water. *Biosens. Bioelectron.* **102,** 49–56 (2018).

[10] G. Choi, D. J. Hassett & S. Choi. A paper-based microbial fuel cell array for rapid and high-throughput screening of electricity-producing bacteria. *Analyst* **140,** 4277–4283 (2015).

APPENDICES

TABLE OF CONTENTS

Appendices 285
A.1. Abbreviations 285
A.2. Chemicals references 287
A.3. Experimental methods 288
A.3.1. Electrospinning 288
A.3.2. Coelectrospinning spinneret design 288
A.3.3. Heat treatments 290
A.3.4. Electrochemical measurements 290
A.3.5. Impedance spectroscopy 290
A.3.6. X-ray diffraction 290
A.3.7. X-ray photoelectron spectroscopy 291
A.3.8. Raman spectroscopy 291
A.3.9. Fourier transform infrared spectroscopy 291
A.3.10. N_2 physical adsorption 291
A.3.11. Mercury intrusion porosimetry 291
A.3.12. Scanning electron microscopy & energy-dispersive X-ray spectroscopy 292
A.3.13. Epifluorescence microscopy 292
A.3.14. Confocal microscopy 292
A.3.15. Cryodesiccation 292
A.3.16. Ball-milling 292
A.3.17. Thermogravimetric analysis & differential scanning calorimetry 292
A.3.18. Bacterial culture 293
A.3.19. 16S rRNA sequencing 294
A.3.20. Microbial fuel cell setup 294
A.3.21. Data treatment 296

APPENDICES

A.1. Abbreviations

(v/v)	Volume proportions
(w/w)	Mass proportions
16S rRNA	Ribosomal ribonucleic acid
ADP	Adenosine diphosphate
AEM	Anion exchange membrane
AFM	Atomic force microscopy
ATP	Adenosine triphosphate
BET	Brunauer–Emmett–Teller theory
BOD_5	Biochemical oxygen demand (during 5 days of incubation at 20 °C in the dark)
CA	Chronoamperometry
CB	Carbon black – *Vulcan XC-72R*
***c*-Cyt**	Cytochrome c
CEM	Cation exchange membrane
cfu	Colony-forming unit
CPE	Constant phase element
CV	Cyclic voltammetry
DET	Direct electron transfer
DMF	N,N-dimethylformamide
DMRB	Dissimilatory metal-reducing bacteria
DNA	Deoxyribonucleic acid
DSC	Differential scanning calorimetry
EDX	Energy-dispersive X-ray spectroscopy
EET	Extracellular electron transfer
EFC	Enzymatic fuel cell
emf	Electromotive force
EPSs	Extracellular polymeric substances
FE-SEM	Field emission scanning electron microscopy
FIB	Focused-ion beam
FTIR	Fourier transform infrared spectroscopy

FWHM	Full width at half maximum
GFP	Green fluorescent protein
IET	Indirect electron transfer
LB	Lysogeny broth
MET	Mediated electron transfer
MFC	Microbial fuel cell
MR-1/L	MR1 minimal medium + 30 mM sodium lactate
MR-1/LF	MR1 minimal medium + 30 mM sodium lactate + 30 mM sodium fumarate
Mtoe	Million ton of oil equivalent
OCV	Open circuit potential
OD_{600}	Optical density at 600 nm
PAN	Poly(acrylonitrile)
PBS	Phosphate-buffered saline medium
PC	Polycarbonate
PCL	Poly(ε-caprolactone)
PEG	Poly(ethylene glycol)
PEO	Poly(ethylene oxide)
PS	Polystyrene
PVA	Poly(vinyl alcohol)
Ref.	Reference electrode – *Ag/AgCl, KCl saturated*
RH	Relative humidity
SEM	Scanning electron microscopy
SEM-FEG	Scanning electron microscopy–field-emission gun
SHE	Standard hydrogen electrode
SSA	Specific surface area
TGA	Thermogravimetric analysis
vol%	Percentage by volume
wt%	Percentage by mass
XPS	X-ray photoelectron spectroscopy
XRD	X-ray diffraction
σ_S	Surface conductivity
σ_T	Transverse conductivity

A.2. Chemicals references

	Chemical	CAS Registry Number	Molecular weight	Provider	Purity
Polymers	Poly(acrylonitrile)	25014-41-9	$M_w \sim 150\,000$	Sigma-Aldrich (USA)	–
	Poly(ε-caprolactone)	24980-41-4	$M_w \sim 14\,000$	Sigma-Aldrich (USA)	–
	Poly(ethylene oxide)	25322-68-3	$M_v \sim 600\,000$	Sigma-Aldrich (USA)	Contains 200-500 ppm BHT as inhibitor
Additives	Poly(ethylene glycol)	25322-68-3	$M_n \sim 3\,000$	Sigma-Aldrich (USA)	–
	Vulcan® XC-72R carbon black	1333-86-4	–	FuelCellStore	–
Solvents	N,N-dimethylformamide	68-12-2	–	VWR	≥99.8%, AnalaR NORMAPUR® ACS, Reag. Ph. Eur. analytical reagent
	Chloroform	67-66-3	–	VWR	99.0-99.4% stabilized, AnalaR NORMAPUR® ACS, Reag. Ph. Eur. analytical reagent

All chemicals were used as received, without further purification. Ultrapure water used for syntheses was obtained from a Milli-Q® Integral 10 system equipped with a Q-POD® dispenser. Electrolytes were prepared using the same system equipped with an E-POD® dispenser.

A.3. Experimental methods

A.3.1. Electrospinning

Electrospinning was performed under a fume hood in a poly(methyl methacrylate) box connected to the lab dry compressed air outlet using the Electrospinz (Blenheim, New Zealand) ES1™ lab-scale generator and apparatus. Fibers were collected on a grounded aluminum foil on a roller (**Figure A.1**). More thorough parameters for each setup are reported in each of the corresponding chapters.

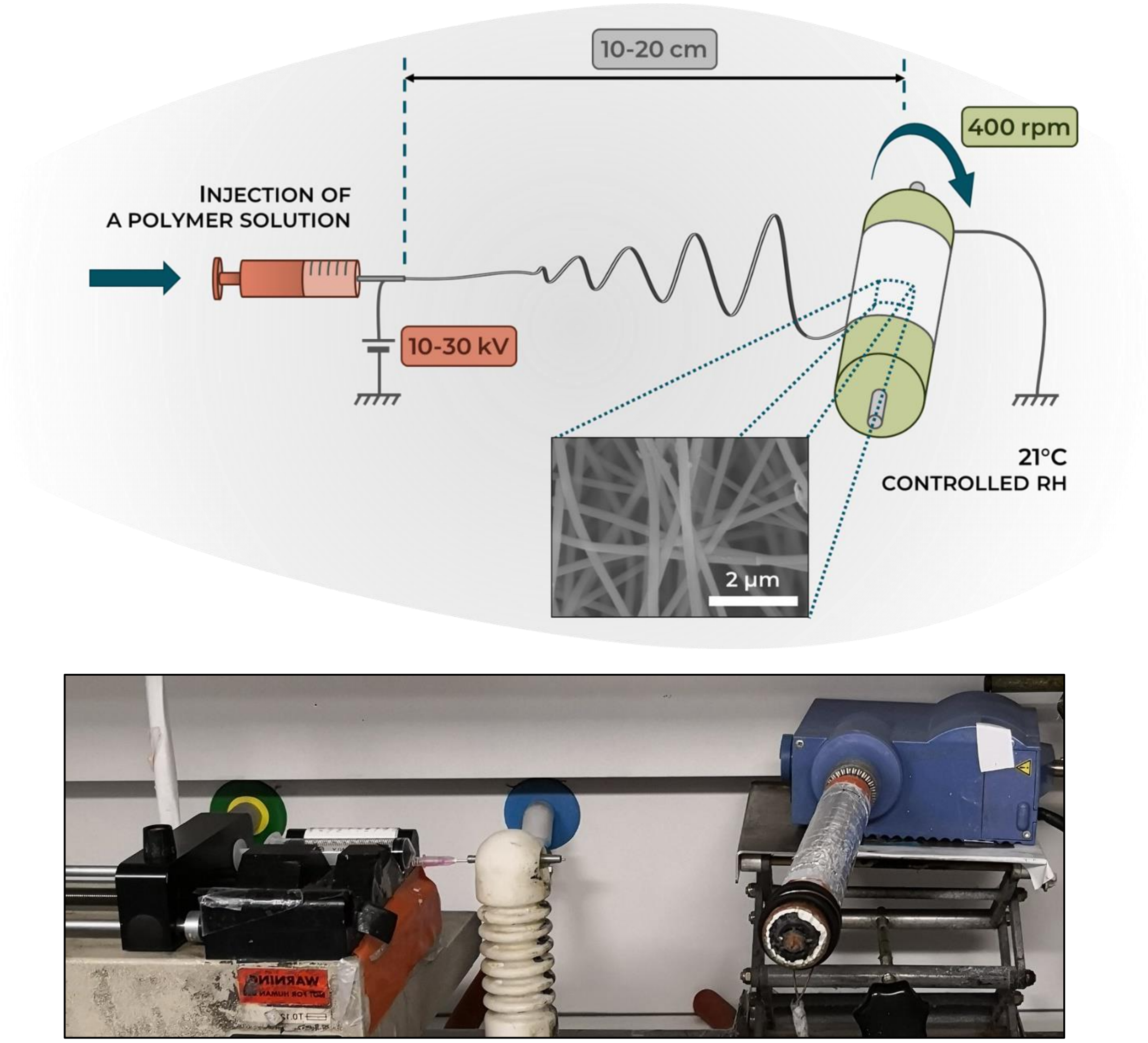

Figure A.1 – Overview of the base electrospinning setup, without box.

A.3.2. Coelectrospinning spinneret design

A coaxial electrospinning apparatus adapted to the laboratory electrospinning platform was developed for the production of coelectrospun fibers. The spinneret (**Figure A.2**) polymer parts were designed on the Autodesk® Fusion 360 software and printed on a Formlabs Form 2 3D-printer in the

FLGPGR04 photopolymer resin (**Figure A.3**). The resin is easily cleanable and resistant to the usual electrospinning solvents.

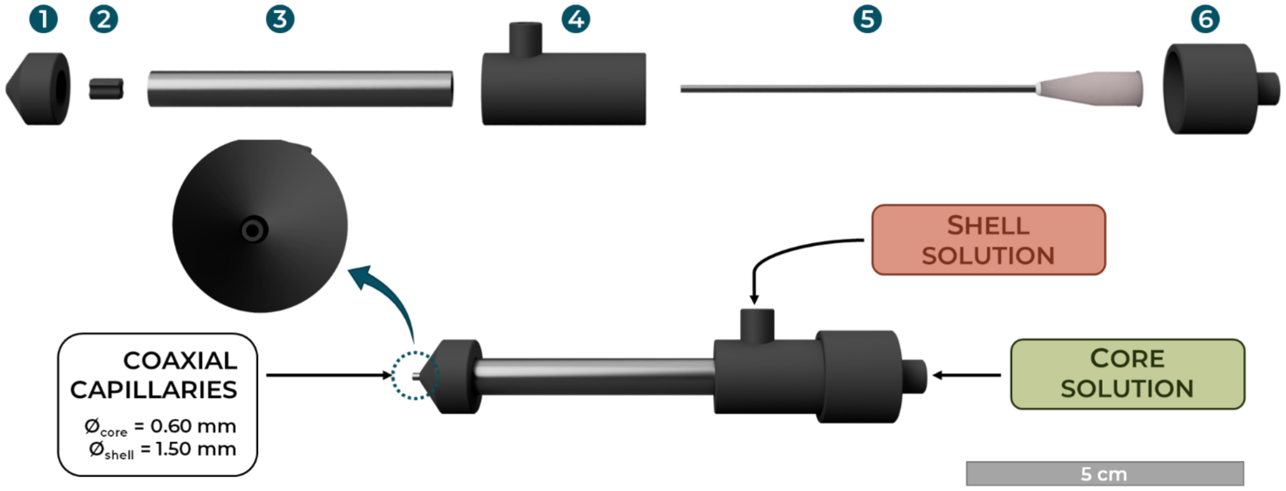
1
2
3
4
5
6
SHELL SOLUTION
CORE SOLUTION
COAXIAL CAPILLARIES
$\varnothing_{\text{core}}$ = 0.60 mm
$\varnothing_{\text{shell}}$ = 1.50 mm
5 cm

Figure A.2 – 3D-printed coaxial electrospinning spinneret.

The spinneret is composed of 5 pieces:

7. 3D-printed nozzle ($\varnothing_{\text{shell}}$ = 1.50 mm);
8. 3D-printed fluted centering piece;
9. Steel tube (Ø = 6 mm);
10. 3D-printed main body with shell solution entry;
11. Blunt-end needle ($\varnothing_{\text{core}}$ = 0.60 mm);
12. 3D-printed cap with core solution entry.

During its assembly, the various parts were sealed together and electrically isolated with tape. The internal needle is set to slightly protrude from the external nozzle.

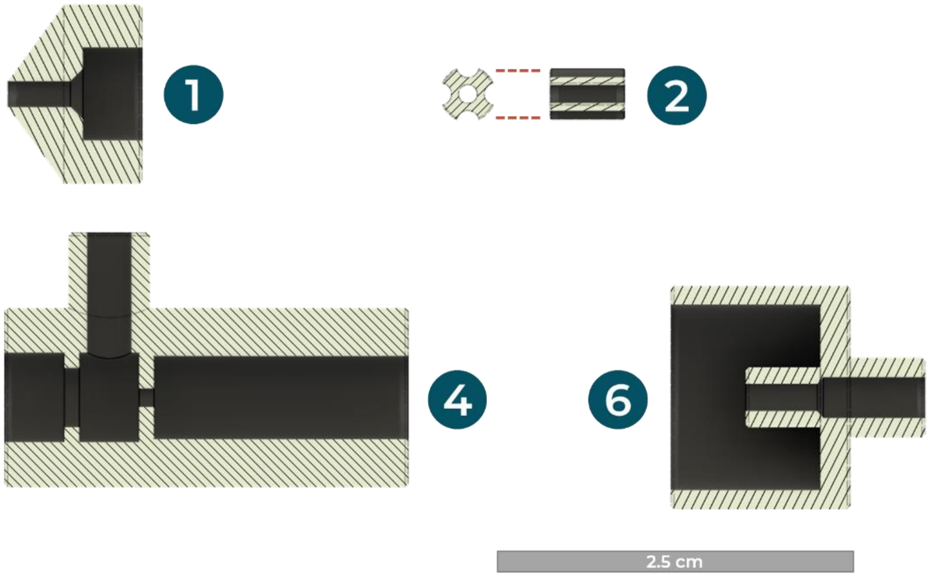

Figure A.3 – Radial cut of the spinneret 3D-printed parts.

A.3.3. Heat treatments

The stabilization step of the PAN membranes is conducted at 280°C under static air for 3 hours in a Thermo Scientific Heratherm oven.

The carbonization of the stabilized membrane is conducted under Ar inert atmosphere (Air Liquide; H_2O (5 bar) < 3 ppm, C_nH_m < 0.5 ppm, O2 < 2 ppm; flow rate around 250 $mL \cdot min^{-1}$) in a custom-made tubular quartz oven (Eraly & Associés, Fontenay-le-Fleury, France) equipped with a West Pro 16 temperature regulator (**Figure A.4**).

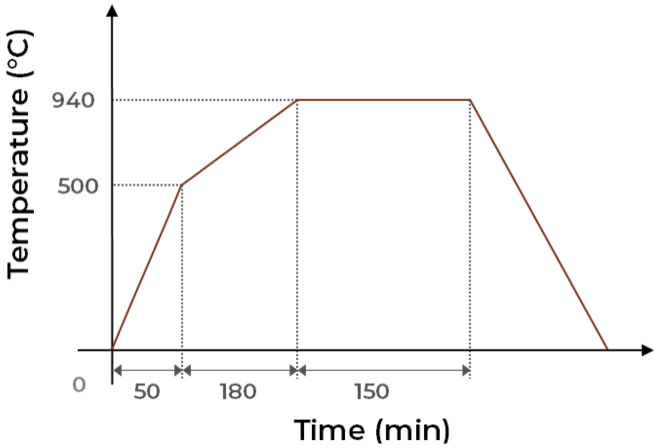

Figure A.4 – Oven settings for the carbonization step.

A.3.4. Electrochemical measurements

Electrochemical measurements (cyclic voltammetry, chronoamperometry, open circuit voltage follow-up and chronopotentiometry) were performed with a Bio-Logic VSP potentiostat (Claix, France) controlled by the software EC-Lab®.

Three-electrode setups used a platinum counter-electrode and an Ag/AgCl, KCl saturated reference. Two-compartment fuel cells electrochemical measurements used an Ag/AgCl, KCl saturated reference.

A.3.5. Impedance spectroscopy

Impedance spectroscopy was performed in Swagelok cell setup on a Solartron Instruments SI 1260 Impedance/Gain-phase analyzer on the ZView software with an AC amplitude of 100 mV and a frequency ranging from 10^7 to 1 Hz.

A.3.6. X-ray diffraction

X-ray diffraction was performed on a Bruker D8 Advance diffractometer with a Cu K_α (λ_1 = 1.5405 Å, λ_2 = 1.5443 Å) radiation source and a LYNXEYE XE detector. The XRD patterns were recorded for 15 minutes in the 2θ range of 30-70° at a continuous scan rate of $4° \cdot min^{-1}$.

A.3.7. X-ray photoelectron spectroscopy

XPS measurements were performed using an omicron NanoTechnology ESCA+ with an Al K_α (hν = 1486.6 eV) radiation source by Antoine Miche (*Laboratoire de Réactivité de Surface*) at the *Institut des Matériaux de Paris Centre* in association with the *Centre National de la Recherche Scientifique*. The emission of photoelectrons from the sample was analyzed at a takeoff angle of 45° under ultrahigh vacuum conditions ($1\cdot10^{-9}$ Pa). The XPS spectra were collected at a pass energy of 20 eV for C1s, O1s, N1s, core XPS levels. The area of the sample analysis is approximately 1 mm^2. The binding energy values were charge-corrected to the carbon C1s excitation set at 285.0 eV. The peak areas were determined after subtraction of the Shirley background. The atomic ratios were calculated after normalization using Scofield factors. The spectrum processing was carried out using the Casa XPS software package.

A.3.8. Raman spectroscopy

Raman spectroscopy was performed on a Renishaw inVia™ Reflex confocal Raman microscope equipped with an Ar laser source (514.5 nm) with Encarnación Raymundo Piñero (*Conditions Extrêmes et Matériaux: Haute Température et Irradiation*). A very low incident power (≈ 1 mW) was used to avoid heating effects or a possible modification of the microstructure. Data was treated with the SpectraGryph 1.2 software to harmonize the baselines of the samples.

A.3.9. Fourier transform infrared spectroscopy

FTIR measurements were performed with solid samples on a PerkinElmer Spectrum 400 spectrometer and treated with the SpectraGryph 1.2 software.

A.3.10. N_2 physical adsorption

The specific surface determination of the samples was conducted by N_2 physical adsorption at 77 K on a BELSORP-max device. Results were treated using the Brunauer–Emmett–Teller theory equation on the range $0.05 \geq P/P_0 \geq 0.20$ on the BELMaster™ 6.1.0.1 software. Samples were degassed for 12 hours under turbomolecular pump vacuum (10^{-5} to 10^{-6} Torr) at 393 K before any BET measurement.

A.3.11. Mercury intrusion porosimetry

The porosity of the samples was analyzed by mercury intrusion porosimetry on a Micromeritics Autopore IV. The micropores and mesopores volumes and the pore size distribution were determined by a NLDFT method with a slit shape pore model applied on N_2 adsorption data. The meso and macro pore size distributions from mercury intrusion porosimetry have been obtained from the pressure vs. intrusion data using the Washburn equation.

A.3.12. Scanning electron microscopy & energy-dispersive X-ray spectroscopy

The microstructure of the electrodes was observed by SEM on a Hitachi S-3400. SEM images were obtained with an accelerating voltage of 8 kV. Samples were metallized with 15 nm of gold prior to observation. Biological samples were air-dried for 24 hours before metallization and subsequent observation.

EDX measurements were performed on an X-Max Oxford EDX detector coupled with the SEM using 10 kV with a silicon standard.

Additional SEM-FEG measurements were performed on a Hitachi SU-70 (*Institut des Matériaux de Paris Centre*) with an accelerating voltage of 10 kV with David Montero.

FE-SEM imaging coupled with focused ion beam was performed on a Zeiss AURIGA CrossBeam Focused Ion Beam Electron Microscope with Stephan Borensztajn (*Institut de Physique du Globe de Paris*) on samples metalized with 15 nm of platinum.

A.3.13. Epifluorescence microscopy

Epifluorescence microscopy was performed on a Zeiss Axio Imager D1. The images obtained were post treated on the ImageJ software.

A.3.14. Confocal microscopy

Confocal microscopy was performed on a Leica TCS SPE and a Leica TCS SP5 with France Lam (*Institut de Biologie Paris-Seine*). The stacked images obtained were post treated on the Zeiss ZEN Blue and ImageJ software.

A.3.15. Cryodesiccation

Cryodesiccation was performed by freezing the samples in liquid nitrogen (-195.79°C) in a centrifuge tube. They are then placed in a Christ Alpha 2-4 LD freeze-dryer inside a vial under high vacuum. The drying operation was performed at -85°C and 0.12 mbar for 24 hours.

Cryodesiccated samples were then stored at 4°C until further use.

A.3.16. Ball-milling

Grinding of samples by ball-milling was performed using zirconium dioxide balls at 80 rpm in a polyethylene vial.

A.3.17. Thermogravimetric analysis & differential scanning calorimetry

Thermal investigations were performed on a TA Instruments SDT Q600 TGA-coupled thermoscale with Benoît Fleury (*Laboratoire Interfaces et Systèmes Électrochimiques*). The two thermoscale beams are tarred with a platinum crucible in each. 7.78 mg of sample is placed in one of the crucible, the other one with the empty reference crucible. Measurements are conducted under compressed air flow with temperature ramp of 5°C·min^{-1} between 20 and 800°C.

A.3.18. Bacterial culture

The growth media were prepared as follow:

Lysogeny broth (LB) Lennox medium (dry medium purchased from Sigma-Aldrich): 10 g·L^{-1} tryptone, 5 g·L^{-1} yeast extract, 5 g·L^{-1} NaCl are dissolved in Milli-Q water and adjusted at pH = 7. The medium is sterilized by autoclaving at 120°C for 20 minutes.

MR-1 minimal medium (chemicals purchased from Sigma-Aldrich): 0.46 g·L^{-1} NH_4Cl, 0.225 g·L^{-1} K_2HPO_4, 0.057 g·L^{-1} $MgSO_4{\cdot}7H_2O$, 0.225 g·L^{-1} KH_2PO_4, 0.225 g·L^{-1} $(NH_4)_2SO_4$ are dissolved in Milli-Q water. The solution is supplemented with solutions of trace elements (3.0 g·L^{-1} EDTA-$Na_2{\cdot}2H_2O$, 1.1 g·L^{-1} $FeSO_4{\cdot}7H_2O$, 0.19 g·L^{-1} $CoCl_2{\cdot}6H_2O$, 0.042 g·L^{-1} $ZnCl_2$, 0.024 g·L^{-1} $NiCl_2{\cdot}6H_2O$, 0.018 g·L^{-1} $Na_2MoO_4{\cdot}2H_2O$, 0.30 g·L^{-1} H_3BO_4, 0.002 g·L^{-1} $CuCl_2{\cdot}2H_2O$, 0.050 g·L^{-1} $MnCl_2{\cdot}4H_2O$ dissolved in Milli-Q water, adjusted to pH = 6.5, autoclaved at 120°C for 20 minutes) and selenite (0.50 g·L^{-1} NaOH, 0.003 g·L^{-1} $Na_2SeO_3{\cdot}5H_2O$, 0.004 g·L^{-1} $Na_2WO_4{\cdot}2H_2O$ in Milli-Q water, autoclaved at 120°C for 20 minutes), each at 0.1 % in volume. The resulting medium is then sterilized by autoclaving at 120°C for 20 minutes and supplemented with solutions of vitamins (4 mg·L^{-1} 4-aminobenzoic acid, 1 mg·L^{-1} D(+)-biotin, 10 mg·L^{-1} nicotinic acid, 5 mg·L^{-1} calcium D-pantothenate, 10 mg·L^{-1} pyridoxamine dihydrochloride, 10 mg·L^{-1} thiaminium dichloride, 50 mg·L^{-1} riboflavin dissolved in Milli-Q water, sterilized by ultrafiltration on a 0.22 µm membrane) and amino acids (2 g·L^{-1} L-glutamic acid, 2 g·L^{-1} L-arginine, 2 g·L^{-1} DL-serine, dissolved in Milli-Q water, sterilized by ultrafiltration on a 0.22 µm membrane), each at 0.1 % in volume. The pH is ultimately adjusted to 7 and the medium sterilized by ultrafiltration on a 0.22 µm membrane.

MR-1/Lactate (MR-1/L) medium: MR-1 minimal medium supplemented with 30 mM of sodium lactate (Sigma-Aldrich).

MR-1/Lactate-Fumarate (MR-1/LF) medium: MR-1 minimal medium supplemented with 30 mM of sodium lactate and 30 mM of sodium fumarate (Sigma-Aldrich).

LB-agar plates: Prepared by dissolving 12 g of agar powder (Sigma-Aldrich) in 1 L of LB medium. The medium is sterilized by autoclaving at 120°C for 20 minutes, and 20 mL of the resulting solution at ~ 60°C was poured into a Petri dish (100 mm x 15 mm) in sterile conditions. The plates were left to cool down and solidify and stored upside down sealed with Parafilm® M at 4°C. The plates were used within a week.

Phosphate-buffered saline medium: Prepared by dissolving PBS tablets (Sigma-Aldrich) in Milli-Q water. Sterilized by ultrafiltration on a 0.22 µm membrane.

The culture protocol of *Shewanella oneidensis* was the following:

Strain conservation: The *Shewanella oneidensis* CRBIP17.141 aliquot provided by the CRBIP is stored at -80°C in a glycerol stock (50 vol% overnight bacterial culture in LB medium, 50 vol% of 1:1 (w/w) glycerol in sterilized Milli-Q water).

Bacterial pre-culture: 15 mL of oxic sterile LB medium is inoculated with a fraction of the thawed aliquot and cultivated for 24 hours at 30°C and 150 rpm in an incubator.

Bacterial culture: 50 mL of oxic sterile MR-1/LF medium is inoculated with 1 mL of the pre-culture medium in sterile flasks for 8 hours at 30°C and then overnight at 21°C. The cell density is then determined by measuring the optical density of the cultured medium at 600 nm (OD_{600}) with a spectrophotometer. All subsequent changes in medium are done by centrifuging the cells at 5000 g for 20 minutes at 4°C before resuspending them in the desired conditions.

A.3.19. 16S rRNA sequencing

The bacterial DNA from wastewater samples was extracted using the ZR Fecal DNA Kit (Zymo Research) according to the provided protocol. The DNA was quantified fluorometrically at 260 nm using the Qubit dsDNA HS Assay Kit (Invitrogen). It was then frozen at -20°C and shipped on dry ice to MR DNA (Shallowater, Texas, USA) for sequencing. Barcoded amplicon sequencing of the hypervariable V3-V4 region of the 16S ribosomal rRNA gene (16S rRNA, primers 341F and 785R) was performed using bTEFAP technology. A single-step 30 cycle PCR using HotStarTaq Plus Master Mix Kit (Qiagen, Valencia, CA, USA) was performed under the following conditions: 94°C for 3 minutes, followed by 28 cycles of 94°C for 30 seconds; 53°C for 40 seconds and 72°C for 1 minute; with a final elongation step at 72°C for 5 minutes. Successful amplification was verified by gel electrophoresis. Resulting amplicon products from different samples were mixed in equal concentrations and purified using Agencourt Ampure beads (Agencourt Bioscience Corporation, MA, USA) and sequenced by Illumina MiSeq (Illumina, USA) paired end (2x 300 bp) sequencing. Sequence data was processed using a proprietary analysis pipeline (www.mrdnalab.com, MR DNA). Paired end reads were merged and barcode and primers sequences were trimmed. Short sequences < 150 bp, sequences with ambiguous base calls, and sequences with homopolymer runs exceeding 6 bp were removed. The remaining reads were then denoised, and clustered at 97% sequence similarity. Singleton sequences and chimeras were excluded from analyses. Taxonomic assignment was based on a local nucleotide BLASTN algorithm search against a curated database derived from GreenGenes, RDPII and NCBI. Between $12 \cdot 10^3$ and $13 \cdot 10^4$ sequences were obtained from each sample.

A.3.20. Microbial fuel cell setup

The MFC lab-scale setup (**Figure A.5**) main body has been custom made in polyethylene, with silicone O-ring ensuring the sealing of the cell (**Figure A.6**).

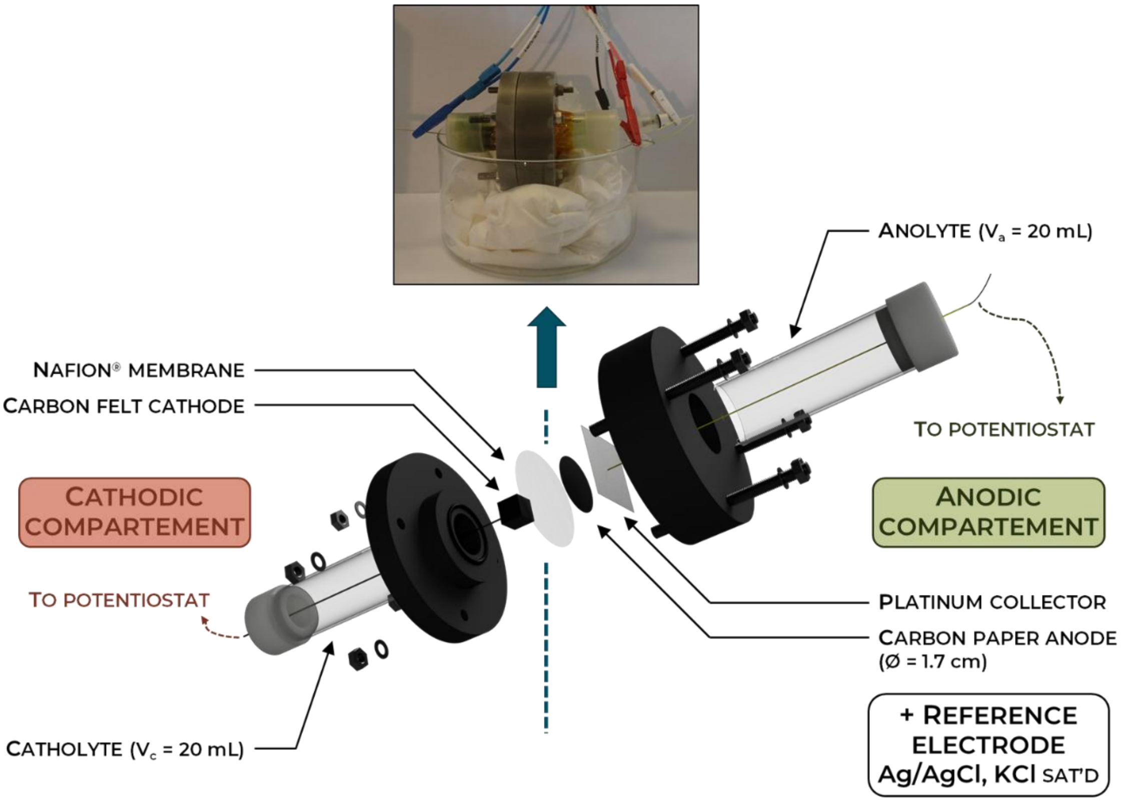
ANOLYTE (V_a = 20 mL)
TO POTENTIOSTAT
NAFION® MEMBRANE
CARBON FELT CATHODE
CATHODIC COMPARTEMENT
ANODIC COMPARTEMENT
TO POTENTIOSTAT
PLATINUM COLLECTOR
CARBON PAPER ANODE (Ø = 1.7 cm)
+ REFERENCE ELECTRODE Ag/AgCl, KCl SAT'D
CATHOLYTE (V_c = 20 mL)

Figure A.5 – Lab-scale two-compartment microbial fuel cell setup.

The 20 mL anodic and cathodic compartments are fabricated from the bodies of Terumo® 30cc syringes. The Nafion® proton exchange membrane (Nafion® NRE-212, 50 µm thick, Sigma-Aldrich) is cut to the setup dimensions (Ø ≈ 2.5 cm) and pretreated with concentrated HNO_3 overnight and subsequently rinsed with distilled water until its neutralization. The platinum mesh collector connected to the denuded part of a WCT30 wire (Radiospare) isolated from the anolyte with 3M™ polyimide 1218 electrical tape and is inserted with the help of a needle through a silicon folding skirt sealing the anodic compartment. The skirt is pierced to allow the insertion of a reference electrode. The carbon felt cathode is connected to a Terumo® hypodermic needle which passes through a silicon folding skirt sealing the cathodic compartment. The assembly is sealed by tightening 4 screws passing through the two parts of the body, ensuring the contact of the platinum mesh with the anode.

All the assembly is conducted under sterile conditions in a biosafety cabinet from sterilized parts (UV light for 30 minutes for the Nafion®, 70 % ethanol in water for the reference electrode and autoclaving at 120°C for 20 minutes for the other parts).

Anode and cathode sides are loaded through the skirts with hypodermic needle with the corresponding electrolytes (catholyte: 150 mM of NaCl (supporting electrolyte) and 100 mM of $K_3[Fe(CN)_6]$; anolyte: MR-1/L sterile or colonized with *S. oneidensis* or wastewaters).

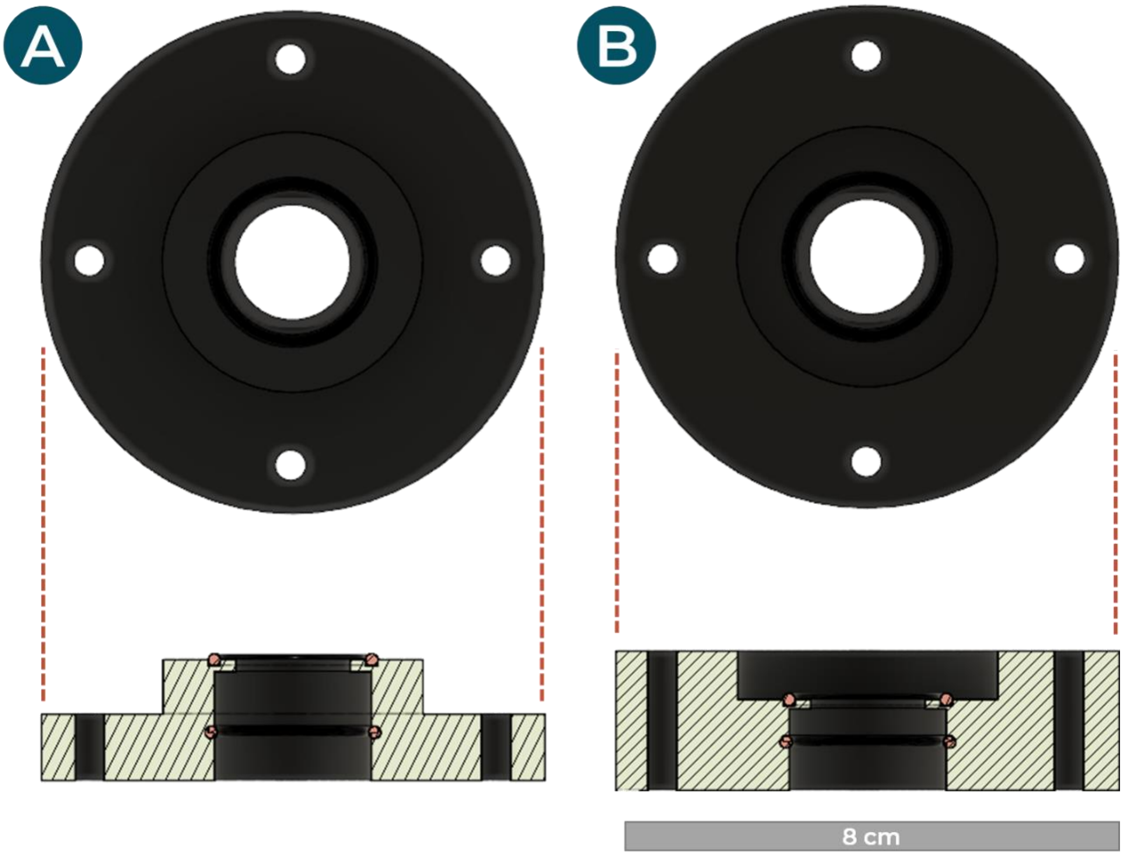

Figure A.6 – Radial cut of the 2 parts of the MFC reactor body: (A) Cathodic side; (B) Anodic side.

A.3.21. Data treatment

Data treatment was performed on Microsoft Excel if not otherwise specified.

Abstract: Amidst anthropogenic climate change, alternatives to fossil fuel power sources must be developed. Originating in an observation by M. C. Potter dating back from 1911[1], increasing research has shown that the idea of harvesting the metabolic activity of microorganisms to generate electricity is realistically achievable. These devices, microbial fuel cells (MFC), focus on converting chemical energy from organic matter into electricity by gathering electrons produced by bacteria degrading these molecules[2]. Such fuel cells may be used as renewable energy sources but a lot of challenges need to be addressed before they become an efficient, stable and profitable technology[3]. Various approaches to tackle these problems exist. For instance, the electronic transfer between the bacterium and the electrode can be improved by working on the organism or the consortium used to degrade the organic matter[4]. Here we seek to improve the material and the architecture of the electrochemical system and especially those of the bacteria-colonized anode. We start from the observations of the limitations of the current electrodes for MFCs to design a better system.

This work focuses on the conception of the bioanode of a microbial fuel cell by electrospinning. This process allows the shaping of nano to micro-scaled polymer fibers through electrically-assisted extrusion[5]. We obtain nonwoven mats of polymer fibers which are made conductive by subsequent heat treatments or by the addition of carbon-based materials. The colonization of these electrospun membranes by the model electroactive bacteria *Shewanella oneidensis* is conducted through diverse approaches: natural biofilm development – either in situ or ex situ – or core-shell encapsulation. Once prepared, the anodes are then integrated into a functional lab-scale fuel cell in order to evaluate their electrochemical characteristics. The impact of the colonization of these conductive electrodes on the electrochemical performances of a full MFC is then discussed. The performances of the novel architectures are assessed and compared with the literature and exhibit remarkable volume-normalized current and power outputs – up to $3.26\cdot10^{3}$ $A\cdot m^{-3}$ and 296 $W\cdot m^{-3}$ vs. $2.08\cdot10^{-3}$ $A\cdot m^{-3}$ and 500 $W\cdot m^{-3}$ for optimized reactors with the same electrolytes and bacteria[6]. A long-term storage method of the bioanodes based on cryodesiccation is henceforth presented. Eventually, the electrodes developed in this work are integrated into an MFC setup including real effluents from wastewaters. Their performances in current generation from an actual power source are investigated and are shown to be encouraging – $4.4\cdot10^{3}$ $A\cdot m^{-3}$ and 438 $W\cdot m^{-3}$.

Keywords: Electrochemistry; Materials; Microbiology; Electrospinning; Biofuel cell; Clean energy.

[1] M. C. Potter. Electrical Effects Accompanying the Decomposition of Organic Compounds. *Proc. R. Soc. B Biol. Sci.* **84,** 260–276 (1911).

[2] K. Rabaey & W. Verstraete. Microbial fuel cells: Novel biotechnology for energy generation. *Trends Biotechnol.* **23,** 291–298 (2005).

[3] B. E. Logan & K. Rabaey. Conversion of Wastes into Bioelectricity and Chemicals by Using Microbial Electrochemical Technologies. *Science* **337,** 686 LP – 690 (2012).

[4] B. E. Logan. Exoelectrogenic bacteria that power microbial fuel cells. *Nat. Rev. Microbiol.* **7,** 375–381 (2009).

[5] J. F. Cooley. Apparatus for electrically dispersing fluids. (1899).

[6] B. R. Ringeisen *et al.* High power density from a miniature microbial fuel cell using Shewanella oneidensis DSP10. *Environ. Sci. Technol.* **40,** 2629–2634 (2006).